

8-2017

## HIGH-THROUGHPUT MAPPING OF THE BIOLOGICAL EFFECTS OF PARTICLE THERAPY

Lawrence Bronk

Follow this and additional works at: [https://digitalcommons.library.tmc.edu/utgsbs\\_dissertations](https://digitalcommons.library.tmc.edu/utgsbs_dissertations)

 Part of the [Medical Biophysics Commons](#)

---

### Recommended Citation

Bronk, Lawrence, "HIGH-THROUGHPUT MAPPING OF THE BIOLOGICAL EFFECTS OF PARTICLE THERAPY" (2017). *The University of Texas MD Anderson Cancer Center UTHealth Graduate School of Biomedical Sciences Dissertations and Theses (Open Access)*. 750.  
[https://digitalcommons.library.tmc.edu/utgsbs\\_dissertations/750](https://digitalcommons.library.tmc.edu/utgsbs_dissertations/750)

This Dissertation (PhD) is brought to you for free and open access by the The University of Texas MD Anderson Cancer Center UTHealth Graduate School of Biomedical Sciences at DigitalCommons@TMC. It has been accepted for inclusion in The University of Texas MD Anderson Cancer Center UTHealth Graduate School of Biomedical Sciences Dissertations and Theses (Open Access) by an authorized administrator of DigitalCommons@TMC. For more information, please contact [digitalcommons@library.tmc.edu](mailto:digitalcommons@library.tmc.edu).

HIGH-THROUGHPUT MAPPING OF THE BIOLOGICAL EFFECTS OF  
PARTICLE THERAPY

by

*Lawrence Fernando Bronk, B.S., M.S.*

APPROVED:

---

David Grosshans, M.D., Ph.D.  
Advisory Professor

---

Laurence Court, Ph.D.

---

Sunil Krishnan, M.D.

---

Steven Lin, M.D., Ph.D.

---

Narayan Sahoo, Ph.D.

---

Jason Stafford, Ph.D.

---

APPROVED:

---

Dean, The University of Texas  
MD Anderson Cancer Center UTHealth Graduate School of Biomedical Sciences

HIGH-THROUGHPUT MAPPING OF THE BIOLOGICAL EFFECTS OF  
PARTICLE THERAPY

A

DISSERTATION

Presented to the Faculty of

The University of Texas

MD Anderson Cancer Center UTHealth

Graduate School of Biomedical Sciences

in Partial Fulfillment

of the Requirements

for the Degree of

DOCTOR OF PHILOSOPHY

by

Lawrence Fernando Bronk, B.S., M.S.  
Houston, Texas

August, 2017

## **Dedication**

This work and my hopes for its future are dedicated to my grandparents,

Lalo and Lala; Eustolio and Delia

and

Grandma and Grandpa; Cynthia and Norman



## Acknowledgements

Being a graduate student, it's difficult to remember all the people who have helped your development due to the sheer amount of aid needed throughout your studies. This number is even more compounded when you've been in graduate school for almost a decade. I will likely be unsuccessful generating a complete list of everyone who has contributed towards my development into a scientist, but I will do my best. With that said, to anyone whom I've had the pleasure of encountering, working with, learning from, or even just sharing some camaraderie with during my graduate studies, please know that I am truly grateful for your involvement in my life during this time.

First and foremost, I would like to sincerely thank my Ph.D. advisor, Dave Grosshans, for his mentorship and stalwart support during my graduate studies. He fanned the flames and invigorated my enthusiasm for research in so (/too) many ways. In his lab, I've learned more biology topics than I ever thought I would. After my stay in the Grosshans' Group, I am almost comfortable saying I'm a radiation biologist as opposed to a "fake biologist". You are a leader in the truest sense whose guidance and involvement has set me up achieve my career aspirations. Thank you.

I would like to acknowledge my supervisory committee, Dr. Laurence Court, Dr. Sunil Krishnan, Dr. Steven Lin, Dr. Narayan Sahoo, and Dr. Jason Stafford, for their insightful discussions, helpful technical suggestions, and valuable recommendations as to research avenues to pursue. A special acknowledgment goes to Dr. Stafford for agreeing to be on my various committees for all 8 years of my time at the GSBS.

I would also like to recognize the direction received from previous committee members from my advisory and examining committees, Dr. Edward Jackson, Dr. James

Bankson, Dr. Oliver Bogler, Dr. Wadih Arap, and Dr. Renata Pasqualini. Thank you all for your advocacy. I would like to extend an additional amount of gratitude to Drs. Arap and Paqualini for facilitating my early career development in their lab. I would also like to give my appreciation to the Schissler and Rosalie B. Hite graduate fellowships for their financial support during my studies.

Hearty thanks go out to all my collaborators and mentors throughout the years. Dr. Wouter Driessen for agreeing to take a fresh physics undergraduate student and teach him some chemistry and biology. Mary Sobieski and Dr. Clifford Stephan for their roles in developing the high-throughput clonogenic assay analysis workflow. Dr. Amir Abdollahi, Dr. Ivana Dokic, Claudia Rittmueller, and Dr. Stephan Brons for enabling my first steps into the fascinating field of heavy ion research. Dr. Erik Sulman and Dr. Ravesanker Ezhilarasan for sparking my research interest in neuro-oncology and with glioma stem cells in particular. I would also like to express my gratitude towards the other members of the Grosshans Lab, Dr. Wei Zhou, Dr. Die Zhang, Dr. Connie Weng, Mr. Thanh Lam, Dr. Jeff Dinh, Mr. Kevin Tran, Ms. Duo Ma, and Mr. Ben Kroger for introducing me to academic neuroscience as well as their constant fellowship as lab mates throughout my graduate experience.

I would like to express my thankfulness to my close collaborators in the Radiation Physics department, Dr. Radhe Mohan, Dr. Uwe Titt, Dr. Howard Thames, Dr. Dragan Mirkovic, Dr. Darshana Patel, and Dr. Chris Peeler. For sharing their knowledge, enthusiasm for radiation biology, and scotch. Also, Dr. Gabriel Sawakuchi and his group members, especially Conor McFadden and David Flint, for solidifying my technical inclination towards microscopy, unfettered confocal microscope access, and their inclusiveness.

Extraordinary recognition goes to Dr. Fada Guan and Mr. Matt Kerr. Gentlemen, it has been a true honor to work those long nights and early mornings with you. Please accept my most candid show of gratitude: without you none of this research would have been possible. Thank you so much for your time and dedication to this line of research.

Finally, I would also like to acknowledge my immediate family. My mother, father, and brother for their aid in nurturing and encouraging my desire and drive to become a scientist to positively affect this world. My children, Arthur and Amelia, for pushing my maturity to develop a bit faster than I planned while making me cognizant of how little sleep a person can actually live on. I would also like to thank my family-in-law for all their acceptance, hospitality, and aid in the transition to parenthood in this tumultuous time of life. And lastly, my wife, Julianna Bronk, for her endless love and support in all of my endeavors and late night experiments.

# HIGH-THROUGHPUT MAPPING OF THE BIOLOGICAL EFFECTS OF PARTICLE THERAPY

Lawrence Fernando Bronk, M.S.

Advisory Professor: David Grosshans, M.D., Ph.D.

Radiation therapy is an essential tool in the cure of many cancer patients. Charged particle based radiation therapies are gaining momentum as the physical dose distributions of ions are superior to standard photons due their limited range. Additionally, charged particle radiation has been shown to have linear energy transfer (LET) specific relative biological effectiveness (RBE) when compared to photons. It is essential to employ accurate biophysical models for particle beams in order to maximize the therapeutic potential of particle therapy through the introduction of biologically optimized treatment planning. The development of such models requires the support of large amounts of accurate physical and biological data for each pristine beam. Unfortunately, such data are limited and difficult to obtain.

This work presents the development of a high-throughput irradiation methodology that utilizes automated high-throughput screening techniques to sample multiple locations along a therapeutic ion therapy beam in a single irradiation. Using a special irradiation apparatus designed and validated by our group, RBEs of adherent lung cancer cell lines at 12 positions along proton beams at the MD Anderson Proton Therapy Center (PTC) and the Heidelberg Ion Therapy (HIT) facility were measured. RBEs for helium and carbon ion

beams were also measured at the HIT facility. This system was further employed to perform image-based, high-throughput mechanistic DNA damage response studies following exposure to particles at varying LETs. Furthermore, the biological response to particles was examined in additional model systems including glioma stem cell spheroids and normal rat brain organoids.

For protons, all model systems demonstrated a rapid rise in RBE beyond the Bragg peak. These findings contrast with several current model predictions which assume the RBE trend linearly scales with proton LET. For the heavier particle measurements, we found absolute RBE values and relative trends comparable to literature values. However, overkill effects occurred for lower LETs than previously reported. DNA damage response assays correlated with RBE measurements.

The discrepancy between model predictions and experimental data, especially in the high-LET regions, requires rigorous experimental validation to ensure the accuracy of existing models. The developed high-throughput irradiation system enables the rapid measurement of biological response data which will contribute to a more complete mapping of particle biological effects as well as biological susceptibilities of different cell types to charged particle radiation. Ultimately, this knowledge will contribute to more comprehensive biophysical models and the production of biologically optimized intensity-modulated particle therapy plans.

## Table of Contents

<b>1. Dedication.....</b>	<b>iii</b>
<b>2. Acknowledgements .....</b>	<b>iv</b>
<b>3. List of Figures.....</b>	<b>xii</b>
<b>4. List of Tables .....</b>	<b>xv</b>
<b>5. List of Abbreviations.....</b>	<b>xvi</b>
<b>6. Introduction.....</b>	<b>1</b>
<b>Overview of radiation therapy and the current work .....</b>	<b>1</b>
<b>Physical mechanisms of action.....</b>	<b>5</b>
<b>Treating cancer with radiotherapy.....</b>	<b>10</b>
<b>Biologically optimized treatment planning.....</b>	<b>11</b>
<b>Biological models and endpoints.....</b>	<b>13</b>
Clonogenic survival .....	13
The linear-quadratic model .....	16
Relative biological effectiveness.....	17
DNA damage repair and complexity.....	19
3-dimensional tissue culture and organoids .....	22
Modeling the relationship of dose, LET, and RBE .....	22
<b>7. Methods.....</b>	<b>24</b>
<b>Monte Carlo Simulations.....</b>	<b>24</b>
<b>2D Cell Culture.....</b>	<b>24</b>
Cryogenic retrieval and cell line stock creation .....	24
Cell lines and media.....	25
Culturing and passaging.....	27
Determining cell concentration.....	27
Traditional clonogenic assay.....	28
High-throughput clonogenic assay.....	29
Doubling time determination .....	30
SF calculation and fitting .....	31
Relative biological effectiveness calculation .....	32
Immunofluorescent staining of DSB markers .....	33
Immunofluorescent imaging of DSB markers.....	36
Immunofluorescence data analysis .....	36
<b>3D Cell Culture.....</b>	<b>54</b>
Glioma stem cell (GSC) lines and media .....	54
GSC maintenance and culturing.....	54

GSC spheroid formation .....	55
Rat brain microtissues (RBMTs) .....	56
Rat brain microtissue receiving and culturing.....	56
RBMT replating.....	57
Spheroidal culture media refreshment.....	58
Spheroid high resolution scans .....	58
Spheroid size measurements .....	59
3D surviving fraction calculation.....	71
Viability .....	73
RBMT immunofluorescent staining.....	73
RBMT immunofluorescent imaging .....	75
RBMT image analysis.....	76
RBMT histology .....	76
Statistical analyses and plotting .....	77
<b>8. Results.....</b>	<b>78</b>
<b>Development of a high-throughput irradiation platform .....</b>	<b>78</b>
<b>Optimizing the high-throughput clonogenic assay .....</b>	<b>95</b>
Fixation timing for optimal colony scoring.....	95
Incubator effects.....	97
Addition of a limit of detection.....	97
<b>Benchmarking traditional vs high-throughput clonogenic assay .....</b>	<b>104</b>
<b>High-throughput clonogenic assay results for adherent cells .....</b>	<b>106</b>
Control radiation: photon SF and RBE .....	106
Particle irradiation surviving fractions.....	110
Proton .....	110
Jig 1.0 .....	110
Jig 2.0 .....	110
Helium.....	111
Carbon.....	112
<b>RBEs.....</b>	<b>124</b>
Proton.....	124
Helium and carbon ions .....	130
<b>High-throughput immunofluorescent results .....</b>	<b>133</b>
Protons at MD Anderson Proton Therapy Center .....	133
Helium and carbon ion irradiations performed at HIT .....	141
<b>GSC high-throughput results .....</b>	<b>147</b>
Growth curves.....	147
Surviving fractions.....	151

RBEs .....	151
<b>Rat brain microtissue response to proton irradiation .....</b>	<b>160</b>
Size .....	160
Viability .....	161
RBMT composition after radiation .....	172
Immunofluorescent staining .....	172
<b>9. Discussion .....</b>	<b>183</b>
<b>10. Conclusion .....</b>	<b>197</b>
<b>11. References .....</b>	<b>200</b>
<b>12. Vita.....</b>	<b>223</b>



## List of Figures

Figure 1. Comparison of the application of protons and photons for radiation therapy .....	4
Figure 2. Basic comparison of the dose deposition of a clinical proton and photon beam. ....	7
Figure 3. The formation of an SOBP. ....	8
Figure 4. LET present within an SOBP. ....	9
Figure 5. Representative DSB foci image.....	21
Figure 6. Overview of Monte Carlo simulation setup vs reality.....	26
Figure 7. Cytation5 software procedure tab.....	37
Figure 8. Cytation5 setup for automated imaging. ....	38
Figure 9. Cytation5 setup for the blue channel. ....	39
Figure 10. Cytation5 setup for the green channel. ....	40
Figure 11. Cytation5 setup for the red channel. ....	41
Figure 12. Overview of CellProfiler workflow for foci scoring.....	42
Figure 13. CellProfiler setup parameters for nuclei detection. ....	43
Figure 14. CellProfiler setup parameters for nuclei expansion.....	44
Figure 15. CellProfiler foci filter for red channel setup.....	45
Figure 16. CellProfiler foci filter for green channel setup.....	46
Figure 17. CellProfiler foci red channel mask setup.....	47
Figure 18. CellProfiler foci green channel mask setup.....	48
Figure 19. CellProfiler measurement parameters to score green foci.....	49
Figure 20. CellProfiler measurement parameters to score red foci. ....	50
Figure 21. Selecting type of measurements for objects detected with a CellProfiler pipeline. .....	51
Figure 22. Correlating measurements between objects in CellProfiler. ....	52
Figure 23. Exporting data in CellProfiler. ....	53
Figure 24. Cell3Imager scan setup.....	60
Figure 25. Cell3Imager high-resolution plate scan.....	61
Figure 26. Cell3Imager well center orientation. ....	62
Figure 27. Cell3Imager well segmentation. ....	63
Figure 28. Cell3Imager spheroid measurement. ....	64
Figure 29 Cell3Imager size measurement pre-processing parameters. ....	65
Figure 30. Cell3Imager size measurement object detection parameters.....	66
Figure 31. Cell3Imager size measurement live or dead detection parameters. ....	67
Figure 32. Cell3Imager measurement window.....	68
Figure 33. Cell3Imager measurement window with scored spheroids displayed.....	69
Figure 34. Cell3Imager plate information window.....	70
Figure 35. Demonstration of TGD determination.....	72
Figure 36. Traditional vs high-throughput clonogenic assays.....	79
Figure 37. Image analysis workflow for the high-throughput clonogenic assay.....	80

Figure 38. Concept of a variable range shifter for high-throughput irradiations.....	82
Figure 39. Simulated proton beam in Lucite used to select sampling locations.....	83
Figure 40. Physical setup for high-throughput irradiations. ....	84
Figure 41. Relative jig doses from film measurement.....	86
Figure 42. Relative doses and LETs calculated for the physical setup of the initial Jig. ....	87
Figure 43. Physical setup for high-throughput irradiations with second Jig design.....	90
Figure 44. Surface tension in a 96-well plate. ....	91
Figure 45. Simulated 81.4 MeV proton beam in Lucite used to select sampling locations for second Jig design. ....	92
Figure 46. Relative dose and LETs per column in the second Jig design. ....	93
Figure 47. Automated colony detection and scoring for H460 cells. ....	96
Figure 48. Raw surviving fraction data from a high-throughput experiment. ....	99
Figure 49. Colony types present in the clonogenic assay at 20x magnification. ....	100
Figure 50. Visualization of the limits of detection. ....	101
Figure 51. Clonogenic SF results following LOD application. ....	102
Figure 52. LOD applied HT clonogenic data over appropriate axes ranges.....	103
Figure 53. Benchmarking of HT versus manual clonogenic assay.....	105
Figure 54. H460 Photon SF for different sources. ....	107
Figure 55. H460 RBE for Cs-137, 6 MV, and 18 MV photon sources. ....	108
Figure 56. HT clonogenic assay H460 results. ....	113
Figure 57. HT clonogenic assay H1437 results. ....	114
Figure 58. HT clonogenic assay H460 results using second version of the Jig.....	116
Figure 59. HT clonogenic assay H460 results from proton irradiations performed at HIT..	118
Figure 60. HT clonogenic assay H460 results from helium ion irradiations performed at HIT. .....	120
Figure 61. HT clonogenic assay H460 results from carbon ion irradiations performed at HIT. .....	122
Figure 62. Initial proton RBE results obtained using the first version of the high-throughput irradiation apparatus. ....	126
Figure 63. Proton RBEs obtained from the second Jig version. ....	127
Figure 64. Compiled proton RBE results.....	128
Figure 65. Proton, helium and carbon ion RBE results from HIT irradiations.....	131
Figure 66. Representative DSB repair kinetics.....	134
Figure 67. Normalized DSB repair kinetics with fit. ....	135
Figure 68. Induction foci vs dose and LET.....	136
Figure 69. Persistent foci vs dose and LET. ....	137
Figure 70. Correlation between persistent DSBs and SF.....	139
Figure 71. Induced and persistent DSBs vs LET for protons. ....	140
Figure 72. Helium ion DSB repair kinetics. ....	143
Figure 73. Temporal DSB repair following exposure to carbon ions.....	144

Figure 74. Dose-normalized induced foci at 30 mins post-irradiation for proton, helium, and carbon ion beams. ....	145
Figure 75. Dose-normalized persistent foci for proton, helium, and carbon ion beams. ....	146
Figure 76. Representative GSC size measurements following irradiation with protons with the HT system. ....	148
Figure 77. 4D representation of GSC23 response. ....	149
Figure 78. Growth constant calculations. ....	150
Figure 79. GS7-11 SFs. ....	152
Figure 80. GSC300 SFs. ....	153
Figure 81. GSC23 SFs. ....	155
Figure 82. GSC RBEs. ....	157
Figure 83. GSC RBEs with applied photon RBE. ....	159
Figure 84. RBMT size response following exposure to photons produced by Cs-137. ....	162
Figure 85. RBMT size response following exposure to 3 keV/ $\mu$ m protons. ....	163
Figure 86. RBMT size response following exposure to 10 keV/ $\mu$ m protons. ....	164
Figure 87. RBMT size response following exposure to 16 keV/ $\mu$ m protons. ....	165
Figure 88. RBMT size comparison at 50 days post-irradiation. ....	166
Figure 89. Fit to day 50 RBMT size data. ....	167
Figure 90. RBE at 50% of RBMT size. ....	168
Figure 91. Viability of RBMTs following exposure to photons and protons with LETs of 3, 10, or 16 keV/ $\mu$ m. ....	169
Figure 92. Response fit to RBMT viability data. ....	170
Figure 93. RBE at 50% viability for RBMTs. ....	171
Figure 94. Immunofluorescent staining of unirradiated control RBMTs at 80 days. ....	174
Figure 95. Immunofluorescent staining of RBMTs at 80 days following exposure to 1Gy. ....	175
Figure 96. Immunofluorescent staining of RBMTs at 80 days following exposure to 2Gy. ....	176
Figure 97. Immunofluorescent staining of RBMTs at 80 days following exposure to 5Gy. ....	177
Figure 98. Immunofluorescent staining of RBMTs at 80 days following exposure to 10Gy. ....	178
Figure 99. Immunofluorescent staining of RBMTs at 80 days following exposure to 20Gy. ....	179
Figure 100. Immunofluorescent staining of RBMTs at 80 days following exposure to 40Gy. ....	180
Figure 101. Quantification of beta III tubulin expression. ....	181
Figure 102. Quantification of GFAP expression. ....	182
Figure 103. Application of measured RBEs to pristine proton beam. ....	194
Figure 104. RBEs applied to a traditional SOBP. ....	195
Figure 105. Achieving a uniform SOBP response. ....	196

## List of Tables

Table 1. Volumes and concentrations used for IF. ....	35
Table 2. Calculated LETs for each proton jig version. ....	94
Table 3. Fitting parameters and RBEs for H460 photon exposures. ....	109
Table 4. H460 and H1437 LQ fitting parameters from Jig 1.0 proton irradiations. ....	115
Table 5. H460 LQ fitting parameters from Jig 2.0 proton irradiations performed at MDA. ....	117
Table 6. H460 LQ fitting parameters from Jig 2.0 proton irradiations performed at HIT....	119
Table 7. H460 LQ fitting parameters from helium ion irradiations performed at HIT. ....	121
Table 8. H460 LQ fitting parameters from carbon ion irradiations performed at HIT.....	123
Table 9. Compiled proton RBE values. ....	129
Table 10. Heavy ion RBE values. ....	132
Table 11. GS7-11 and GSC300 LQ fitting parameters.....	154
Table 12. GSC23 LQ fitting parameters. ....	156
Table 13. Compiled GSC RBE values. ....	158

## List of Abbreviations

CFU	colony forming unit
CTV	clinical treatment volume
DAPI	4',6-diamidino-2-phenylindole
DDR	DNA damage response
DNA	deoxyribonucleic acid
DMSO	dimethyl sulfoxide
DSB	double strand break
EGF	epidermal growth factor
FBS	Fetal bovine serum
GFAP	glial fibrillary acid protein
GSC	glioma stem cell
Gy	Gray (J/kg)
FGF	fibroblast growth factor
HIT	Heidelberg Ion Therapy Center
HR	homologous recombination
HT	high-throughput
IF	immunofluorescence
IMPT	intensity modulated proton therapy
Jig	high-throughput irradiation apparatus
LEM	local effect model
LET	linear energy transfer
Linac	linear accelerator

LPL	lethal potentially lethal
LOD	limit of detection
LQ	linear quadratic
LQL	linear quadratic linear
MC	Monte Carlo
MDA	MD Anderson Cancer Center
MFO	multi-field optimized
MKM	microdosimetric-kinetic-model
NBM	neural basal medium
NHEJ	non-homologous end joining
NSCLC	non-small cell lung cancer
PBS	phosphate buffered saline
PE	plating efficiency
PFA	paraformaldehyde
PIDE	particle irradiation data ensemble
PSPT	passively scattered proton therapy
PTC	Proton Therapy Center
RBE	relative biological effectiveness
RBMT	rat brain microtissue
RMF	repair-misrepair-fixation
RT	room temperature
TGD	tumor growth delay
SD	standard deviation

SE	standard error
SEM	standard error of the mean
SF	surviving fraction
SFM	serum free media
SFO	single field optimized
SOBP	spread-out Bragg peak

## Introduction

Overview of radiation therapy and the current work

Radiotherapy is the targeted application of high-energy radiation to damage and kill cancer cells while sparing surrounding healthy tissues. Approximately 60% of cancer patients receive radiation in their treatment regime, often as the primary curative modality (1, 2). Historically, external source radiation delivery was achieved using high energy gamma photons produced from the radioactive decay of unstable elements. The most prevalent radioisotope utilized was Cobalt-60 ( $T_{1/2} = 5.3$  years) which produces photons with energies of 1.17 MeV and 1.33 MeV for an average energy of 1.25 MeV. Co-60 is still presently used in many areas around the world, especially in locations without consistent access to electricity. The development of the linear accelerator (linac) in the 1920s eventually enabled the generation of bremsstrahlung photons, also known as x-rays, with clinical application beginning in the late 1950s (3). Later, the development of linear and circular particle accelerators allowed for the acceleration of particles heavier than electrons to clinically relevant energies.

While external beam radiotherapy is most often delivered with photons, or x-rays, in recent years, there has been a growing interest towards utilizing charged particles to treat patients. The motivation for using charged particle radiation as opposed to photons was initially based on protons having a finite range allowing for improved dose distributions covering the target tumor volume while reducing distal normal tissue damage (Figure 1). However, it became evident that ions also exhibit unique biological effects compared to photons with the biological response being directly related to the particle type as well as its energy. Harnessing the differential biological effects of a given therapeutic ion beam by



placing the regions with minimum biological effect in normal tissues and those with increased efficacy in the tumor volume are the main tenants driving biologically optimized particle therapy.

Due to the purposed benefits associated with charged particle or ion therapy, it is becoming an increasingly utilized radiation therapy modality. As the overall cost of particle therapies continues to drop, it is predicted that the number of centers will increase dramatically (4). While the most common form of charged particle therapy centers solely use protons, there are 11 centers in the world already utilizing ions heavier than protons for clinical treatments.

The clinical benefits of proton therapy, and to some degree particle therapy, remain controversial due to the significantly increased costs and the as yet unconfirmed therapeutic advantage compared to standard photon-based therapies for many disease presentations; however, within the scientific literature, there is increasing evidence suggesting certain ions present optimal peak to entrance dose biological effect as well as unique biological responses to charged particle radiation including metastatic suppression and anti-tumor immune activation (5-7).

In the current clinical practice of proton radiation therapy, the relative biological effectiveness (RBE) of protons is a constant factor of 1.1 (8-10). This uniform RBE value designates that to achieve an iso-effective response as compared to a photon-based treatment, the dose delivered by protons must be reduced by 9.1%, an assumption derived from experimental data mainly obtained at the middle of a spread-out Bragg peak (SOBP) region from passive-scattering proton therapy (PSPT). Protons, being one of the lightest charged particles frequently used in the clinic, are likely subject to a reduced signal to noise ratio

when performing biological measurements due to the relatively small proportion of the beam exhibiting high RBE, resulting in an unclear relationship between biological outcomes.

The standard proton beam delivery technique is now transitioning to a more advanced beam scanning technology. This development allows for intensity-modulated proton therapy (IMPT) by optimizing each constituent proton beamlet. While efforts have been made to associate physical quantities with preclinical models to predict biologic effects of protons, most of the existing models were developed based on data generated with PSPT and may not be suitable to accurately predict the biological consequences for scanning beams due to the differences in beam characteristics.

To facilitate the rapid measurement of accurate and precise proton beam biological effects, our group has developed a methodology employing biological screening techniques and a unique irradiation system (11). This method can readily be applied to additional particle types used or under consideration for clinical use. Coupling these two high-throughput methods has enabled for efficient mapping of the biological effects of proton and heavier charged particle radiation in several model systems spanning both cancer and normal tissue.



Figure 1. Comparison of the application of protons and photons for radiation therapy. A demonstrative treatment plan for a cranio-spinal irradiation (top) and focal radiation therapy in the brain (bottom) from Dinh et al. published in Translational Cancer Research. Treatment with protons results in improved dose distributions and reduces excess radiation to off target volumes. Image from (12).

## Physical mechanisms of action

The main requirement for external beam therapy is that the radiation must penetrate through tissue to reach the deep-seated tumor volume. Charged particle and photon radiation therapies ultimately achieve this effect but with different dose deposition profiles. X-rays are the most common radiation used for cancer treatment. The metric used to denote the type of photons delivered in the clinical setting is the accelerating potential experienced by the electrons used to generate the x-rays. Accelerating voltage ranges are vendor and machine-specific, however, values between 4 and 18 MV are typical. The photon beam produced within a linac utilizing the bremsstrahlung effect will contain a spectrum of photon energies from a maximum energy of the accelerating potential to low energies. Low energy photons are typically filtered out prior to leaving the linac. Upon entering a material, photons primarily interact with the electrons present in an energy-dependent manner. These interactions ionize local atoms by imparting energy to overcome electron binding energy thus ejecting electrons from their initial location. The energized electrons will traverse the material and deposit all the gained energy before finally coming to rest. In essence, a photon beam can be viewed as creating a distributed electron field.

While photon interactions are stochastic in nature, protons constantly interact with the medium they are traversing through with the energy deposition described by the Bethe equation. As such, charged particles (electrons, protons, heavy ions, etc.) continuously lose energy via electronic interactions as they traverse through a material. The rate of energy loss increases as the particles lose energy. This phenomenon results in a dose deposition profile in which the deposited energy is low at the entrance of a material and slowly increases with depth. Towards the end of the particle range, the imparted energy rapidly increases and

abruptly drops to near zero when the particles stop via nuclear interactions. The highest point of a charged particle dose deposition curve is known as the Bragg peak. In clinical practice, most commonly, multiple beams are summed to apply a uniform dose over the tumor volume. The summation of multiple particle beams to form a uniform dose volume is known as a spread-out Bragg peak (SOBP) (Figure 3).

Physical parameters typically used to describe the particle energy transference over the sensitive volume include the track- and dose-averaged linear energy transfer ( $LET_t$  and  $LET_d$ ), with  $LET_d$  more frequently cited (Figure 4). Listing the depth of the measurement as a quantifying metric for comparison is also common due to inherent limitations and complications Monte Carlo (MC) code packages experience with low energy physics interactions. A further confounding factor is that the particles within a clinically relevant volume can exhibit a large energy distribution making the determination of LET effects difficult.

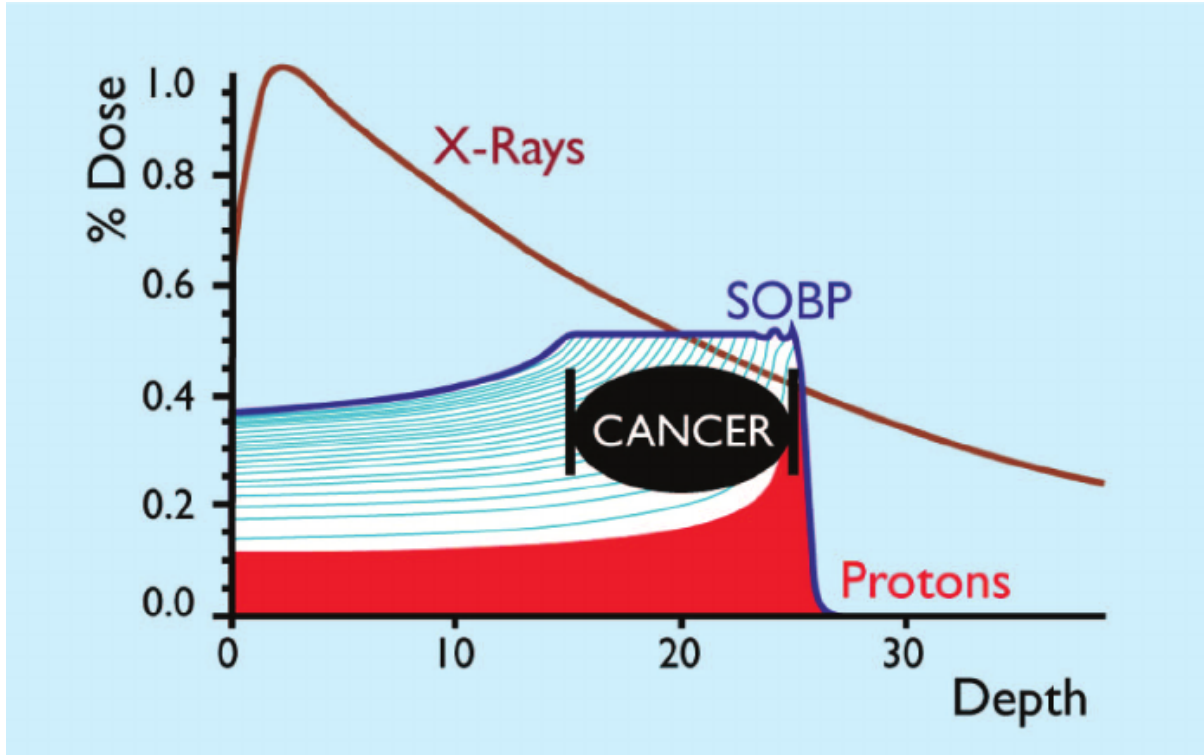


Figure 2. Basic comparison of the dose deposition of a clinical proton and photon beam. Upon entering a material, photon beams have an initial increase in the dose deposition as the photons interact with the material's electrons and the ejected electron buildup reaches electronic equilibrium. After this point, photons deposit dose in a stochastic manner following an exponential decay relationship. Protons, being charged particles, have a finite range within a material. This range is dependent on the initial particle energy. For a deep-seated tumor, the radiation beam must penetrate the patient to reach the volume resulting in dose deposited in healthy tissue. The photon beam will continue beyond the tumor volume, depositing dose to distal tissues whereas the proton beam is made to stop after the cancerous volume. Published by the Australian National Proton Facility Steering Committee in 2001. Accessed from (13).

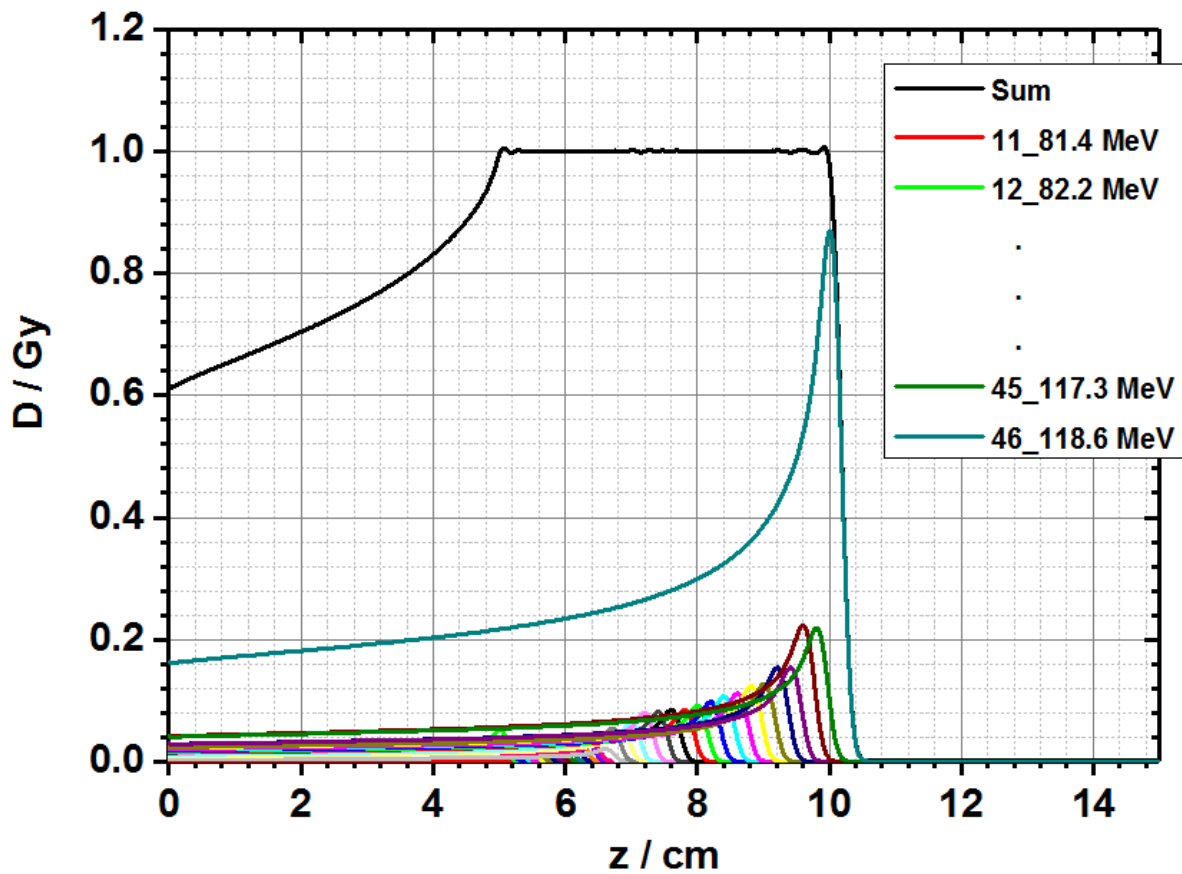


Figure 3. The formation of an SOBP. The current practice in proton therapy is to treat the tumor volume with a uniform physical dose and uniformly apply the biological correction factor of 1.1 to the total irradiated volume. A spread-out Bragg peak is created by the superposition of multiple beam energies. Historically this spread was achieved by passing the beam through a multi-tiered spinning modulation wheel that would effectively present different material thicknesses to the beam entering the treatment room from the beam line. Newer spot scanning technology changes the beam energy at the synchrotron to achieve a similar effect.

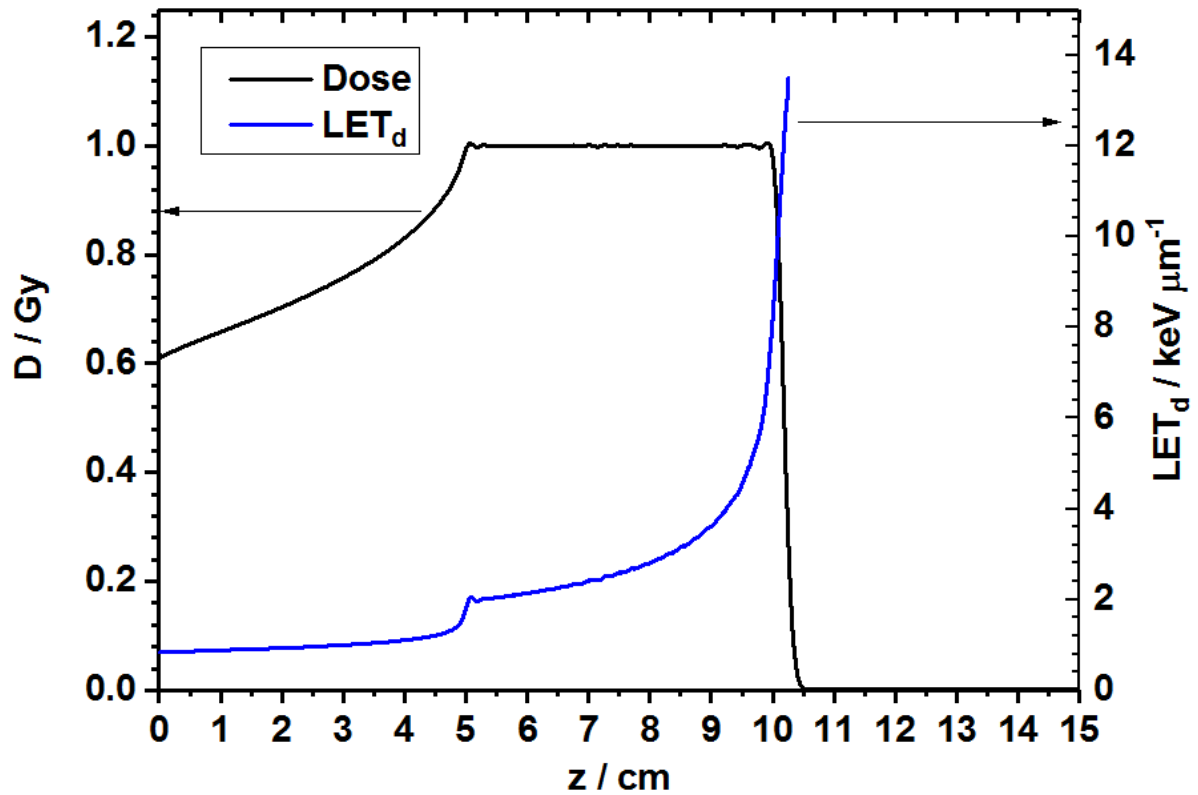


Figure 4. LET present within an SOBP. The LET present within the entrance plateau of a clinical proton beam is initially low. The SOBP is created by the addition of protons with numerous energies. As the protons within a given beamlet begin to slow down and stop their LET increases. The first LET increase is due to the lowest energy protons stopping within the SOBP. The LET then increases with depth as a relatively larger portion of the total beam begins to stop. The distal portion of the SOBP is derived from a single initial beam energy (Figure 3). The superposition of numerous beamlets within an SOBP serves to broaden the energy spectrum in any region of the SOBP. Many radiobiological experiments in the literature have been performed mid-SOBP.



## Treating cancer with radiotherapy

The understanding of cancer as a disease and how best to treat the condition is a constantly evolving landscape. The current understanding of cancer is that it is not a single disease, but rather a blanket term for a condition where normal cell processes have become dysfunctional. In opposition to normally functioning tissues, the preeminent hallmarks of cancer were defined in 2000 by Weinberg and Hanahan in a seminal work as: sustaining proliferative signaling, evading growth suppressors, resisting cell death, replicative immortality, sustaining angiogenesis, and metastatic potential (14). In a 2010 update, the additional traits of avoiding immune destruction, promoting genomic instability and subsequent mutation, abnormal metabolism, and inflammation were added (15).

The primary aim of radiation therapy is to deliver a sufficient dose to halt and reverse tumor progression. At the cellular level, the effect of tumor response is usually referred to as causing cell death. In this context, “death” is an ambiguous term. The delivery of ionizing radiation serves to reduce tumor burden through available mechanisms of physical cell death such as apoptosis or reproductive death such as mitotic catastrophe resulting in cellular senescence. The tumor control probability is sigmoidal in nature indicating a limited number of clonogenically viable cells present within a tumor, and thus tumor control results at a threshold damage level which effectively reduces the number of these cells to zero. Cancer cell death and thus tumor control increases with radiation dose; however, the delivery of a radiation dose to achieve the desired clinical outcome is ultimately limited by pathological tolerances of the normal tissues adjacent to the tumor. The normal tissue complication function also presents as a sigmoidal response above which complications are expected to rise rapidly (3). The normal response and tolerance to radiation exposure is tissue specific.

As the biological control processes, i.e. tumor suppressive effects, in normal tissue cells are by definition functional, radiation damage will either be repaired or the irreparably damaged cell will undergo apoptosis.

### Biologically optimized treatment planning

In the current clinical practice of proton therapy, techniques such as PSPT are routinely used. In PSPT, a pristine proton beam is scattered laterally and modulated longitudinally to create the SOBP (16). This volume is shaped by introducing materials into the beam to conform it to the three-dimensional shape of the clinical treatment volume (CTV). The largest contributing proton beam within a PSPT delivery is from the beam required to reach the distal end of the CTV. As such, most of the dose to the formation of the distal edges of beams are produced from a single beam energy.

IMPT is a newer modality where the dose is delivered to the target volume by magnetically scanned small pristine proton beams. In contrast to PSPT, scanning beam delivery increases the conformality of high dose regions to the target volumes. IMPT is an evolving technology and there is ambiguity in the field as to what it comprises (17, 18). One definition of IMPT is the application of scanning beams in any manner. However, recent trends indicate IMPT should be categorized into single field optimized (SFO) or multi-field optimized (MFO) IMPT. In SFO-IMPT, inverse planning is employed to optimize beamlet intensities of each beam to independently conform to the entire target volume. In MFO-IMPT, there is simultaneous optimization of all beamlets of all beams to deliver a homogeneous prescription dose to the target while limiting the dose to critical volumes of normal tissues to within tolerance levels. For complex target shapes and anatomic

geometries, MFO-IMPT most effectively allows for optimal balancing of tumor coverage and normal tissue sparing (19-21).

With both PSPT and SFO-IMPT the treatment is optimized to create a uniform dose in the target volume without consideration of the varying biological effectiveness of the particles in the beam. Thus, the distal high LET regions of PSPT and SFO beams are nearly always in normal tissues distal to the target volume. With current MFO-IMPT techniques, the location of high LET regions is uncontrollable. To reduce the probability of normal tissue injury, current practitioners attempt to avoid placing such biologically active regions in sensitive normal tissues, sometimes at the cost of compromising tumor dose or even raising normal tissue doses (22).

With MFO-IMPT's ability to control each individual beamlet intensity, there is no impediment to selectively placing high LET and/or RBE regions within the tumor volume while avoiding normal tissues. This delivery strategy would effectively allow for improved normal tissue sparing and dose escalation to targets while ensuring treatments meet the standard of care. Two obstacles exist for this implementation. First, the appropriate biologic effect models for use in treatment planning are unknown, specifically for normal tissues. Secondly, the optimization of IMPT involves adjustment of intensities (weights) of thousands of beamlets comprising multiple beams aimed at the target from different directions. Typically, the optimization process iteratively minimizes the objective function composed of multiple competing sub-objectives. For biological effect (or LET)-based optimization, LET distributions must be computed. Conventional semi-empirical methods of dose calculation are not sufficiently accurate, whereas the most accurate methods, i.e., Monte Carlo techniques are relatively slow.

## Biological models and endpoints

### Clonogenic survival

A ubiquitous trait of cancer is the ability of the cells to sustain continual clonal reproduction given ideal circumstances. In the laboratory setting this characteristic translates to a single viable biologically immortal cell such as cancer or bacteria sufficiently replicating to form a cluster of cells. These clusters of cells are referred to as colonies, as the method of reproduction is asexual. The most common assay in the field of radiation biology is the clonogenic assay which is designed to test the ability of a treatment to affect the clonogenicity, the ability to form colonies, of cells. In this assay, single cells are exposed to a variable of interest and allowed to grow for a time period to form colonies (23). Following an insult such as radiation exposure, cells will attempt to repair damage sustained if possible. Following this repair period, the fate of the cell is determined. Possible cell fates include apoptosis, autophagy, senescence, quiescence, necrosis, necroptosis, etc., however, the clonogenic assay combines all cell fates to measure a single metric, the reproductively viable survival. Clonogenically viable cells will replicate and form colonies while irreparably damaged cells will be unable to form a colony of at least 50 cells. A colony is generally defined as a cluster of 50 or more cells (24). While damaged cells may still attempt to continue through the cell cycle, with some replicating, the probability of a non-clonogenically viable cell to undergo 5-6 population doublings to successfully form a colony of at least 50 cells is low.

There are complicating factors that must be considered when utilizing the clonogenic assay. An intrinsic limitation within the clonogenic assay is cell counting accuracy. Even at the theoretical limit, the associated counting and seeding error for a standard cell solution is

approximately 15%-30% (25, 26). This error results in inherent noise to clonogenic data and introduces compounding uncertainty when the number of cells per dose are counted separately.

All cell lines have inherent biological sensitivities to culturing conditions that may or may not affect the outcome of a clonogenic experiment. The impact of stress induced by plating on the clonogenicity cells can be minimized by plating the cells prior to irradiation and allowing them to reattach and recover (27). However, the effects of cell synchronization can result in systematic changes in the observed radiosensitivity (28).

Conversely, seeding cells following radiation exposure adds factors that contribute to the biological endpoint, resulting in increased uncertainty. Immediate post-irradiation plating involves the effects of cell detachment during seeding while the cells are still repairing radiation-induced damage (29). In particular, detaching cells and placing them into suspension alters the cellular and thus nuclear shape from cylindrical to spherical. This morphological change has been shown to result in a change of radiosensitivity due to the increased number of neighboring chromosomes available for exchange (30, 31). In addition to anchorage-dependent signaling and morphologic changes adherent cells undergo during detachment, enzymatic detachment solutions, such as trypsin, cleave membrane-bound adhesion molecules that function as major signalers in cellular stress responses, including apoptosis (30, 32-34). Post-irradiation cell detachment can further confound determination of RBE because photons and ions have different effects on cell adhesion and motility (35-38). As such, immediate post-irradiation plating readouts involve coupling the effect of the radiation treatment with cellular reattachment, except in the plating efficiency control used to determine overall surviving fraction (SF) levels. Another complicating factor of post-

irradiation plating is the possible contribution of repair of potentially lethal damage to cell survival depending on the experimental conditions and timeline (24, 39-41).

Additional effects reported in the literature affecting the clonogenic assay readout are multiplicity, clump effects, seeding density effects, and the bystander effect. The clonogenic assay assumes that a colony is formed from a single cell. This is achieved by preparing and seeding a single-cell suspension as well as preventing the forming colonies from clumping. Multiplicity refers to the effect present when a colony forming unit (CFU) is derived from multiple cells and can occur when the seeding solution does not solely consist of single cells, but also contains doublets, triplets, etc. (42, 43). Seeding multiple cells per CFU serves to artificially increase the measured radioresistance of a cell line as multiple lethal hits are required to inactivate a CFU derived from more than a single cell. Low values of multiplicity exhibit small effects on the overall SFs, and can be corrected by determining the multiplicity of the seeding solution at the time of irradiation. The effects of clumps in a clonogenic seeding solution result in a similar effect as high multiplicity (44).

Seeding density effects occur when the plating efficiency of a given cell line is dependent on the number of cells placed within an assay well (45). This artifact is particularly troublesome because it typically affects plates seeded at a lower cell density such as the plating efficiency standard and thus impacts the overall normalization of the SF results. In order to minimize this effect, plating efficiency can be measured over a range of concentrations to ensure linearity prior to experimentation.

The bystander effect is reported in the literature as the effect cellular damage and subsequent loss of clonality or death have on surrounding cells (46). It has been reported that culturing unirradiated cells with cells exposed to radiation reduces the clonogenicity of the

unirradiated cells. The exact extent this role plays in effecting the outcome of clonogenic experiments is unclear.

The colony readout also determines the accuracy and reproducibility of the clonogenic assay. With an increasing amount of damage and thus cell death, additional changes are observed in cellular morphology. In particular, cells become smaller or larger and the presence of giant cells is frequently reported (47-49). This cellular morphology can be mistaken for viable colonies when scoring by the unaided eye or automated techniques.

Ideally, the conversion of raw clonogenic data to the corresponding SF via normalization to the controls followed by further normalization when comparing RBEs has the effect of minimizing the contribution of extraneous biological effects with the assumption that they are present with all conditions and colony scoring is reproducibly performed. The complicating factors associated with the clonogenic assay are well described as it has been used first in the field of microbiology and then in mammalian cell lines to assess cellular reproductive integrity after an insult for more than 60 years (47). As such, the understanding of this simple assay has produced a rich amount of relevant literature to draw upon. Although applying the results of *in vitro* assays to *in vivo* models has its own complications and is frequently met with skepticism, clonogenic survival is by far the most well correlated cellular based assay for tumor control probability, with substantial evidence establishing the relation between the two methods (50-53).

#### The linear-quadratic model

There are many effect models used to fit the results of the clonogenic assay. These models include but are not limited to the linear-quadratic (LQ), linear-quadratic-linear

(LQL), lethal potentially lethal (LPL), microdosimetric-kinetic-model (MKM), repair-misrepair-fixation (RMF), and local effect model (LEM). The simplest and most common model used is the LQ model. In the LQ model, the ability of radiation to induce a lethal DNA lesion is given as:

$$L \propto \alpha D + \beta D^2$$

Where D is the dose delivered, and  $\alpha$  and  $\beta$  are fitting parameters representing the amount of directly lethal and potentially lethal lesions. With the assumption that lethal lesions are Poisson distributed within a population of cells, the surviving fraction is then:

$$SF = e^{-L} = e^{-(\alpha D + \beta D^2)}$$

The LQ model has been shown to be an accurate model over a large range of doses from sparsely-ionizing radiation, such as those delivered by photons; however, based on microdosimetric considerations of the radiation track structure, deviations from the assumption that lethal lesions are Poisson distributed within a population of cells are expected for densely ionizing radiations such as heavy ions (54). For protons, being light ions, the expected deviations from the LQ-model are ambiguous.

#### Relative biological effectiveness

RBE is defined as the ratio of doses between two types of radiation to produce an equal biological response:

$$RBE = \frac{Dose_{Control}}{Dose_{Test}} (at\ isoeffect)$$

The type of control radiation is usually photons generated from Co-60 or 250 kVp x-rays; however, practically, no de facto control radiation is currently established (5, 9). Other



photon sources typically found in preclinical biological irradiators and thus frequently cited as photon control radiations are the gamma rays produced from Cs-137, and 125 and 320 kVp x-rays. Clinically utilized photon sources are also found as control radiations with 6 MV x-rays being the most common. The selection of a control radiation is critical as the literature suggests differential responses between these sources with lower energy sources typically resulting in higher RBEs than higher energy sources (55-57).

Quantifying and understanding differential biological responses is an active area of research within radiobiology. Current proton therapy clinical practice attributes a spatially uniform RBE value of 1.1 while this value continues to be debated, for ions heavier than protons, the clinically used RBEs are spatially variant and on the order of 2-4 (58).

In a recent review, Paganetti systematically obtained and analyzed hundreds of published clonogenic data points to characterize proton RBE (9). This review stated that although the use of an RBE of 1.1 is acceptable when using large clinical SOBPs, the literature does support increased RBE values of 1.15 mid-SOBP, 1.35 at the distal edge of the SOBP, and 1.7 in the distal falloff of a SOBP. The review stresses the large spread of the existing clonogenic data in the literature and emphasizes the unmet need for experimental protocol standardization. In particular, Paganetti found that when attempting to fit the compiled clonogenic dataset to a linear model to determine data trends, the results of the analysis were heavily dependent on whether the associated clonogenic data errors were taken into account. In many cases, the trends changed when the reported errors were accounted for. However, the range of reported errors was also found to vary to a degree that was deemed to be unrealistic. Paganetti called for comprehensive results reporting of model fit parameters and errors.

## DNA damage repair and complexity

It is generally accepted that the most prominent biological effector of radiation damage is the DNA contained within the cell nucleus (59). The DNA damage response (DDR) is a complex process involving numerous proteins and effectors. The main types of DNA damage induced by radiation exposure are base damage, single-strand breaks, and double-strand breaks (DSB). DSBs are the most difficult DNA lesion to repair and are thus considered the most lethal form of DNA damage. The two major DSB repair pathways are non-homologous end joining (NHEJ) and homologous recombination (HR) (60).

Homologous recombination is an error free method of DSB repair that requires an undamaged DNA template found in a sister chromatid. NHEJ is an error-prone process where the hanging ends of a DSB are ligated to one another. For normal mammalian cells, the only time duplicate DNA strands are present and HR can occur is during late S phase and the following gap phase, G2, prior to the completion of mitosis. Conversely, the NHEJ pathway may be utilized at all times of the cell cycle. Even when a duplicate DNA template is available, cells will not always utilize the HR pathway for repair. The comprehensive mechanism determining DNA repair pathway selection is still being elucidated, but it is clear that it is a multifaceted process (61-63).

Markers of DNA damage assessment include the repair proteins which accumulate at the site of a DSB. When imaged these proteins appear as small foci when the DNA damage is localized within a small region of the nucleus subsequently recruiting repair proteins (Figure 5). DNA damage repair kinetics following irradiation can be measured by fixing cells at different time points post-exposure, labeling the repair proteins, and scoring the number of foci present. There are many repair proteins involved in DNA repair, and thus potential

markers for measuring the DDR kinetics. Studying the total induction and repair of DSB foci requires foci markers that are recruited to the site of DNA damage for all induced DSBs, and are thus upstream of the repair pathway selection process. Two well established ubiquitous DSB markers are  $\gamma$ H2AX and p53 binding protein 1 (53bp1) (64, 65) In response to DSBs, ser139 on the histone H2AX becomes phosphorylated by members of the PI3K family forming  $\gamma$ H2AX. This modification is thought to aid in the recruitment of repair proteins to the site of damage. 53bp1 binds to damaged chromatin following histone modification and plays a crucial role in the regulation of repair pathway selection (61).

Persistent DNA damage, particularly DSBs, has been described as a mechanistic marker directly related to cellular survival. It also serves as a predictive marker of genomic instability (66-69). It is thought that the complexity of the induced DNA lesion is directly related to the probability of successful repair. There is significant evidence suggesting that exposure to radiation with increasing LETs yields complex DSBs resulting in increased biological effectiveness (64, 70-73).

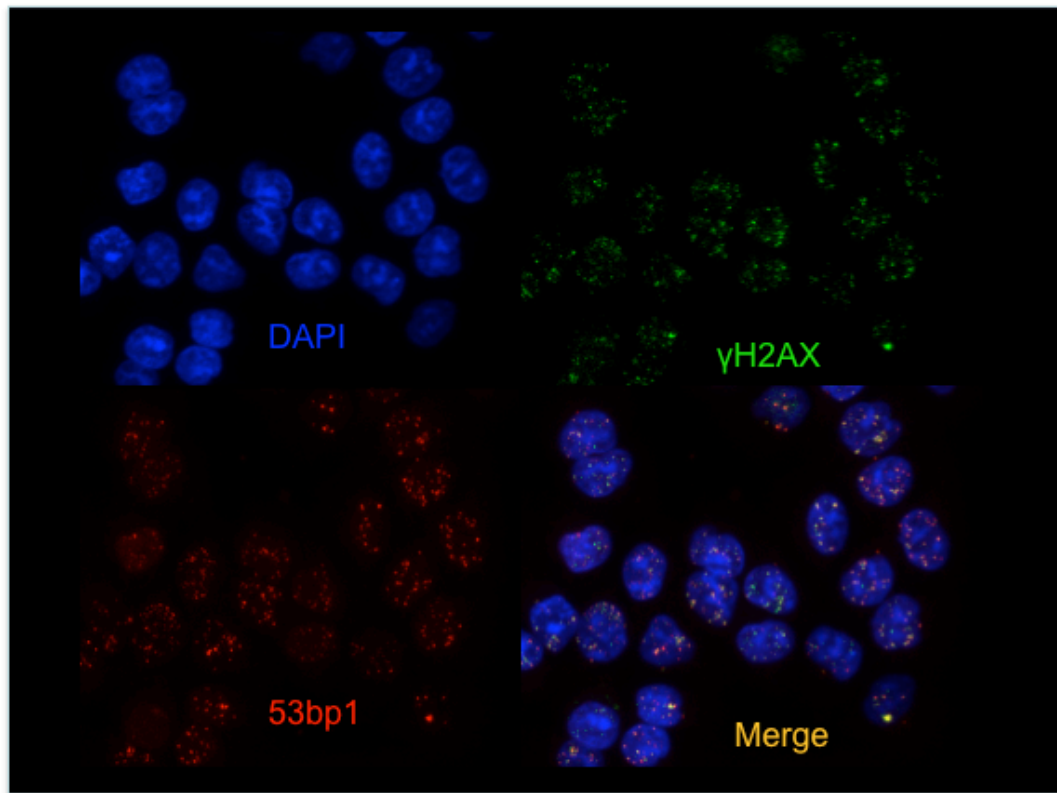


*Figure 5. Representative DSB foci image. A common method to measure DSB repair kinetics is to label the proteins involved in the DNA repair. Two established ubiquitous DSB markers in the literature are  $\gamma$ H2AX and 53bp1.*

### 3-dimensional tissue culture and organoids

In recent years there has been an active effort within the biomedical research community to transition to advanced *in vitro* models that more closely recapitulate *in vivo* settings than 2-dimensional *in vitro* experiments (74, 75). The motivation for this shift is to increase the translation success rate from basic *in vitro* studies to improved clinical outcomes (76, 77).

The crucial roles that both the tumor microenvironment and host immune system play in the response to therapeutic treatment has entered the forefront of the cancer research field (78-82). In simplified adherent monolayer models, interactions between the myriad of cell types present within *in vivo* settings are not present. Additionally, even within the same cell line, gene and protein expression levels vary when cultured in two or three dimensions (75, 83). Mounting evidence has demonstrated that three-dimensional organoid models are more representative of *in vivo* settings than classic cellular monolayers.

### Modeling the relationship of dose, LET, and RBE

Dose and LET<sub>d</sub> are the two key physical parameters commonly used in reporting the RBE of protons which have been used as input parameters in several radiation response models (84-86). Currently, there exist two major viewpoints for the relationship between RBE and LET<sub>d</sub>: linear and non-linear. The McNamara model is a recently devised phenomenological model based on all published *in vitro* datasets at the time of its development (2015). This model predicts a linear relationship between proton RBE and LET<sub>d</sub> (84). Other earlier developed phenomenological models also support a linear relationship (85-88). However, the latest version of the LEM currently used for carbon ion therapy (LEM

IV), perhaps the most developed and mechanistically sound model, predicts a non-linear behavior of RBE with  $LET_d$  (89).

Not all biological response models use LET as a parameter. For example, the RMF model is a mechanism-based model that accounts for DNA damage induction and repair (90). Polster *et al.* compared RBE values along an SOBP created by PSPT beams calculated using eight different models (90-93). Their calculations show that the RBE values from all tested models have obvious differences from each other and from experimental data (94). The discrepancy between model predictions and experimental data is one of the main motivations for the presented work with the goal to increase experimental verification of the accuracy of existing models.

## Methods

### Monte Carlo Simulations

Monte Carlo simulations using the latest releases of the Geant4 simulation software package were used to calculate the doses and LETs associated with particle beams (95, 96). The results of a MC simulation are directly dependent on how well the simulation setup parallels the physical experimental the setup (Figure 6). This includes the corresponding physical parameters of the materials utilized. The results of MC simulations presented in this work are from collaboration with medical physicists. Dr. Fada Guan performed all MC simulations for proton irradiations performed at MDA. All MC calculation results presented for irradiations performed at HIT were calculated by Dr. Darshana Patel.

### 2D Cell Culture

#### Cryogenic retrieval and cell line stock creation

Cell lines stocks arrive as frozen 1mL-2 mL aliquots in culture media or FBS with 5% dimethyl sulfoxide (DMSO). Upon arrival, the cells were rapidly thawed in a 37°C water bath and 1:10 diluted in warm culture media within a standard 15 or 50 mL conical tube. The cells were then pelleted via centrifugation at 1200 rpm for 5 minutes and the liquid solution was aspirated to remove DMSO from the solution. The cell pellet is then resuspended in culture media, plated into tissue-culture treated plasticware, and incubated at 37°C and 5% CO<sub>2</sub> for expansion. When culture confluence reaches approximately 70-90%, cells are collected and 1.5 mL aliquots are dispensed in cryo-vials at a concentration of 2E6 cells per vial using a freezing media consisting of 10% DMSO in FBS. The stocks are then placed

within a freezing container to achieve a freezing rate of  $-1^{\circ}\text{C}/\text{min}$  and placed in a  $-80^{\circ}\text{C}$  freezer overnight. The aliquots are then transferred to a liquid nitrogen cryostat for long-term storage.

#### Cell lines and media

Two non-small cell lung cancer (NSCLC) cell lines, NCI-H460 (HTB-177) and NCI-H1437 (CRL-5872), were obtained from American Type Culture Collection (ATCC). The culture media utilized with these cell lines was RPMI 1640 supplemented with 10% fetal bovine serum (FBS) and 1% penicillin-streptomycin.



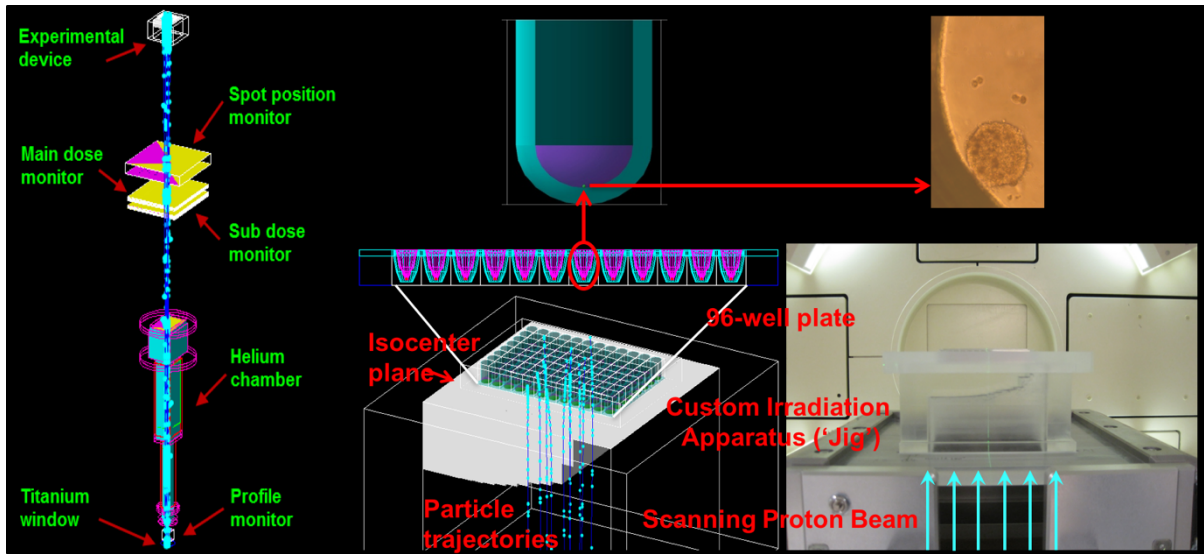


Figure 6. Overview of Monte Carlo simulation setup vs reality. The accuracy of Monte Carlo simulations is directly dependent on how representative the simulation is of the actual setup as well as to what accuracy the material physical properties are known (e.g. density, interaction cross sections, ionization potential, etc.).

## Culturing and passaging

Cell lines are cultured in a humidified incubator at 37°C and 5% CO<sub>2</sub>. Subculturing is typically performed when cell confluency reached 70% to 90%. The cells are collected using a detachment solution such as a digestion or protease agent that cleaves cellular membrane proteins. In particular, culture media is aspirated from the edge of the tissue culture flask. A quick wash is performed using warm 0.25% trypsin-EDTA (trypsin). The wash solution is aspirated, and replaced with fresh 0.25% trypsin for cellular detachment. The amount of trypsin used was 1 mL per 25cm<sup>2</sup> of culture vessel surface area. The culture container is then placed in a humidified incubator for detachment to occur. For a fresh 0.25% trypsin solution this period was approximately 2-3 minutes. Time for detachment increases for older solutions and lower trypsin concentrations. Complete detachment is confirmed using an inverted light microscope at a low magnification (4-10x) and examining the edges of the culture vessel. If necessary, additional mechanical cellular detachment was utilized by ***gently tapping*** along the periphery of a flask. Following cell detachment, the digestion agent is neutralized by adding culture media at a volume at least 4x the volume of the trypsin. For example, 3 mL of trypsin used for cellular detachment in a T-75 flask is diluted to a total of 15 mL by the addition 12 mL of culture media. The cellular solution is then diluted into a new culture vessel with culture media and returned to the incubator for attachment and growth. Typically dilution factors are 1:5-1:10.

## Determining cell concentration

Cells are detached and initially diluted to create a single cell suspension as in the section above. The concentration and viability of cells within the solution is determined by

dye exclusion. A sample of the stock cell solution is diluted with an equal volume of 0.04% trypan blue. Viable cells will prevent the dye from entering the cell while the dye will stain non-viable cells by penetrating the membrane. The dye-cell solution is then dispensed into the appropriate container for the respective counting method to be used. Manual counting was performed using a hemocytometer. An EVE Automated Cell Counter was used for low-throughput automated counting, and a Vi-Cell XR system was used for high-throughput automated counting. For both the hemocytometer and low-throughput automated counting the cell solution is dispensed within a small rectangular chamber slide via capillary action. The slide is then inserted into an automated cell counting system utilizing image based scoring to score viable and dead cells.

#### Traditional clonogenic assay

Exponentially growing cells (approximate confluency 70-90%) were detached and the cell concentration of the single cell suspension was determined as previously described. The stock solution was diluted to form a single dispensing solution with a concentration of 1 cell per  $\mu\text{L}$ . For the standard 6-well clonogenic assay, cells were seeded at concentrations ranging from 100-3000 cells per well in a total volume of 3 mL per well. To promote even cell spatial distributions within each well of the 6-well plate, the time following cell plating and placement within an incubator was minimized. Cells were allowed to attach and stabilize in culture for 8-10 hours before irradiation. The 6-well plates were brought into the treatment room one at a time for irradiation and immediately returned to culture following radiation exposure. Control plates were sham irradiated. Following irradiation, cells were cultured for 10-14 days for colony formation. After colonies formed the media was decanted and cells

were fixed and stained at RT with 2-3 mL of 0.4-0.5% crystal violet in ethanol for 5-10 minutes. The crystal violet solution within each well is then collected with an autopipette and returned to the stock solution for future use. Excess crystal violet solution is removed by submerging the plates into a bucket of warm water. The plates are then tapped on a cloth such as paper towels or laboratory wipes, inverted and placed on an absorbent bench pad, and allowed to dry overnight before analysis. Colony counting was manually performed under a stereomicroscope to score only colonies with 50 or more cells.

#### High-throughput clonogenic assay

The dispensing solution used for standard 6-well clonogenic assays was the same as used for the 96-well high-throughput clonogenic assays. If available, the cell seeding was performed with a semi-automated liquid dispenser such as an ELISA plate washer for consistent and rapid cell plating. Experiments performed at MD Anderson utilized a BioTek MultiFlo FX Microplate Dispenser. When automated dispensing options were unavailable, cells were plated using a 12 well multichannel pipette. For the high-throughput clonogenic assays cells were seeded at a constant 100 cells per well in a total volume of 100  $\mu$ L per well. Following cell plating, 96-well plates required a 60 minute RT incubation for sufficient cell attachment to prevent movement when returned to culture at 37°C (97). As with the traditional clonogenic assay method, cells were allowed to attach and stabilize in culture for 8-10 hours before irradiation. Two plates per dose level were irradiated to achieve 16 replicates per LET-dose combination. After a cell line dependent colony formation time period (5-5.5 days for the H460 cells and 7-7.5 days for the H1437 cell line), cells were fixed and stained with 0.4-0.5% crystal violet in ethanol. The culture media was removed using the

“swish and flick” method. Liquids are removed by inverting the uncovered microplates over a sink with running water and rapidly flicked in air. For the high-throughput clonogenic method, the crystal violet solution is placed within a vessel such that at least one 96-well microplate can be submerged for 5-10 minutes at RT. Following staining, the plate is inverted and gently tapped against the side of the container to remove the crystal violet solution. The plate is then serially dipped into two buckets containing warm water to dilute and remove the excess dye solution. Water is removed by flicking the plates in air over the sink and then tapping the plates on absorbent cloth. The plates are then inverted and angled on their lids for at least one day to facilitate drying prior to further analysis. High-content automated laser confocal analysis with an IN Cell Analyzer 6000 was used to identify colonies containing 50 cells or more. Four overlapping fields per each well in a 96-well microplate were obtained using a 4x objective with a 0.2 numerical aperture and the IN Cell Analyzer’s 5.5-Mp sCMOS camera (2560×2160 pixels) with a 6.5-μm pixel size. The excitation wavelength was 640 nm (red) and the emission wavelength was 706 nm (Cy5). The GE Developer v1.9 software was used to stitch the four fields together with a 5% overlap creating a composite image for each entire well. Colonies and cells were identified and masks generated from object filters of feature size and intensity. The cells were linked to colonies, and only colonies containing 50 or more cells were scored.

#### Doubling time determination

Estimates for established cell line doubling times were initially determined by literature searches. Follow up measurements were performed by plating single cell suspensions, returning the plate to culture, and counting the number of cells present under a

microscope at later time points such as 24 and 48 hours after seeding. The doubling time for the H460 cell line was also measured by plating replicate flasks, counting the number of viable cells within a replicate over a time course, and fitting the number of cells to an exponential growth function.

#### SF calculation and fitting

The plating efficiency (PE) for a cell line was defined as:

$$PE = \frac{C_{0Gy}}{N_{0Gy}}$$

Where  $C_{0Gy}$  is the number of colonies formed in the unirradiated control plate and  $N_{0Gy}$  is the number of cells seeded in the unirradiated control plate. The SF was determined by normalizing the number of colonies present within an experimental condition, dose-LET, to the average number of colonies of the unirradiated control plates:

$$SF = \frac{C}{PE * N}$$

Where C and N are the number of colonies counted and number of cells seeded within a well respectively. The limit of detection (LOD) for the clonogenic assays was defined as 1 colony per well or an SF lower bound of  $1/(N*PE)$ . Dose levels where the averaged SF value was lower than the LOD were omitted from analysis. The obtained data was fit to the linear-quadratic equation:

$$SF = e^{-(\alpha D + \beta D^2)}$$

Where D is the delivered dose and  $\alpha$  and  $\beta$  are parameters to be fit by a  $1/Y^k$  weighted nonlinear regression. An appropriate weighting factor, k, was determined following the

method found in (98) where k is determined by performing a robust linear regression to the logarithm of the replicate variance versus the logarithm of the replicate mean. For proton and photon irradiated cells k was set equal to 1 and for carbon and helium ions k was set to 2.

#### Relative biological effectiveness calculation

Relative biological effectiveness (RBE) is defined as the ratio of doses to achieve an isoeffect:

$$RBE = \frac{Dose_{Control}(at\ isoeffect)}{Dose_{Test}}$$

Where  $D_{Control}$  is the dose of the control radiation and  $D_{Test}$  is the experimental radiation quality being interrogated. RBE for a given radiation quality was determined from the results of the linear-quadratic model fit by solving for the dose required for a chosen biological effect level using the quadratic formula:

$$\beta D^2 + \alpha D + \ln(SF) = 0$$

$$D = \frac{-\alpha + \sqrt{\alpha^2 - 4\beta \ln(SF)}}{2\beta}$$

The RBE errors were calculated by propagating the error associated with the fitting parameters  $\alpha$  and  $\beta$  as:

$$\sigma_{RBE} = |RBE| * \sqrt{\left(\frac{\delta D_\gamma}{\delta \alpha_\gamma}\right)^2 \sigma_{\alpha_\gamma}^2 + \left(\frac{\delta D_\gamma}{\delta \beta_\gamma}\right)^2 \sigma_{\beta_\gamma}^2 + \left(\frac{\delta D_p}{\delta \alpha_p}\right)^2 \sigma_{\alpha_p}^2 + \left(\frac{\delta D_p}{\delta \beta_p}\right)^2 \sigma_{\beta_p}^2}$$

## Immunofluorescent staining of DSB markers

The temporal repair kinetics of DNA DSBs were assessed by immunofluorescent (IF) labeling of established DSB repair protein foci formation following irradiation. Single cell suspensions were plated into glass-bottom 96-well microplates (Matriplate) such that the confluency at the time of irradiation was between 40 and 60%. Typically, 20,000-40,000 cells per well were seeded 8-12 hours prior to irradiation. The glass-bottom of the 96-well plate should ideally correspond to the thickness of a No. 1.5 coverslip (160-190  $\mu\text{m}$ ). The plates were irradiated using the high-throughput system and returned to culture for repair to occur for multiple time intervals. Irradiated cells were fixed at the time points of 0.5, 2, 4, 8, 12, 18, and 24 or 30 hours following irradiation. Control plates that received no radiation exposure were fixed at the initial and final time points. Fixation was achieved with 4% paraformaldehyde in phosphate buffered saline (PBS) for 10 minutes at room temperature (RT). The fixative was removed and cells were washed in PBS 3 times before short-term storage at 4°C for the remaining duration of the experimental time course. IF staining followed the fixation and subsequent washes of the final time point plates. Cells were permeabilized and nonspecific antibody binding blocked by incubation with a 0.3% Triton X-100/10% goat serum PBS solution for 2 hours at RT. For primary labeling, the cells were incubated with unlabeled antibodies either overnight (14-18 hours) at 4°C or for 1 hour at room temperature. 53BP1 primary antibodies used were either a murine monoclonal antibody (clone BP13, Chemicon) or rabbit polyclonal (ab21083, Abcam). The concentration of the primary antibody used was 1  $\mu\text{g}/\text{ml}$ . The antibody dilution buffer was 5% goat serum/0.3% Triton X-100/PBS. Following primary antibody incubation, cells were washed 3 times for 10 minutes at RT with 0.1% Triton X-100/PBS. Cells were then incubated with the appropriate



(goat anti-mouse and goat anti-rabbit) highly cross-adsorbed secondary antibody conjugated to either AlexaFluor488 or AlexaFluor594 dye in 5% goat serum/0.3% Triton X-100/PBS at a concentration of 1  $\mu$ g/mL (1:2000, Life Technologies) for 1-2 hours at RT covered in aluminum foil. Following secondary antibody incubation, the cells were washed with 0.1% Triton X-100/PBS three times for 10 minutes at RT. Nuclei were labeled by incubation with 1  $\mu$ g/ml of 4',6-diamidino-2-phenylindole (DAPI) in PBS for 5-10 minutes RT. The plates were then washed 3 times with PBS for 5 minutes at RT prior to addition of mounting media, the final protocol step. Liquid removal within the IF procedure was achieved using the “swish and flick” method. Solutions within the IF protocol were dispensed by either a 12 well multichannel pipette or semi-automated microplate liquid dispenser as quickly as possible to ensure samples did not dry.

*Table 1. Volumes and concentrations used for IF.*

<b>Name</b>	<b>Solution</b>	<b>Volume/well [μL]</b>
Fixation solution	4% PFA	150
Washing buffer	0.1% Triton X-100	200-300
Blocking and permeabilization buffer	0.3% Triton X-100 10% Goat serum	150-200
Antibody dilution buffer	0.1% Triton X-100 5% Goat serum	125
Mounting media	Commercial Glycerol-based (DAKO, FluoroMount-G)	100

## Immunofluorescent imaging of DSB markers

Plates were imaged on a Cytation5 Cell Imaging Multi-Mode Reader utilizing automated microscopy with a 20x in air objective. The plate geometry was registered within the platform's Gen5 software. The imaging protocol was set to collect images at 16 locations within each well resulting in 1536 images per glass-bottom microplate (Figure 7). The protocol run time was approximately 4 hours per plate. The locations were set up as a 4x4 grid with 700-1000  $\mu\text{m}$  spacing between each field of view (Figure 8). At each location a default autofocus scan was performed on the blue (DAPI) channel to determine the scan height (Figure 9). Three images were then sequentially captured corresponding to the fluorescently labeled components in the blue (nuclei), green (foci), and red (foci) channels (Figure 10, Figure 11). The images were then exported for analysis.

## Immunofluorescence data analysis

The general procedure to determine the average number of foci per nucleus was to identify DAPI-labeled nuclei and DSB-repair protein foci as image masks and quantify the number of nuclei-associated foci using CellProfiler 2.2.0 (Broad Institute) (Figure 12). The modules and the settings used in the CellProfiler pipeline for the foci analysis are shown in Figure 13 to Figure 23. The settings were manually benchmarked by eye on a subset of the captured images.

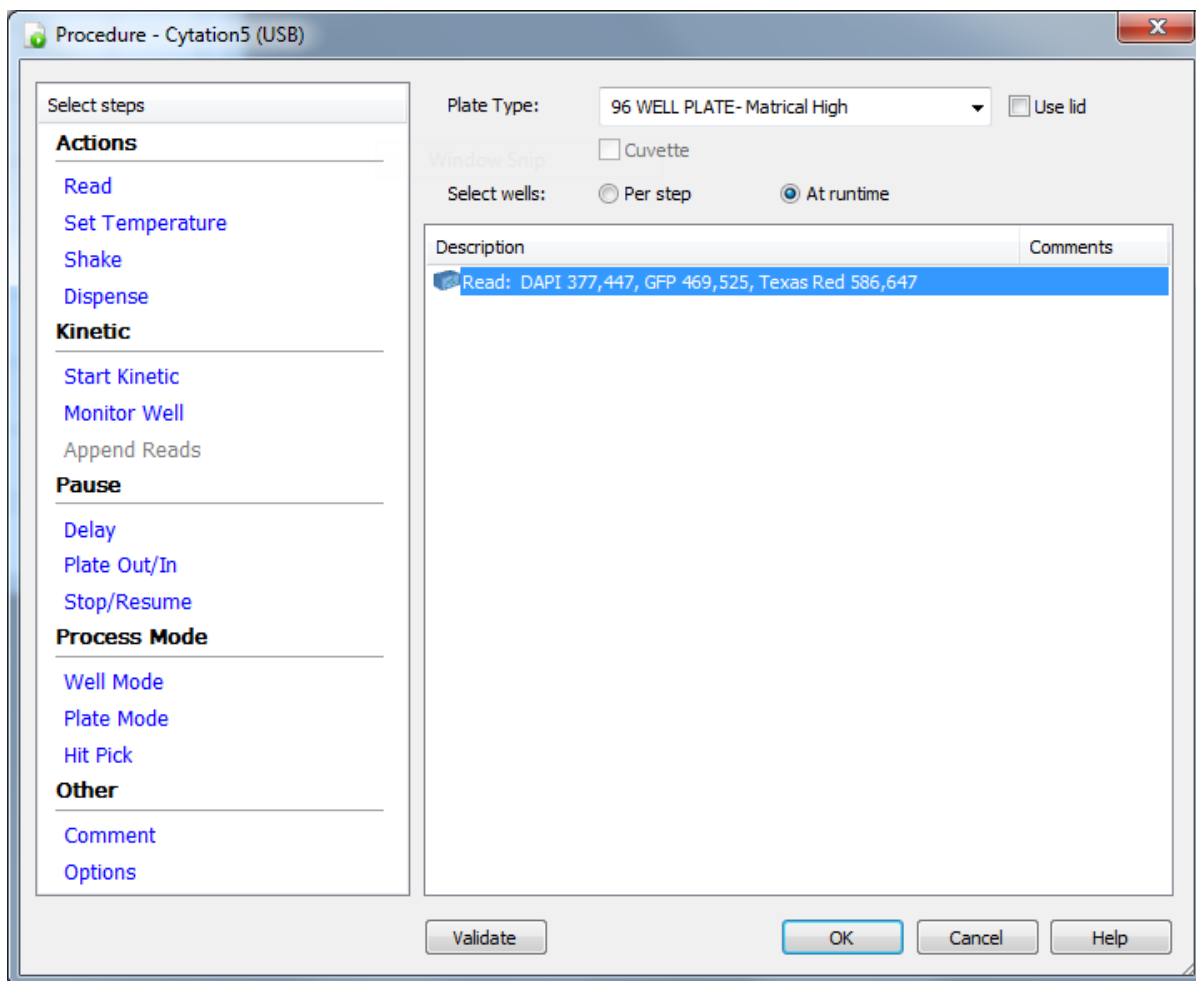


Figure 7. Cytation5 software procedure tab.

Read Step

Step Label:  Full Plate

Objective: Phase 20x Image: 394 x 291  $\mu\text{m}$

Channels

<input type="radio"/> 1	<input type="radio"/> 2	<input checked="" type="radio"/> 3	<input type="radio"/> 4
Color: <span style="border: 1px solid black; padding: 2px;">DAPI 377,447</span>	Color: <span style="border: 1px solid black; padding: 2px;">GFP 469,525</span>	Color: <span style="border: 1px solid black; padding: 2px;">Texas Red 586,647</span>	
Exposure: <input type="checkbox"/> Auto	Exposure: <input type="checkbox"/> Auto	Exposure: <input type="checkbox"/> Auto	
LED: <span style="border: 1px solid black; padding: 2px;">7</span>	LED: <span style="border: 1px solid black; padding: 2px;">7</span>	LED: <span style="border: 1px solid black; padding: 2px;">10</span>	
Integration time: <span style="border: 1px solid black; padding: 2px;">150</span>	Integration time: <span style="border: 1px solid black; padding: 2px;">700</span>	Integration time: <span style="border: 1px solid black; padding: 2px;">1000</span>	
Gain: <span style="border: 1px solid black; padding: 2px;">0</span>	Gain: <span style="border: 1px solid black; padding: 2px;">0</span>	Gain: <span style="border: 1px solid black; padding: 2px;">7</span>	
<span style="border: 1px solid black; padding: 2px;">Options...</span>	<span style="border: 1px solid black; padding: 2px;">Options...</span>	<span style="border: 1px solid black; padding: 2px;">Options...</span>	

Horizontal offset from center of well ( $\mu\text{m}$ ): 0

Vertical offset from center of well ( $\mu\text{m}$ ): 0

☐ Single Image Set

☒ Image Montage

☐ Image Z-Stack

Montage (rows x columns): 4 x 4

Tile Overlap

☐ No overlap    ☐ Auto for stitching    ☒ Custom

Columns: -700  $\mu\text{m}$       Rows: -700  $\mu\text{m}$

Advanced options...
OK
Cancel
Help

*Figure 8. Cytation5 setup for automated imaging.*

Channel 1: DAPI 377,447

☒ Auto-focus  
☐ Fixed focal height [plate bottom elevation (2750  $\mu\text{m}$ ) + offset]  
☐ Focal height from first channel (+ offset)


Offset ( $\mu\text{m}$ ):

☐ Perform illumination correction


**Auto-Focus Options**

☒ Use default focus options

Focus method:

Minimum focus metric ratio:  
 Minimum focus delta ( $\mu\text{m}$ ):

Scan distance ( $\mu\text{m}$ ): 
 % of capture exposure for focus:

Scan increment ( $\mu\text{m}$ ): 
 Offset from bottom of well ( $\mu\text{m}$ ):  

Use alternate metric for scan ☐
 Mark as out-of-focus if less than min FM ☐

Bright field wide scan distance ( $\mu\text{m}$ ):   
 Bright field wide scan increment ( $\mu\text{m}$ ):   
 Bright field narrow scan distance ( $\mu\text{m}$ ):   
 Bright field narrow scan increment ( $\mu\text{m}$ ):

**Auto-Exposure Options**

Target exposure %:   
 Skip % (0.1 increments):   
 Integration threshold (msec):

**Vibration Detection Options**

CV Threshold:   
 Images to average:   
 (1=disabled; >1=enabled)

Figure 9. Cytation5 setup for the blue channel.

Channel 2: GFP 469,525 Σ

☐ Auto-focus  
☐ Fixed focal height [plate bottom elevation (2750 μm) + offset]  
☒ Focal height from first channel (+ offset)


Offset (μm):

☐ Perform illumination correction


**Auto-Focus Options**

☒ Use default focus options

Focus method: Auto focus with optional scan

Minimum focus metric ratio:  
 Minimum focus delta (μm):

Scan distance (μm): 
 % of capture exposure for focus:

Scan increment (μm): 
 Offset from bottom of well (μm):  

Use alternate metric for scan ☐
 Mark as out-of-focus if less than min FM ☐

Bright field wide scan distance (μm):   
 Bright field wide scan increment (μm):   
 Bright field narrow scan distance (μm):   
 Bright field narrow scan increment (μm):

**Auto-Exposure Options**

Target exposure %:   
 Skip % (0.1 increments):   
 Integration threshold (msec):

**Vibration Detection Options**

CV Threshold:   
 Images to average:   
 (1=disabled; >1=enabled)

*Figure 10. Cytation5 setup for the green channel.*

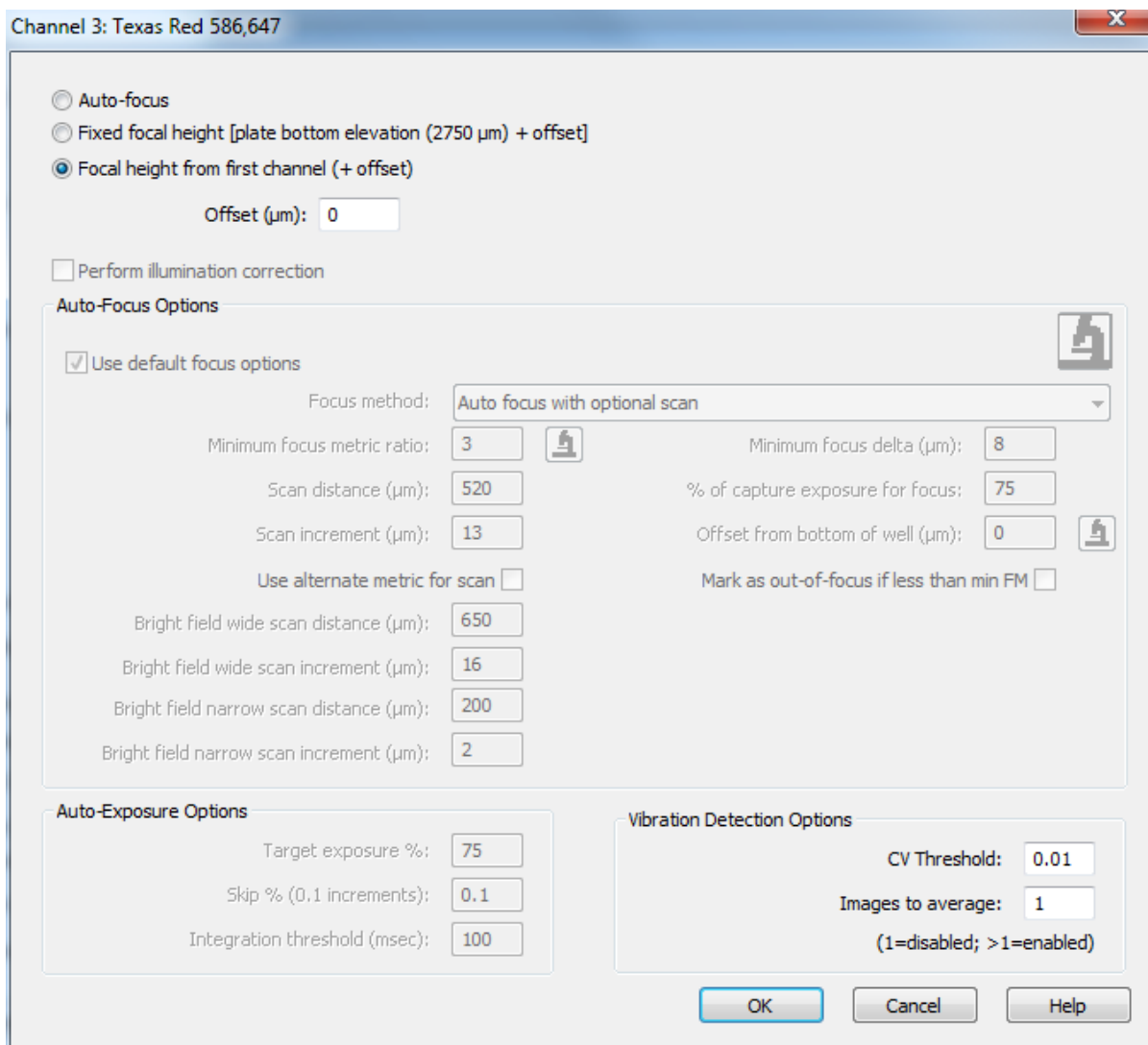
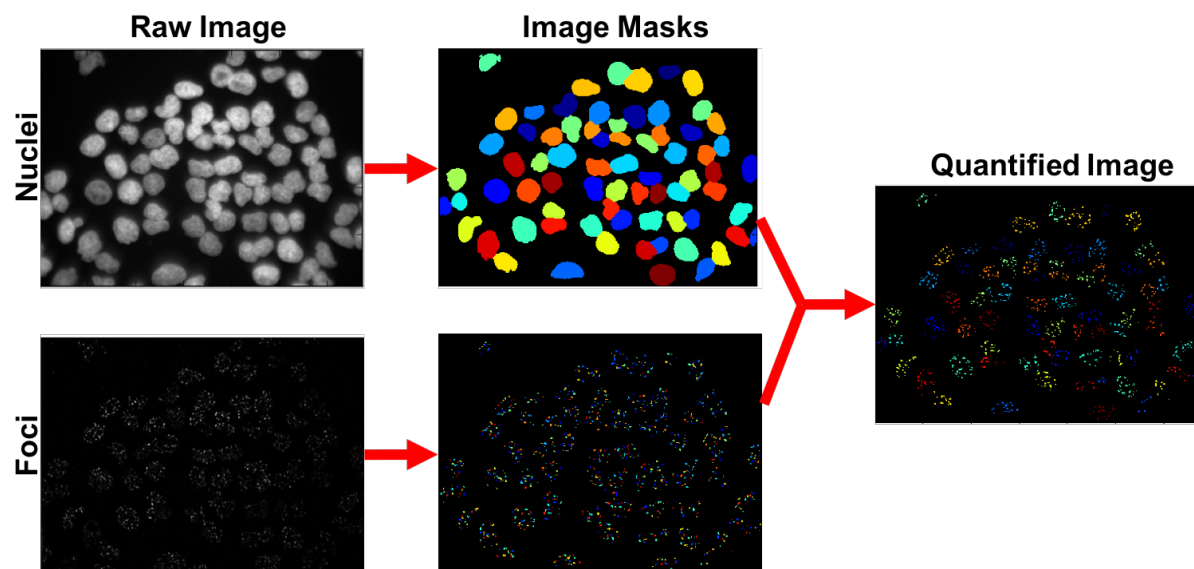


Figure 11. Cytation5 setup for the red channel.





*Figure 12. Overview of CellProfiler workflow for foci scoring.*

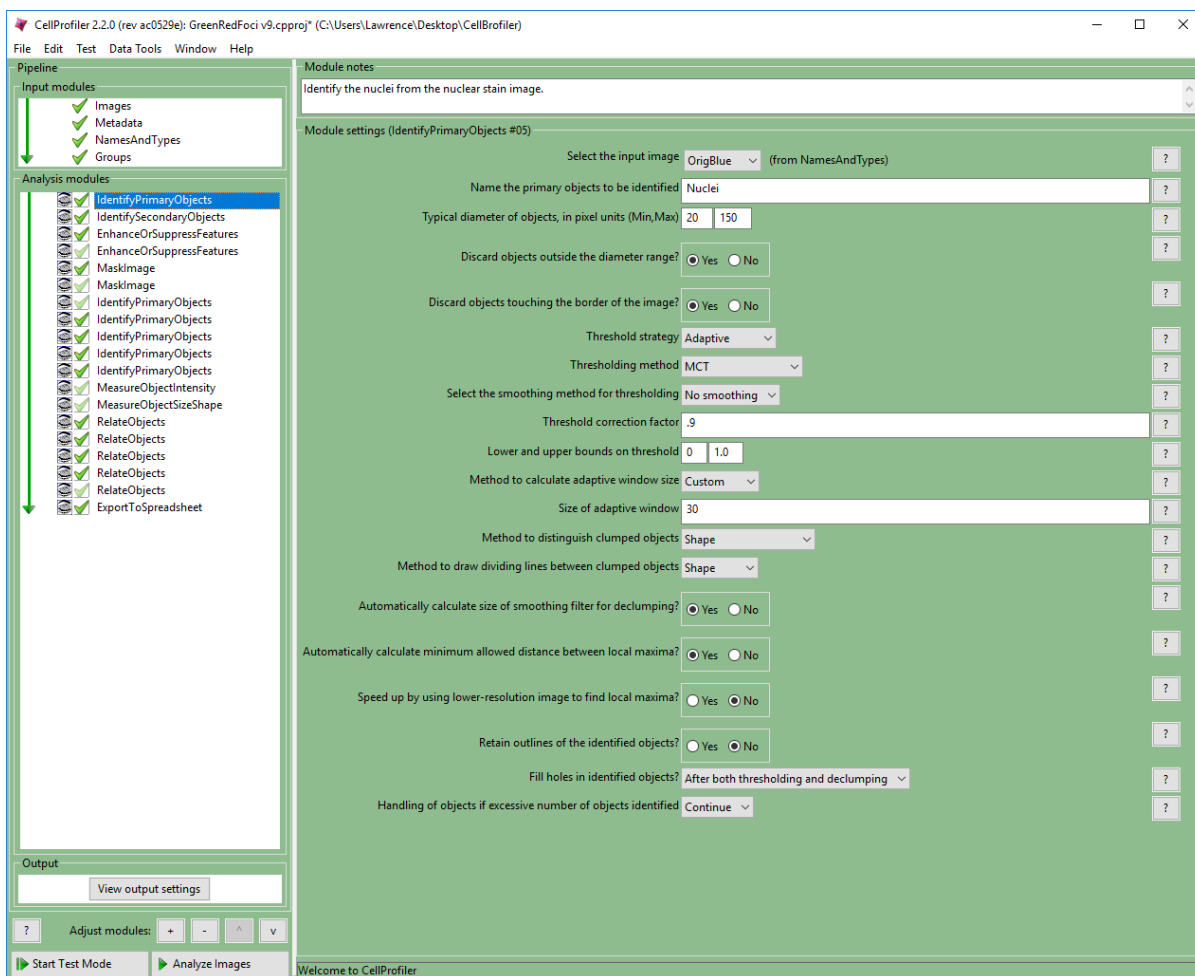


Figure 13. CellProfiler setup parameters for nuclei detection.

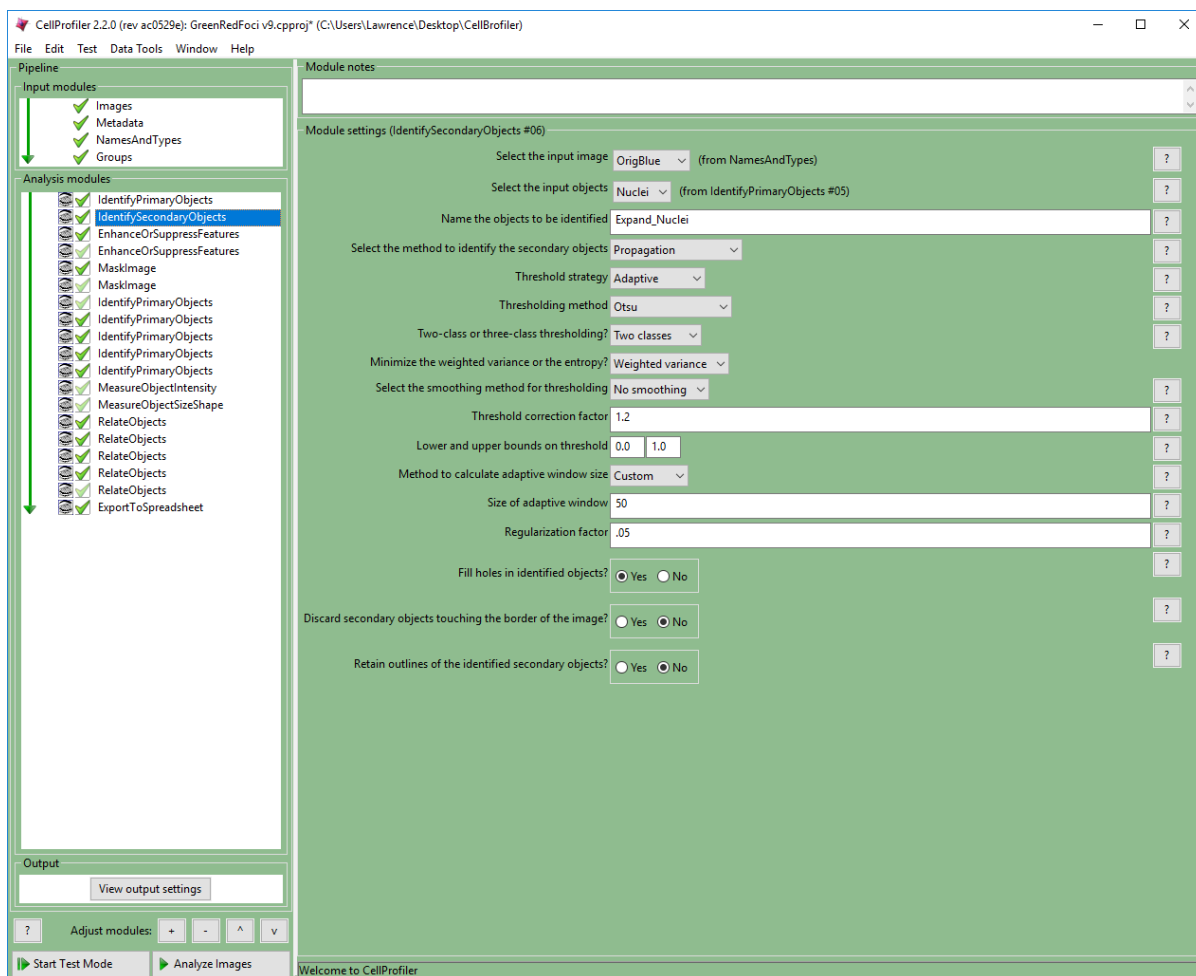


Figure 14. CellProfiler setup parameters for nuclei expansion.

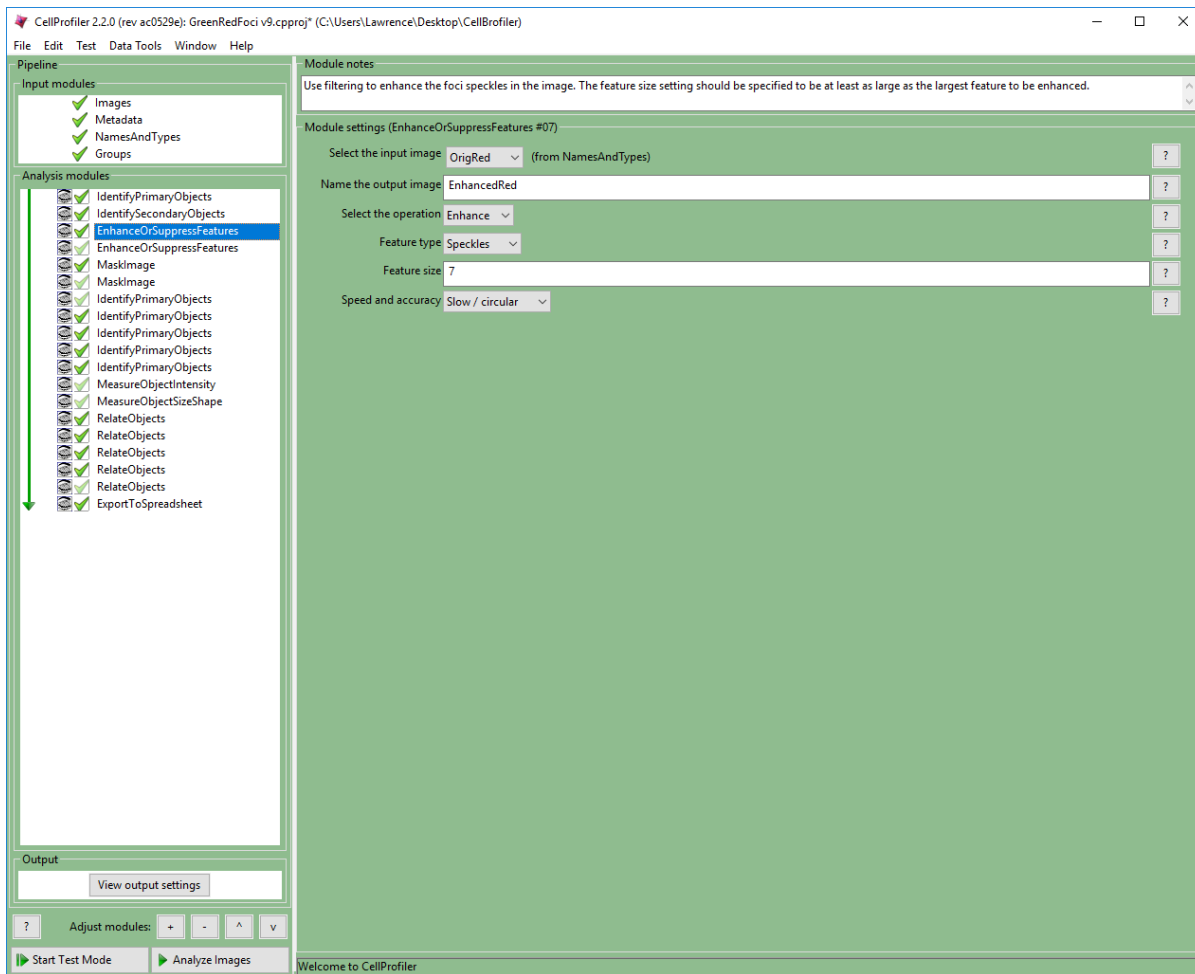


Figure 15. CellProfiler foci filter for red channel setup.

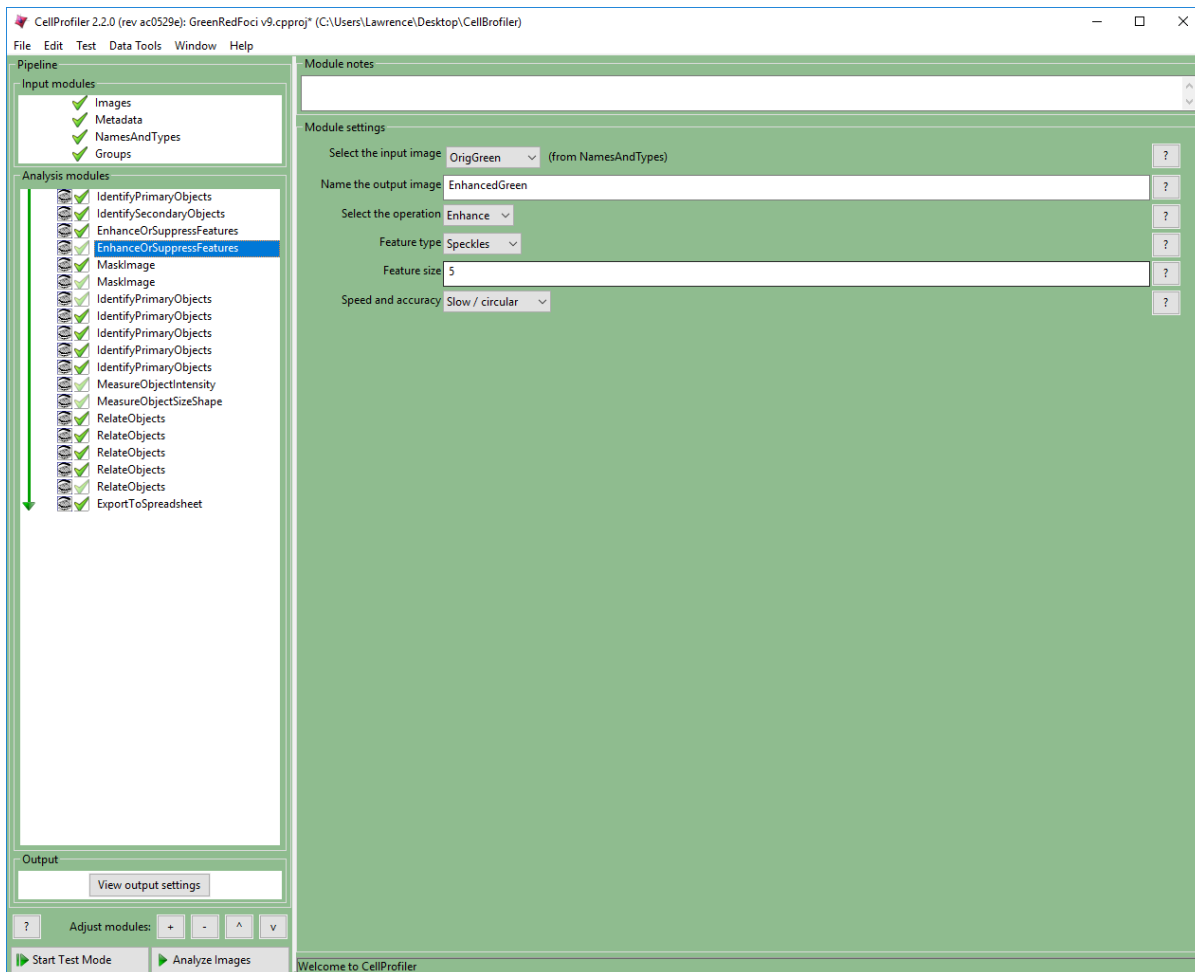


Figure 16. CellProfiler foci filter for green channel setup.

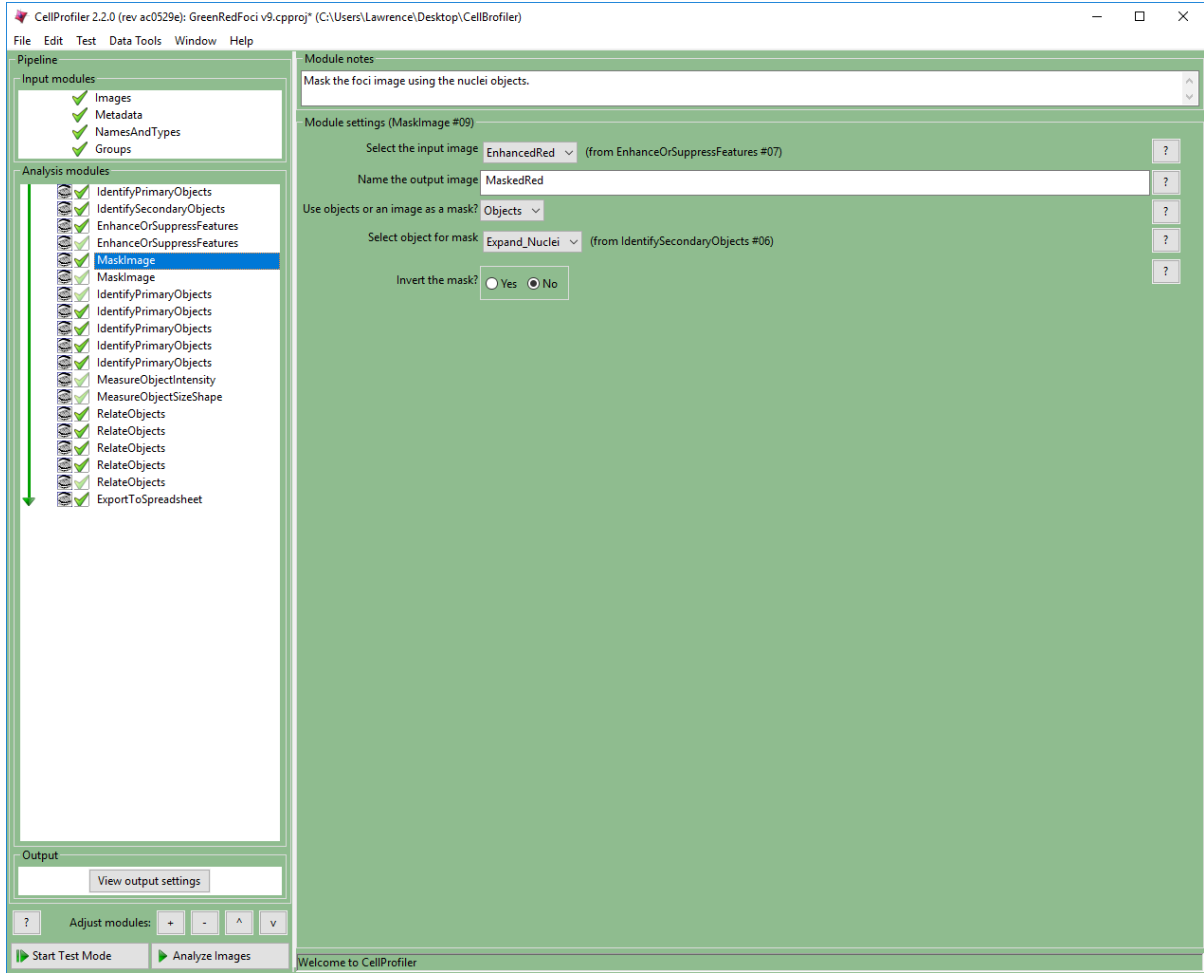


Figure 17. CellProfiler foci red channel mask setup.

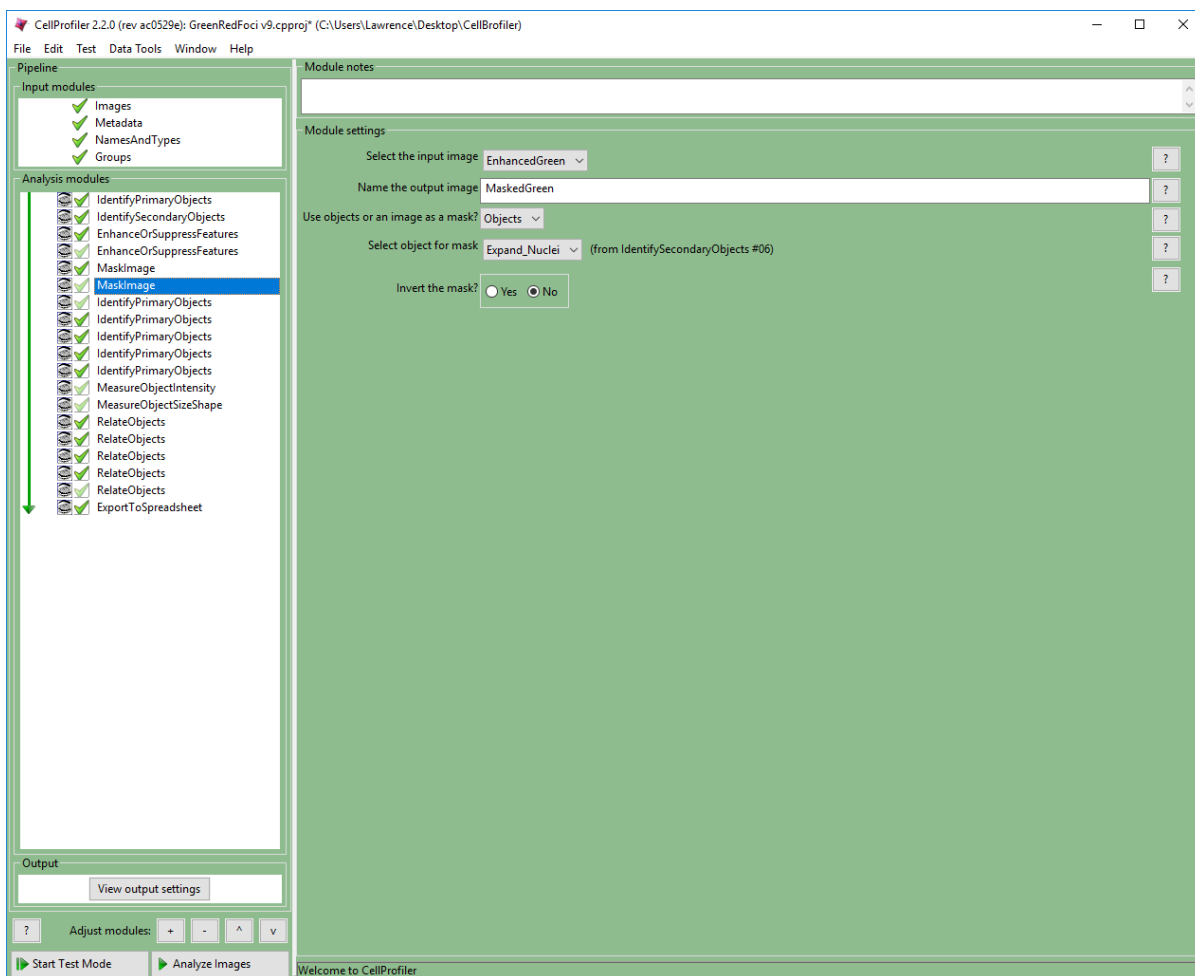


Figure 18. CellProfiler foci green channel mask setup.

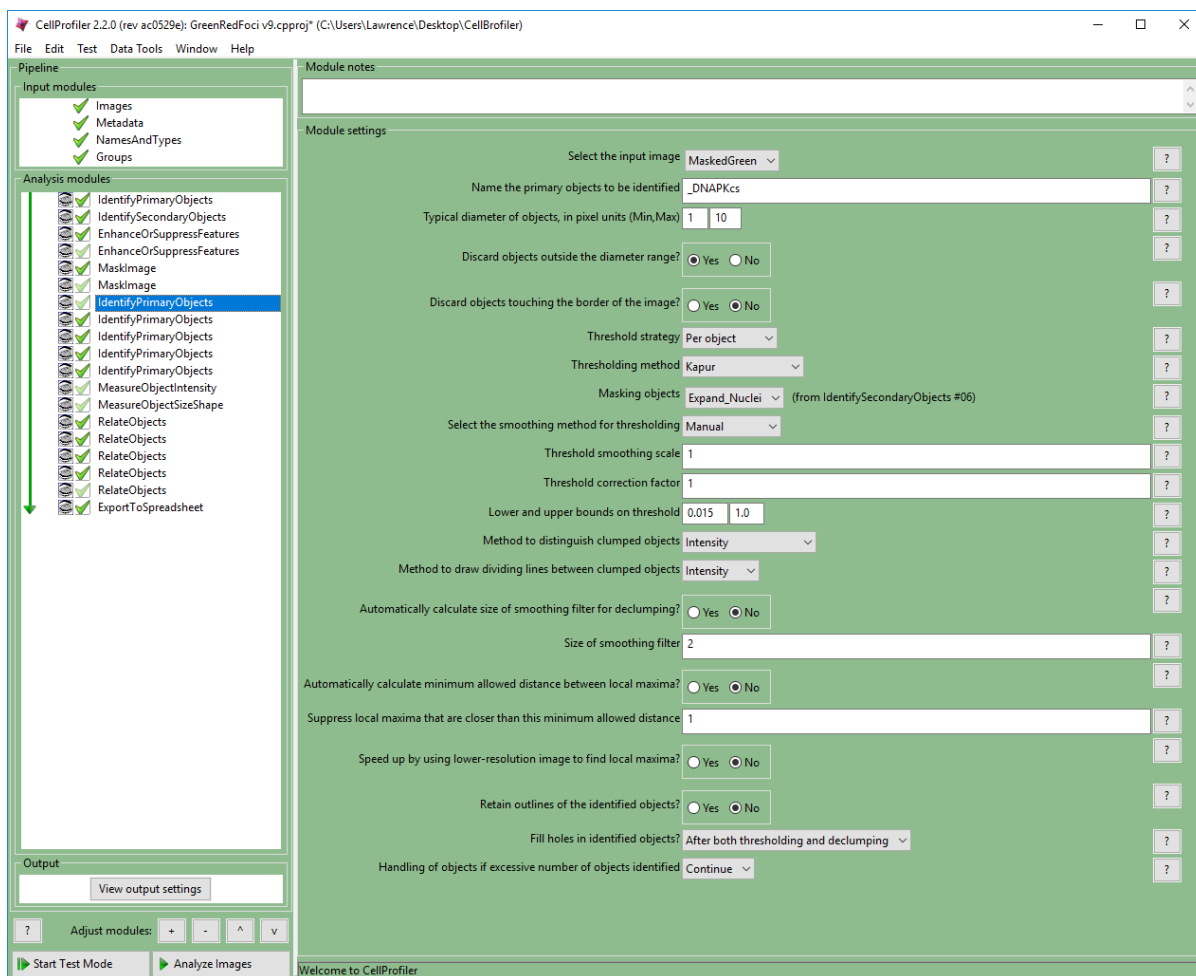


Figure 19. CellProfiler measurement parameters to score green foci.



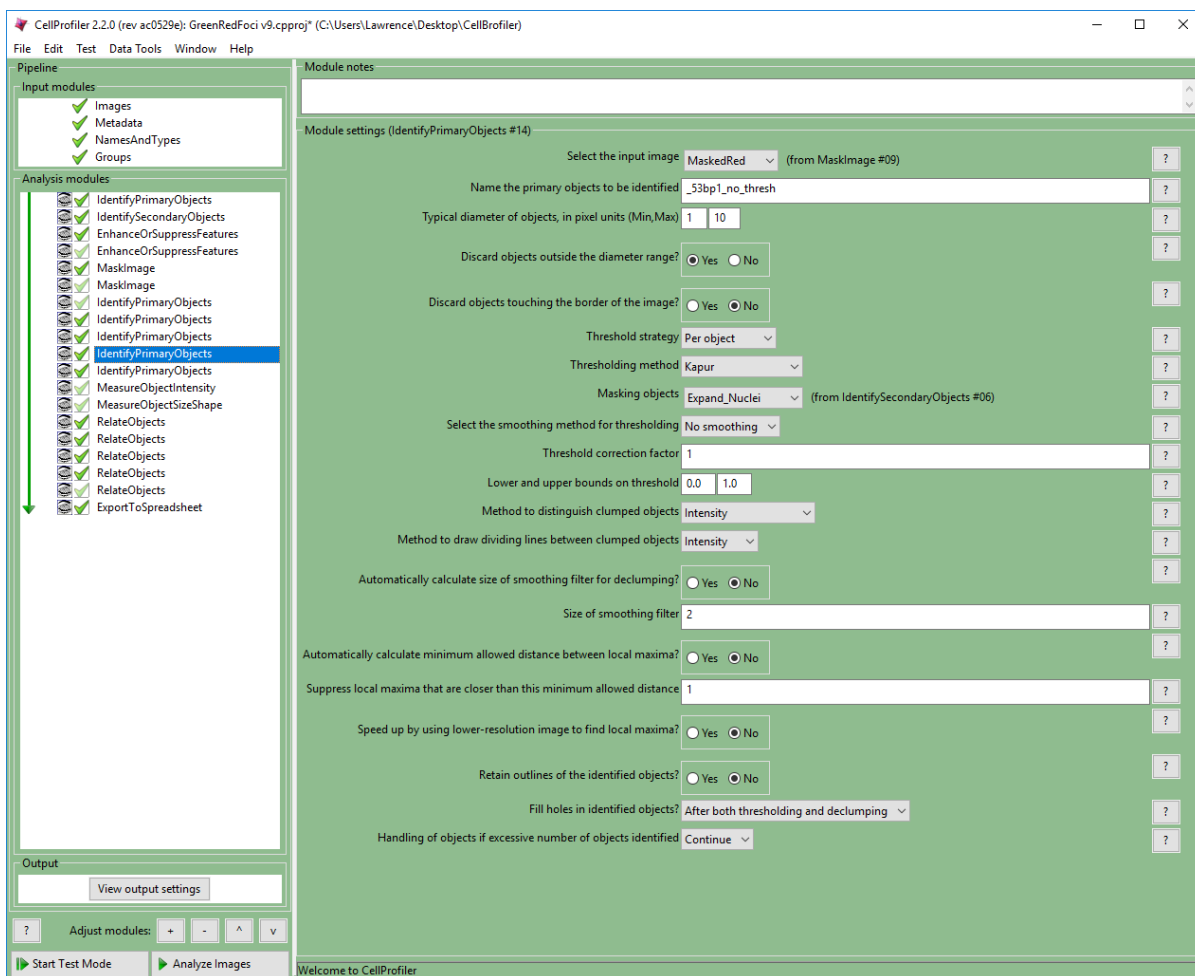


Figure 20. CellProfiler measurement parameters to score red foci.

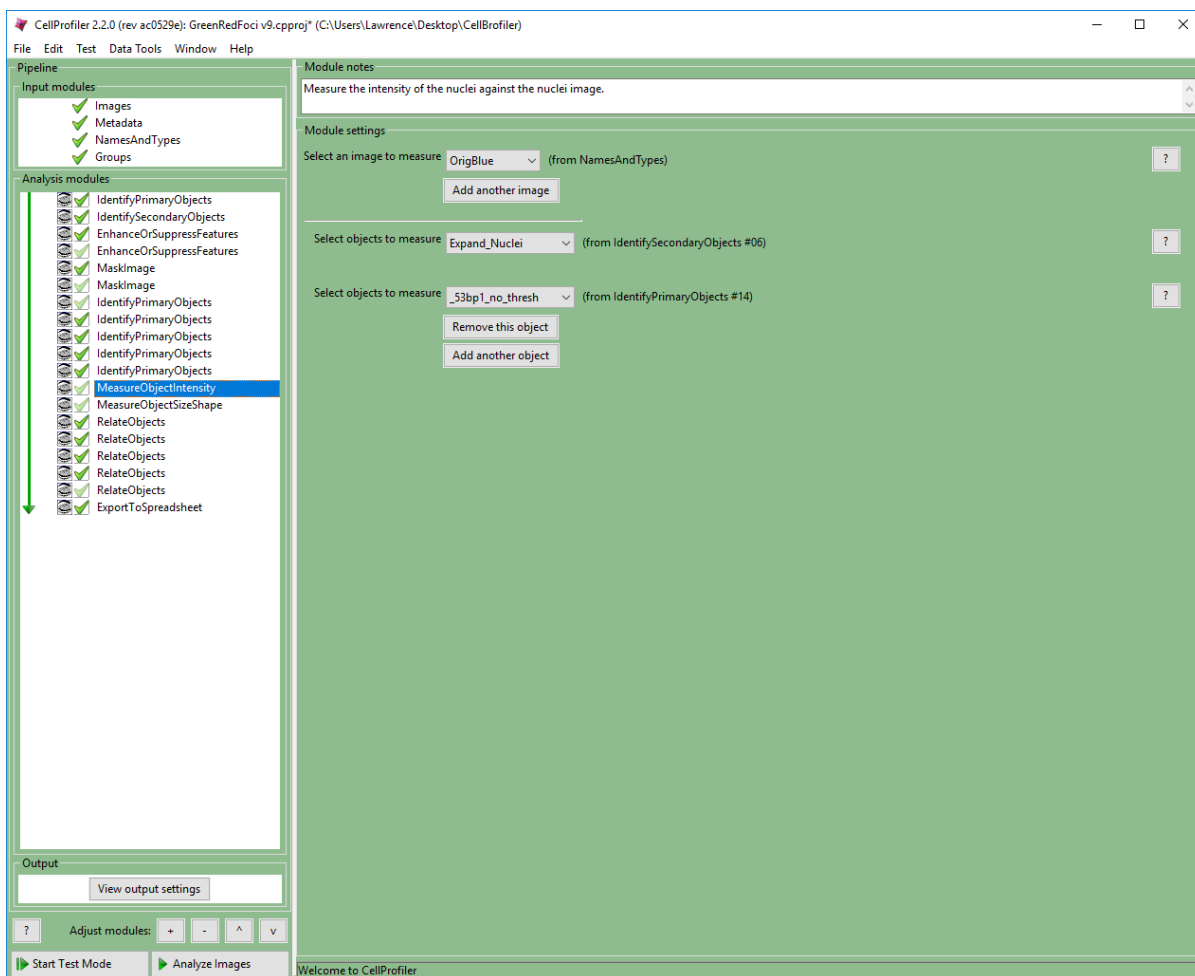


Figure 21. Selecting type of measurements for objects detected with a CellProfiler pipeline.

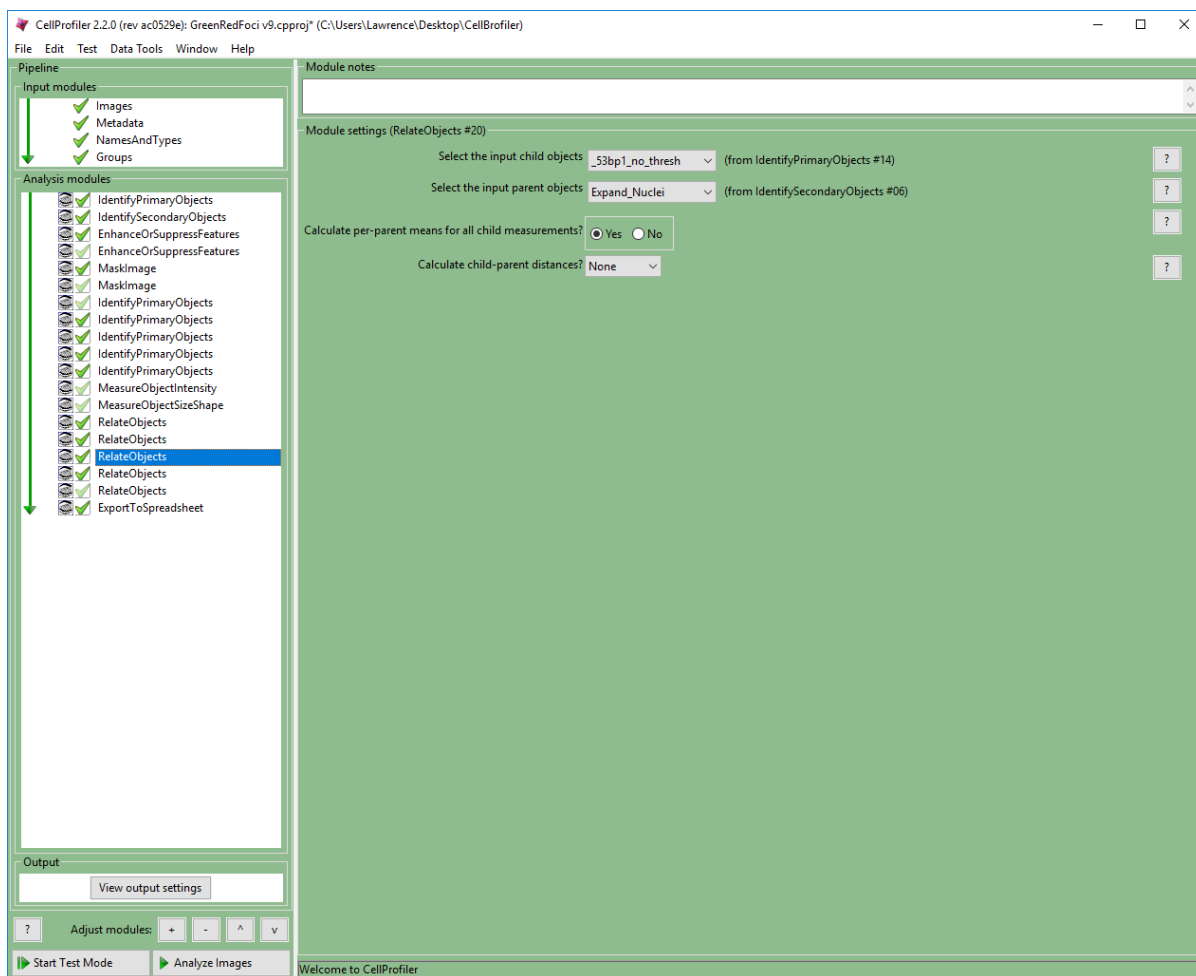


Figure 22. Correlating measurements between objects in CellProfiler.

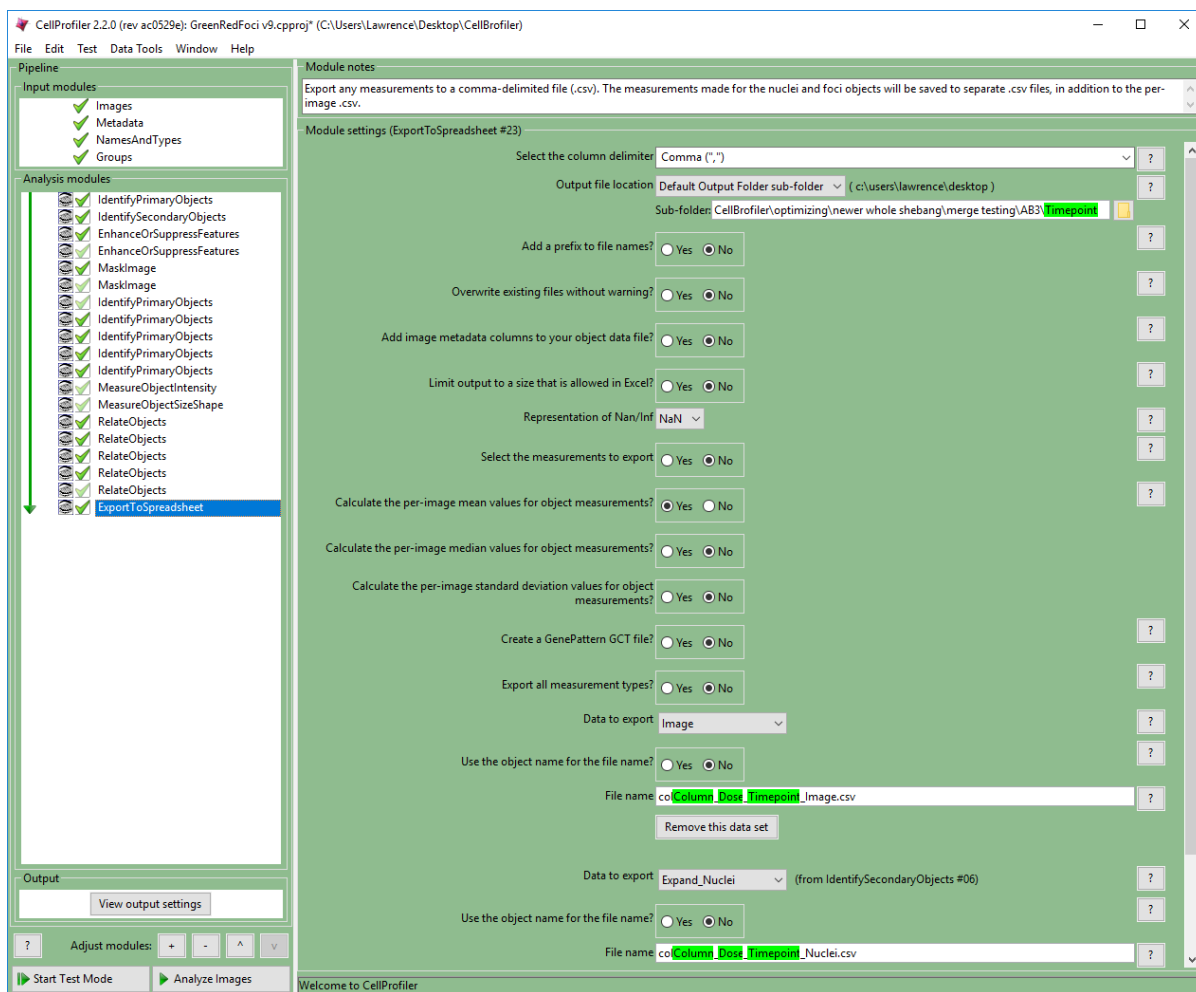


Figure 23. Exporting data in CellProfiler.

## 3D Cell Culture

### Glioma stem cell (GSC) lines and media

Patient-derived GSCs were obtained from Dr. Erik Sulman. The GSCs are cultured in Neural Basal Medium (NBM) consisting of DMEM/F-12 media, 10% B-27 serum-free supplement, EGF (20 ng/ml), FGF (20 ng/ml), and 1% normocin in a humidified incubator at 37°C and 5% CO<sub>2</sub>. GSC cell lines used for this work were GSC23, GS7-11, and GSC300.

### GSC maintenance and culturing

In the absence of serum GSC cultures grow *in vitro* as a spheroidal suspension. General GSC maintenance consisted of monitoring cultures for pH-dependent media color change and neurosphere formation. NBM was refresh once it took on a yellow color due to the solution becoming acidic as indicated by the pH indicator, phenol red. Media changes were achieved by transferring the cell suspension solution into a sterile conical tube, washing the stock T-75 flask with 5mL of serum free media (SFM; DMEM/F-12 media with no additives) and placing the wash volume into the tube. The cell suspension is then centrifuged for 5 minutes at 1300 rpm at RT. Following centrifugation, the supernatant is removed, the cell pellet is resuspended in fresh NBM, the solution is transferred into a tissue culture flask, and the flask is returned to the incubator. Once neurospheres have formed within a culture, the cell line must be passaged by forming a single cell suspension and subculturing the cells. Passaging the GSCs follows a similar procedure to a media change. All steps are performed at RT. The cells are collected and centrifuged at 1300 rpm for 5 minutes. The supernatant is aspirated and the cell pellet is resuspended in 2 mL of 0.05% trypsin-EDTA and incubated at

37°C for no more than 2 minutes. Trypsinization is then halted by the addition of an equal volume of defined trypsin inhibitor and mixing the solutions with additional pipetting. 11 mL of SFM is then added to the cell solution and a single cell suspension is created by further pipetting of the solution (3-12 times). The cell solution is then centrifuged at 1300 rpm for 5 minutes after which the supernatant is removed and the cell pellet is resuspended in NBM. The single cell stock solution is then diluted into a new tissue culture flask with additional NBM. Typical split ratios are 1:2-1:5 depending on the confluency of the original flask.

#### GSC spheroid formation

Uniform spheroids were formed by adding an appropriate number of GSCs to microplates conducive to spheroid formation. GSCs were collected, trypsinized, and resuspended to form a single cell suspension. The cell concentration was determined and the stock solution was diluted to make a plating solution with a concentration of 5 cells per  $\mu\text{L}$ . 200  $\mu\text{L}$  per well of the plating solution was then dispensed into ultra-low attachment round bottom plates to achieve 1000 cells per well. The round bottom plates were then centrifuged for 5 minutes at 200g at RT to promote cell aggregation. Following centrifugation, a sample of the wells are examined utilizing a light field microscope to ensure cell clustering. If further aggregation is required, the plates may receive additional centrifugation. The cell aggregates are returned to culture for at least 3 days for spheroid formation to occur. Following the initial incubation period, the wells are examined under a light field microscope to ensure spheroid formation prior to use.

## Rat brain microtissues (RBMTs)

The normal brain tissue organoid system utilized was developed by and available pre-commercially from InSphero, Inc. In this model complete neonatal rat brain tissue is harvested and homogenized. The homogenate is coalesced into spheroids above a low adhesion 96-well plate (GravityTrap) utilizing a modified hanging drop method that yields one organoid per well. The resulting RBMT organoids have been found to be suitable for long-term culturing (>3 months) while exhibiting composition and maturation analogous to native tissue.

## Rat brain microtissue receiving and culturing

Once spheroid formation is completed and passes quality assurance testing including viability and size measurements, the maintenance culturing media is replaced with a shipping media. The wells of each plate are sealed with a sterile silicone insert, the plate is lidded, and then each plate is individually sealed within a plastic microplate bag. The tissues are shipped in an insulated container with heat packs and electronic temperature monitoring to ensure tissue viability. When the RBMT package arrived, the temperature log files were accessed and examined for any threshold alarms. With no temperature alarms present, the tissue media was visually inspected for abnormalities such as indications of contamination or evaporation. If no concerns were noted with the delivery inspection, the tissues were then prepared for maintenance culture. The RBMTs are shipped with a buffered media that does not require CO<sub>2</sub>. The shipping media must be exchanged with the maintenance media for traditional culturing in a humidified incubator at 37°C and 5% CO<sub>2</sub>. This media change is achieved by first removing the outer plastic seal of each plate and inverting each plate 5 times. The plates

are then centrifuged at 200g for 2 minutes at RT. The RBMTs are then moved back to a biological cabinet to remove the silicone well sealer by firmly holding the plate down with one hand while the other hand slowly peels the sealer with uniform pressure starting from one end of the plate. The shipping media is removed using a multichannel pipette by angling the tips along the edge of the wells and slowly (approximately 30  $\mu\text{L/s}$ ) aspirating the majority of the shipping media (90  $\mu\text{L}$ ). Once the shipping media is removed, 75  $\mu\text{L}$  per well of warm maintenance medium is dispensed with the multichannel pipette. The plates are relidded and the spheroid morphology is visually examined under a light field microscope. The plates are then placed in a humidified incubator at 37°C and 5%  $\text{CO}_2$  to recover and normalize overnight. RBMTs plate scans are acquired the following day to measure spheroid sizes.

#### RBMT replating

If necessary, the tissues are separated into different plates to be exposed to the desired experimental conditions. Wells of the plates receiving RBMTs are prefilled with 100  $\mu\text{L}$  of maintenance media and wells to not be experimentally utilized are filled with 200  $\mu\text{L}$  of PBS. The plates are then placed in an incubator for 15 minutes before the replating commences. The transfer microplates were the same ultra-low attachment 96-well round bottom plates as those used for the GSC spheroid culturing and irradiations. Replating the RBMTs is achieved using large bore or orifice 200  $\mu\text{L}$  pipette tips. The tip is placed to cover most of a well opening and 50  $\mu\text{L}$  of media is siphoned with sufficient speed to draw in the spheroid. The tip is visually examined after each aspiration to ensure that a spheroid is contained within the



media. The 50  $\mu$ L of media containing the spheroid is then transferred to the appropriate pre-filled well. Once a transfer plate contained all required spheroids, it was re-lidded and held slightly above eye level such that the well bottoms could be visualized to confirm the presence of spheroids within each well. The microplates are then placed in a humidified incubator at 37°C and 5% CO<sub>2</sub> to recover and normalize for at least 8 hours before experimental use.

#### Spheroidal culture media refreshment

For long term culturing (>3-5 days), both GSC and RBMT microplate spheroid cultures require that the medium be intermittently refreshed. Media changes were performed by placing the tips of a multichannel pipette against the well edges and sliding the tips down approximately half the height of the wells while avoiding the well bottoms. Half the media volume was then slowly removed. For the RBMTs and the first two weeks of GSC spheroid cultures media changes were performed every 3-5 days. The GSC spheroid cultures require increased media change frequency as they grow as indicated by the phenol red pH indicator present in the media.

#### Spheroid high resolution scans

Spheroidal culture size measurements were taken at 4800 dpi on a Cell3Imager flatbed scanner. The focal plane of the scanner is adjustable and required optimization by brand for each tissue culture plate utilized. The value for the Corning 96-well round bottom ultra-low adhesion plates used was 13.00 mm. Insphero GravityTrap plates required 2

imaging heights, one for the plate center and the other for the peripheral wells. Using a plate map, the outer wells scan height was set to 13.85 mm and the inner wells were scanned at 13.70 mm.

### Spheroid size measurements

Following the capture of a high-resolution scan, spheroid size was determined using image based analysis and the Cell3Imager analysis software package. Prior to analysis, the scanned image is segmented into individual well images using the well spacings defined within the respective plate geometry file. A region of interest within the well area is then defined for analysis. The recipes used to measure the spheroid size of the spheroids were user trained algorithms. The scanner software settings as well as the size measurement recipe are shown in Figure 24Figure 34.

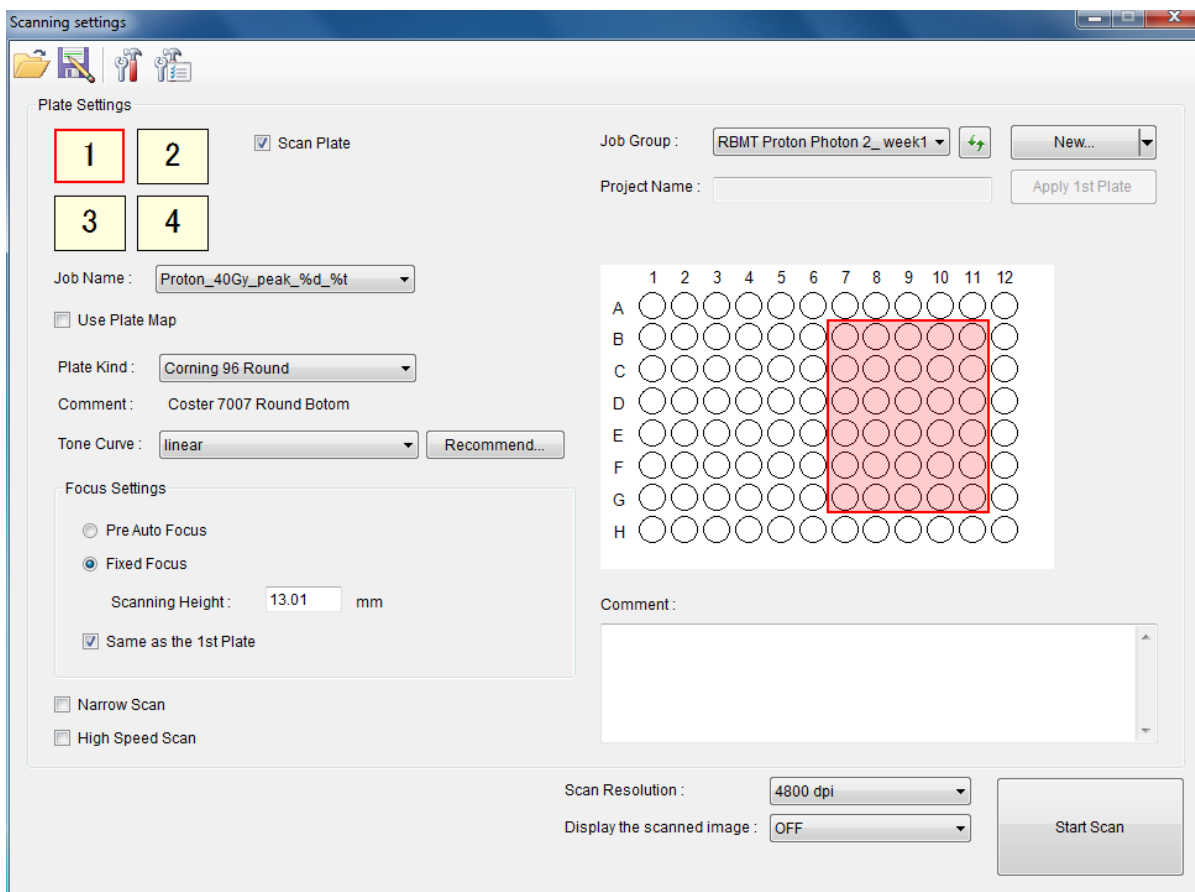


Figure 24. Cell3Imager scan setup.

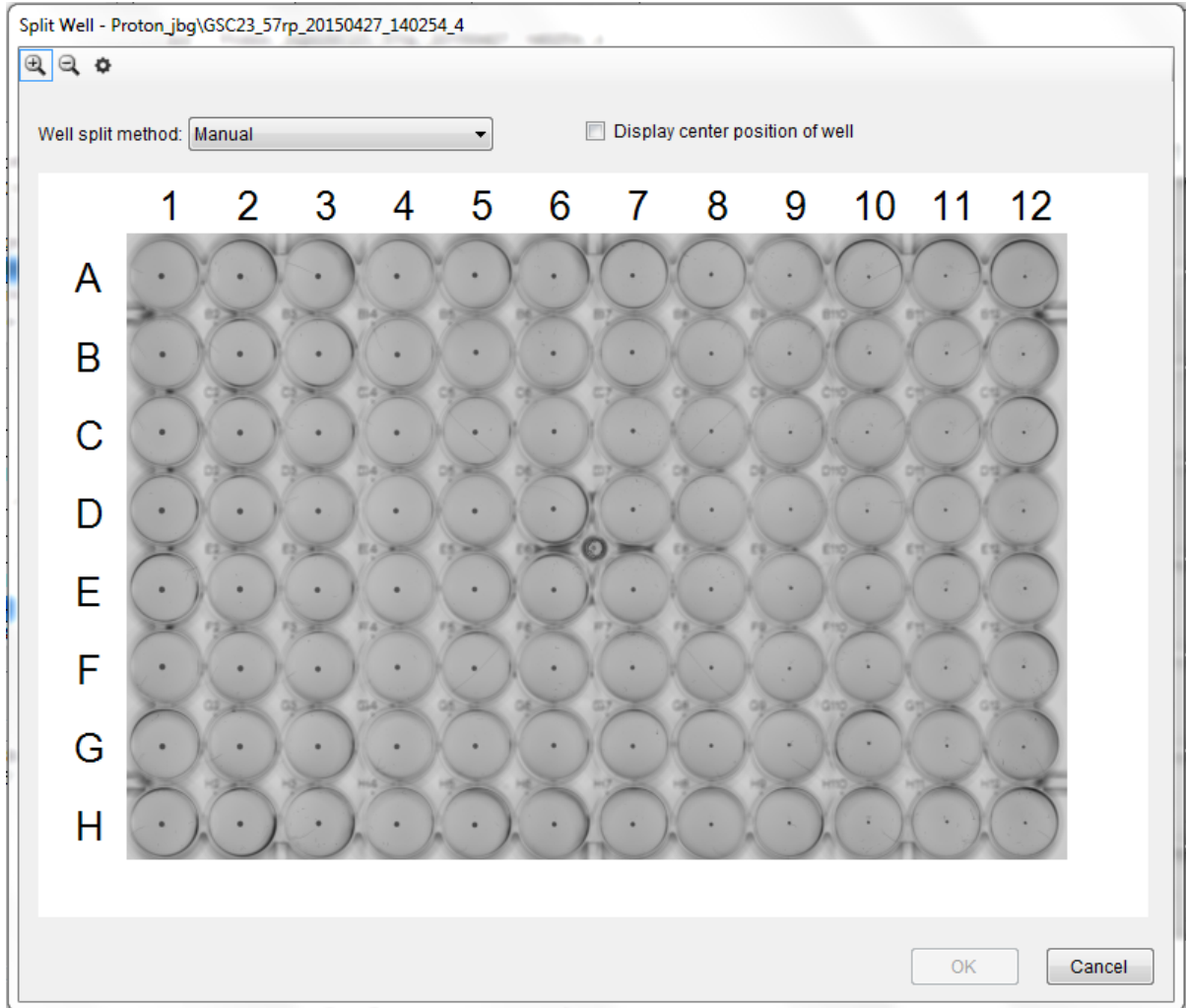


Figure 25. Cell3Imager high-resolution plate scan.

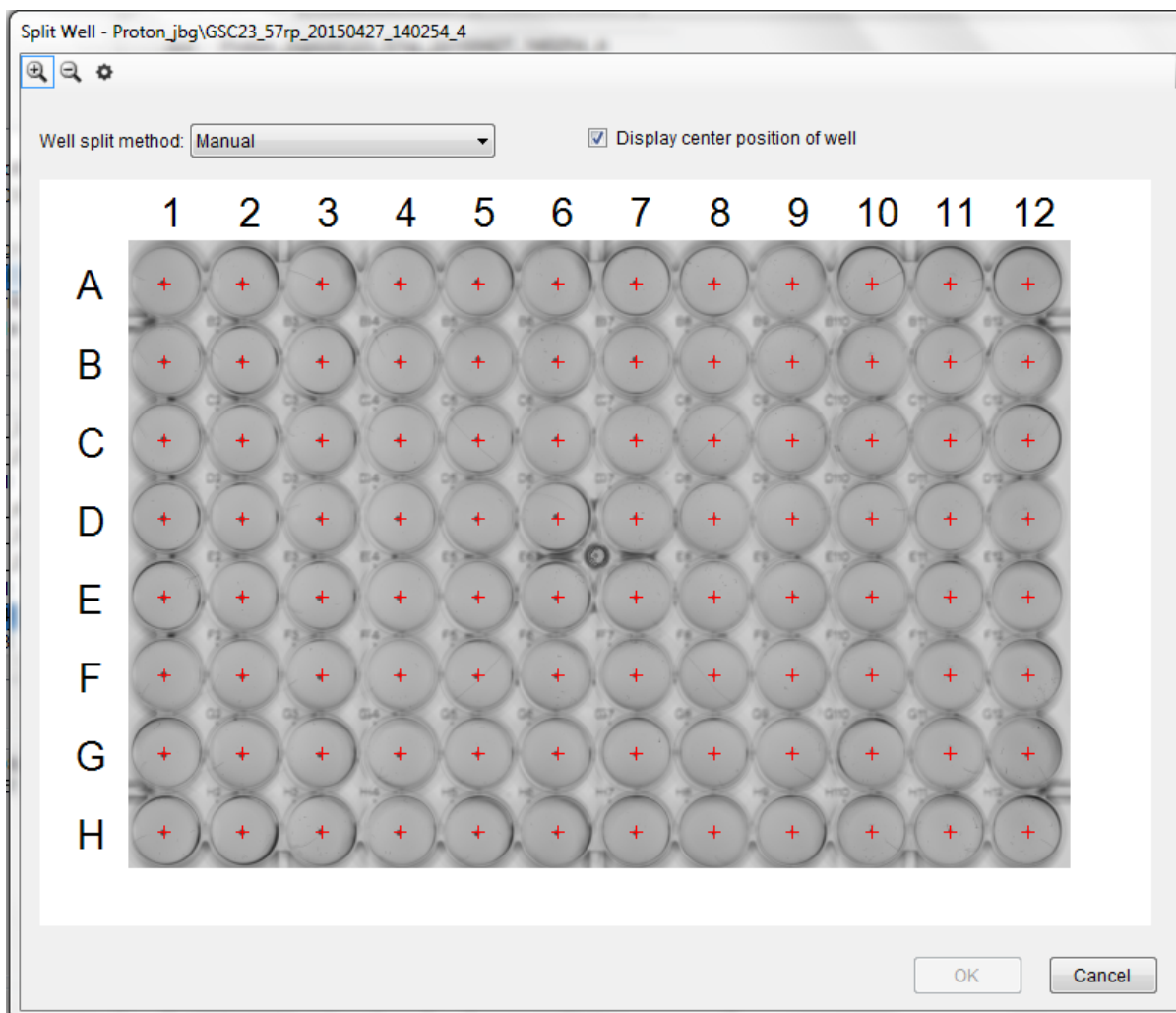
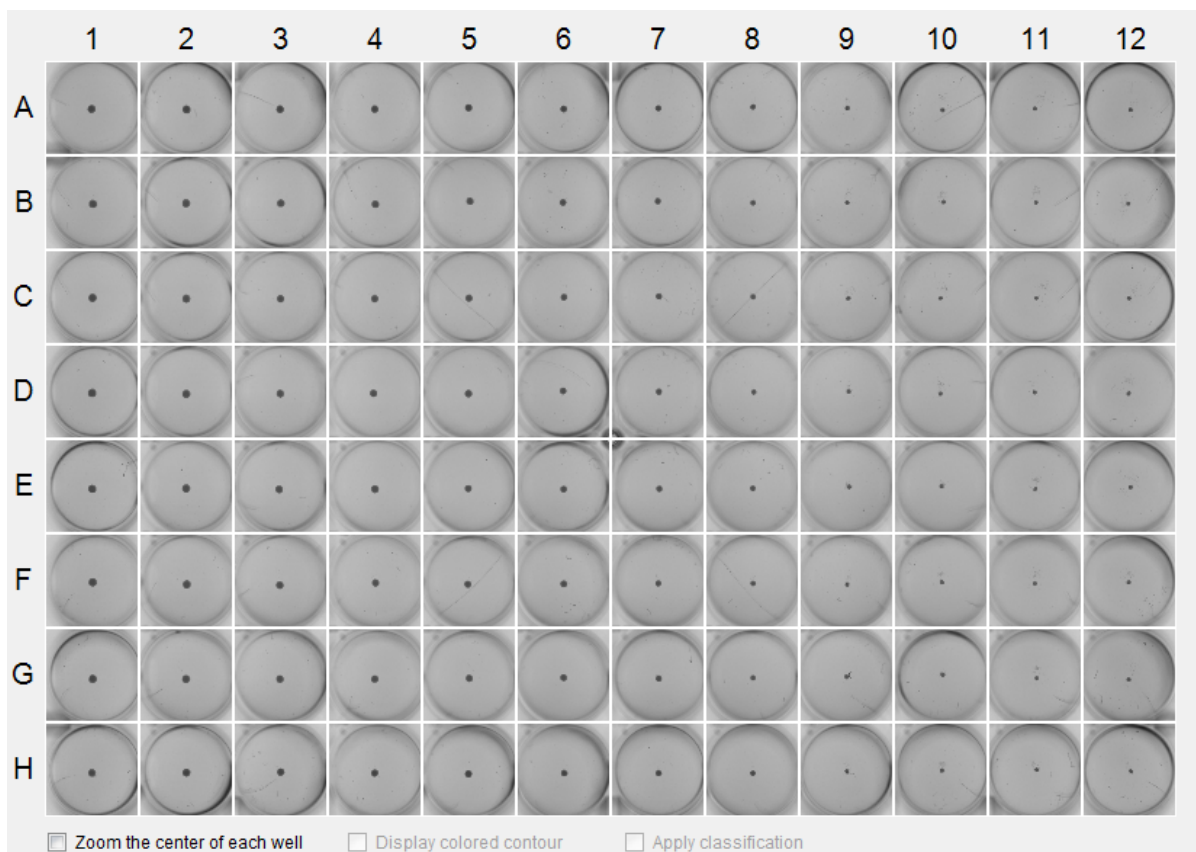


Figure 26. Cell3Imager well center orientation.



*Figure 27. Cell3Imager well segmentation.*

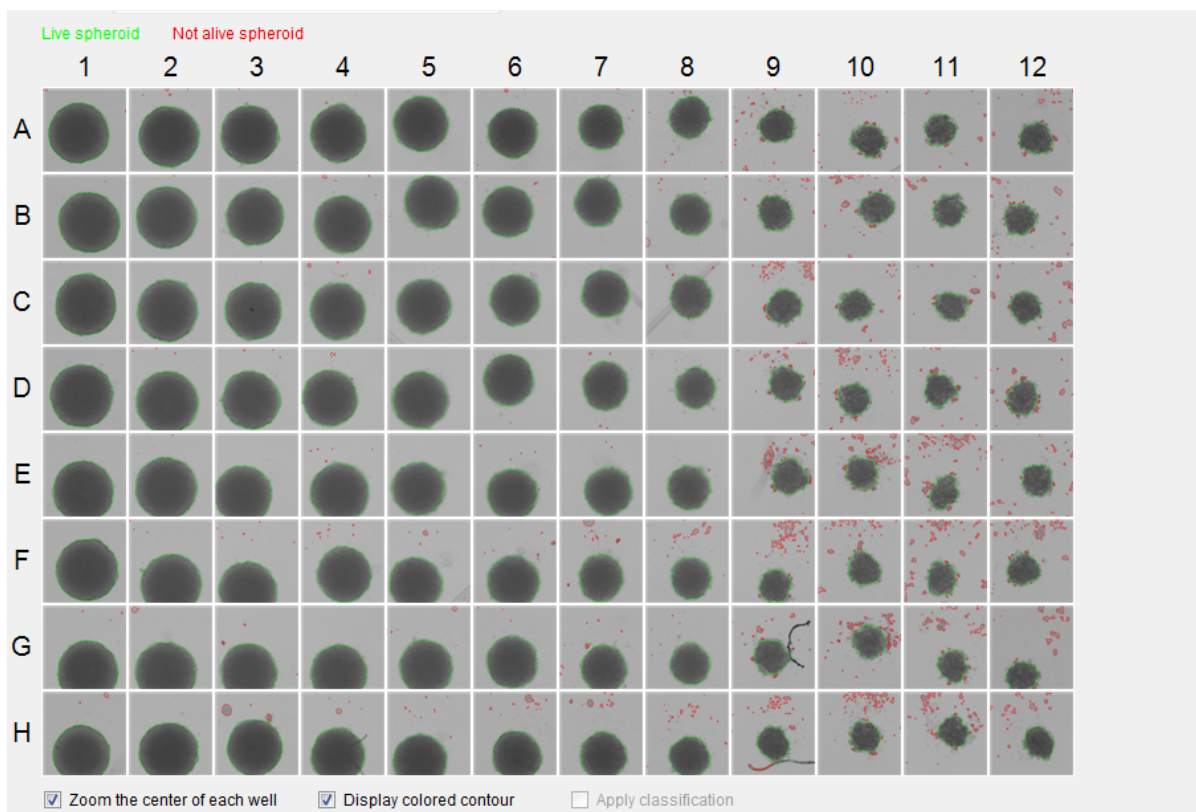


Figure 28. Cell3Imager spheroid measurement.

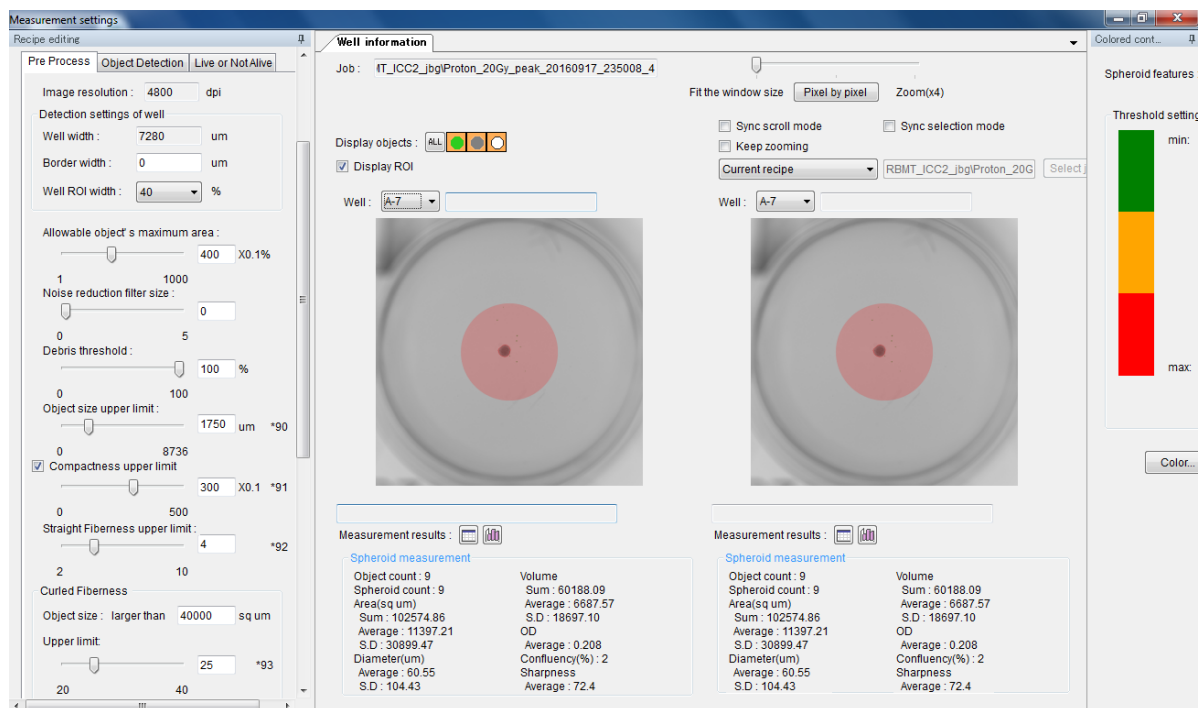


Figure 29 Cell3Imager size measurement pre-processing parameters.



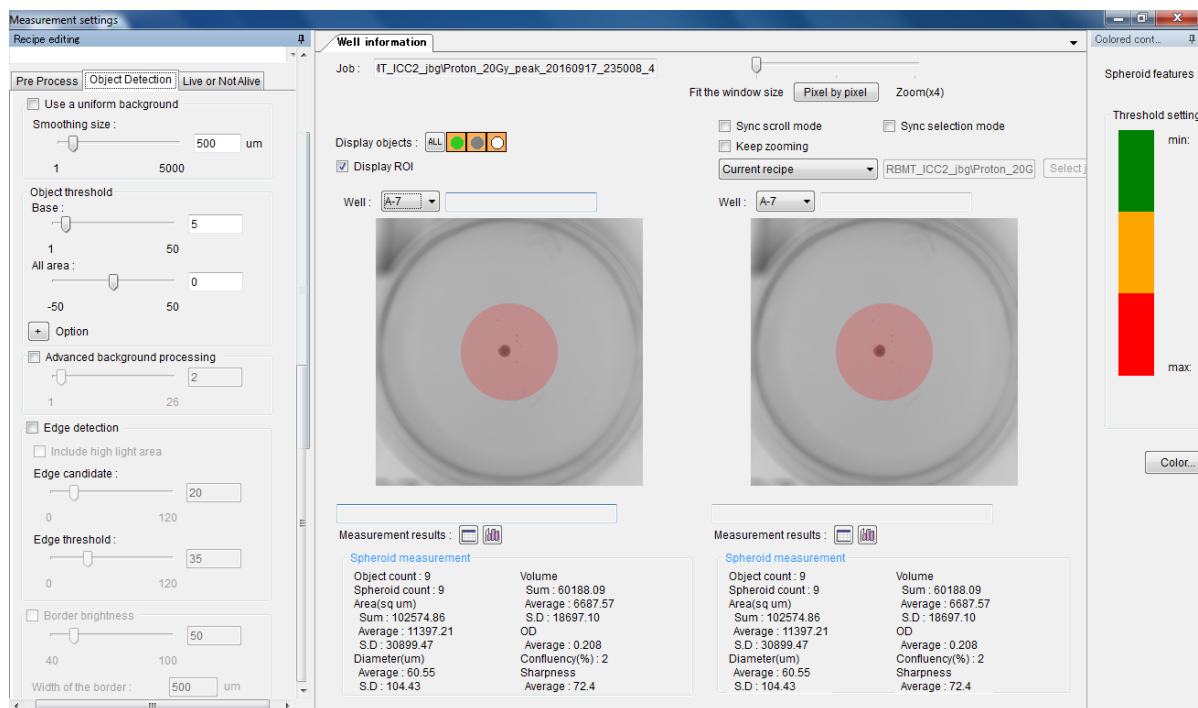


Figure 30. Cell3Imager size measurement object detection parameters.

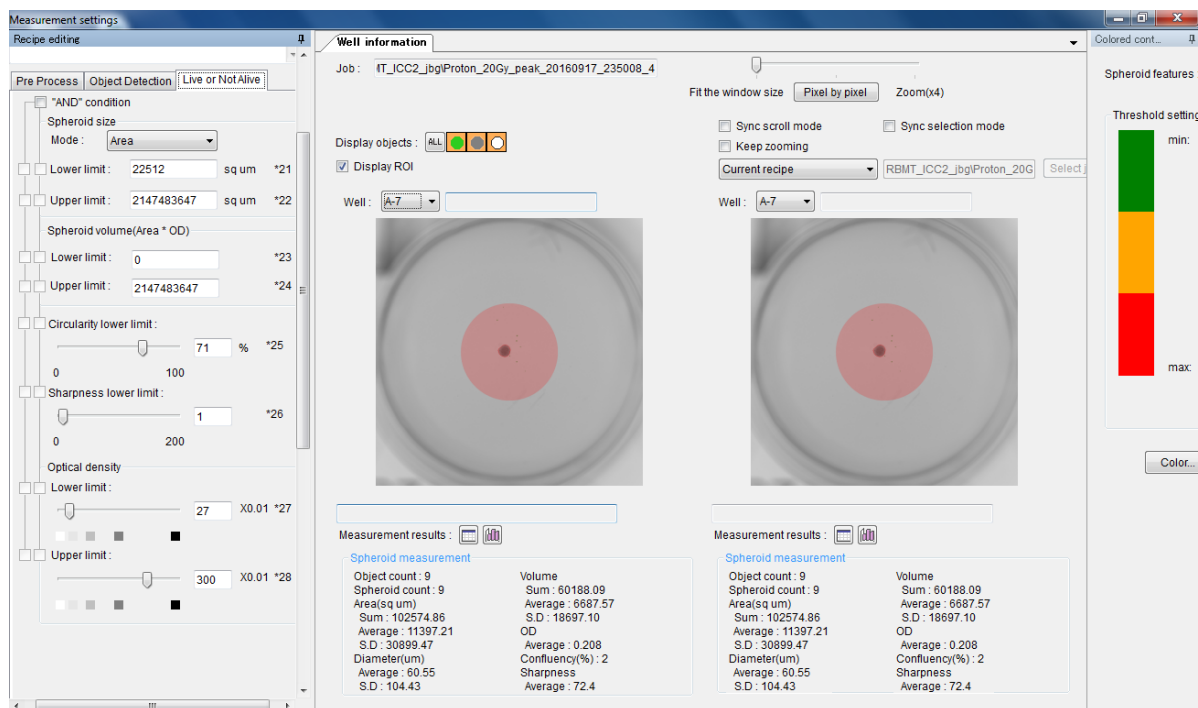


Figure 31. Cell3Imager size measurement live or dead detection parameters.

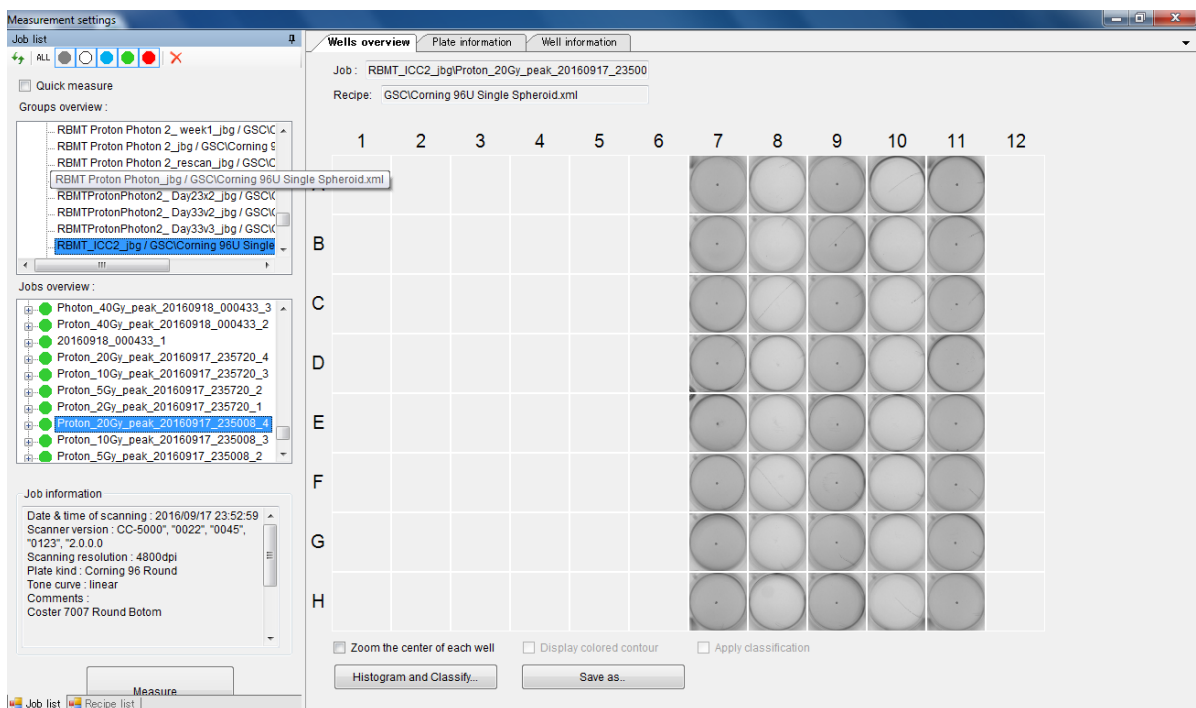


Figure 32. Cell3Imager measurement window.

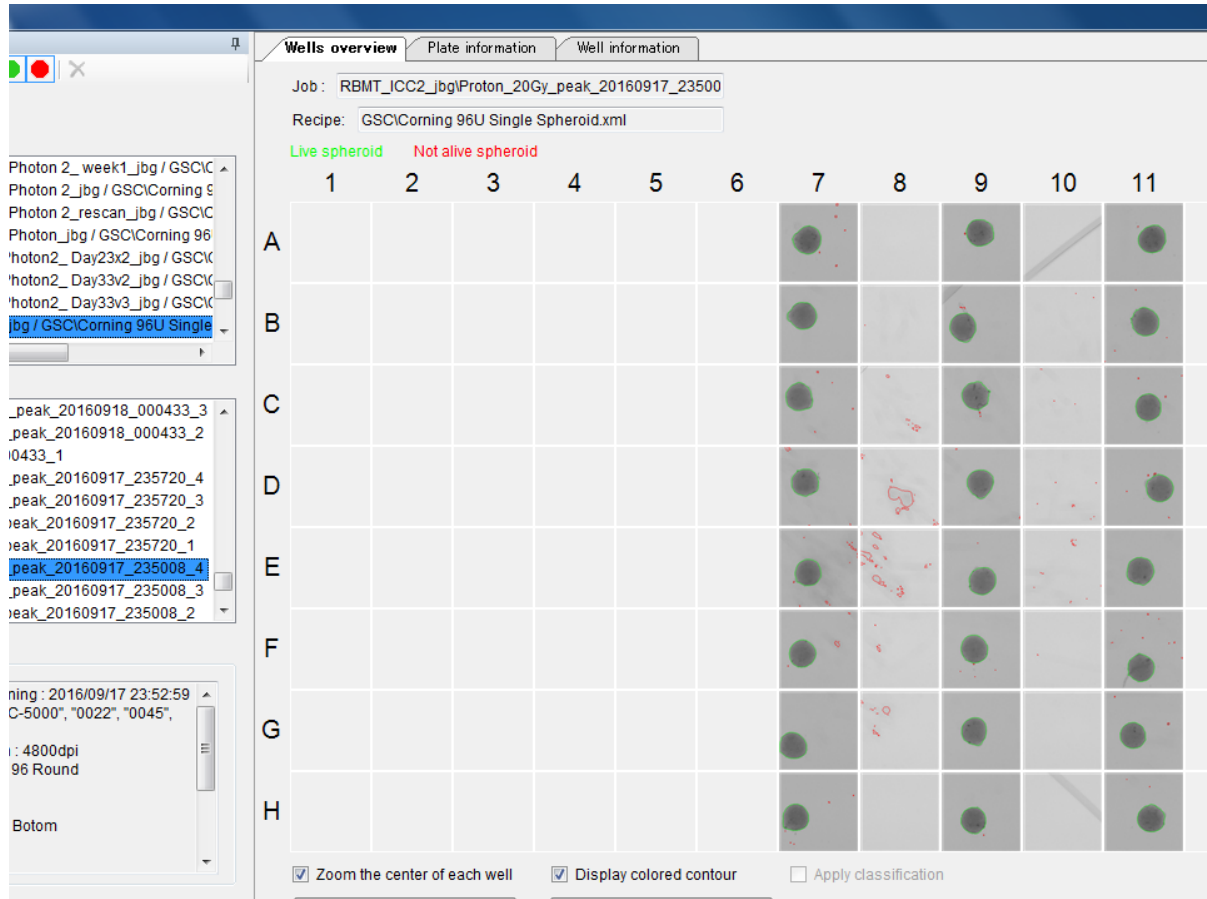


Figure 33. Cell3Imager measurement window with scored spheroids displayed.

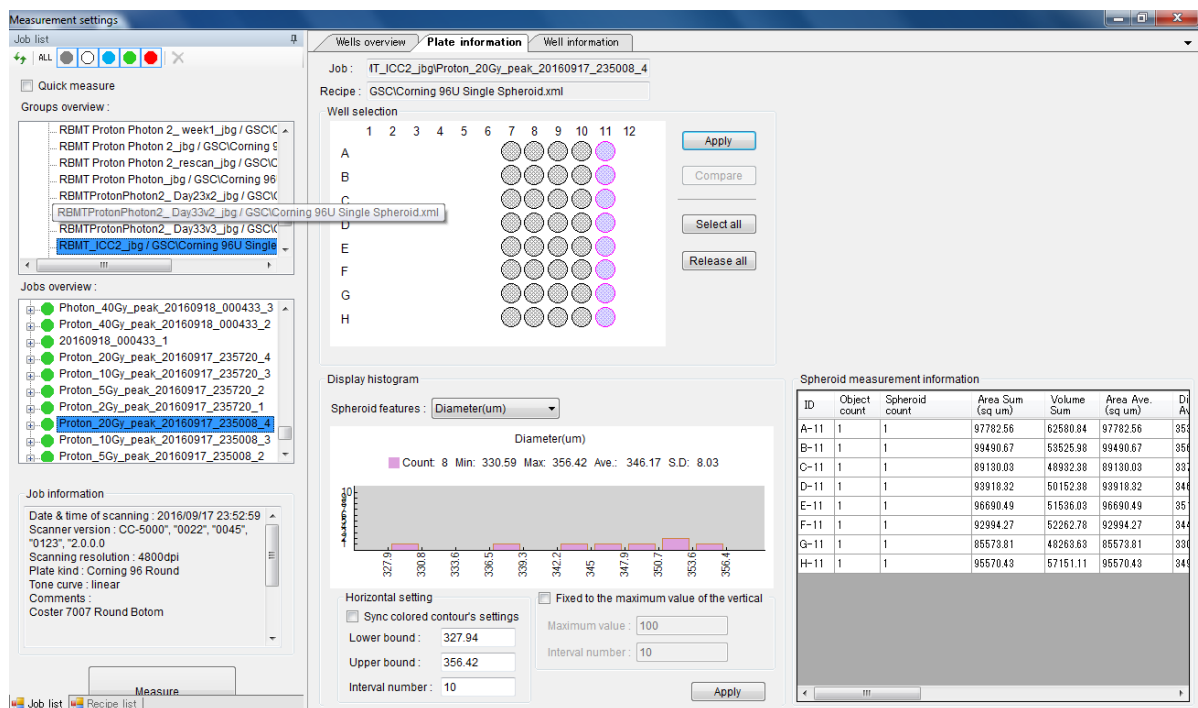


Figure 34. Cell3Imager plate information window.

### 3D surviving fraction calculation

Surviving fractions of clonogenically immortal cancer spheroid cultures were determined from a longitudinal series of size measurements over a time period of 30 days by adapting the method of Demidenko (99). Demidenko demonstrated SF can be determined from tumor size measurements as:

$$SF = e^{(-k \cdot TGD)}$$

Where k is the growth constant and TGD is the tumor growth delay. The growth constant is calculated by fitting the size of the unirradiated control condition to the exponential growth equation:

$$Size = e^{k \cdot t}$$

The TGD is the time difference for an unirradiated tumor and an irradiated tumor to reach iso-response. For this work the response level was set to be when the average tumor spheroids' volume increased by a factor of 16 from the initial size. TGDs were calculated using linear interpolation between measured spheroid sizes.

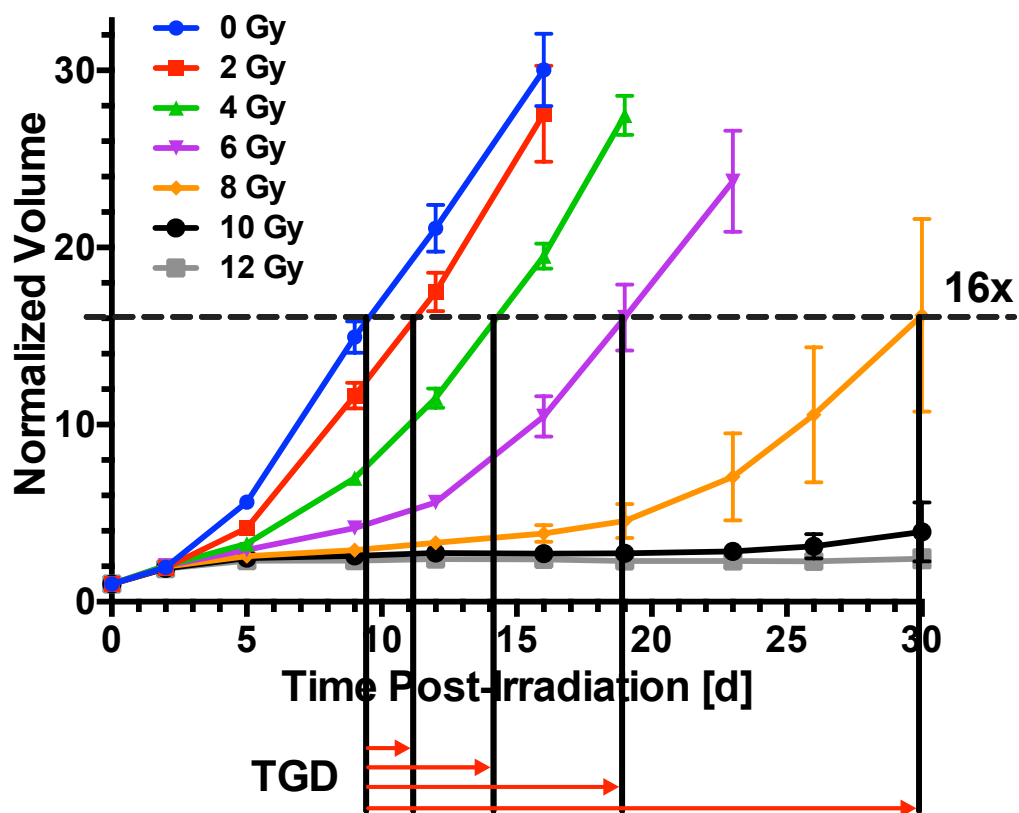


Figure 35. Demonstration of TGD determination. TGD is experimentally determined using linear interpolation from the measured growth curves.

## Viability

Spheroid viability was assessed using the Realtime-Glo MT Cell Viability Assay, a non-lytic bioluminescent reporter assay which enables real time viability monitoring. The assay consists of two reagents: a luciferase-based additive and a cell permeable, pro-substrate form of luciferin. Both reagents are added to the culturing media. The pro-substrate is reduced to luciferin within viable cells and released from the cells into the surrounding tissue culture media. The reduced pro-substrate is rapidly used by the luciferase media additive to produce a bioluminescent reaction and thus signal. The assay has the benefit of being non-toxic enabling additional assays on the spheroids such as terminal histology and immunofluorescence staining. Caution must be exercised when using this assay as the readout is dependent on the sample metabolism and thus temperature.

## RBMT immunofluorescent staining

RBMTs were transferred into the wells of a standard 24-well tissue culture plate using the same method as during replating. Replicate tissues were placed within the same well. 1 mL of 4% PFA in PBS was added to each well to fix the RBMTs. The plate was placed on a laboratory rocking platform for 45 minutes at room temperature for fixation to occur. The fixative was removed by carefully pipetting as much of the solution as possible (typically 900-950  $\mu$ L) while avoiding the microtissues. Specifically, liquid removal between steps was performed by tilting the plate between 30° and 45° and placing the tip of a 1 mL pipette at the bottom edge of the well near the superior portion of the well (i.e. where the liquid is least thick when the plate is tilted) and siphoning the solution while moving the pipette along the bottom edge. As the volume reduces, the tissues will begin to move with the



solution towards the tip. When the tissues begin to move, the pipette should be moved to the other side of the well, the plate tilted away from the tip, and any additional solution that can be removed should be pipetted while the tissues move towards the tip again. Once the fixative is removed, the tissues are then washed with 1 mL of PBS with rocking four times at RT for 10 mins. The RBMTs are permeabilized with 1 mL of 1% Triton X-100 in PBS for 1 hour with rocking at RT. The tissues are then blocked for 2 hours with rocking at RT with 1 mL per well of 10% goat serum/0.3% Triton X-100/PBS. The primary antibody incubation was performed overnight at 4°C with rocking. The antibodies were diluted in 5% goat serum/0.3% Triton X-100/PBS. Each well contained 500 µL of primary antibody solution. The primary antibody used to label neurons was a rabbit polyclonal to beta III tubulin (1:1200, Abcam, ab18207). Glial cells were labeled by a chicken polyclonal antibody to glial fibrillary acidic protein (GFAP) (1:2400, Abcam, ab4674). Primary antibody concentrations were typically 1 µg/mL. After the primary incubation, the RBMTs were washed four times using 1 mL per well of 0.1% Triton X-100/PBS for 20 minutes each at RT with rocking. The spheroids were then stained overnight at 4°C with rocking. 500 µL per well of highly cross-adsorbed goat anti-rabbit and goat anti-chicken secondary antibodies respectively conjugated to AlexaFluor488 and AlexaFluor594 dye diluted in 5% goat serum/0.3% Triton X-100/PBS at a concentration of 1 µg/mL (1:2000, Life Technologies) was used for the secondary staining. During the secondary antibody incubation and all the following steps the plate was wrapped in aluminum foil to protect the fluorescent dyes from light. Following secondary antibody incubation, the cells were washed with 0.1% Triton X-100/PBS four times for 20 minutes at RT. If an optional nuclear staining was performed, the RBMTs would be incubated while protected from light with 1 mL of DAPI (1 µg/mL) per well for 60 mins at

RT with rocking. The RBMTs are washed an additional three times with 0.1% Triton X-100 for 10 minutes at RT with rocking. Following the IF staining protocol, the RBMTs were mounted on 8-well chamber slides with replicate tissues placed within the same well. A cut 200  $\mu$ L pipette tip was precoated in serum and then used to manually transfer the RBMTs from the 24-well plate to the appropriate well on the chamber slide without the use of a pipette. Transferring tissues without a pipette was achieved by holding the pipette tip with the thumb and the middle finger so that the index finger can access the open top end of the tip. Adjusting the pressure applied to the top of the tip when submerged will generate suction. The RBMTs were first visualized under a light microscope. The pipette tip was placed adjacent to the tissues, and the pressure within the tip was reduced to create suction to draw in the tissue. The pipette tip is then placed at the appropriate location on the chamber slide and pressure is applied to expel the liquid and RBMT. The transfer process is repeated for all conditions. Once all the desired RBMTs were transferred to a chamber slide, a drop of mounting media (20-25  $\mu$ L) was applied to each well. The slides were covered with a No.1 glass slide, protected from light, and allowed to set overnight. The next day coverslip edges are sealed with clear nail polish. The sealed slides are protected from light and placed at 4°C for storage.

#### RBMT immunofluorescent imaging

RBMT confocal imaging was performed using an Olympus IX83 microscope with a 60x oil immersion objective. RBMT imaging consisted of four 512x512 pixel fields forming a rectangle (2x2) to capture the entire spheroid. The image plane spacing was set to 0.5 $\mu$ m and the total stack height was adjusted to capture an entire spheroid. The microscope pin hole size was set to 80  $\mu$ m. The pixel dwell time was 2  $\mu$ s. Laser parameters were 0.3% blue (473

nm) laser power and 1.2% green (543 nm) laser power. The gain was set to 475 V for the green channel and 600 V for the red channel. Kalman 2x averaging was used per line. Each image was captured sequentially to prevent spectral cross over.

### RBMT image analysis

Maximum intensity projection images of each RBMT field stack were stitched to create a single composite image per RBMT using the Fiji package of ImageJ. The Grid/Collection addon was used to perform a row by row, right and down, linear blend fusion (100). The composite images were scored by thresholding the channels and calculating the integrated pixel intensity. The thresholds were determined from the control conditions. For both the red (beta-III tubulin) and the green (GFAP) channels the thresholding range was set to be 30 to 255.

### RBMT histology

RBMTs were transferred and replicates pooled into 1.5 mL microcentrifuge tubes. Tissues were allowed to settle at the bottom of the tube. A quick spin in a tabletop centrifuge was performed prior to media removal to ensure tissues were settled. Excess culture media was removed by inserting a 200  $\mu$ L pipette tip at the liquid surface, slowly releasing plunger, and moving the tip down the tube with the decreasing media level. The aspiration is stopped when the spheroid cluster begins to be disturbed by the liquid removal. 500  $\mu$ L of 4% PFA in PBS is added to each tube for spheroid fixation. The fixation conditions are rocking at RT for 60 minutes. Following fixation, the fixative is removed as before, and the spheroids are

washed three times in PBS for 10 minutes each at RT with rocking. Organoids are then removed from the microcentrifuge tube using a pipette with a wide-bore tip and placed within a droplet on a piece of parafilm. Excess PBS is removed by touching the droplet with the edge of an absorbent cloth such as a Kimwipe. The tissues should be present on the parafilm with little liquid surrounding them. The fixed tissues are then embedded in 2% agarose/PBS by dispensing a small droplet over the RBMTs. The agarose is allowed to cool until solidified at which time it is removed from the parafilm and placed within a histological cassette containing pre-wetted sponges. The cassettes are submerged in 70% ethanol requiring that they are labeled with pencil. The container holding the histological cassettes is then submitted to the core facility for standard histological processing with the directions to embed the agarose plugs with the flat end at the top of the paraffin block.

#### Statistical analyses and plotting

Statistical analyses and plotting were done using GraphPad Prism 7.0. SF data are shown on a semilog scale as mean  $\pm$  standard error of the mean (SEM). Data were fit using a weighted, nonlinear regression to the linear-quadratic model. The extra sum-of-squares  $F$  test was used to compare clonogenic survival curves as a function of LET. The foci data and GSC growth curves are shown as mean  $\pm$  95% confidence interval. SFs calculated for GSCs are presented as mean  $\pm$  standard deviation (SD). RBMT size, viability, and relative expressions are presented mean with replicates. RBE standard errors were calculated by propagating the standard error of the  $\alpha$  and  $\beta$  fits.

## **Results**

### **Development of a high-throughput irradiation platform**

The development of the high-throughput irradiation system was initiated by the desire to apply high-throughput clonogenic assays towards particle radiation biology studies with a focus on improving the statistical power and speed of traditionally laborious studies (Figure 36). As opposed to the traditional clonogenic assay typically performed in 6-well plates, the high-throughput clonogenic assay utilizes a 96-well microplate plate increasing the number of replicates by a factor of 16. The readout of the high-throughput clonogenic assay in our studies is performed using an automated high content screening system (IN Cell Analyzer 6000) to image the wells and perform colony identification and scoring (Figure 37). The use of automation with the clonogenic assay results in a shorter turnaround time from colony staining to data analysis and results.

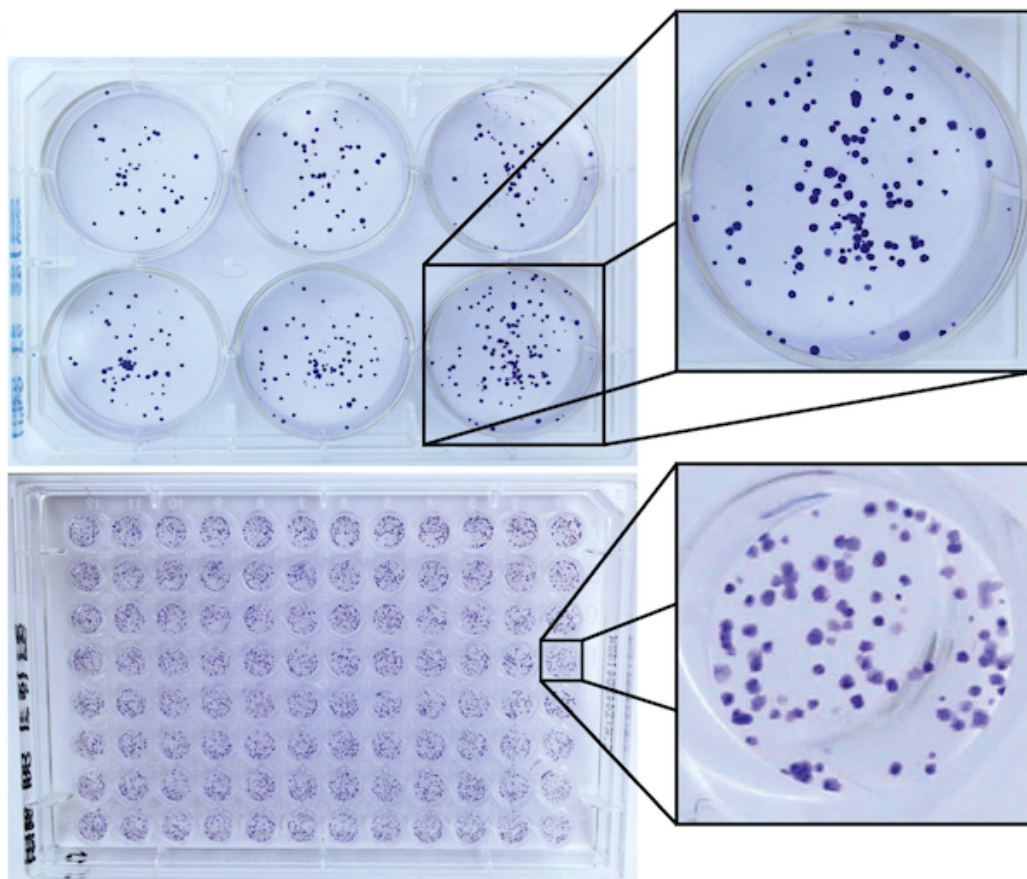


*Figure 36. Traditional vs high-throughput clonogenic assays. The clonogenic assay is typically performed in 6-well plates (top). A 96-well microplate contains 16 times more data wells. Qualitatively, the colonies and their distributions within the wells for the two setups appear similar. Image reproduced from (11).*

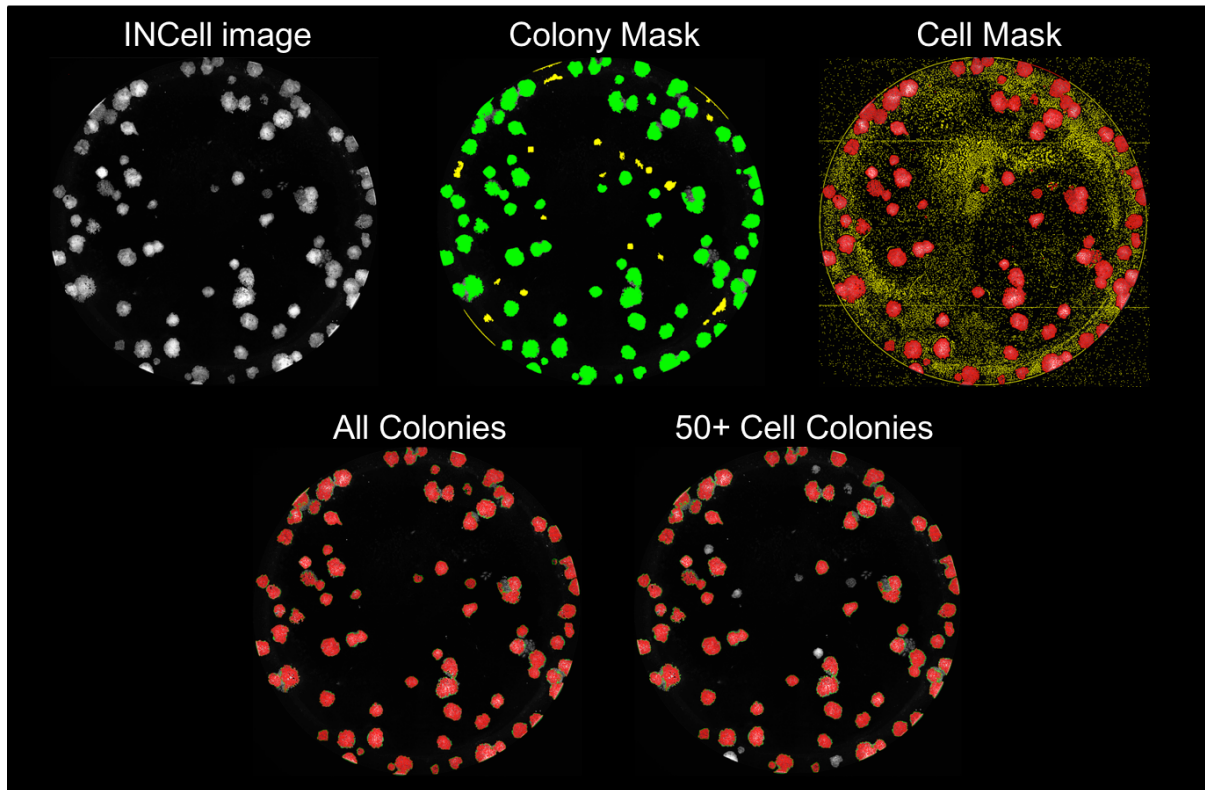


*Figure 37. Image analysis workflow for the high-throughput clonogenic assay. The general image analysis for the high-throughput clonogenic assay consists of imaging the wells in four quadrants with a 4x objective followed by stitching the images together to form a complete image of each well. A size and threshold filter is applied to the image to create colony masks. Within the colony mask, a sieve filter is applied to determine the number of cells contained within each colony. Colonies with more than 50 cells are scored as viable. Image reproduced from (11).*

To apply the high-throughput clonogenic assay towards the study of proton biological response, we interposed a multi-tiered pattern of material between the 96-well microplate and the proton beam (Figure 38). This design enabled the sampling at 12 different locations along the beam path by aligning the steps of the material with the columns of the 96-well plate resulting in 8 replicates per condition per plate.

A calibrated Geant4 Monte Carlo simulation of The MD Anderson Proton Therapy Center's 79.7 MeV proton beam in water was performed to calculate the relative dose and LETs for a 5  $\mu\text{m}$  target size along the beam path (Figure 6 left, Figure 39). 12 locations along the dose-deposition profile were sampled by the high-throughput irradiation apparatus. Lucite, the material used for compensators at the Proton Therapy Center, was chosen to construct the jig necessitating the determination of the water equivalent thickness of Lucite to match the desired depths. The high-throughput irradiation apparatus was milled out of a single Lucite block using a high precision CNC machine (Figure 40). The setup directly inserts into the proton therapy snout with the proton beam incident from below. The microplate sits on top of the jig. A plate holder was fabricated to ensure plate positioning such that the columns align with the respective Lucite steps.



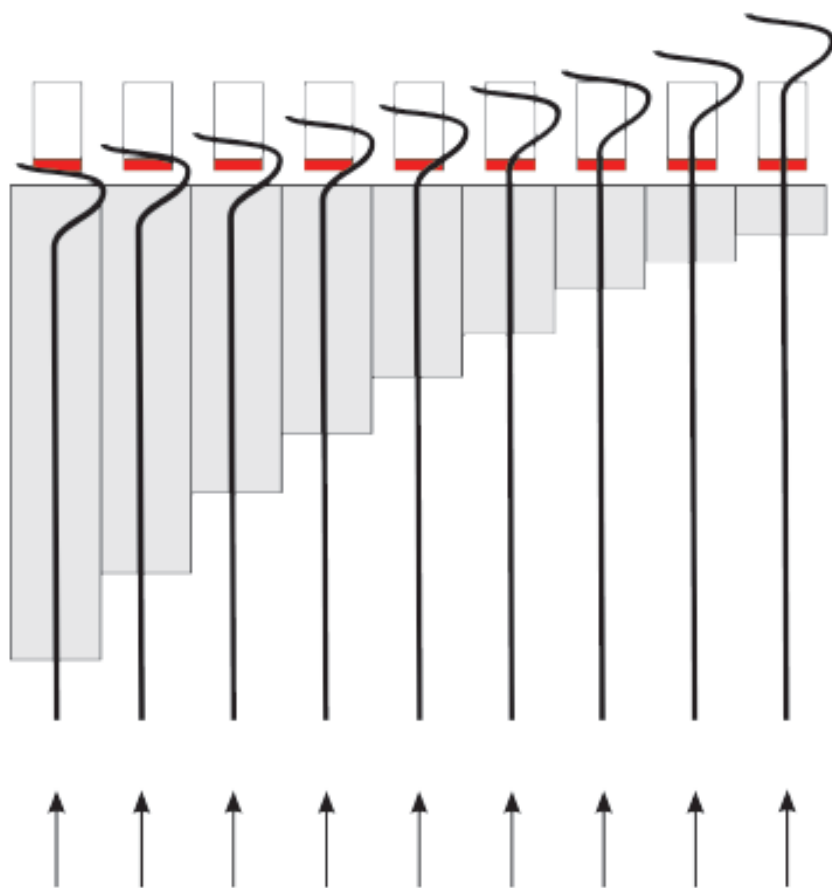


*Figure 38. Concept of a variable range shifter for high-throughput irradiations. The general concept used for high-throughput irradiations is the design of a multi-tiered plate holder. Altering the thickness of the steps samples different locations along the beam. Aligning the steps of the holder with the columns of a 96-well microplate results in a single dose-LET combination delivered to each well within the column per irradiation. A standard 96-well plate has 12 columns indicating 12 locations along the beam can be sampled with 8 replicates for each dose-LET combination. Image reproduced from (11).*

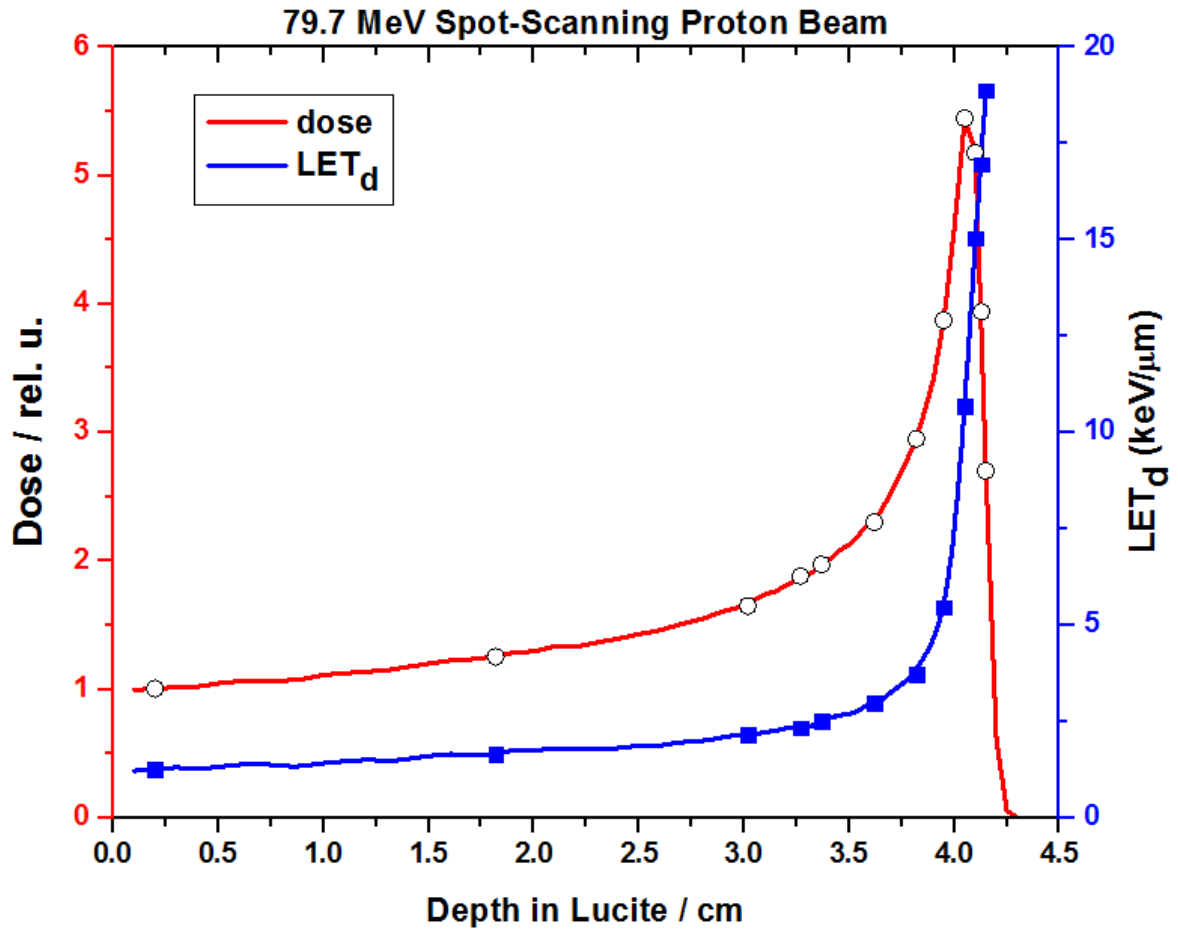
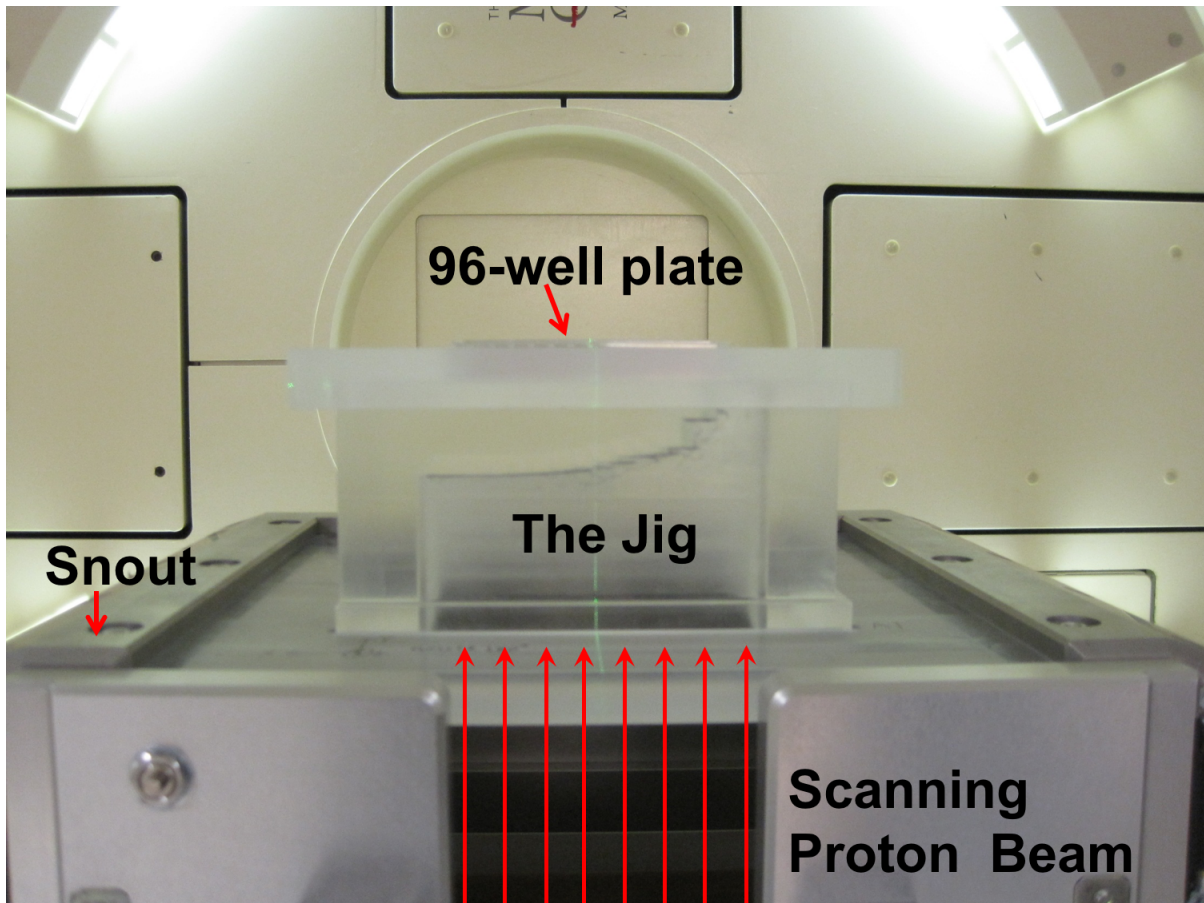


Figure 39. Simulated proton beam in Lucite used to select sampling locations. Monte Carlo simulations were performed to determine the dose deposition profile (red) and corresponding (LETs) along a 79.7 MeV proton beam at the PTC. Using these simulated results as a guide, the corresponding thickness of Lucite required to sample a dose-LET combination was determined. The points along the curves demonstrate the sampling locations for the initial Jig design. Image reproduced from (11).



*Figure 40. Physical setup for high-throughput irradiations. The high-throughput irradiation apparatus was constructed from a Lucite block with a high-precision and high-accuracy milling machine. The Jig was designed to directly insert into the snout of the proton gantry to facilitate reproducible setup. The biological samples sit on top of the holder and are irradiated from the bottom of the plate.*

Once the jig construction was completed, the dose peak of the system was calibrated by irradiating a stack of EBT3 films placed on top of the setup. The films were scanned, and the dose peak was found to fall within the thickness associated with column 9 in between films 3 and 4 of the stack indicating the need to insert 3 EBT3 films below the 96-well plate during irradiations to achieve a dose peak in column 9 (Figure 41).

The physical irradiation geometry (beam line, jig, EBT3 films, 96-well plate, etc.) was modeled and proton radiation exposure simulated in Geant4 to determine the doses and LETs a layer of adherent cells are exposed to for each column thickness. Cell thickness has been reported to range between 3 and 7  $\mu\text{m}$ . For the high-throughput irradiation setup, the cell layer is modeled as a 5  $\mu\text{m}$  water layer. The simulations of the physical setup were in good agreement with expectations. The doses were found to rise with increasing depth until the peak dose in column 9 after which they dropped off (Figure 42). The LETs were found to continually increase with the sampling depth. The rate of LET increase is initially slow until the proximal portion of the Bragg peak at which point there is a rapid increase in the LET as the protons begin to stop.

The Monte Carlo simulations were validated by intermittent ionization chamber measurements placed above the high-throughput setup. The Monte Carlo predictions and ion chamber measurements were consistently found to be within 1% (11).

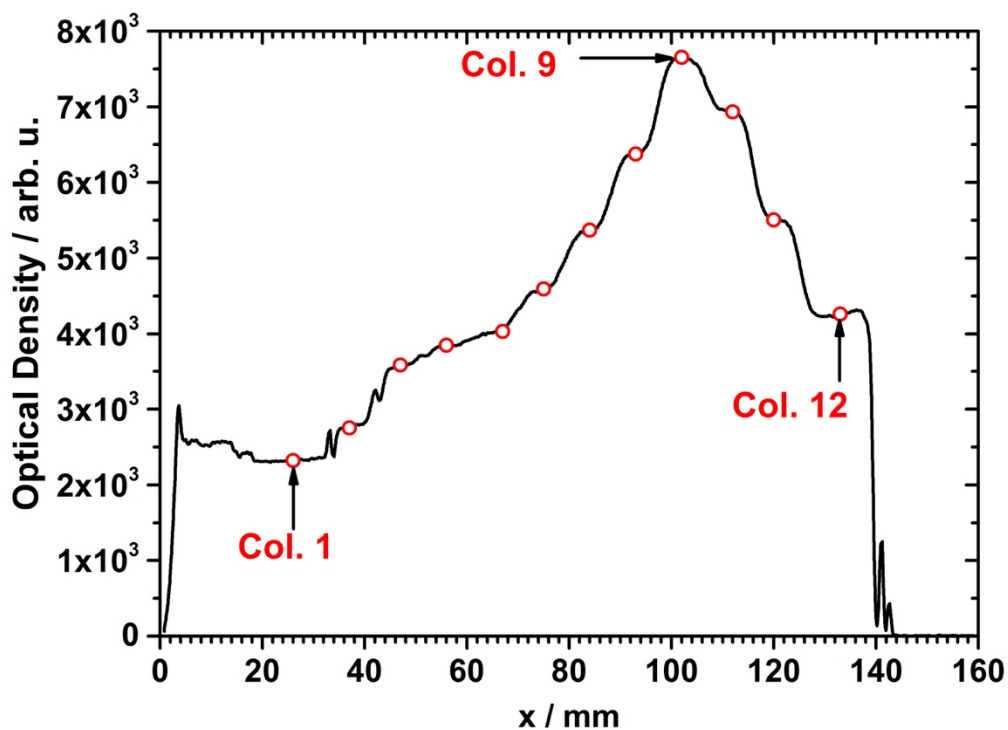


Figure 41. Relative jig doses from film measurement. The relative doses of the high-throughput setup were determined by placing a stack of EBT3 on top of a 96-well plate and performing an irradiation test. The films demonstrated a dose peak in column 9 between films 3 and 4 of the stack. It was thus decided to insert 3 films below the plate for all irradiations to shift the dose peak of the beam into column 9. For all clonogenic irradiations using the initial Jig design, three EBT3 films were placed underneath the irradiated 96-well plates. It should be noted that the same 96-well plate design from a single manufacturer was used for all clonogenic experiments at MDA. Image reproduced from (11).

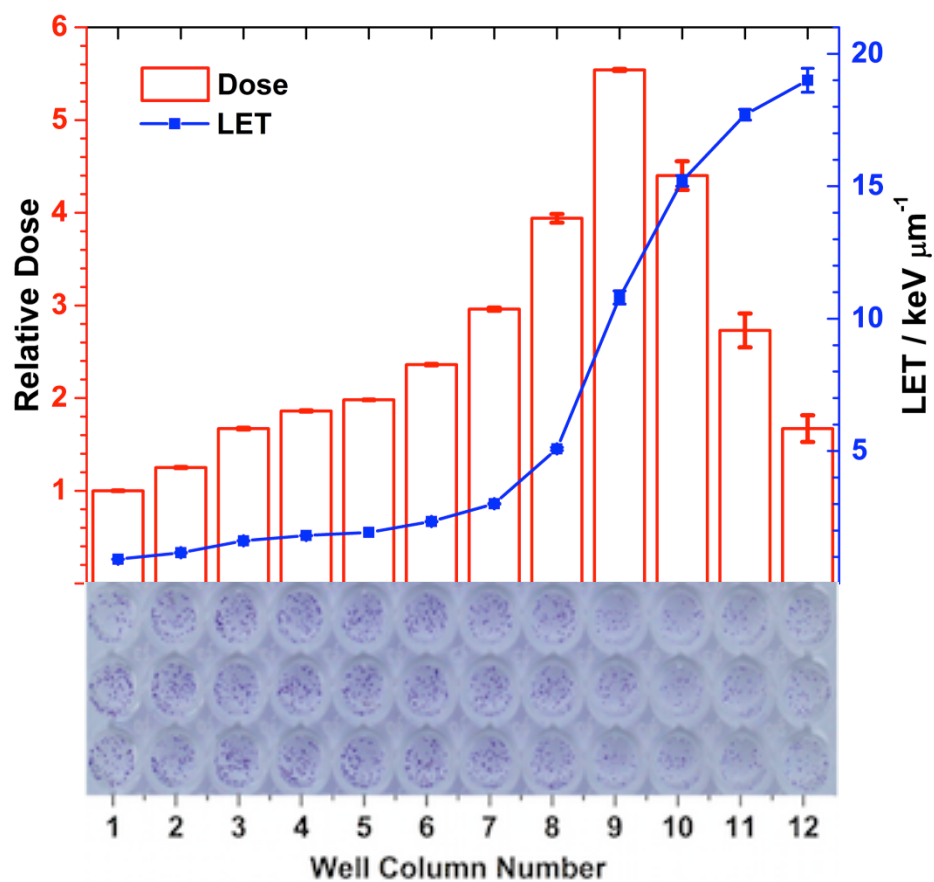


Figure 42. Relative doses and LETs calculated for the physical setup of the initial Jig. The doses and LETs received for column of the 96-well plate were determined by simulating the experimental setup utilized (Figure 6). Image reproduced from (11).

A new jig was developed after gaining experience with the design, construction, and implementation of the initial jig (Figure 43). The updated setup was able to hold two plates simultaneously further increasing the irradiation throughput by a factor of 2 over the initial design. The updated jig was also designed to be more flexible with regards to the irradiation orientation. Many ion therapy centers make use of fixed horizontal beam lines to remove the large costs associated with gantry-based systems. Experimental beam lines found within many ion therapy centers also frequently consist of a fixed horizontal beam line. The liquid surface tension of the cell culture media in a 96-well plate was found to be sufficient to prevent spillage at any plate orientation as long as the plate was handled gently (Figure 44). The second high-throughput irradiation setup was thus able to be placed in either a horizontal or vertical orientation.

The initial jig design was found to sample low LET protons (1-5 keV/ $\mu\text{m}$ ) in 8 out of the 12 columns with 7 out of the 12 columns sampling LETs between 1 and 3 keV/ $\mu\text{m}$ . Given the range of proton LETs typically simulated for *in vitro* experiments being between 1 and 20 keV/ $\mu\text{m}$ , our team designed the next jig to evenly sample proton LETs over the entire range. In particular, the design goal was to achieve a biological response measurement for every 1-2 keV/ $\mu\text{m}$  proton LET increment. Following the previously developed methodology, an 81.4 MeV proton beam was simulated in water to determine material thickness for the desired LET samplings (Figure 45). The next version of the high-throughput irradiation apparatus setup was simulated to calculate the dose and LET the cell layer in each column would be exposed to. The new jig simulations results indicated that the new jig evenly samples the proton LETs over the range of 1-20 keV/ $\mu\text{m}$  (Figure 46, Table 2).

Utilizing similar methodology to the proton setups utilized at the MD Anderson Proton Therapy Center, high-throughput irradiation setups were designed for heavier ions (helium, carbon, oxygen) available at the Heidelberg Ion Therapy (HIT) Center.



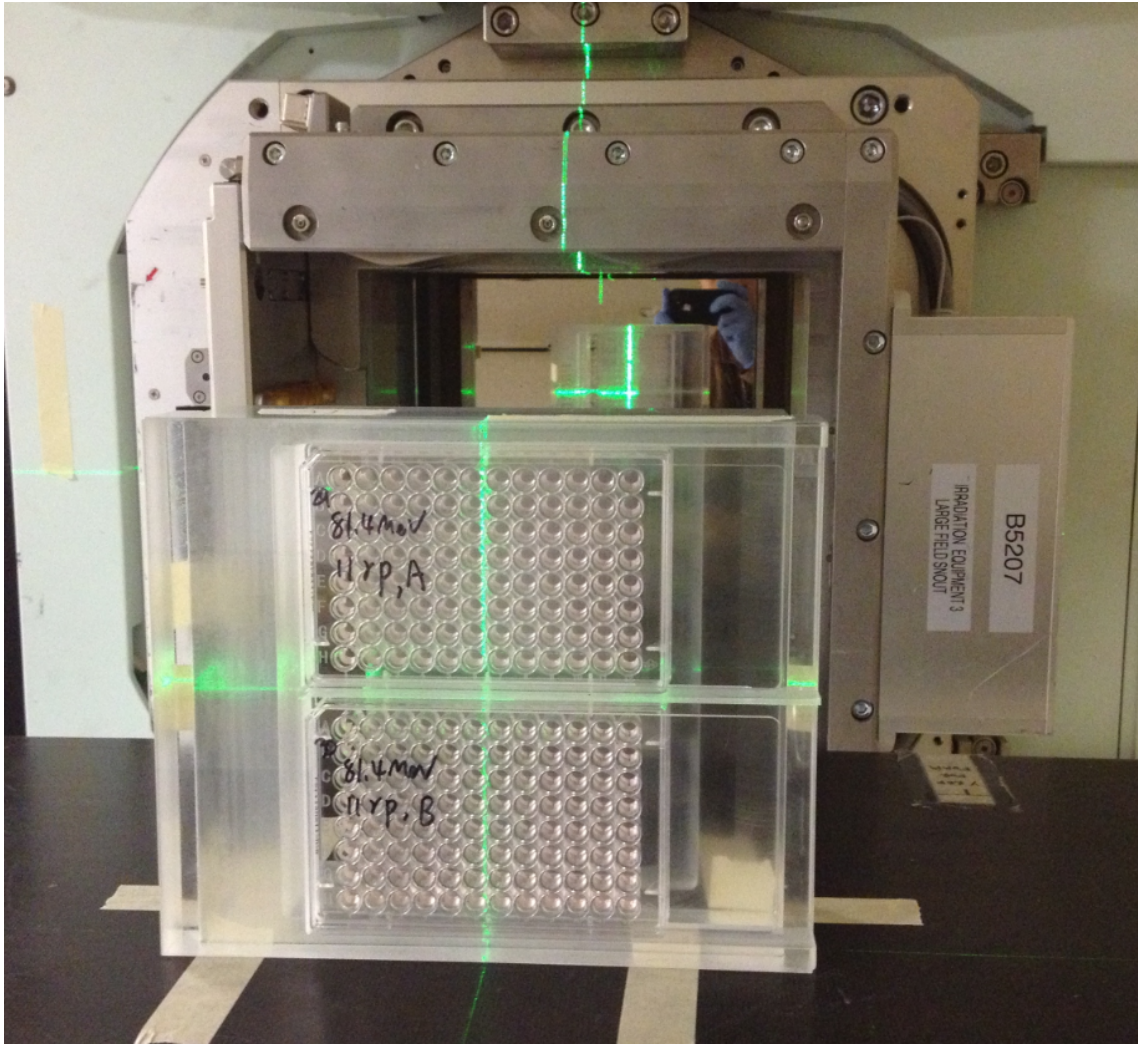


*Figure 43. Physical setup for high-throughput irradiations with second Jig design. Following the experience obtained with the initial high-throughput irradiation apparatus design, several changes were made in the second version of the high-throughput irradiation apparatus. Irradiation throughput was further improved by a factor of 2 by adding the ability to hold two plates per irradiation. The second design also included a flexible irradiation orientation (horizontal and vertical).*

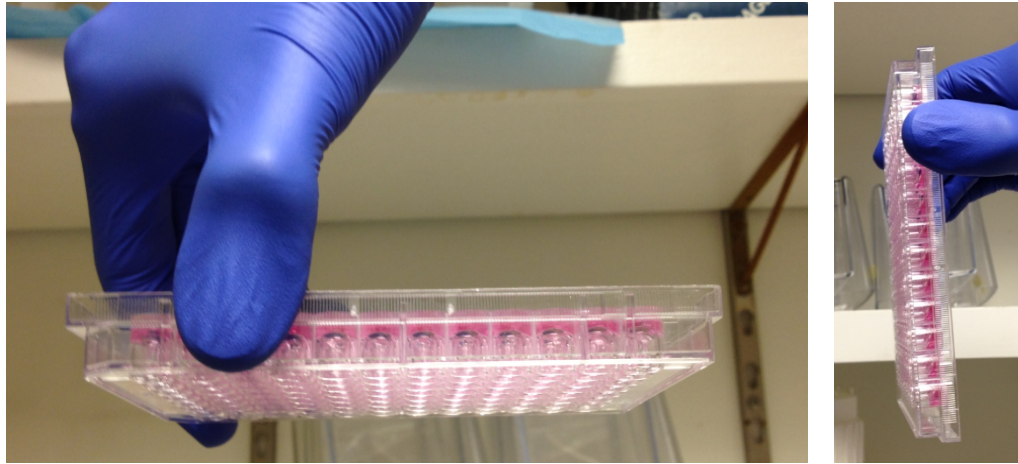


*Figure 44. Surface tension in a 96-well plate. The surface tension present within a standard 96-well microplate with round wells is sufficient to prevent the culture media from spilling out at any plate orientation assuming the plate does not experience a large acceleration. For 96-well plates with square wells, the media can be contained using plate sealers.*

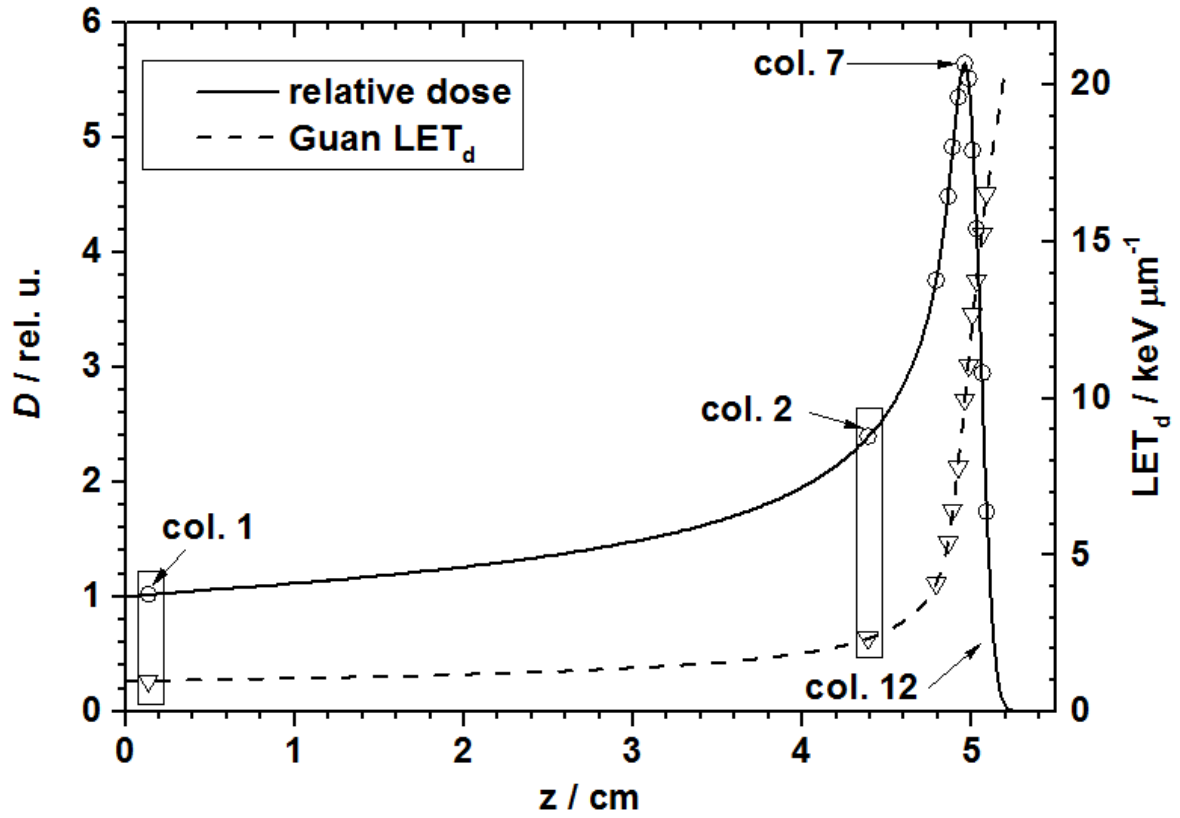


Figure 45. Simulated 81.4 MeV proton beam in Lucite used to select sampling locations for second Jig design. The focal design alteration for the second high-throughput irradiation apparatus was the increased LET sampling in the range of 5-20 keV/μm (triangles).

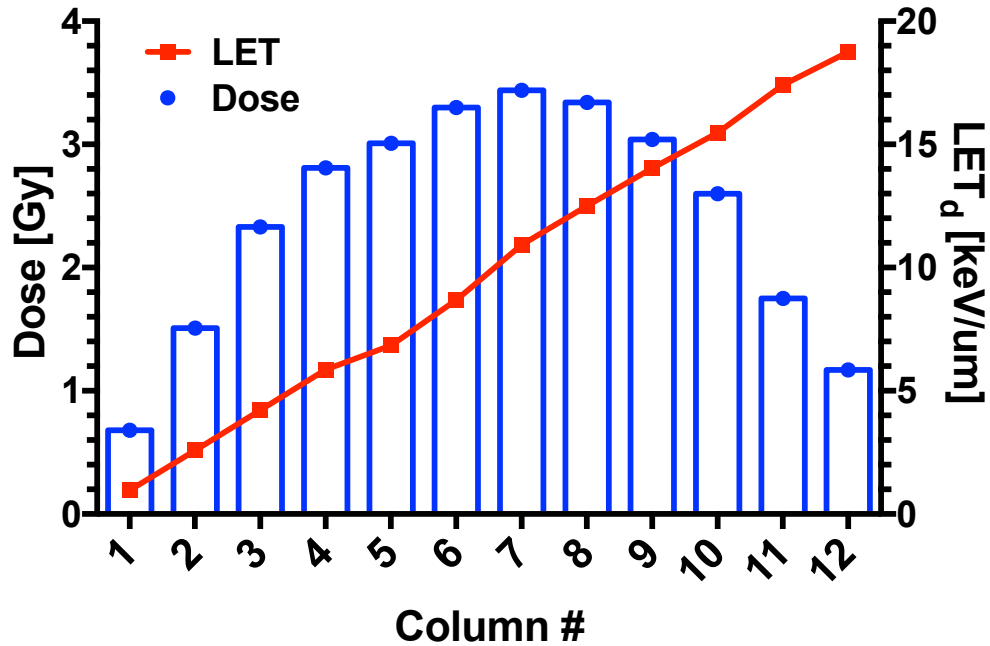


Figure 46. Relative dose and LETs per column in the second Jig design. The experimental setup of the second version of the Jig was designed to not require film shims underneath the sample plates. The MC simulation of the experimental setup predicated an even sampling of LETs over the typical experimental range of 1-20 keV/ $\mu$ m. The LET was found to increase with increasing column number (and corresponding Lucite step depth). The dose peak was found to be in column 7.

*Table 2. Calculated LETs for each proton jig version.*

Column	LET [keV/ $\mu\text{m}$ ]	
1	1.0	0.9
2	1.2	2.5
3	1.6	4.1
4	1.9	5.8
5	2.0	6.7
6	2.5	8.5
7	3.3	10.6
8	5.1	12.1
9	11.0	13.5
10	14.8	14.9
11	17.0	16.8
12	18.3	18.0

## Optimizing the high-throughput clonogenic assay

### Fixation timing for optimal colony scoring

The automated scoring algorithm initially uses a size and intensity filter to detect and create a colony image mask of objects present within each well (Figure 37). A cell filter is then applied to determine the number of cells within each object and only those with at least 50 cells are scored as viable colonies. Given the automated scoring algorithm and limited space available for growth within a 96-well compared to a 6-well plate, the timing of colony fixation plays a crucial role in determining data quality. The optimal fixation time allows for colonies to be both detected and scored while avoiding overgrowth and clumping loss on colony scoring (Figure 47). The assay requires that cells have sufficient time to form a colony of 50 or more cells requiring a minimum of 5.5 doublings. If colonies are fixed prior to reaching 50 cells, they will be detected but not scored as viable by the detection algorithm. If the colonies are allowed to overgrow on the available surface area, adjacent colonies will begin to impinge on one another causing errors in automated colony counting. In effect this artifact translates to an increased scoring efficiency but an absolute decrease in colony detection.

The fixation time point for optimal colony scoring is thus cell line dependent based on the cell line's doubling time as well as colony size and number of cell seeded per well. The doubling time for each cell line can be used as a guide for the appropriate minimum fixation time point post-seeding, but the optimal conditions must be verified by performing an initial control time course experiment of colony formation for each cell line to be used in the high-throughput assay.

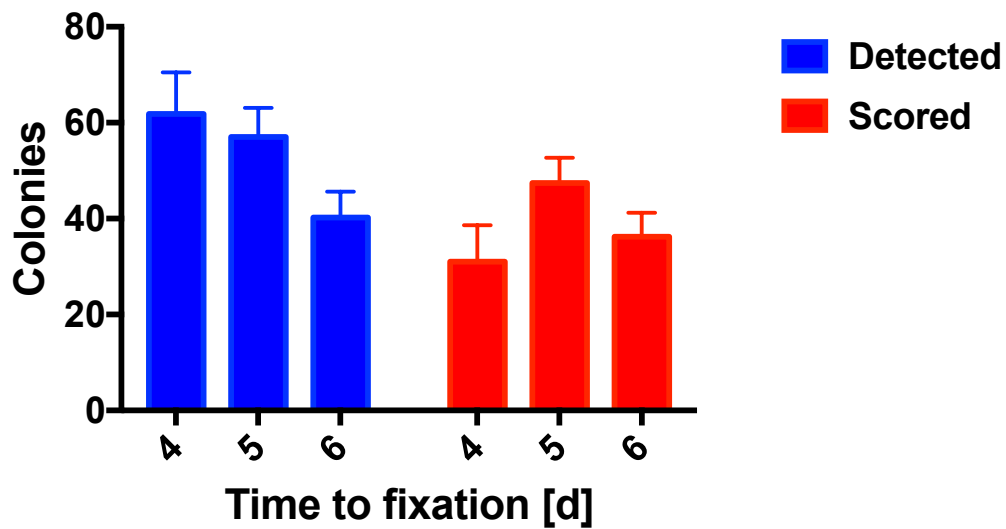


*Figure 47. Automated colony detection and scoring for H460 cells. The automated detection and efficient scoring of colonies in the high-throughput clonogenic assay requires cell line specific optimization. With the limited growth area present within the well of a 96-well microplate, colonies can easily merge and not be algorithmically declumped if the fixation time point is too late resulting in a reduction in colony detection (day 6). Alternatively, early fixation results in colony detection but reduced viable colony scoring due to a lower cell number per colony detected (day 4). The optimal fixation and staining time point for the assay is when the number of scored colonies is a maximum (day 5).*

## Incubator effects

An undesirable variability in seeding uniformity was noted in the initial experiments for the high-throughput clonogenic assays. In particular, the effect was frequently observed in the outer wells of the 96-well microplates. The affected wells exhibited colony merging along their periphery preventing individual colonies from being distinguishable even by the human eye. It was determined that this clumping effect was due to uneven cell seeding and was ultimately attributable to a temperature-sensitive edge effect. Uniform distribution of cells within all wells was thus achieved by allowing the cells to attach for 60-90 minutes at room temperature on the benchtop.

## Addition of a limit of detection

As expected, the initial results from the high-throughput clonogenic assays demonstrated a decreasing surviving fraction with increasing dose (Figure 48). However, we observed instances where the SF would decrease to a relative minimum, then slightly increase, and finally further decrease with dose but with a shallower slope. Fitting the conditions with this effect to the linear-quadratic model resulted in poor or impossible weighted fits by non-linear regression. Examining the wells exposed to the highest dose (20Gy) and comparing the colonies to control conditions revealed that no colonies were actually present indicating that cell clusters and giant cells were incorrectly being scored as viable colonies (Figure 49). The uncertainty associated with measurements of low SF conditions were also noted to increase with decreasing SF conditions due to the inclusion of replicates with SFs of 0.

These observations lead to the conclusion that the application of a limit of detection (LOD) was needed to circumvent the addition of artefactual signals in the high-throughput



clonogenic assay results (Figure 50). If all cells seeded form a colony, the SF LOD is theoretically  $1/N$  where  $N$  is the number of cells seeded within a well. For example, with 100 cells seeded, the SF LOD is  $1/100 = 0.01$ . However, as the readout within the clonogenic assay is the CFU, the LOD must be adjusted to account for the number of CFUs as each cell seeded will not necessarily form a colony. As such, the SF LOD for a given experiment was defined as:

$$LOD = \frac{1}{CFU(0Gy)} = \frac{1}{N * PE}$$

Where  $N$  is the number of cells seeded within a well and  $PE$  is the plating efficiency of the cell line determined under control conditions. Once a given condition reached the experimental LOD, the further SF data was excluded from analysis (Figure 51). The LOD application was found to remove the artefactual trends observed for SF as it approached the LOD. The resulting data was found to fit the LQ model well (Figure 52).

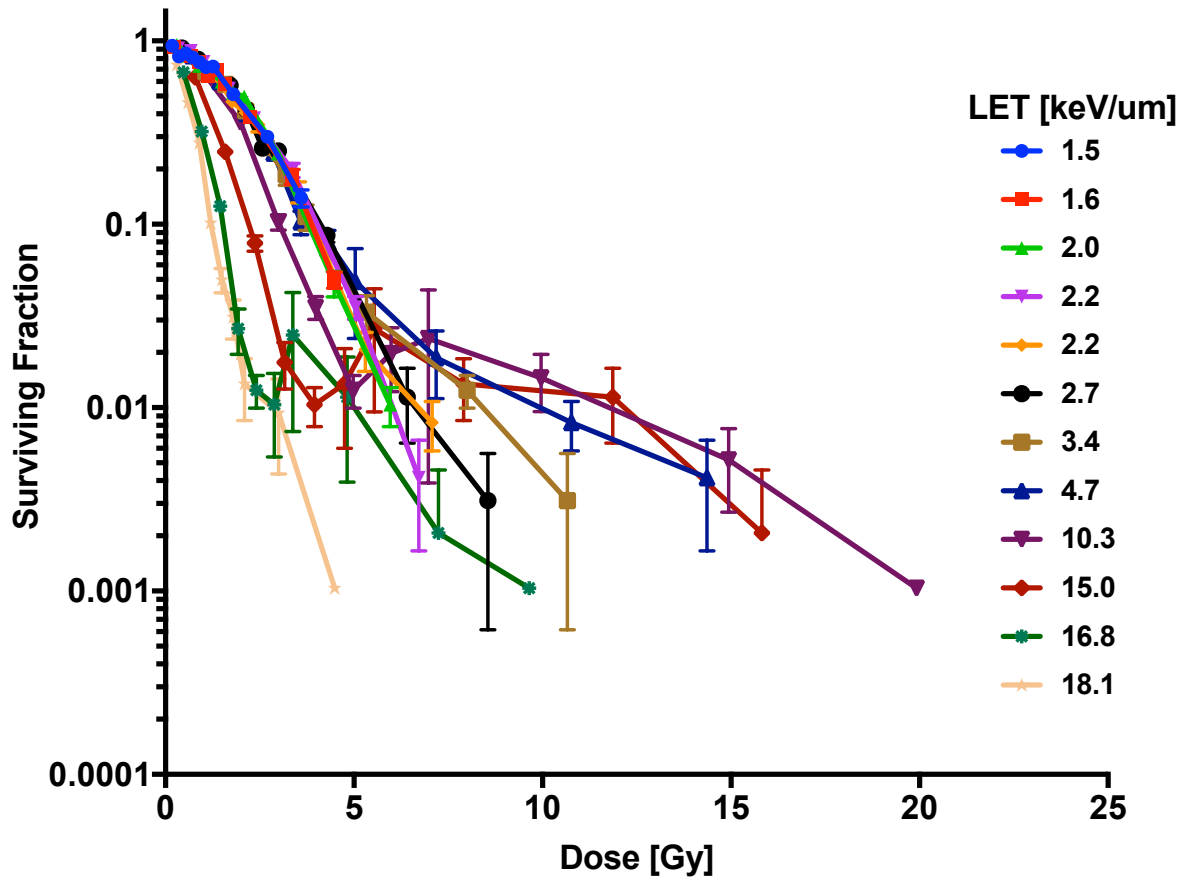
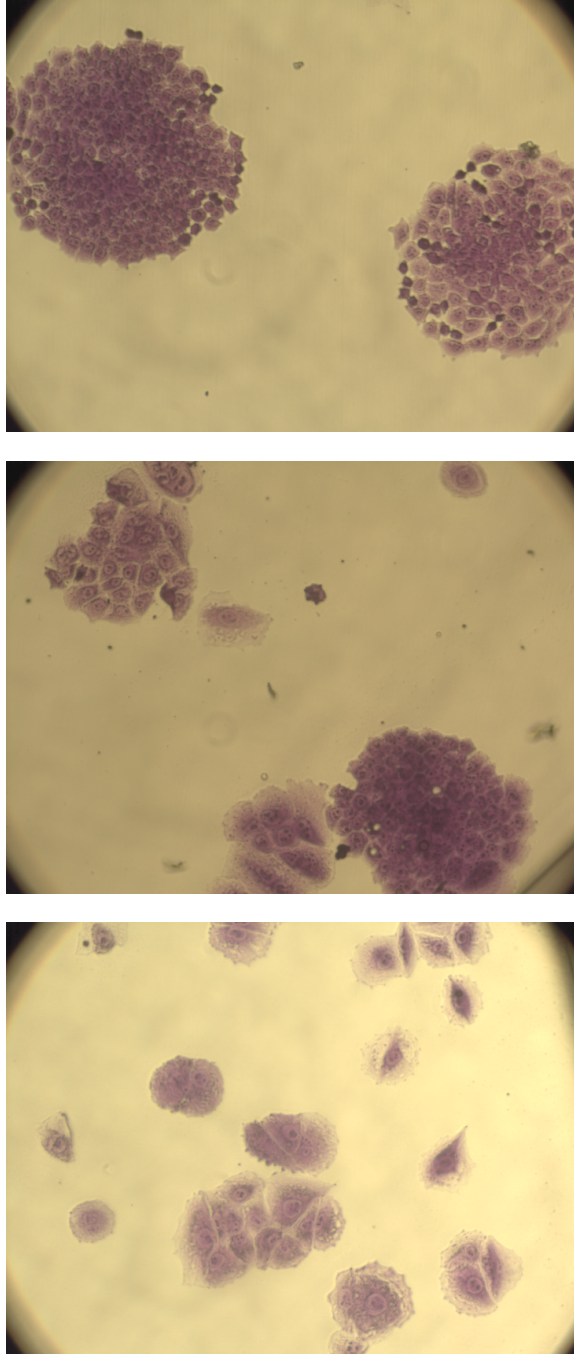
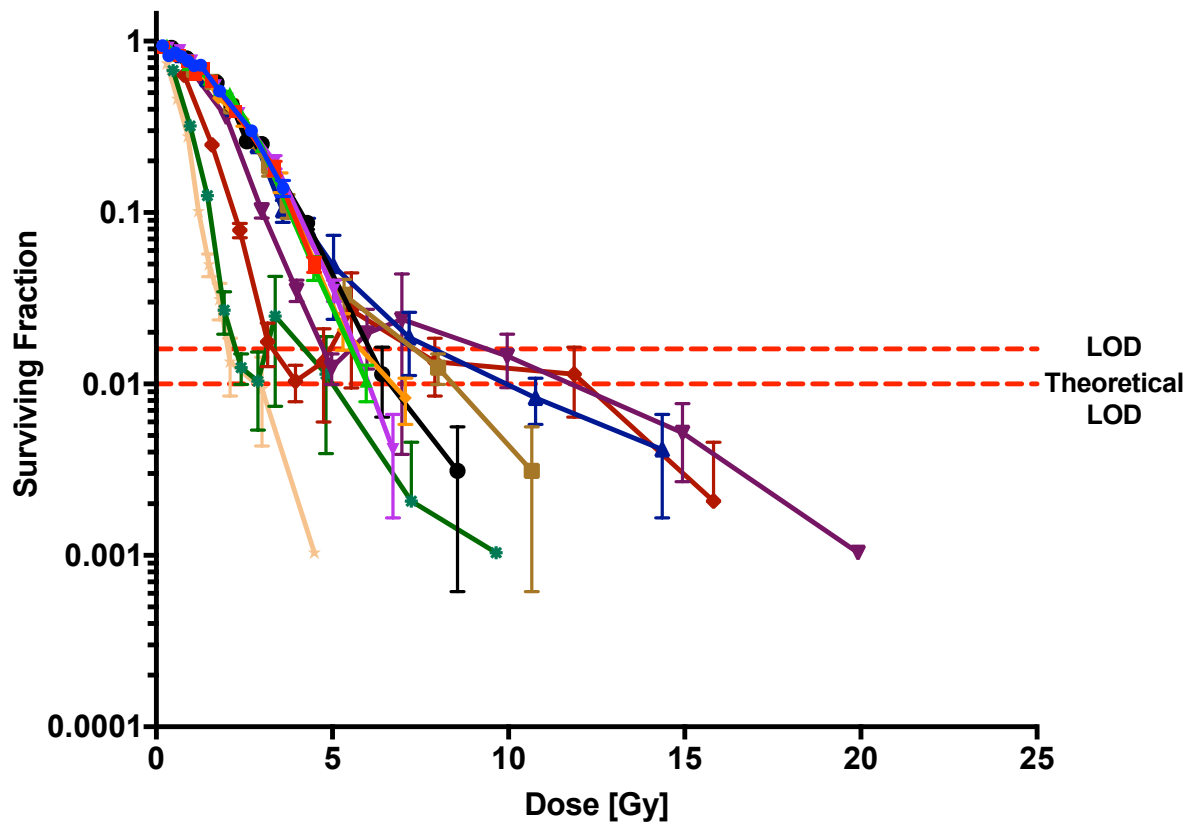


Figure 48. Raw surviving fraction data from a high-throughput experiment. The LQ model did not fit the data generated. It was noted that the SFs would drop with increasing doses to an SF of approximately 0.01. At this SF value the results for each condition would frequently present an altered trend such as an increase in SF before further reduction with dose or a slower rate of SF reduction.



*Figure 49. Colony types present in the clonogenic assay at 20x magnification. Altered cellular morphology following irradiation with highly biologically active radiation (dose-LETs) was observed in the stained colonies under a bright-field microscope. Highly damaged cells were generally larger than undamaged cells and giant cells were frequently noted. It was determined for low SFs these combined effects were errantly being scored as viable colonies resulting in spurious results at low SFs.*



*Figure 50. Visualization of the limits of detection.* To eliminate the background present within the clonogenic assay, a limit of detection (LOD) was applied to the SF data. The LOD value is calculated for each experiment by determining the number of colony forming units seeded into each plate.

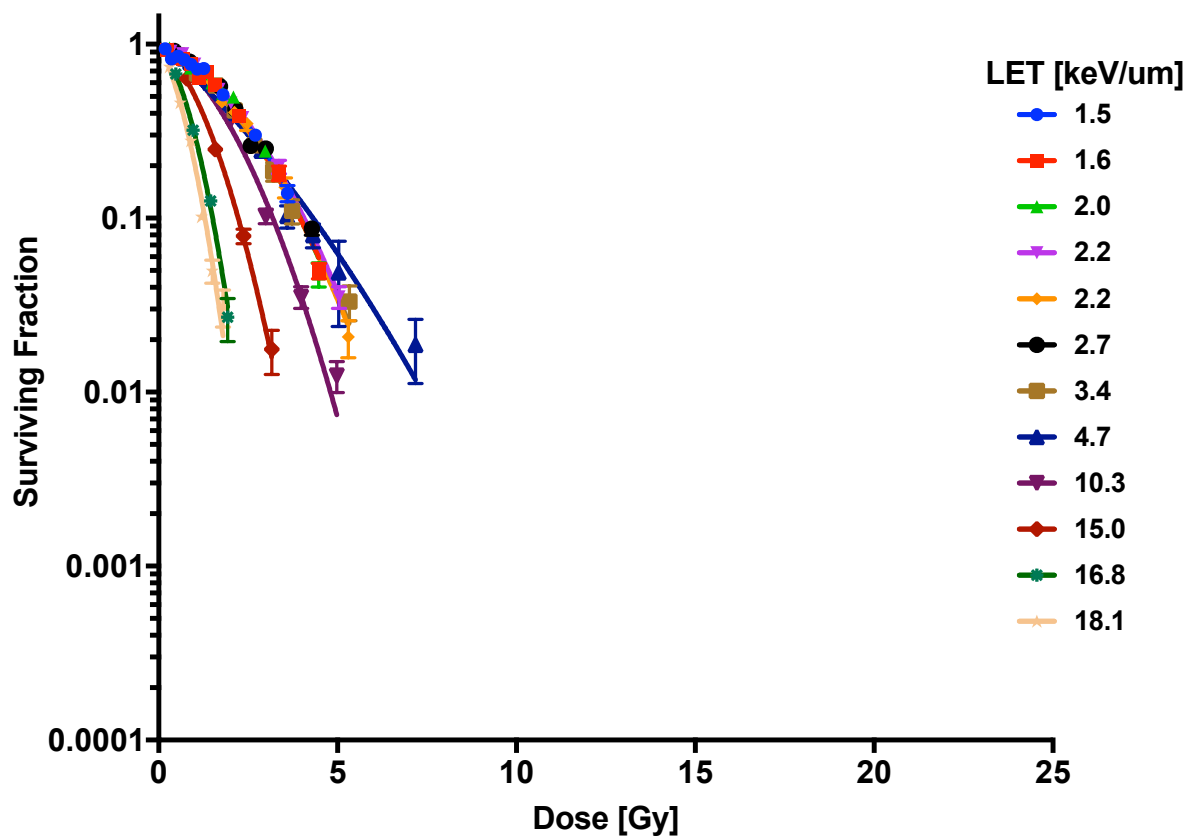


Figure 51. Clonogenic SF results following LOD application. Once the SF for a given condition falls below the LOD determined for the experimental run, the following values are excluded from further analysis.

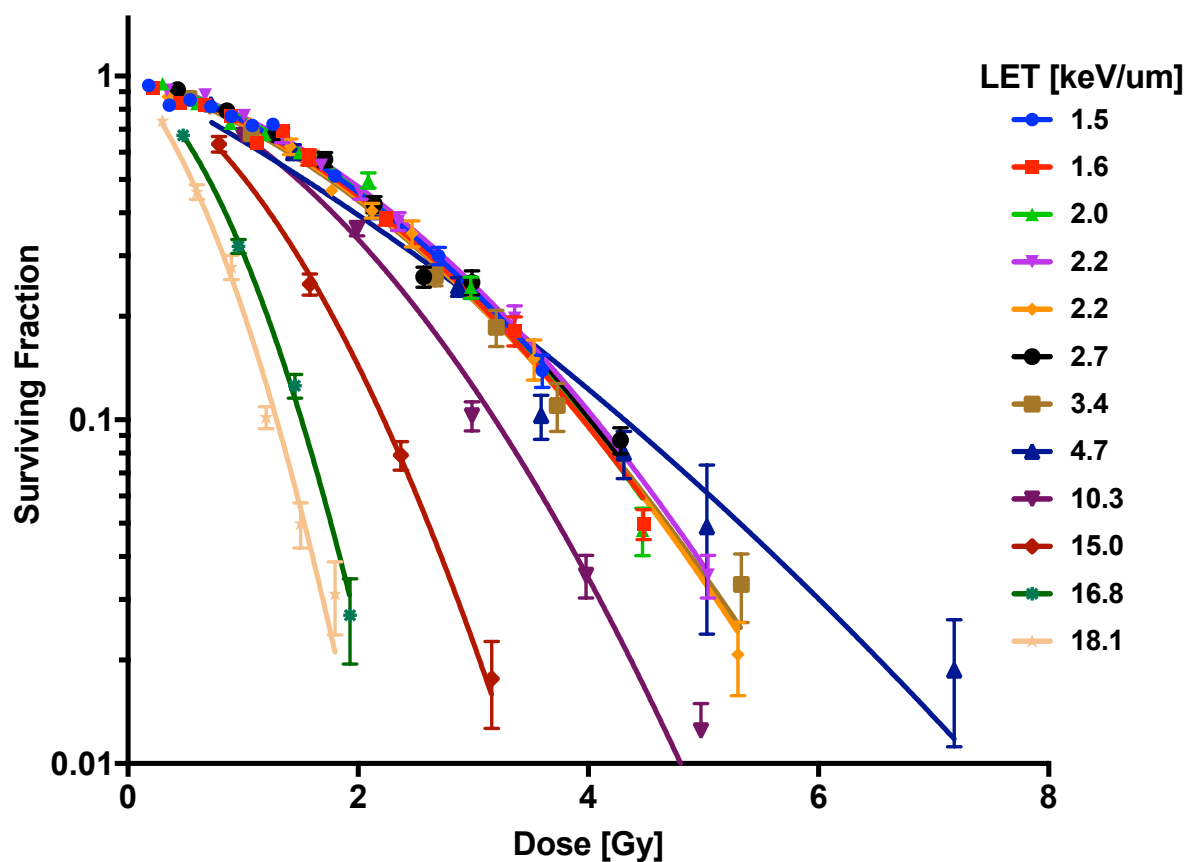


Figure 52. LOD applied HT clonogenic data over appropriate axes ranges. With the application of a LOD, the results from the high-throughput clonogenic assay are well modeled by the LQ model using a weighted-nonlinear regression fit.

## Benchmarking traditional vs high-throughput clonogenic assay

The high-throughput clonogenic assay was benchmarked against the traditional clonogenic assay manually performed in 6-well plates for the H460 cell line. Cells were seeded, allowed to attach and normalize before exposure to gamma photons produced from a Cs-137 source. Plates from each clonogenic method were simultaneously irradiated for each dose level. After 5 days the high-throughput clonogenic plates were stained and submitted for automated analysis. The traditional method plates were allowed to form colonies for 12 days before staining and manual scoring. SFs were calculated from the results. Qualitatively, the SF values appeared to be in good agreement. Both conditions were fit by a weighted, non-linear regression to the linear quadratic equation. The resulting fits were found to be not statistically different by the extra sum of squares F-test (Figure 53).

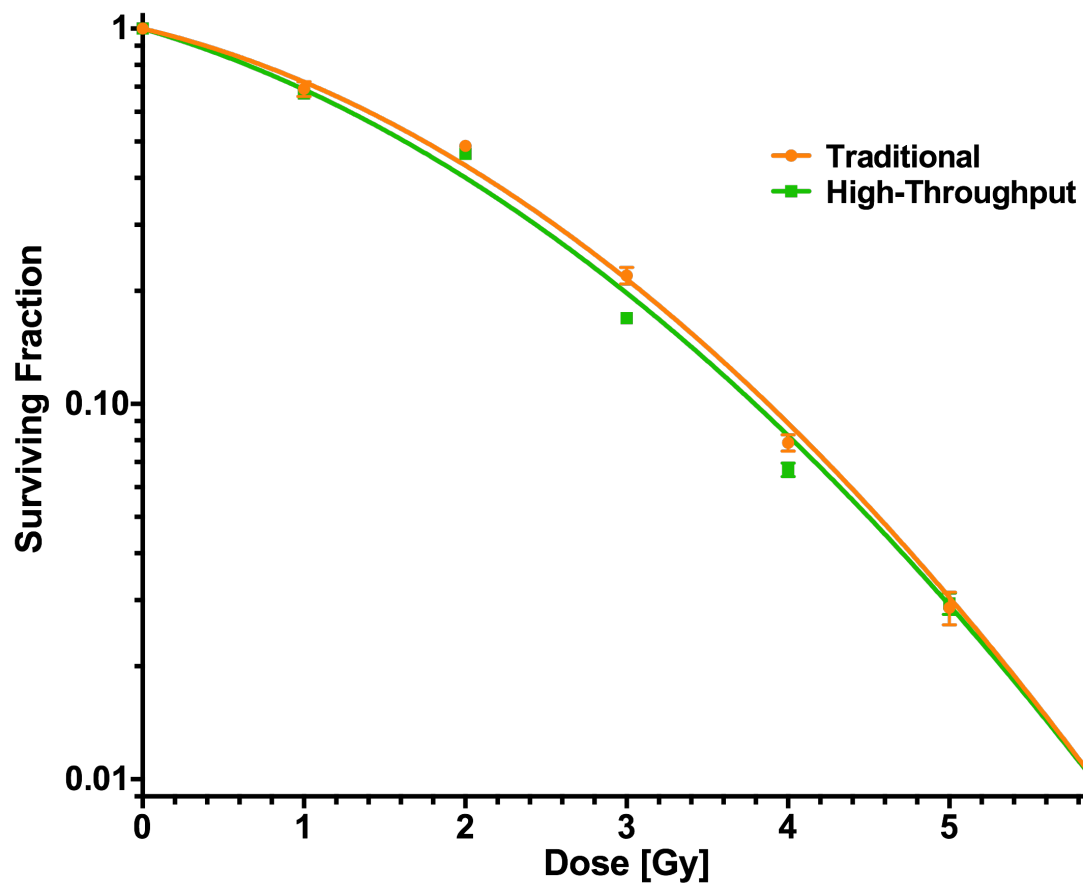


Figure 53. Benchmarking of HT versus manual clonogenic assay. The H460 cells were seeded in either 6-well or 96-well plates, irradiated in a Cs-137 biological irradiator, and then subjected to either the high-throughput or traditional clonogenic assay. The results of the assays underwent SF analysis with subsequent  $1/Y$ -weighted fitting to the LQ model. The fits were found to be not statistically different via the extra sum-of-squares  $F$  test. Error bars are standard error of the mean (SEM). Reproduced from (11).



## High-throughput clonogenic assay results for adherent cells

### Control radiation: photon SF and RBE

H460 cells were prepared and subjected to the high-throughput clonogenic following exposure to photon radiation of different energies. The photon sources used were a Cs-137 biological sample irradiator and a clinical Varian linear accelerator. The photon energies tested were 6 MV and 18 MV for the linear accelerator. Cs-137 produces gamma photons with an energy of 662 keV. Following exposure to a range of doses, cells were allowed to form colonies for 5-5.5 days before staining and fixation followed with subsequent data readout using the high-throughput microscope. The results from the photon experiments indicated a differential survival response dependent on experimental conditions (Figure 54). Exposure to higher photon energies resulted in increased SF for a given dose. The SF results were fit to the LQ model to facilitate RBE calculation (Table 3). The 18MV photon condition was set as the control radiation as it demonstrated the highest SFs. The RBEs were calculated for three biological endpoints: SF levels of 0.5, 0.1, and 0.01 (Figure 55). When normalized to the 18MV condition, the RBEs for Cs-137 were found to be 1.17, 1.10, and 1.08 at SFs of 0.5, 0.1, and 0.01 respectively. The 6MV RBEs were found to be 1.06, 1.05, and 1.05 for the SFs of 0.5, 0.1, and 0.01 respectively.

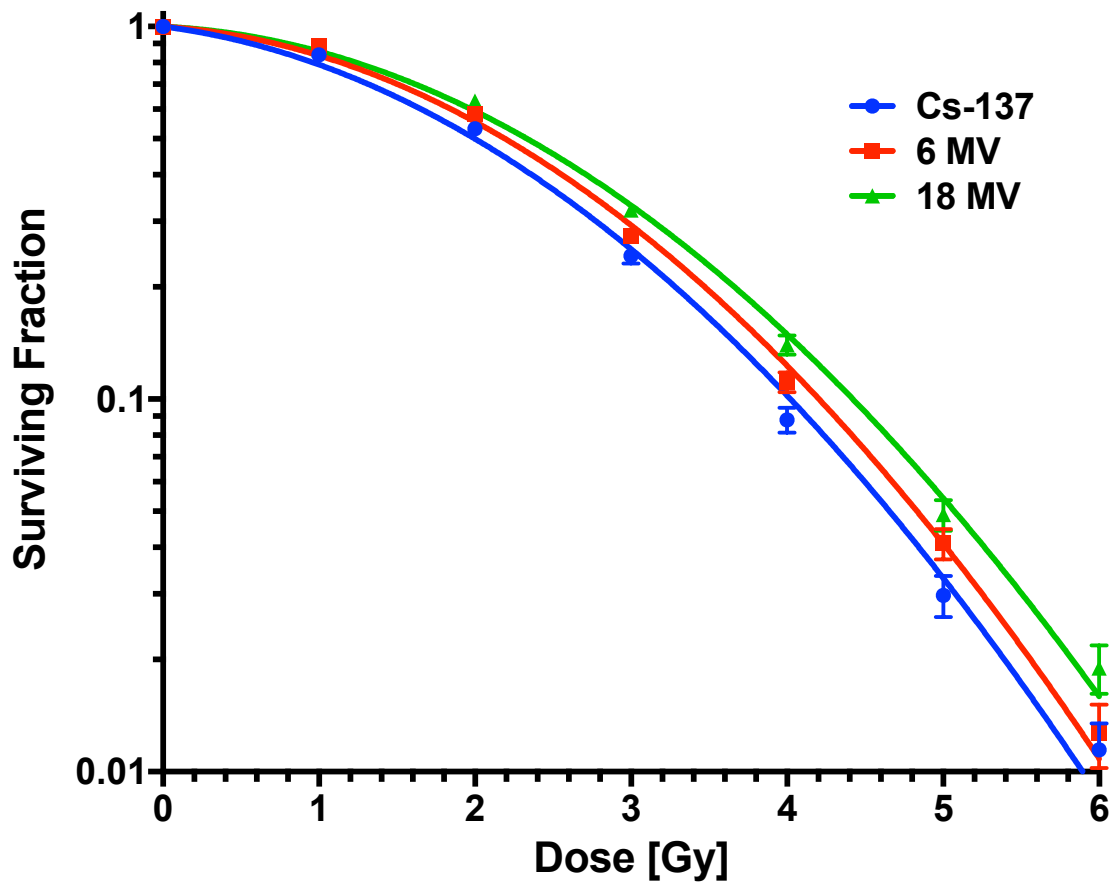


Figure 54. H460 Photon SF for different sources. Cells were prepared for the high-throughput clonogenic assay and exposed to photons from a preclinical biological irradiator with a Cs-137 source, and 6 MV and 18 MV x-rays from a clinical linear accelerator. SF and LQ model fitting to the clonogenic data was performed. Lower SFs were observed for irradiation with photons of lower energy. Error bars represent the 95% confidence intervals.

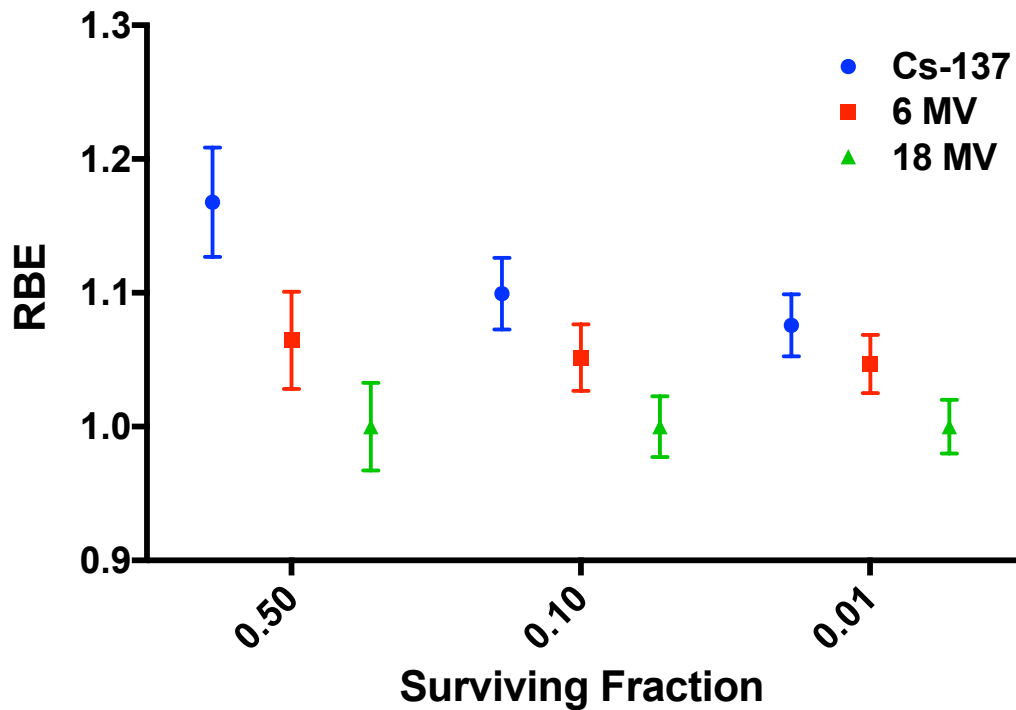


Figure 55. H460 RBE for Cs-137, 6 MV, and 18 MV photon sources. RBEs for Cs-137 and 6 MV were calculated from the results of the high-throughput clonogenic assay performed with photons produced from Cs-137, 6 MV, and 18 MV. Results were normalized to the 18 MV results because this condition resulted in the least cell kill of all the tested radiations. Both Cs-137 and 6 MV photons were found to have larger biological effects than 18 MV photons with Cs-137 have the largest effects. These results indicate differential biological response with photon energies for the H460 cell line. Additionally, they highlight the importance of considering the type of control photon radiation used when comparing RBE results. Error bars represent the standard error (SE).

Table 3. Fitting parameters and RBEs for H460 photon exposures.

			<b>Cs-137</b>	<b>6 MV</b>	<b>18 MV</b>
$\alpha$			0.1242	0.06452	0.04727
$\beta$			0.1115	0.1149	0.1071
<i>RBE</i>	SF	0.50	1.17	1.07	1
		0.10	1.10	1.05	1
		0.01	1.08	1.05	1

## Particle irradiation surviving fractions

### Proton

#### Jig 1.0

Using the initial jig design, the biological response of H460 and H1437 NSCLC cell lines was measured at the selected jig depths using a 79.7 MeV proton beam and the high-throughput clonogenic assay (Figure 56, Figure 57). For both cell lines, the SF was found to decrease with increasing dose for all LET samples tested. SFs were found to decrease more rapidly with exposure to protons of increasing LETs. This effect was especially prominent for columns sampling LETs above 11 keV/ $\mu\text{m}$ , the value associated with the dose peak. In the context of the high-throughput irradiation apparatus, the term “dose peak” denotes the column simulated to have the largest relative dose. This value is the closest value to the Bragg peak that is sampled, but it does not necessarily coincide with the actual Bragg peak. The SF data were fit to the LQ model with resulting fitting parameters shown in Table 4. The  $\alpha$  and  $\beta$  fitting parameters were both found to increase with irradiation with protons of increasing LET. The ratio of  $\alpha$  and  $\beta$  was found to decrease with increasing LET. The control radiation used for most experiments was from a preclinical biological irradiator using a Cs-137 source due to availability and ease of use.

#### Jig 2.0

The updated jig design was used to perform the high-throughput clonogenic assay on the H460 cell line exposed to 81.4 MeV protons at MD Anderson’s Proton Therapy Center (Figure 58). This setup was also used at the HIT facility in DKFZ to expose H460 cells to

80.6 MeV protons (Figure 59). SF analysis was performed following proton radiation exposure, fixation and staining, colony scoring. The LQ model was fit to the SF data to enable comparisons (Table 5, Table 6). The experimental results for the second version of the high-throughput irradiation apparatus presented similar trends as exposures with the initial design. Namely, SFs were found to be inversely proportional to exposure with increasing doses and LETs. The increased sampling of LETs over the experimental range demonstrated clearer stratification between the results. Irradiation with increasing LET values systematically resulted in lower SFs for all LETs tested. The results obtained at MDA between the initial and second generation jig are similar; however, direct comparison between the two setups is not possible due to different LETs being examined. For the irradiations performed at HIT, the general trends between the LETs sampled are similar to those found from proton irradiations at MDA, but the overall radiosensitivity appears to be lower. The  $\alpha$  and  $\beta$  fitting parameters for the experiments performed at MDA also follow the pattern as before where both increase with the LET. The LQ fitting results from the experimental run at HIT demonstrated a different trend where  $\alpha$  was found to decrease with increasing LET and  $\beta$  was found to increase with exposure to increasing LET radiation.

## Helium

Using the same methodology developed for the high-throughput proton irradiations, high-throughput measurements of the H460 cell line response to 336.3 MeV helium ions were performed at the HIT facility in collaboration with the Abdollahi group (Figure 60). The SFs were found to decrease with increasing dose for a given LET exposure. The SF reduction rate was found to increase with LET until 52.6 keV/ $\mu$ m. SF reduction then began to

increase for LETs tested above this value. The LQ model was fit to the clonogenic data with fitting parameters shown in Table 7.  $\alpha/\beta$  was found to decrease until 12.2 keV/ $\mu\text{m}$  after which it continually increased. The SF data at the highest LET tested for helium ions, 81.2 keV/ $\mu\text{m}$ , was found to consist of only an  $\alpha$  component.

## Carbon

High-throughput measurements of the H460 response to carbon ions with initial energy of 1802.5 MeV were performed and data fit to the LQ model (Figure 61, Table 8). The SFs were found to be lower for exposure with increasing carbon ion LETs. The SFs found for columns 5, 6, and 7, with LETs of 78.2, 90.4, and 114.7 keV/ $\mu\text{m}$  respectively, were found to be approximately the same. Irradiations with LETs above 114.7 keV/ $\mu\text{m}$  were found to have a decreasing rate of SF reduction. The  $\alpha/\beta$  was found to be approximately constant for the conditions 114.7 keV/ $\mu\text{m}$ , after which it was found to rapidly rise. A pure  $\alpha$  component fit was found for the highest LET tested for carbon ions, 296.4 keV/ $\mu\text{m}$ .

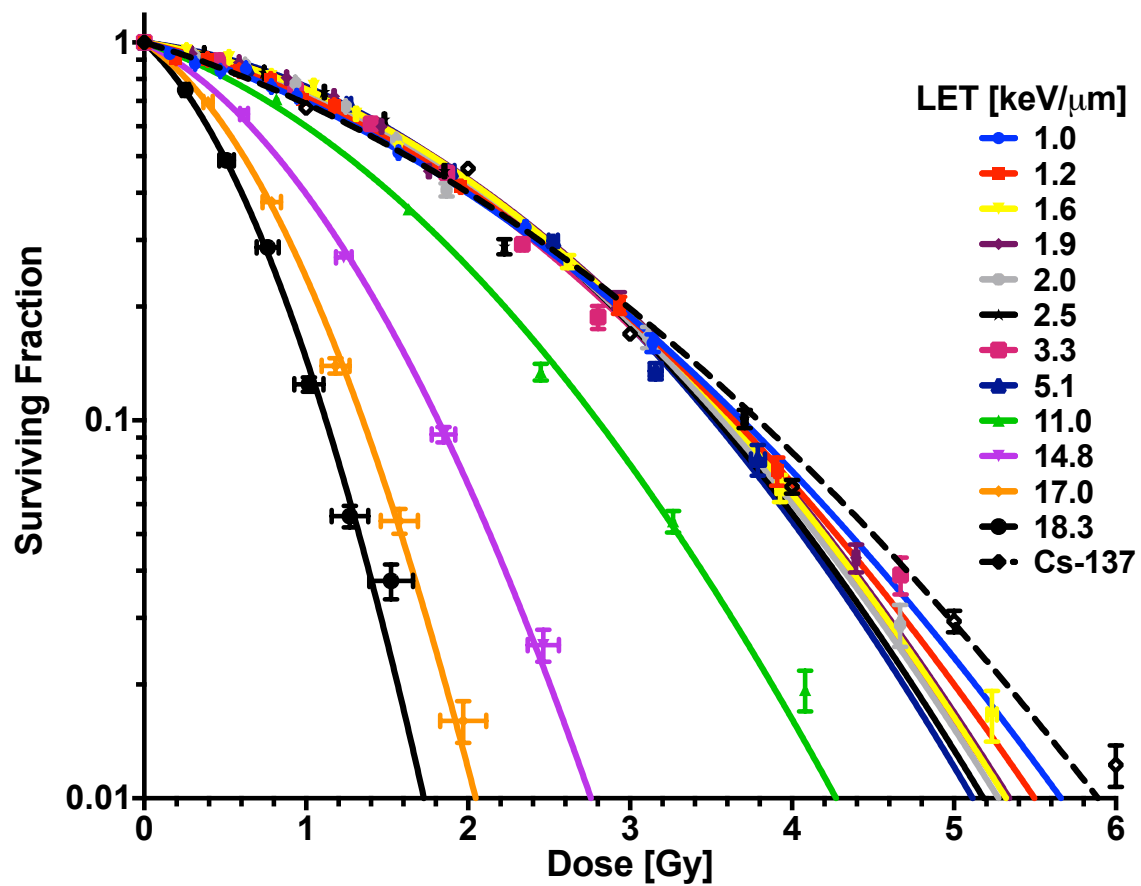


Figure 56. HT clonogenic assay H460 results. H460 SF was found to decrease with increasing proton LET especially for locations situated near and distal to the Bragg peak ( $\geq 11.0$  keV/μm). Error bars are SEM.



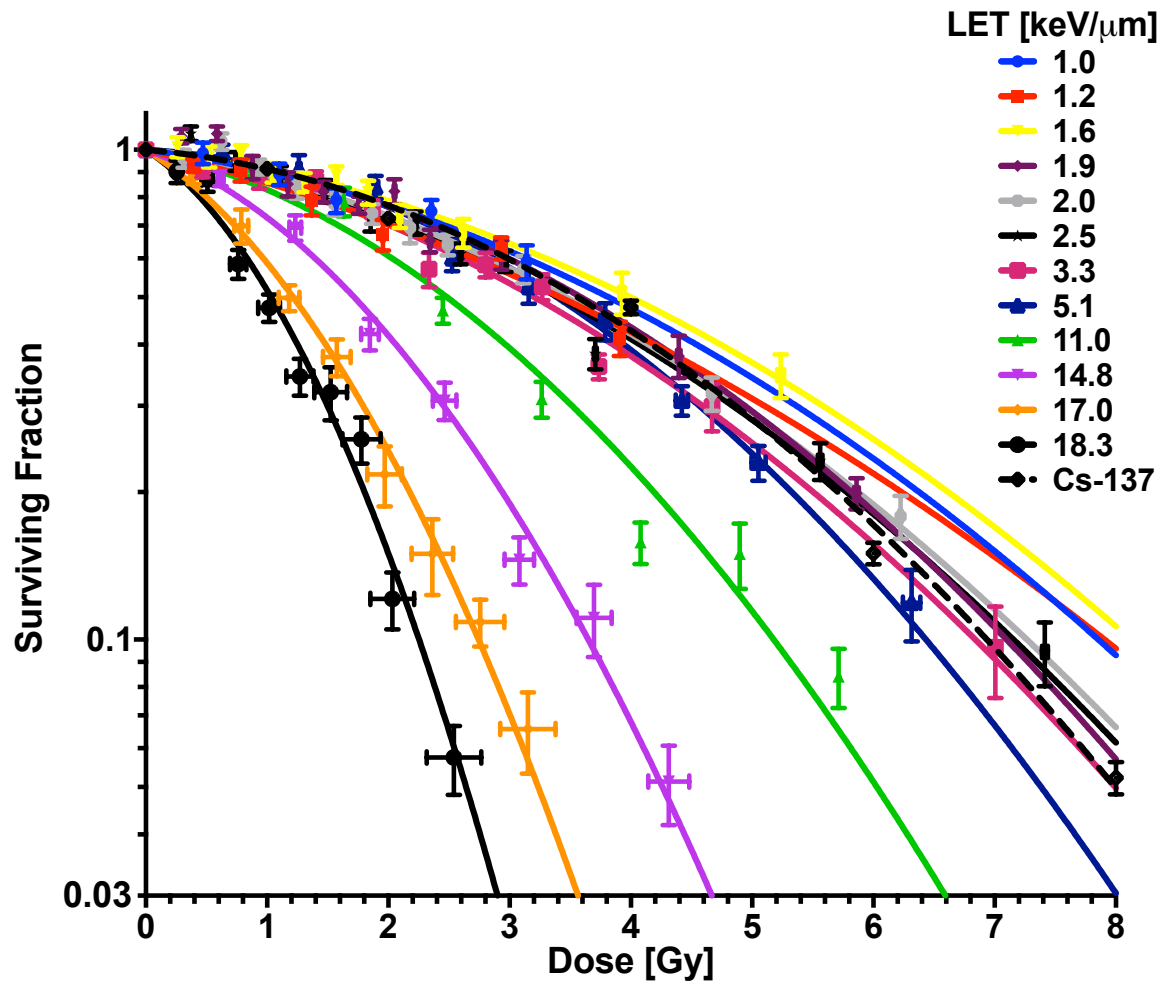


Figure 57. HT clonogenic assay H1437 results. Similar to the H460 cell line results, the H1437 SF was also found to decrease with increasing proton LET especially for locations situated near and distal to the Bragg peak ( $\geq 11.0$  keV/μm). The H1437 cell line was found to be overall more radioresistant than the H460 cell line. Error bars are SEM.

Table 4. H460 and H1437 LQ fitting parameters from Jig 1.0 proton irradiations.

Cell line:		H460				H1437			
Column	LET [keV/ $\mu$ m]	$\alpha$	$\beta$	$\alpha SE$	$\beta SE$	$\alpha$	$\beta$	$\alpha SE$	$\beta SE$
1	1.0	0.267	0.097	0.015	0.007	0.076	0.028	0.049	0.019
2	1.2	0.226	0.111	0.014	0.006	0.135	0.020	0.039	0.013
3	1.6	0.151	0.134	0.013	0.006	0.067	0.027	0.021	0.006
4	1.9	0.149	0.133	0.013	0.006	0.059	0.037	0.020	0.005
5	2.0	0.166	0.134	0.014	0.007	0.094	0.031	0.019	0.005
6	2.5	0.137	0.145	0.016	0.008	0.096	0.032	0.018	0.004
7	3.3	0.205	0.124	0.017	0.008	0.110	0.033	0.022	0.005
8	5.1	0.115	0.153	0.019	0.008	0.034	0.050	0.025	0.006
9	11.0	0.338	0.173	0.024	0.010	0.126	0.062	0.035	0.009
10	14.8	0.498	0.424	0.038	0.025	0.201	0.118	0.048	0.017
11	17.0	0.648	0.782	0.047	0.040	0.357	0.176	0.065	0.031
12	18.3	0.910	1.016	0.056	0.062	0.371	0.289	0.074	0.046
Photons (Cs-137)		0.290	0.083	0.016	0.004	0.050	0.041	0.012	0.002

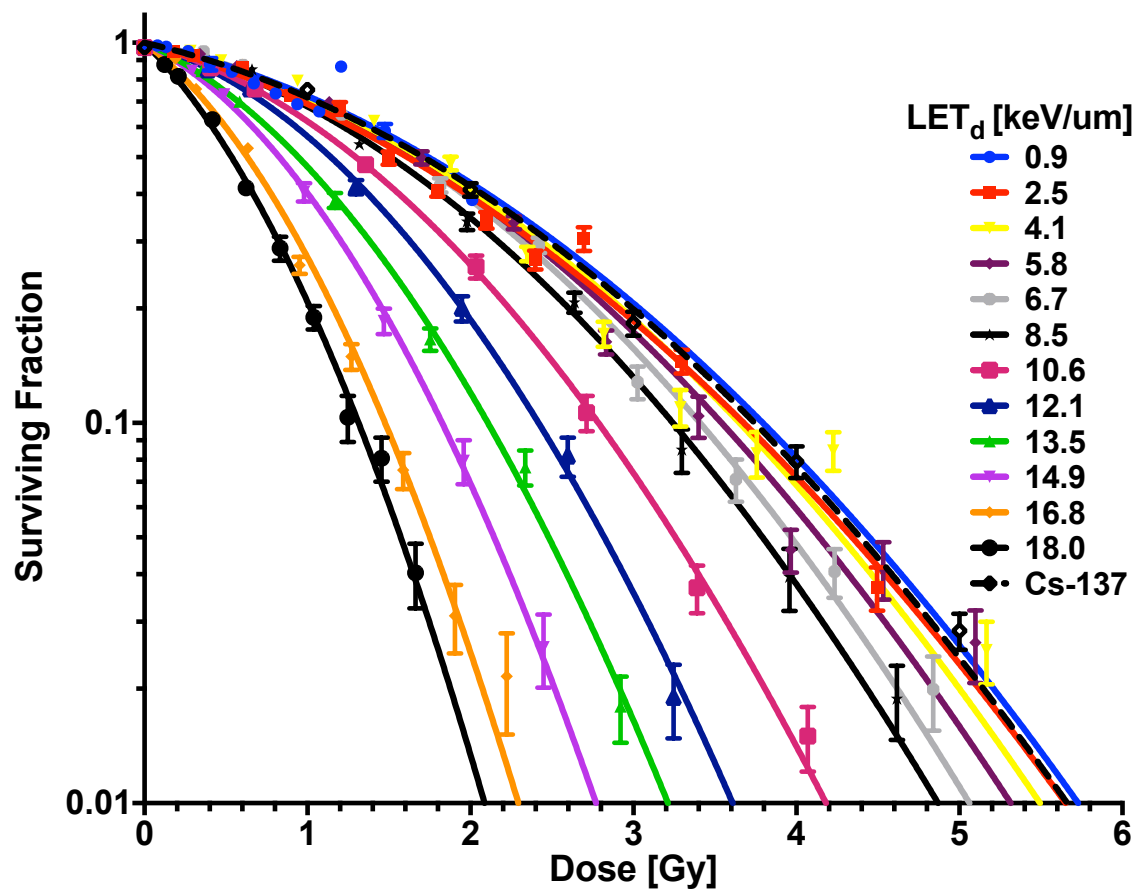


Figure 58. HT clonogenic assay H460 results using second version of the Jig. The second Jig design demonstrated a decreasing SF following exposure to increasing proton LET. The increased LET sampling achieved an improved stratification in the observed LET-dependent separation. Error bars are SEM.

Table 5. H460 LQ fitting parameters from Jig 2.0 proton irradiations performed at MDA.

Column	LET [keV/ $\mu$ m]	$\alpha$	$\beta$	$\alpha$ SE	$\beta$ SE
1	0.9	0.221	0.102	0.032	0.023
2	2.5	0.276	0.095	0.022	0.009
3	4.1	0.220	0.113	0.025	0.009
4	5.8	0.219	0.122	0.027	0.009
5	6.7	0.192	0.142	0.026	0.009
6	8.5	0.241	0.145	0.029	0.011
7	10.6	0.280	0.196	0.032	0.014
8	12.1	0.295	0.272	0.040	0.021
9	13.5	0.443	0.308	0.044	0.025
10	14.9	0.486	0.424	0.060	0.040
11	16.8	0.753	0.547	0.070	0.055
12	18.0	0.981	0.587	0.077	0.072
Photons (Cs-137)		0.228	0.103	0.024	0.008

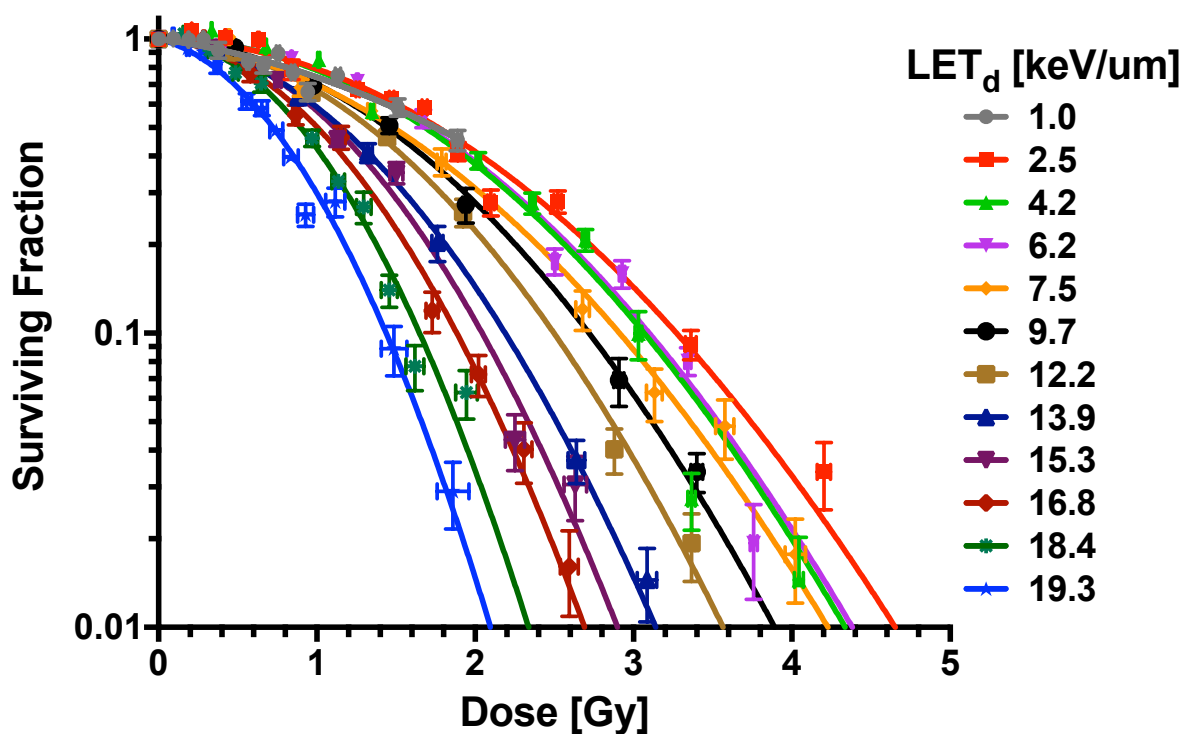


Figure 59. HT clonogenic assay H460 results from proton irradiations performed at HIT. The second version of the HT proton Jig was brought to the HIT facility and used to perform a HT clonogenic experiment. Increased cell kill was found for irradiations with protons of higher LET. Oddly, the overall radiosensitivity of the H460 to proton radiation appeared to be increased for the cell line used at HIT. Error bars are SEM.

Table 6. H460 LQ fitting parameters from Jig 2.0 proton irradiations performed at HIT.

Column	LET [keV/ $\mu$ m]	$\alpha$	$\beta$	$\alpha$ SE	$\beta$ SE
1	1.0	0.1686	0.1301	0.04669	0.035
2	2.5	0.0266	0.2069	0.0354	0.01651
3	4.2		0.2447		0.01817
4	6.2		0.2397		0.01617
5	7.5	0.1313	0.2265	0.04995	0.02066
6	9.7	0.06618	0.287	0.04555	0.02252
7	12.2	0.05833	0.3457	0.05304	0.02863
8	13.9	0.09816	0.4353	0.06224	0.03815
9	15.3	0.02242	0.5399	0.06824	0.04531
10	16.8	0.08363	0.6043	0.07933	0.05163
11	18.4	0.02477	0.8317	0.0841	0.06806
12	19.3	0.3071	0.9	0.085	0.08837

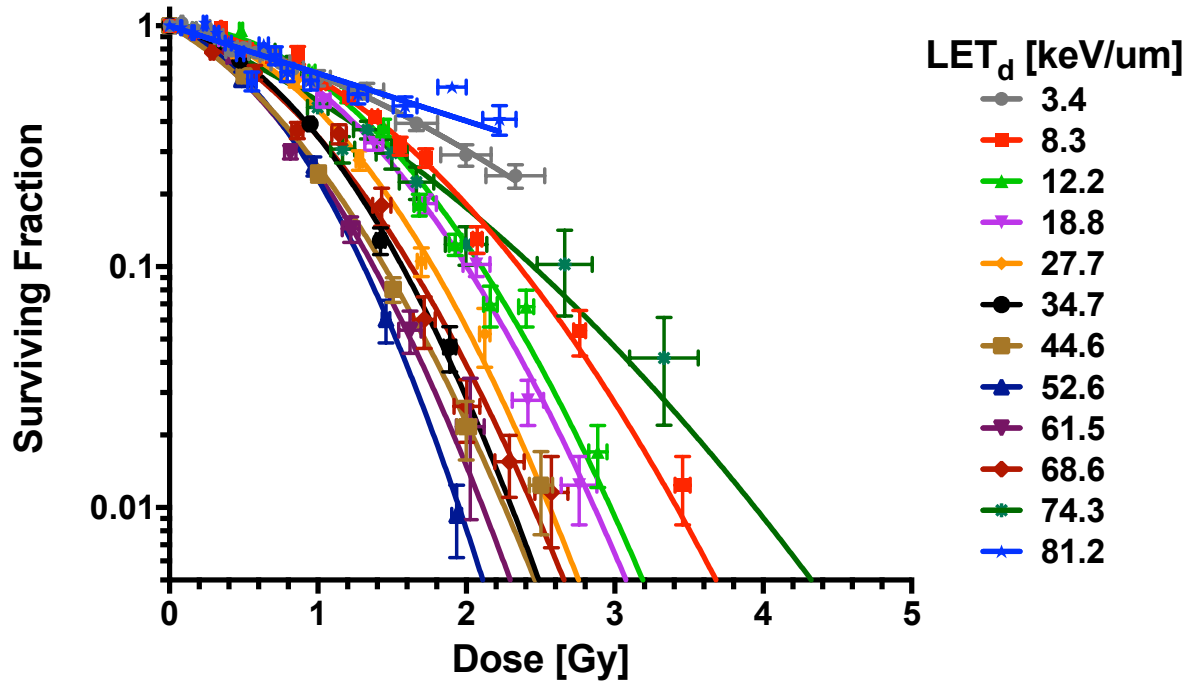


Figure 60. HT clonogenic assay H460 results from helium ion irradiations performed at HIT. A HT irradiation jig was developed for use with a 336.3 MeV helium ion beam. Clonality was found to be reduced with increasing helium ion LET until 52.6 keV/ $\mu\text{m}$ . For LETs sampled greater than 52.6 keV/ $\mu\text{m}$ , the SFs were found to increase. Error bars are SEM.

Table 7. H460 LQ fitting parameters from helium ion irradiations performed at HIT.

Column	LET [keV/ $\mu\text{m}$ ]	$\alpha$	$\beta$	$\alpha$ SE	$\beta$ SE
1	3.4	0.3478	0.1235	0.04229	0.02947
2	8.3	0.1575	0.3478	0.04289	0.02685
3	12.2		0.521		0.03335
4	18.8	0.0824	0.533	0.05286	0.03371
5	27.7	0.1682	0.6363	0.09879	0.07514
6	34.7	0.3413	0.7179	0.1067	0.08596
7	44.6	0.7887	0.5532	0.1058	0.08154
8	52.6	0.5314	0.9366	0.1428	0.1279
9	61.5	0.728	0.6872	0.1413	0.1227
10	68.6	0.4933	0.564	0.09448	0.06784
11	74.3	0.5648	0.1526	0.07399	0.04276
12	81.2	0.4548		0.05455	



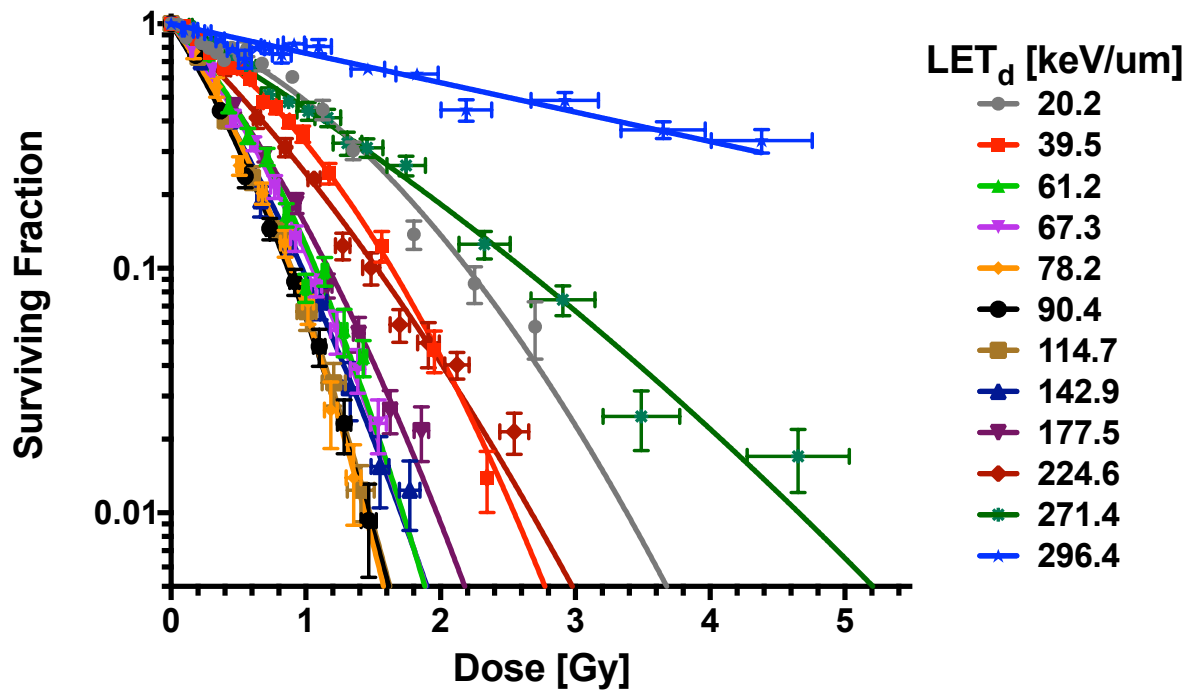


Figure 61. HT clonogenic assay H460 results from carbon ion irradiations performed at HIT. A HT irradiation apparatus was designed for use with 1802.5 MeV carbon ions. Similar to the helium ion results, an inflection point was found for carbon ion irradiations at 90.4 keV/ $\mu$ m. The SFs for cells exposed to carbon ions below this threshold LET were found to continually decrease. For exposure to LETs above 90.4 keV/ $\mu$ m the SFs were found to grow. Error bars are SEM.

Table 8. H460 LQ fitting parameters from carbon ion irradiations performed at HIT.

Column	LET [keV/ $\mu$ m]	$\alpha$	$\beta$	$\alpha$ SE	$\beta$ SE
1	20.2	0.4614	0.2661	0.04714	0.03238
2	39.5	0.6798	0.443	0.05285	0.04668
3	61.2	1.256	0.8256	0.1201	0.1331
4	67.3	1.431	0.7269	0.1126	0.1199
5	78.2	1.614	1.104	0.1833	0.2274
6	90.4	1.938	0.8291	0.1465	0.1733
7	114.7	1.738	0.9374	0.1422	0.17
8	142.9	1.923	0.4556	0.141	0.14
9	177.5	1.446	0.4512	0.1038	0.09332
10	224.6	1.221	0.1874	0.07654	0.05326
11	271.4	0.744	0.05245	0.03614	0.01746
12	296.4	0.277		0.02576	

## RBEs

### Proton

The RBE results for the H460 and H1437 cell lines using the first iteration of the jig design were calculated by comparison to Cs-137 gamma photon exposed conditions (Figure 62). Both cell lines exhibited similar trends in RBE vs LET response. Overall, the RBE was found to increase with LET. The portions of the beam proximal to and including the Bragg peak (columns 1-9; 1-11 keV/ $\mu\text{m}$ ) exhibited a linear increase in RBE from 1.03 to 1.36 for the H460 cell line. At positions distal to the Bragg peak (columns 10-12; 14.8-18.3 keV/ $\mu\text{m}$ ), the RBE for the H460 cells was found to increase rapidly with LET from 2.09 at 14.8 keV/ $\mu\text{m}$  to a maximum value of 3.38 at 18.3 keV/ $\mu\text{m}$ .

The RBE trend calculated from the SF results obtained using the second iteration of the jig for the H460 cell line were found to match the initial results for proton irradiations performed at MD Anderson (Figure 63). In fact, the increased LET sampling resulted in an overall smoother trend. More thorough LET sampling in the regions between 5 and 10 keV/ $\mu\text{m}$  demonstrated a supralinear trend from the entrance to the Bragg peak region of the beam. Above the dose peak LET of 10.6 keV/ $\mu\text{m}$ , the RBE was again found to rapidly rise. The largest deviations between the two observed RBE trends were observed at the highest LETs for each experimental setup with the initial jig design obtaining higher values.

RBEs for proton irradiations performed at HIT were calculated using the published Cs-137 response values obtained at MDA for the initial Jig experiments. Compiling all the proton RBE results for the H460 cell line for the two jigs and the two therapy centers results in similar RBE vs LET trends (Figure 64). Compared to the results obtained at MDA, the

RBE values found from the experiment at HIT were higher for positions proximal to the peak dose and lower for the distal portions of the beam. The overall observation of increased RBE following exposure to protons of increasing LET was consistent between experiments. This increase was gradual and approximately linear for protons in the plateau region to the Bragg peak with corresponding LETs between 0.9 keV/ $\mu\text{m}$  and 10 keV/ $\mu\text{m}$ . For LETs above this value the RBE was found to rise at an increased rate. The maximum RBE values measured are within the range of 2.6 and 3.4. Table 9 summarizes the obtained RBE data for all proton experiments performed.

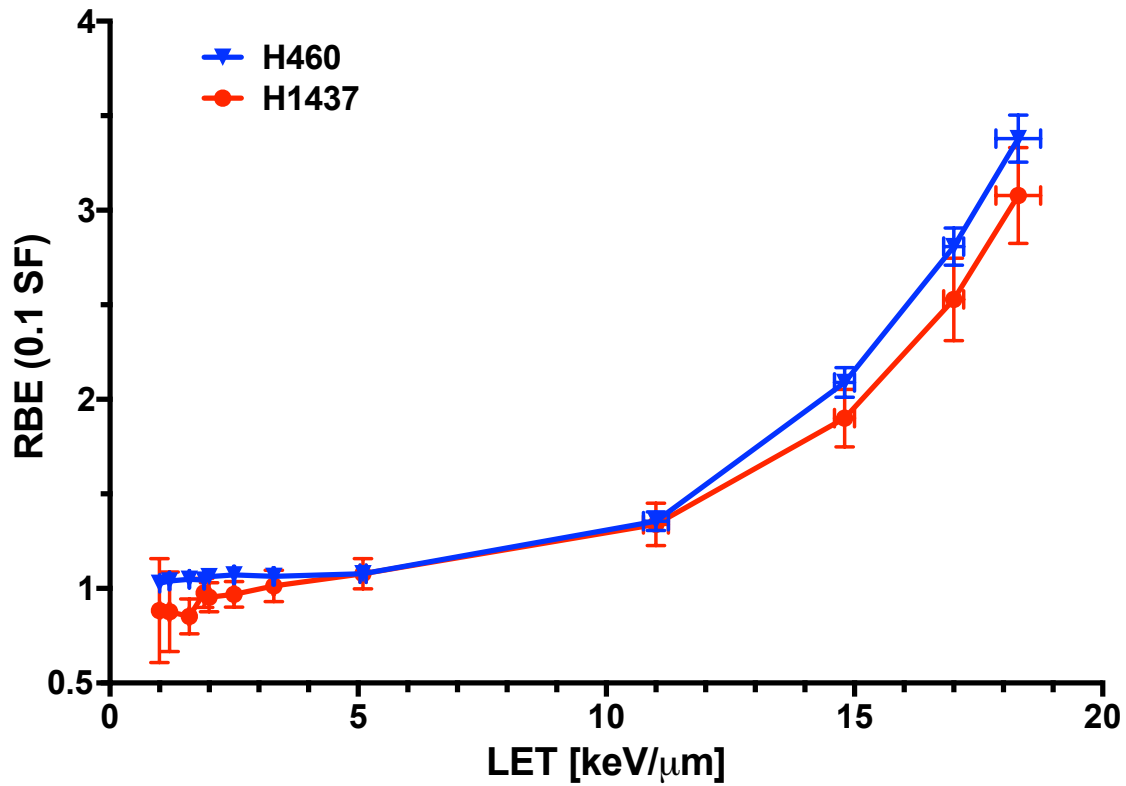


Figure 62. Initial proton RBE results obtained using the first version of the high-throughput irradiation apparatus. The LET-dependent RBE for both the H460 and H1437 cell lines was found to be similar. The RBE was found to linearly increase from the entrance to the dose peak; for LETs in the 1-10 keV/μm range. Above 10 keV/μm, the RBE was found to rapidly rise. Error bars are SE.

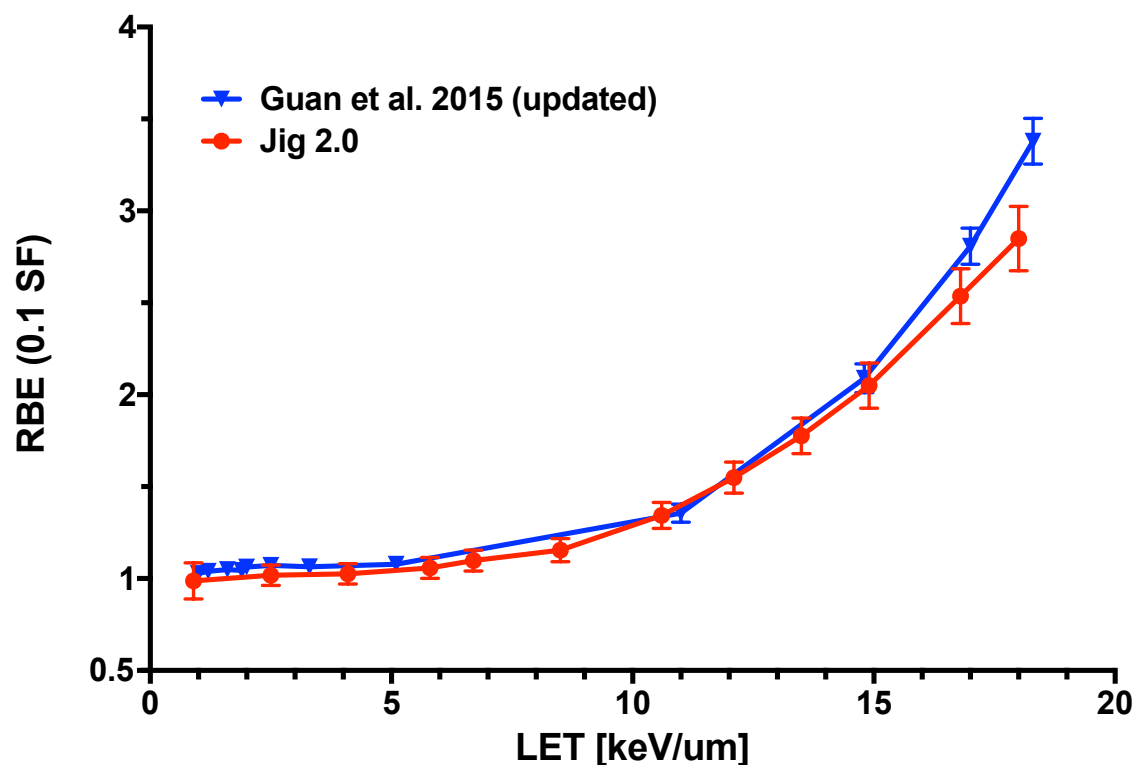


Figure 63. Proton RBEs obtained from the second Jig version. The H460 RBE was found to be similar between the initial (Guan et al.) and second version (Jig 2.0) of the HT irradiation apparatus. The increased LET sampling from 5 to 10 keV/μm demonstrated a supralinear response for the region proximal to the dose peak (red). For locations distal to the dose peak, the RBE response was found to rise at an increased rate compared to the proximal region. Error bars are SE.

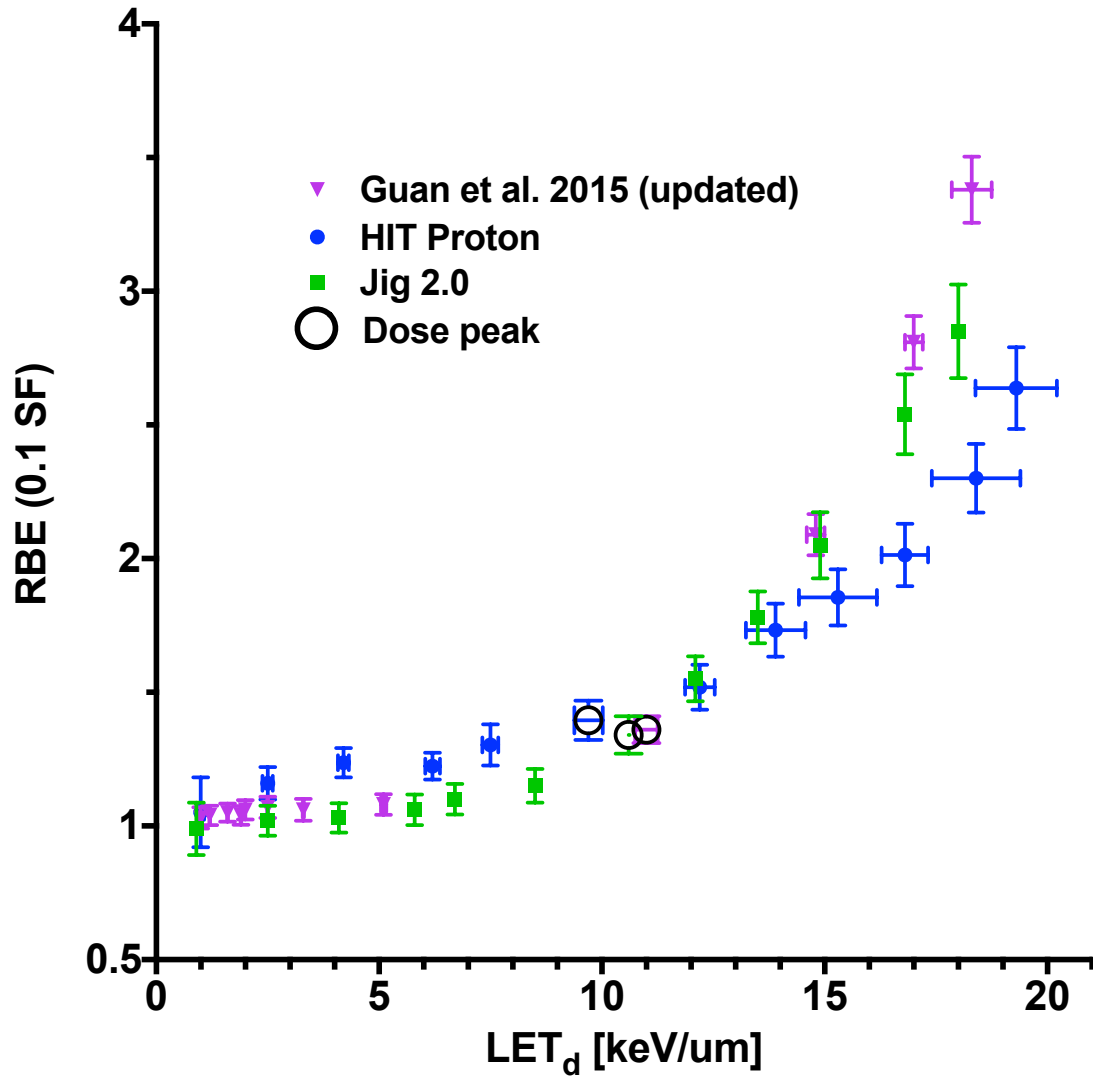


Figure 64. Compiled proton RBE results. The proton RBE results from irradiations at HIT demonstrated a continual increase with LET (blue). The rate of RBE increase is lower for LETs associated with the proximal region of the beam (blue, circle). For LETs present in the distal region of the proton beam the rate of RBE increase was larger. The general trends of RBE between proton irradiations performed at MDA PTC and HIT were qualitatively comparable; however, the RBEs found in the range of 1-10 keV/ $\mu$ m were systematically higher for the HIT dataset than those found in datasets generated at MDA (purple, green). The RBE trend reversed for LETs above approximately 10 keV/ $\mu$ m where the HIT dataset demonstrates persistently lower RBEs than the MDA datasets. Error bars are SE.

Table 9. Compiled proton RBE values.

Column	H460						H1437	
	Jig 1.0		Jig 2.0 MDA		Jig 2.0 HIT		Jig 1.0	
	LET [keV/ $\mu$ m]	RBE	LET [keV/ $\mu$ m]	RBE	LET [keV/ $\mu$ m]	RBE	LET [keV/ $\mu$ m]	RBE
1	1.0	1.03	0.9	0.99	1.0	1.05	1.0	0.88
2	1.2	1.04	2.5	1.02	2.5	1.16	1.2	0.88
3	1.6	1.05	4.1	1.03	4.2	1.24	1.6	0.85
4	1.9	1.04	5.8	1.06	6.2	1.22	1.9	0.98
5	2.0	1.06	6.7	1.10	7.5	1.30	2.0	0.95
6	2.5	1.07	8.5	1.15	9.7	1.40	2.5	0.97
7	3.3	1.06	10.6	1.34	12.2	1.52	3.3	1.01
8	5.1	1.08	12.1	1.55	13.9	1.73	5.1	1.08
9	11.0	1.36	13.5	1.78	15.3	1.86	11.0	1.34
10	14.8	2.09	14.9	2.05	16.8	2.01	14.8	1.90
11	17.0	2.81	16.8	2.54	18.4	2.30	17.0	2.53
12	18.3	3.38	18.0	2.85	19.3	2.64	18.3	3.08



## Helium and carbon ions

Calculating RBEs for the helium and carbon ion experiments performed at the HIT facility using the previously measured response of H460 cells to Cs-137 photons resulted in unique RBE trends compared to the proton irradiations (Figure 65, Table 10). The helium RBE was found to continually increase from the initial value of 1.21 for exposure to helium ions with an LET of 3.4 keV/ $\mu\text{m}$  present at the beam entrance to a maximum value of 2.90 at 52.6 keV/ $\mu\text{m}$ . For LETs sampled above 52.6 keV/ $\mu\text{m}$ , the RBE was found to rapidly decrease to a minimum value of 0.75 at 81.2 keV/ $\mu\text{m}$ .

The carbon ion RBE followed a similar pattern as helium ions. The entrance RBE was measured to be 1.72 at 20.2 keV/ $\mu\text{m}$ . The RBE increased with carbon ion LET until a maximum value of 4.38 for carbon ions with an LET of 90.4 keV/ $\mu\text{m}$ . Above this LET, the RBEs were found to decrease until the lowest value measured of 0.46 at the highest LET sampled, 296.4 keV/ $\mu\text{m}$ .

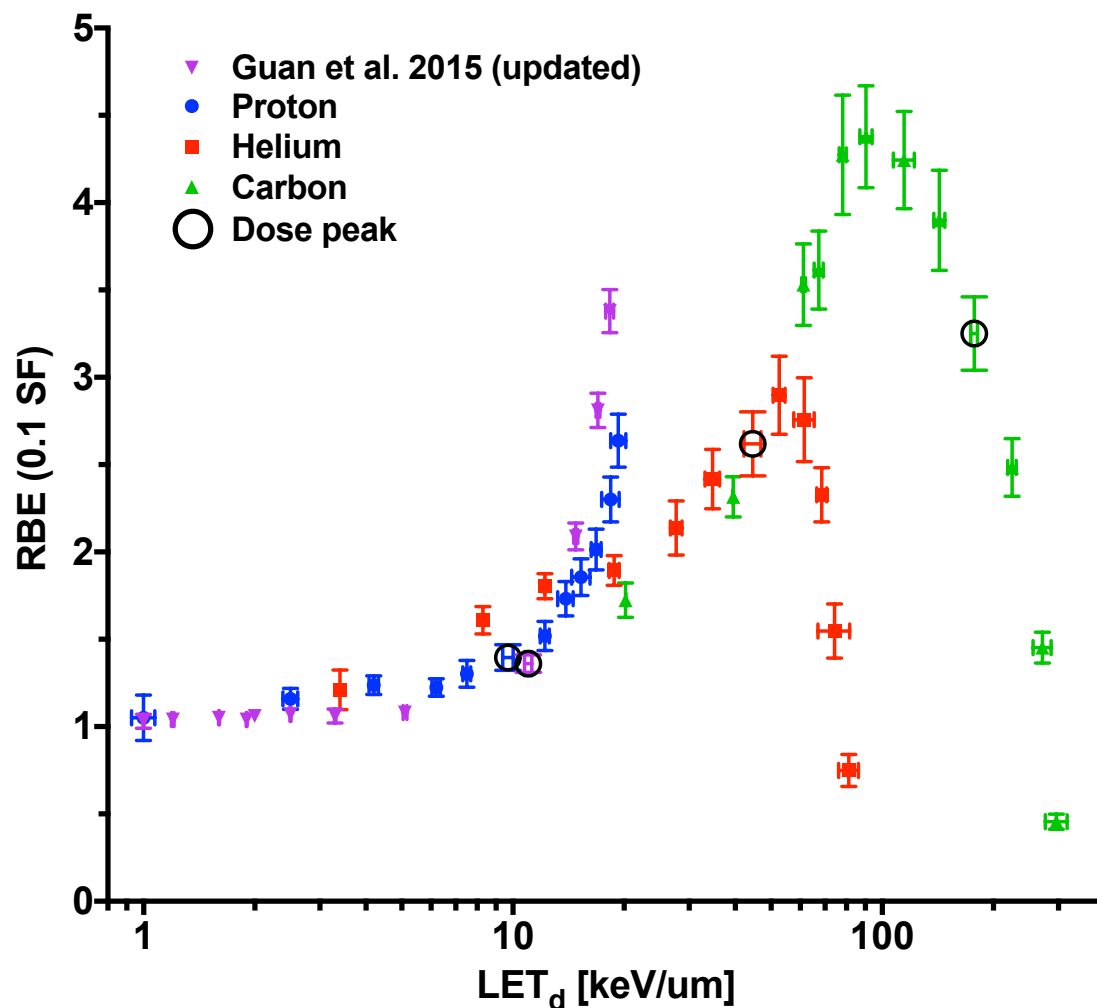


Figure 65. Proton, helium and carbon ion RBE results from HIT irradiations. The helium and carbon ion datasets demonstrated an increase in RBE until an ion-specific LET value at which point the RBEs were found to reduce from the maximum. This feature was not present in the proton RBE. Error bars are SE.

Table 10. Heavy ion RBE values.

Column	Helium		Carbon	
	LET [keV/ $\mu\text{m}$ ]	RBE	LET [keV/ $\mu\text{m}$ ]	RBE
1	3.4	1.21	20.2	1.72
2	8.3	1.61	39.5	2.32
3	12.2	1.80	61.2	3.53
4	18.8	1.89	67.3	3.61
5	27.7	2.14	78.2	4.27
6	34.7	2.42	90.4	4.38
7	44.6	2.62	114.7	4.24
8	52.6	2.90	142.9	3.90
9	61.5	2.76	177.5	3.25
10	68.6	2.33	224.6	2.48
11	74.3	1.55	271.4	1.45
12	81.2	0.75	296.4	0.46

## High-throughput immunofluorescent results

### Protons at MD Anderson Proton Therapy Center

The second version of the irradiation apparatus was used to performed high-throughput DNA damage repair kinetic studies. Cells were seeded on glass bottom plates and subjected to a single dose of protons. Following irradiation, the plates were returned to culture for repair to occur. Plates were fixed over a time course of 24-30 hours following irradiation for subsequent immunofluorescent DSB foci staining. Plates were imaged on an automated microscope at 20x magnification with 16 images per well obtained. The images were analyzed with the CellProfiler software package to measure the foci within each nucleus.

For all dose-LETs sampled, the results of the foci scoring analysis demonstrate the greatest number of foci at the initial fixation time point at 30 minutes post-irradiation followed by a reduction until the terminal assay time point (Figure 66). For proton irradiations, the DSB repair kinetics were modeled by a standard exponential decay function (Figure 67). The foci repair half times were found to increase with increasing proton LET.

To determine the dose dependence of DSB induction and persistence following proton exposure, cells were irradiated to dose levels corresponding to peak doses of 0.96, 1.92, and 3.44 Gy using the second iteration of the jig. The number of foci at 30 minutes following irradiation was found to increase from the 0.96 and 1.92 Gy peak dose exposures; however, a saturation in early foci was found for exposures associated with the 3.44 Gy peak dose for LETs above 2.59 keV/ $\mu$ m (Figure 68). A linear response between dose and the number of persistent foci, was observed (Figure 69).

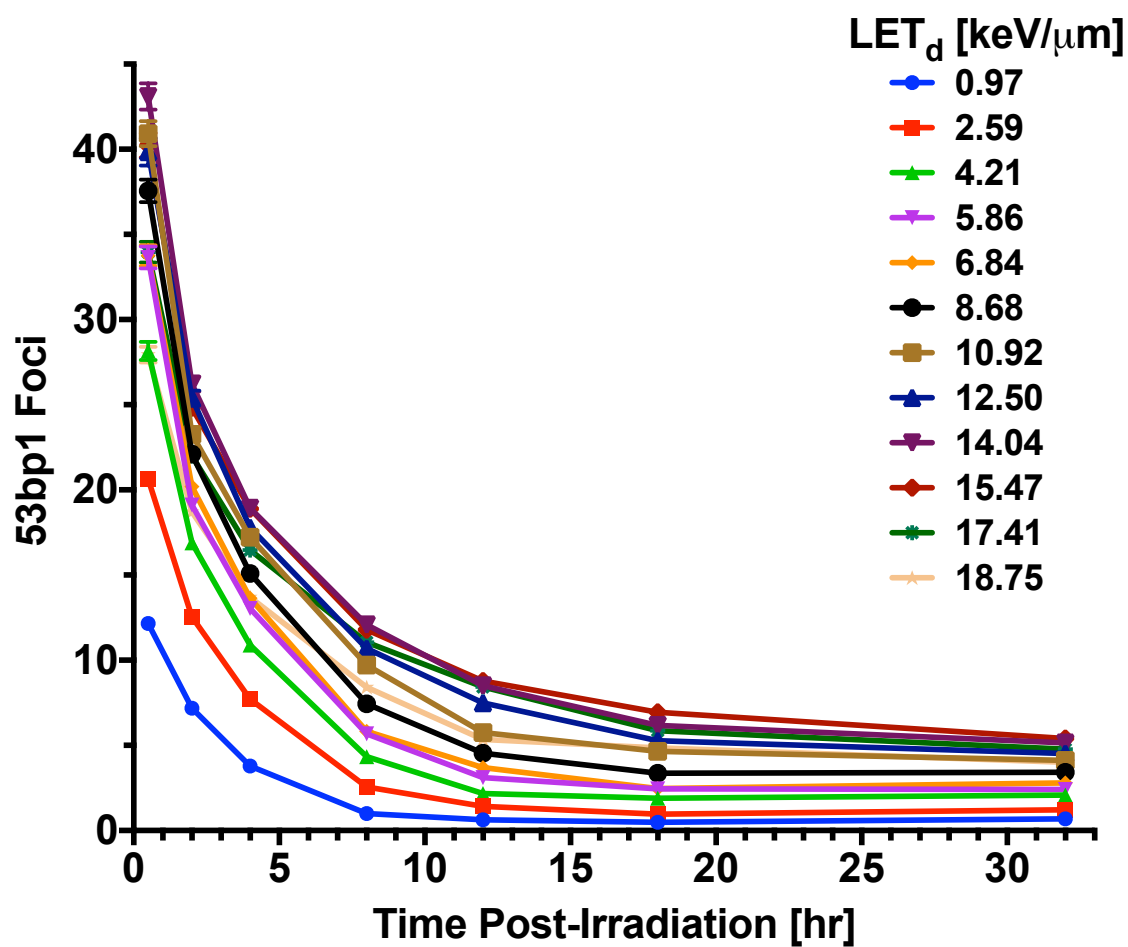


Figure 66. Representative DSB repair kinetics. H460 cells were exposed to a peak dose of 1.92 Gy and returned to culture for fixed periods of time before fixation and immunofluorescent labeling the DSB repair protein 53bp1. Error bars represent 95% confidence intervals.

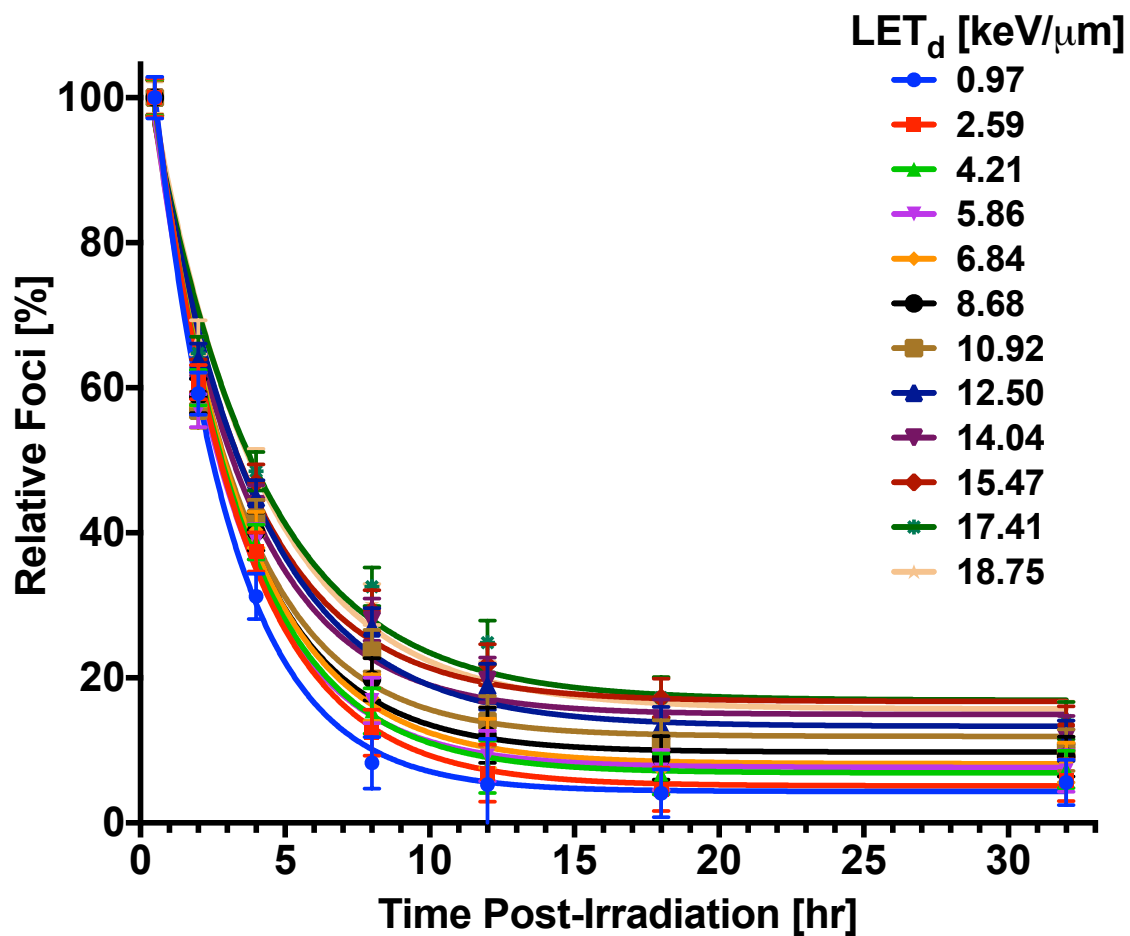


Figure 67. Normalized DSB repair kinetics with fit. Data was analyzed by subtracting the background and normalizing to the initial value of induced foci at 30 minutes. Error bars represent 95% confidence intervals.

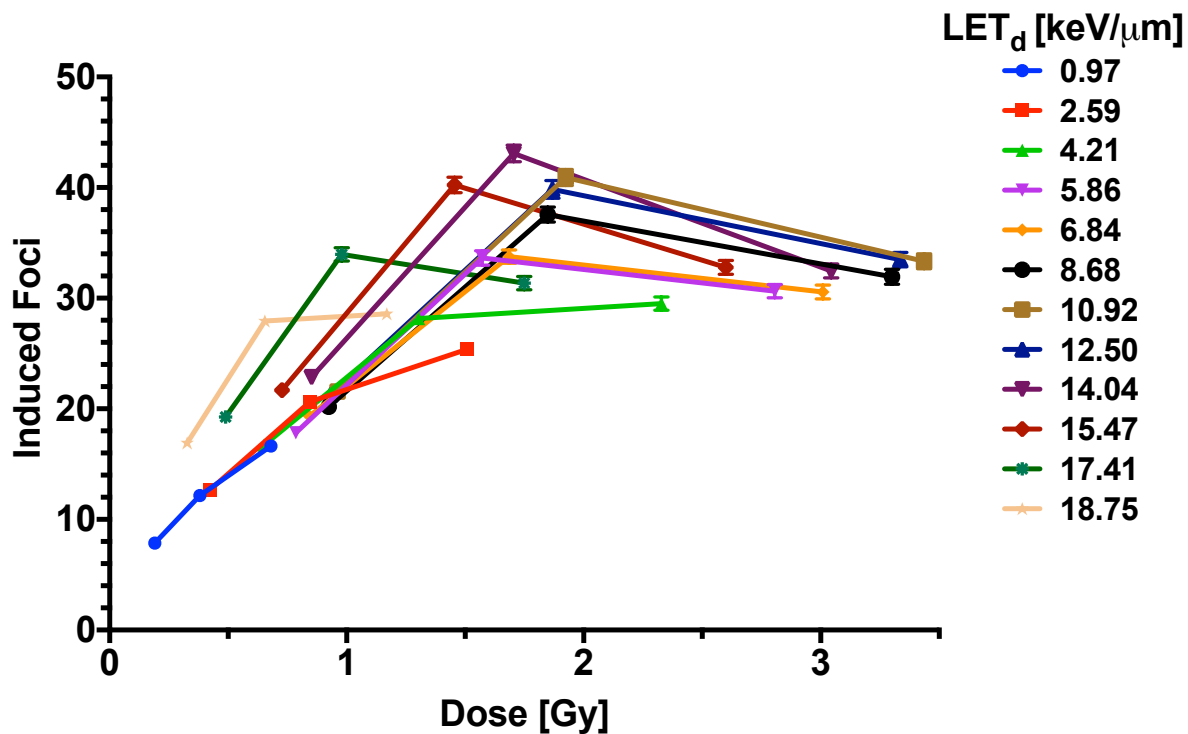


Figure 68. Induction foci vs dose and LET. H460 cells were exposed to 3 different dose levels using the HT irradiation setup. The number of induced DSBs was set as the number of foci at 30 minutes post-irradiation. The number of initial foci detected demonstrated a saturation for conditions at the highest dose levels for LETs above 2.59 keV/μm. Error bars represent 95% confidence intervals.

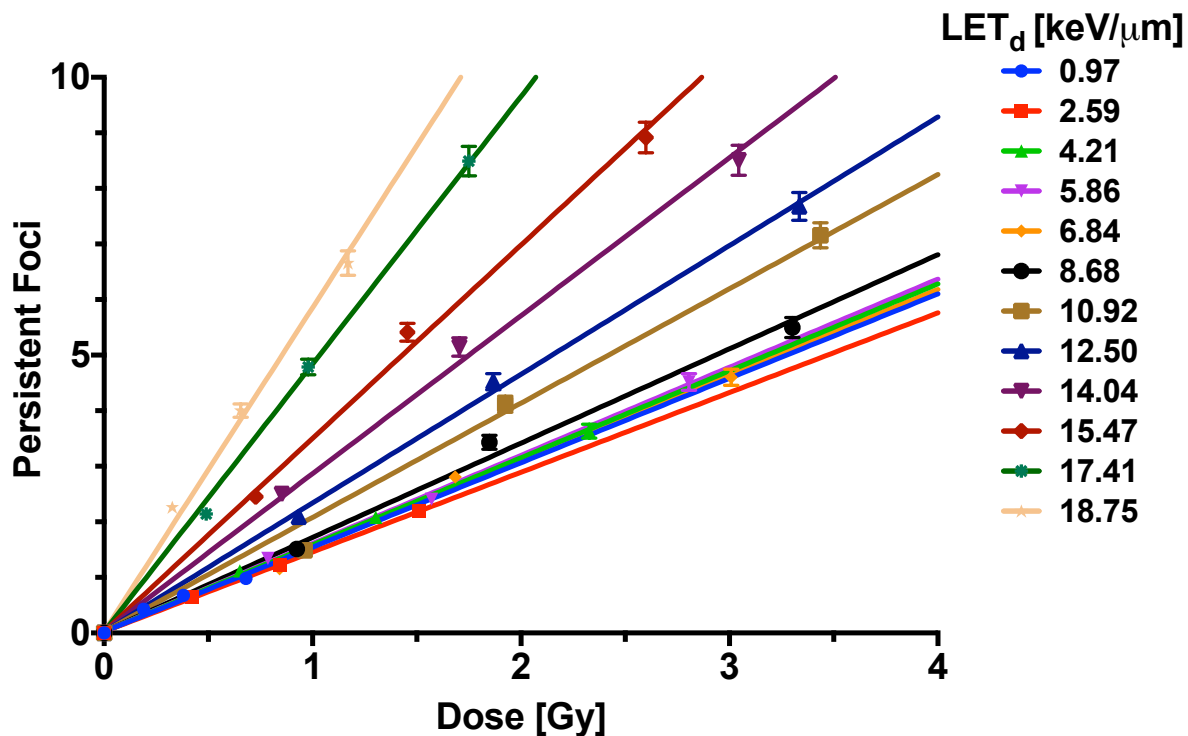


Figure 69. Persistent foci vs dose and LET. Persistent foci were defined as DSB foci above background present at the terminal fixation time point in an experiment. The amount of persistent foci was found to increase with exposure to increasing proton LET regardless of delivered dose with the exception of the lowest LET tested. The number of persistent foci for a given LET condition was found to be linearly proportional to the dose delivered (lines). Error bars represent 95% confidence intervals.



A linear quadratic model was used to compare the number of persistent DSBs for a given dose-LET combination with the corresponding surviving fraction determined from the high-throughput clonogenic assays (Figure 58) (Figure 70). The correlation between the number of persistent DSBs and SF indicated that there was a relationship between the mechanistic DSB and the functional biological response of colony formation. When normalized for dose, the number of induced foci was found to be similar for the LET extremes sampled (Figure 71). The induction trend decreased from LETs of 0.97 keV/ $\mu$ m to 10.92 keV/ $\mu$ m where the minimum number of foci were found. The number of induced foci at 30 mins following irradiation then increased above 10.92 keV/ $\mu$ m to the maximum value at 18.75 keV/ $\mu$ m. The dose-normalized persistent foci were found to be consistent from 2.59 keV/ $\mu$ m to 6.84 keV/ $\mu$ m whereas the 0.97 keV/ $\mu$ m condition exhibited a higher value than those present in this range. For the LETs sampled above 6.84 keV/ $\mu$ m, in the range in 8.68 keV/ $\mu$ m and 18.75 keV/ $\mu$ m, the number of persistent foci per Gy was found to rapidly rise (Figure 71).

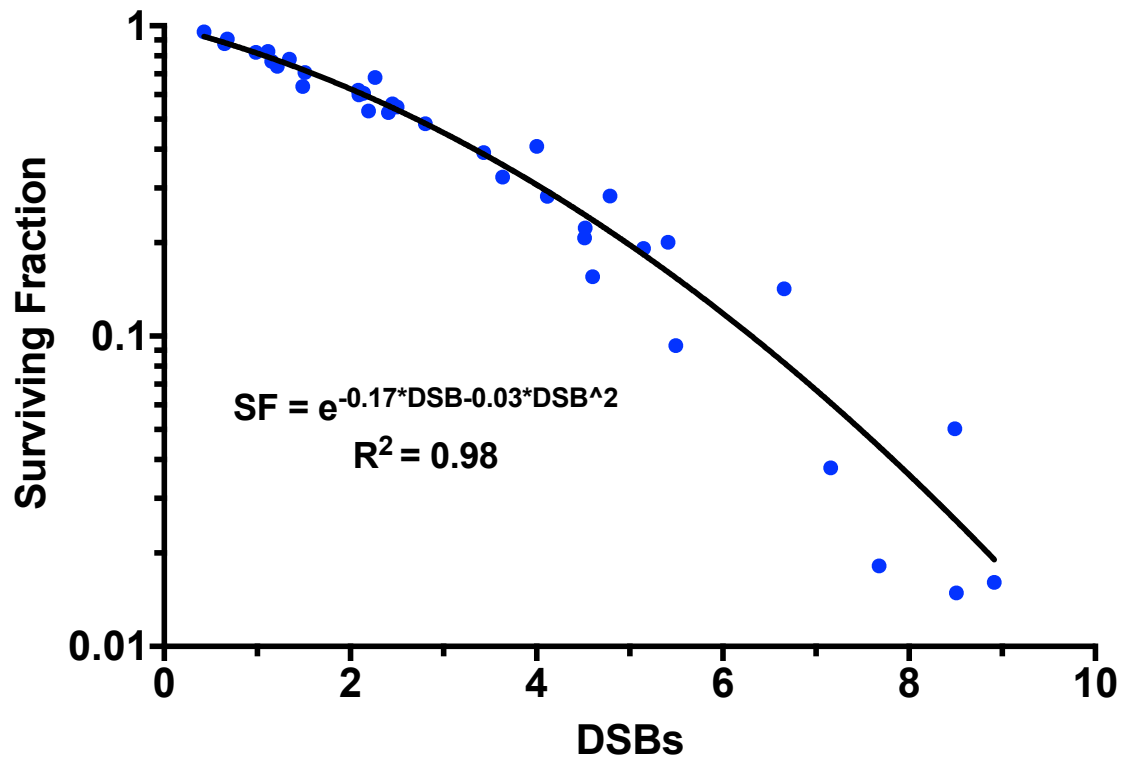


Figure 70. Correlation between persistent DSBs and SF. A linear quadratic correlation was found between the number of persistent foci present and the respective SF resulting from the corresponding dose-LET combination.

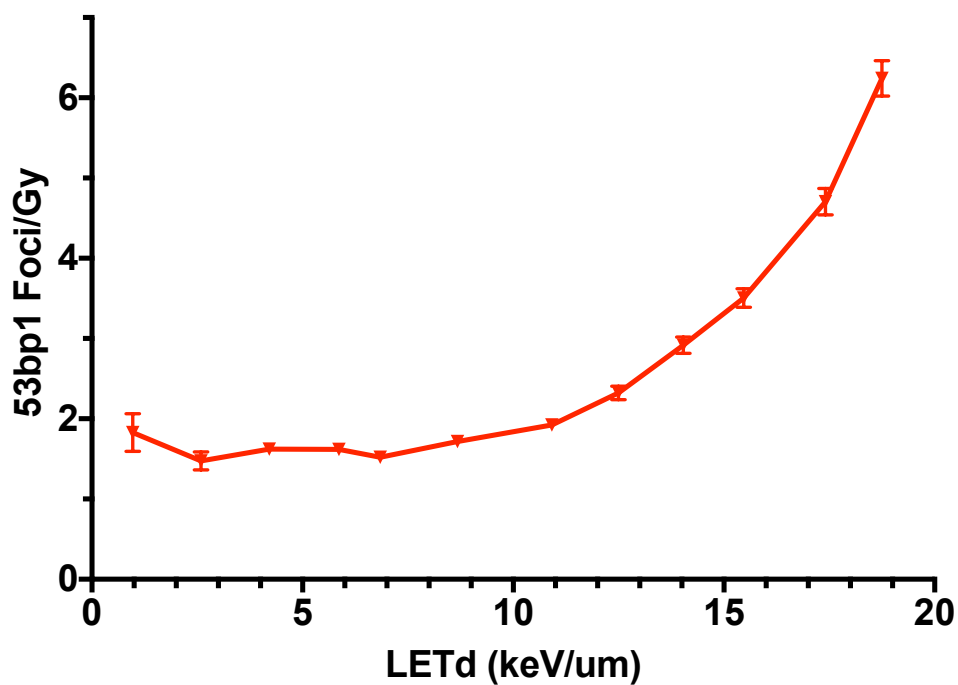
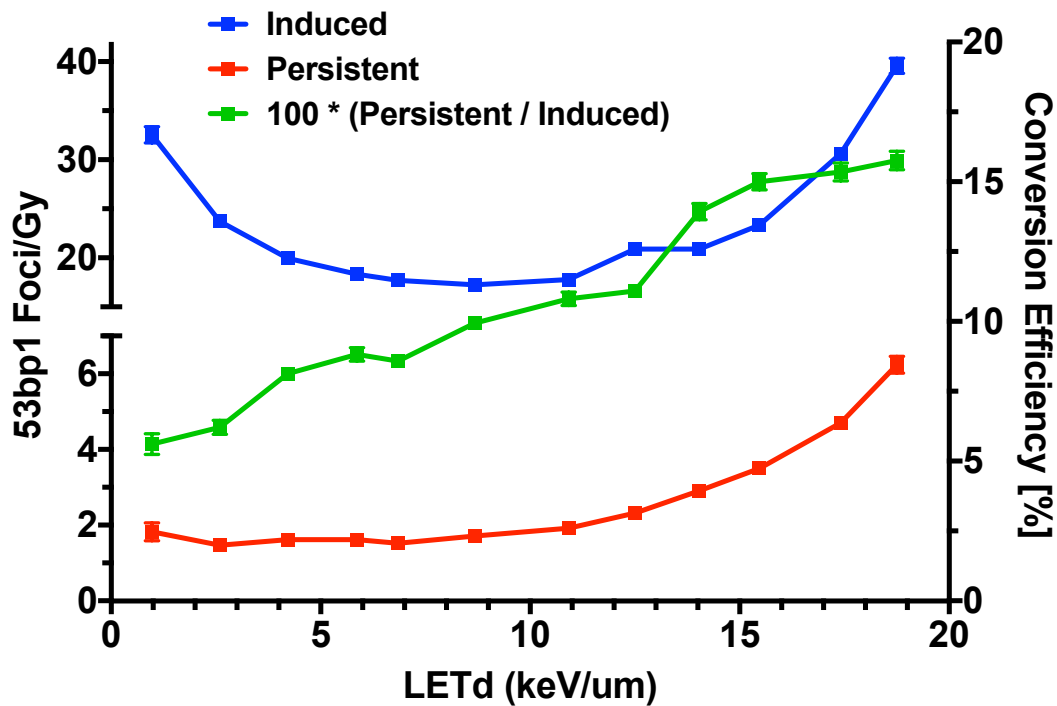


Figure 71. Induced and persistent DSBs vs LET for protons. Dose normalizing the number of induced and persistent foci demonstrated the energy-normalized DSB induction (blue) and persistence (red) efficiency for each proton LET. The relationship between dose-normalized persistent DSB foci and LET appeared analogous to those observed for RBE vs LET. Error bars represent 95% confidence intervals.

## Helium and carbon ion irradiations performed at HIT

The immunofluorescent DSB foci repair assay was performed for H460 cells irradiated by helium or carbon ions at HIT. The peak dose the cells were exposed to was 3.13 Gy for helium ions and 2.80 Gy for carbon ions. The repair kinetics for cells exposed to helium ions were appropriately fit to an exponential decay equation (Figure 72). The repair time course for cells exposed to carbon ions was fit by an exponential decay equation for the LETs sampled between 20.1 keV/ $\mu$ m and 134.1 keV/ $\mu$ m as well for 301.5 keV/ $\mu$ m, the highest LET sampled. The LETs of 170.5, 224.1, and 271.4 keV/ $\mu$ m were unable to be modeled by a simple exponential model due to a shared trend between these conditions where an initial reduction in the number of foci was observed up to approximately 4 hours post-irradiation. DNA repair was then followed by an increase in the number of foci from the 4 hour time point in the 8 and 12 hour time points followed by a reduction at the terminal time point assayed (Figure 73). Similar repair trends where the 8 or 12 hour time points exhibited an increased foci signal compared to the previous time points were observed in the LETs between 60.0 and 134.5 keV/ $\mu$ m, but these LET conditions were able to be fit to an exponential reduction model.

The dose-normalized induction foci for the helium and carbon ions were found to decrease with increasing LETs (Figure 74). For helium ions, the number of dose-normalized persistent foci was found to increase with LET until a maximum at 57.6 keV/ $\mu$ m. For higher LETs above 57.6 keV/ $\mu$ m, the number of persistent foci was found to consistently decrease (Figure 75). A similar trend in the number of persistent foci versus LET for carbon ions was observed. For irradiation with carbon ions, the number of persistent foci was found to

increase from 20.1 to 86.5 keV/ $\mu\text{m}$ . The trend was then reversed for LETs above 86.5 keV/ $\mu\text{m}$  (Figure 75).

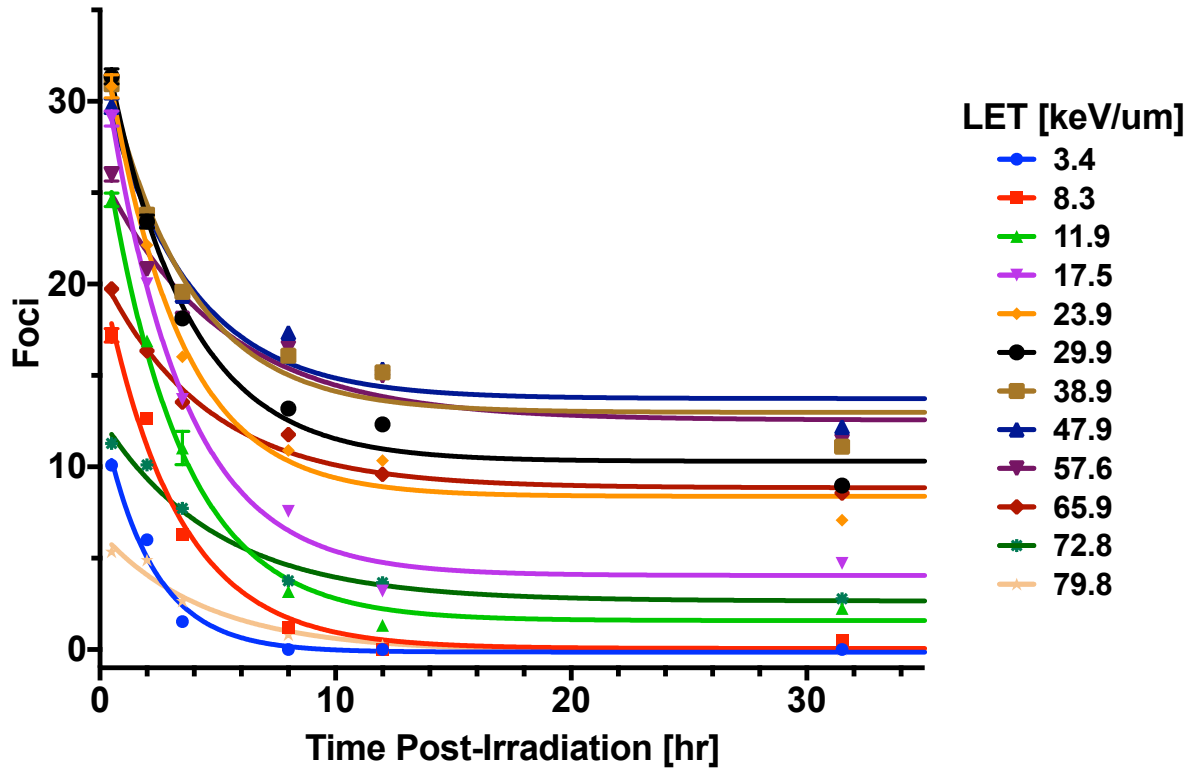


Figure 72. Helium ion DSB repair kinetics. H460 cells were irradiated to a peak dose of 3.13 Gy with a 336.3 MeV helium ion beam at the HIT facility. DSB repair was measured via 53bp1 foci staining. Data points were fit with to a one phase decay equation. Error bars represent 95% confidence intervals.

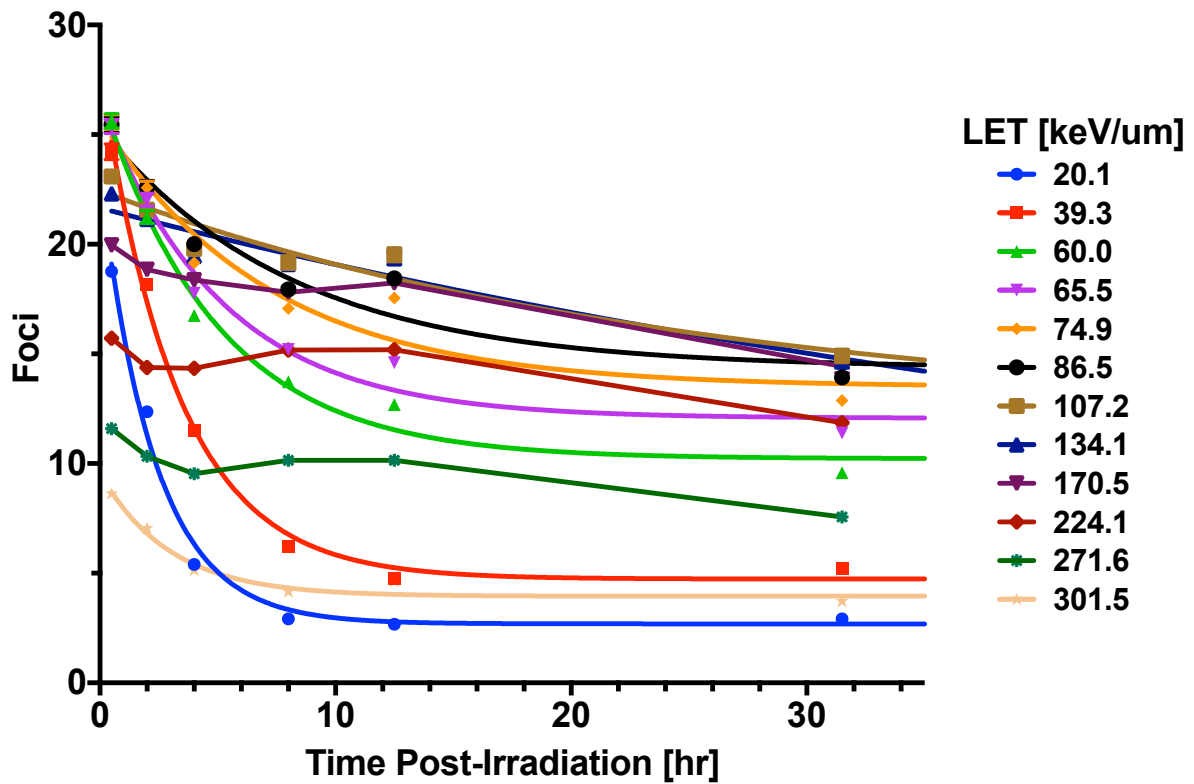


Figure 73. Temporal DSB repair following exposure to carbon ions. 53bp1 foci staining was performed on H460 cells following a peak dose exposure of 2.80 Gy from an 1802.5 MeV carbon ion beam. A single phase decay model was fit to the results. Fitting did not converge for the 170.5, 224.1 and 271.6 keV/ $\mu$ m conditions. Error bars represent 95% confidence intervals.

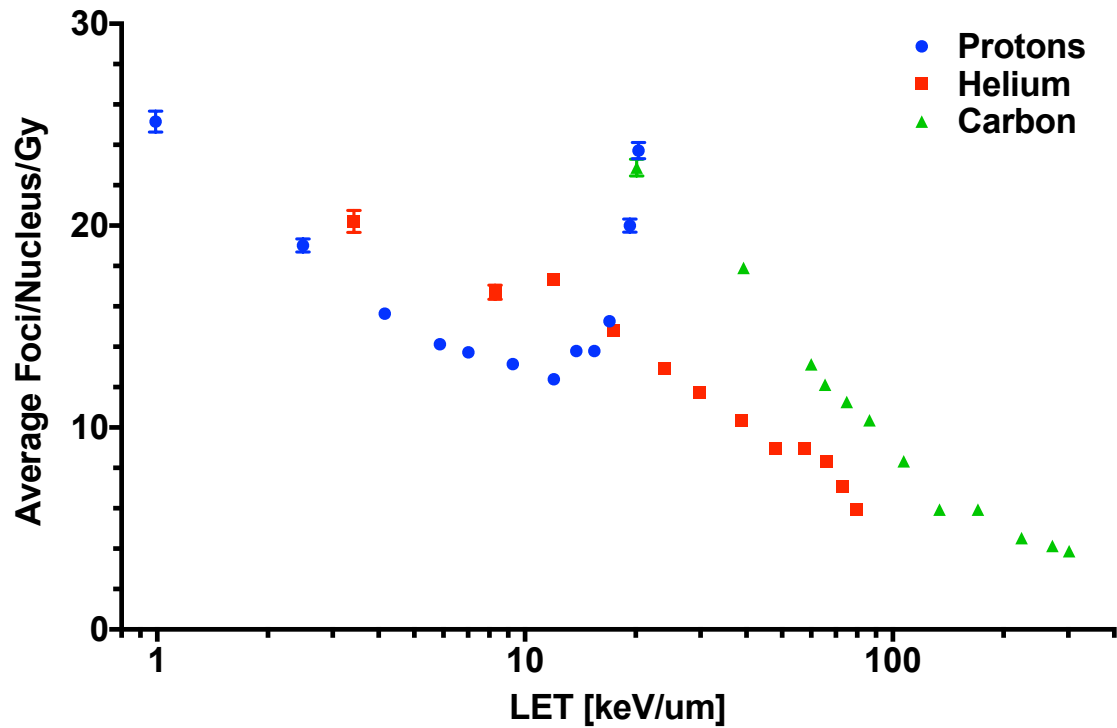


Figure 74. Dose-normalized induced foci at 30 mins post-irradiation for proton, helium, and carbon ion beams. With increasing particle LET, the helium and carbon ions exhibited consistent downward trends within the number of induced foci per Gy. The proton beam followed a downward trend with increasing LET until the peak dose LET after which the foci induction efficacy was found to increase with LET. Error bars represent 95% confidence intervals.



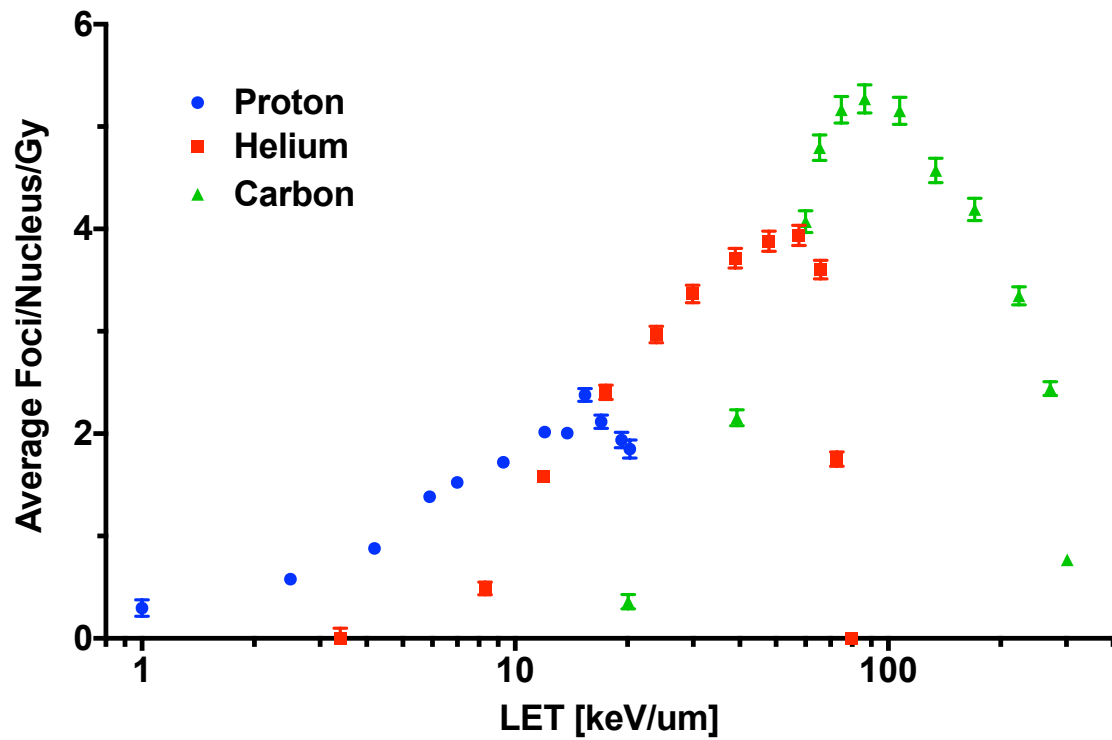


Figure 75. Dose-normalized persistent foci for proton, helium, and carbon ion beams. The dose-normalized persistent foci trends correspond with the RBEs at 0.1 SF. Error bars represent 95% confidence intervals.

## GSC high-throughput results

### Growth curves

To test the effect of proton radiation quality in an additional *in vitro* system glioblastoma stem cell (GSC) lines were chosen as a unique model of interest. GSCs are patient derived cell lines that grow as a spheroidal suspension. GS7-11, GSC300, or GSC23 single spheroids per well were formed using ultra-low attachment round bottom plates. The spheroids were exposed to proton radiation in the initial version of the high-throughput irradiation system with subsequent spheroid size measurements over a time course of approximately 30 days. The size measurements demonstrated an LET dependent increase in spheroid growth delay with increasing dose (Figure 76). Alternatively, the biological response mapping demonstrated that preventing spheroid regrowth required lower doses for high-LET (Figure 77). The spheroids were found to exponentially grow for smaller volumes (Figure 78). The spheroid growth was found to linearize for larger spheroid sizes, likely a result of hypoxia occurring at the core. The maximum spheroidal diameter typically achieved in control and low biological damage conditions was between 1.0 and 1.3 mm.

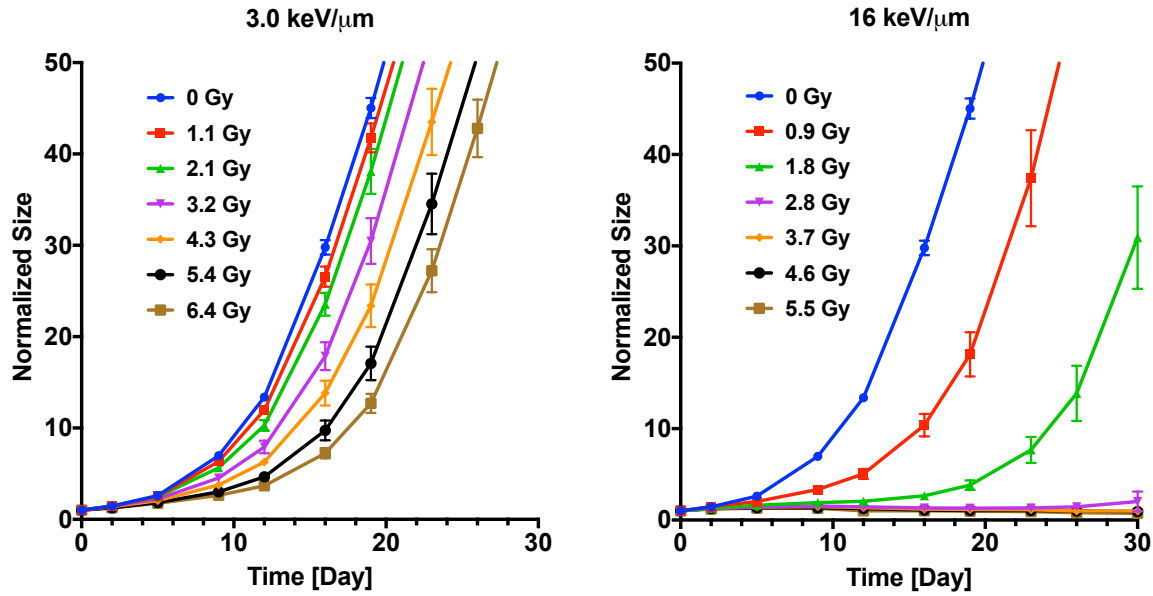
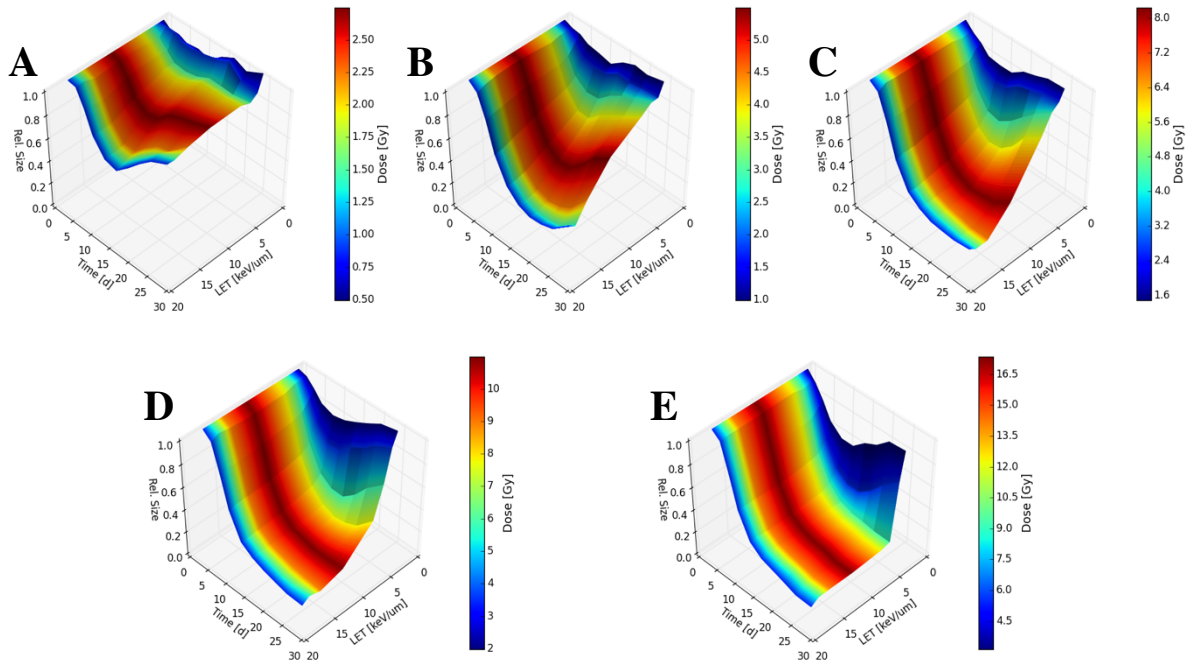


Figure 76. Representative GSC size measurements following irradiation with protons with the HT system. The growth response of GS 7-11 spheroids following irradiation with LETs of 3.0 and 16 keV/μm. Both conditions receive approximately the same dose per irradiation which was near half the peak dose. The spheroids subjected to the 16 keV/μm protons were found to have a larger growth delay as well as no growth at doses above 2.8 Gy. Complete growth prevention was not achieved even at a dose of 6.4 Gy for the 3.0 keV/μm condition. Error bars represent 95% confidence intervals.



*Figure 77. 4D representation of GSC23 response.* The surface plots demonstrate the technical changes faced when analyzing mapped biological responses with additional physical parameters. Peak doses in column 9 of (A) 2.75 Gy, (B) 5.50 Gy, (C) 8.24 Gy, (D) 10.99 Gy, and (E) 17.35 Gy were delivered to GSC23 spheroids using the initial jig design. The biological response was observed at lower doses for high LET protons. With increasing dose, the growth was prevented for both low and high LETs indicating the LOD of the assay had been reached. Plots were generated using matplotlib in the Python coding language with the assistance of Landon Wootton, PhD.

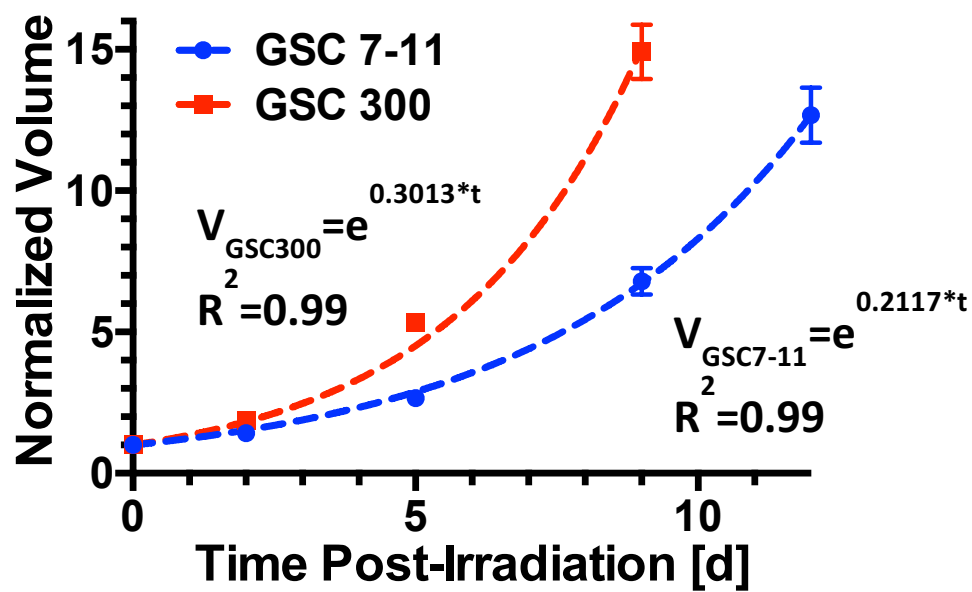


Figure 78. Growth constant calculations. Normalized GSC spheroid growth were fitted with a general exponential growth equation. Error bars are standard deviations (SD).

## Surviving fractions

Using the size measurements of control and irradiated spheroids, the resulting SFs were calculated by determining the cell line specific growth constant and the growth delay between the experimental and control conditions (99). For all GSC lines tested, irradiation with increasing LET was found to result in reduced clonogenic survival (Figure 79-Figure 81). The GSC SF data was fit to the LQ model (Table 11, Table 12). In general, column 8 (4.7 keV/ $\mu\text{m}$ ) exhibited increased survival compared to other conditions.

## RBEs

Using the LQ model fits to the SF data, RBEs at 0.1 SF were calculated for the GSC cell lines tested (Figure 82). As previously observed, the proton RBE was found to rapidly rise beyond the Bragg peak value of 10.2 keV/ $\mu\text{m}$ . The RBEs for the GSC23 cell line were calculated with a control radiation of 6MV x-rays whereas the reference source for GS7-11 and GSC300 was Cs-137. An additional RBE of 1.07 for Cs-137 was applied to the GSC data to normalize the results for comparison (Figure 83). The GSC RBEs for LETs less than 10 keV/ $\mu\text{m}$  were approximately 0.9-1.1. The RBEs for the distal portions of the proton beam (i.e. LET > 10 keV/ $\mu\text{m}$ ) were found to be in the range of 2-6.

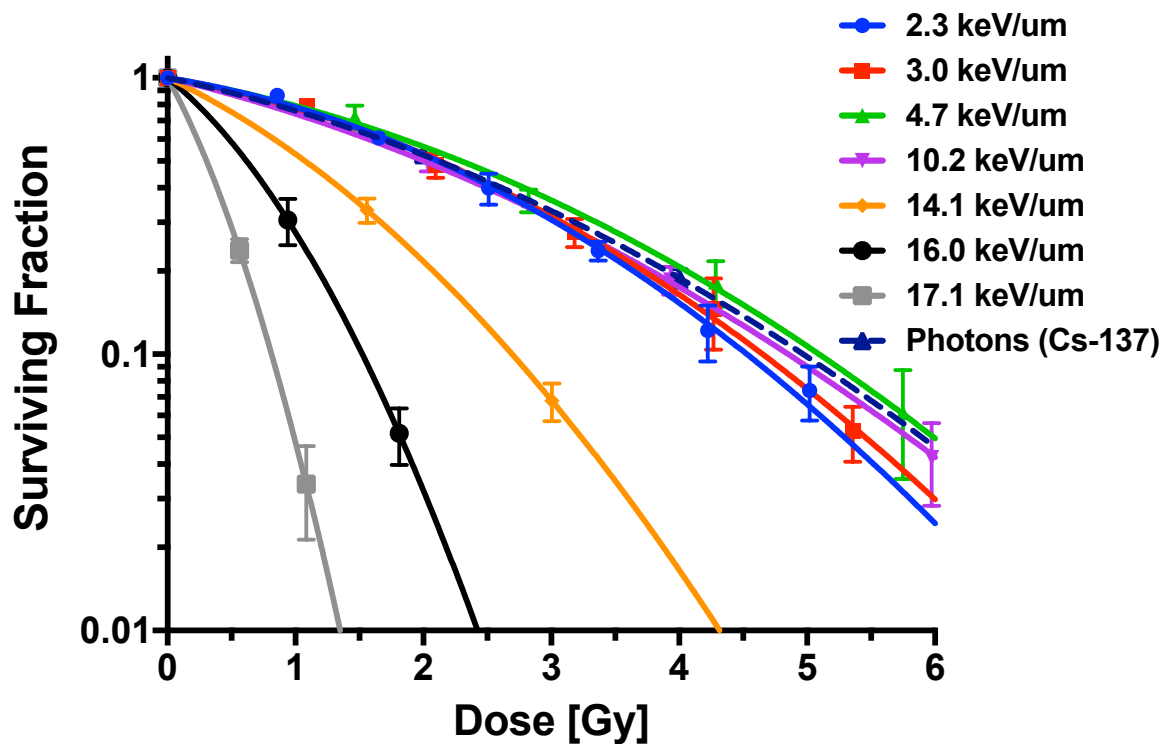


*Figure 79. GS7-11 SFs.* The SFs for the GS7-11 GSC line irradiated in the initial version of the HT irradiation setup were found to follow a similar trend as observed for the H460 and H1437 cell lines. SF was found to decrease with increasing doses. Cell kill was enhanced for proton LETs beyond the peak dose value of 10.2 keV/ $\mu\text{m}$ . Error bars are SD.

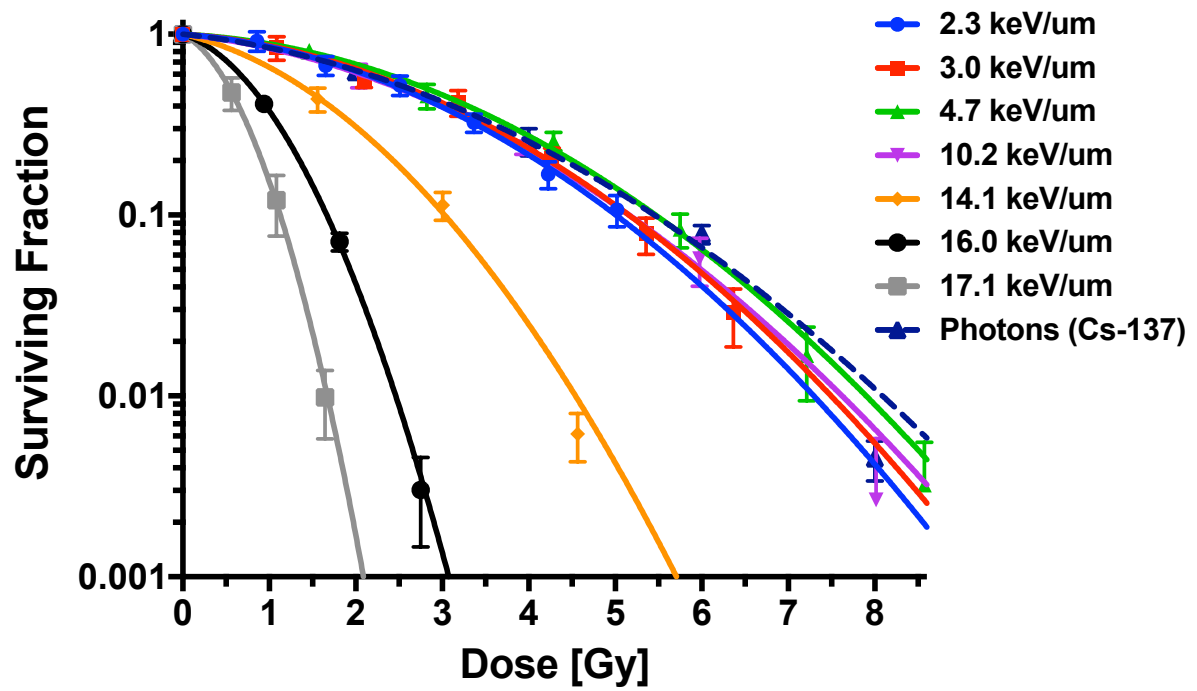


Figure 80. GSC300 SFs. SF reduction was increased by exposure to protons of increasing LETs. The GSC300 cell line was found to have a higher intrinsic radioresistance than the GS7-11 line as evident by the increased dose required to induce the same SF. Error bars are SD.



Table 11. GS7-11 and GSC300 LQ fitting parameters.

Cell line:	GS7-11				GSC300			
LET [keV/ $\mu$ m]	$\alpha$	$\beta$	$\alpha SE$	$\beta SE$	$\alpha$	$\beta$	$\alpha SE$	$\beta SE$
2.3	0.169	0.075	0.018	0.005	0.085	0.075	0.023	0.006
3.0	0.183	0.067	0.022	0.006	0.076	0.072	0.022	0.006
4.7	0.179	0.054	0.026	0.006	0.058	0.066	0.017	0.004
10.2	0.254	0.045	0.019	0.005	0.116	0.064	0.023	0.005
14.1	0.504	0.130	0.041	0.018	0.253	0.168	0.043	0.016
16.0	0.856	0.431	0.115	0.086	0.365	0.612	0.040	0.028
17.1	1.943	1.089	0.178	0.227	0.565	1.311	0.166	0.174
Photons (Cs-137)	0.226	0.048	0.015	0.005	0.119	0.056	0.020	0.004

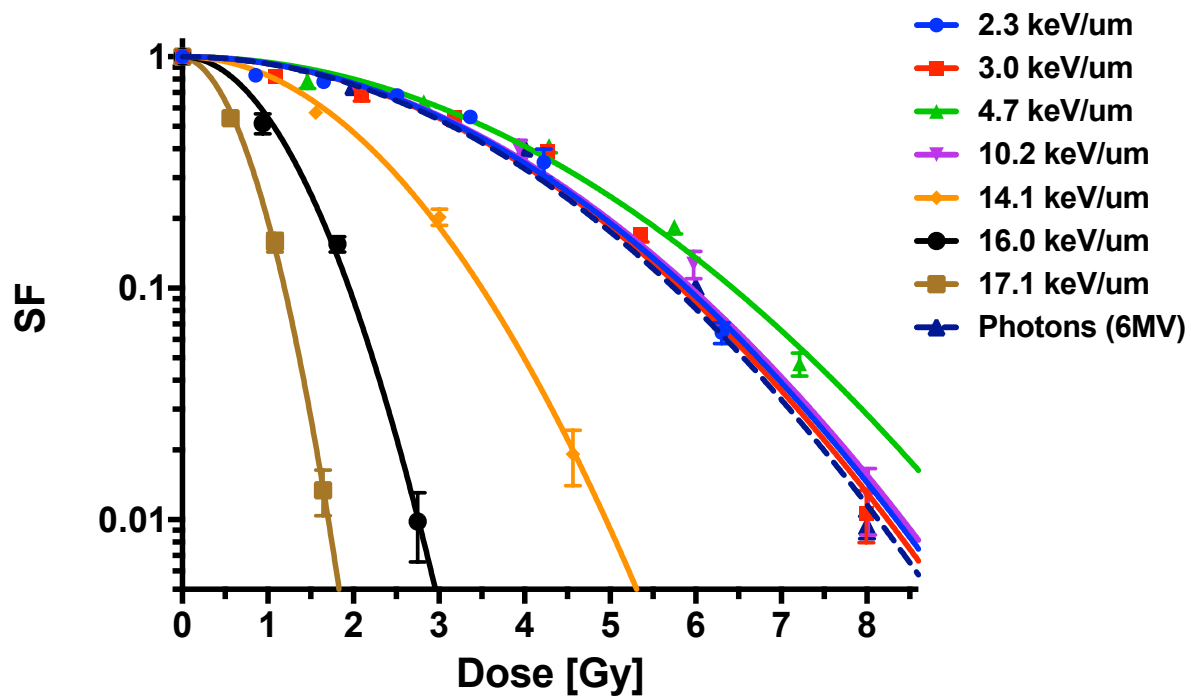
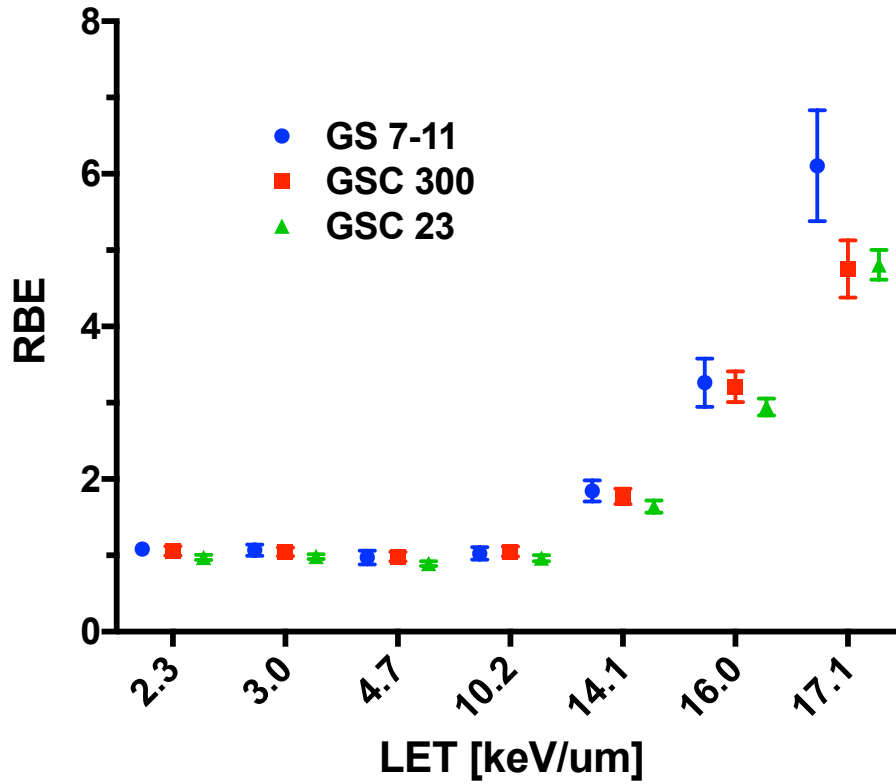


Figure 81. GSC23 SFs. SFs for the GSC23 cell line were obtained using the initial version of the HT irradiation apparatus and spheroid growth delay measurements. The SF was found to be significantly lower following high LET proton exposure. Error bars are SD.

Table 12. GSC23 LQ fitting parameters.

Cell line:	GSC23			
LET [keV/ $\mu\text{m}$ ]	$\alpha$	$\beta$	$\alpha$ SE	$\beta$ SE
2.3		0.066		0.003
3.0		0.068		0.003
4.7		0.056		0.003
10.2		0.065		0.004
14.1	0.000	0.188	0.042	0.009
16.0	0.000	0.606	0.079	0.057
17.1	0.123	1.510	0.091	0.063
Photons (6MV)	0.000	0.070	0.017	0.004



*Figure 82. GSC RBEs.* RBEs were calculated for the GSCs by taking the ratio of the dose of the respective photon control radiation to achieve an SF of 0.1 to the dose require for the assayed proton LETs to achieve the same response. The RBE for all GSCs used was found to be approximately 1 for LETs less than 10.2 keV/ $\mu$ m. The RBE was found to systematically rise for all LETs above this value. Error bars are SE.

*Table 13. Compiled GSC RBE values.*

LET [keV/ $\mu$ m]	RBE		
	GS7-11	GSC300	GSC23
2.3	1.08	1.06	0.97
3.0	1.07	1.05	0.99
4.7	0.97	0.98	0.89
10.2	1.03	1.05	0.96
14.1	1.84	1.77	1.64
16.0	3.26	3.21	2.95
17.1	6.11	4.75	4.81

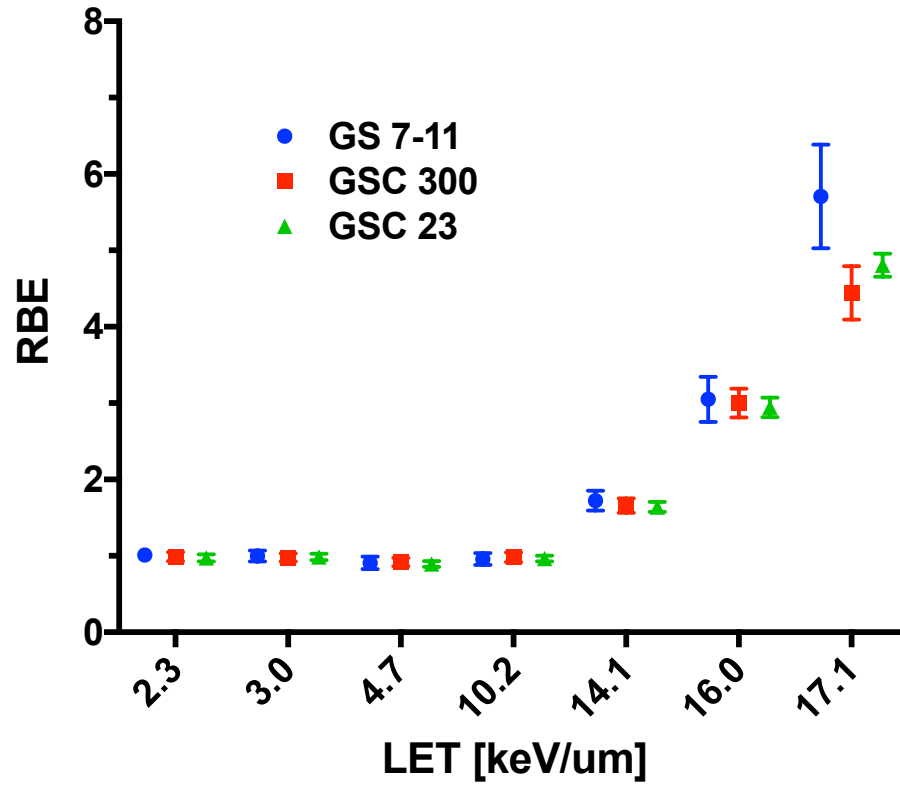


Figure 83. GSC RBEs with applied photon RBE. The control radiation for the GSC23 experiments was 6 MV photons; however, the control radiation for the GS7-11 and GSC300 cell lines was gamma rays from Cs-137. The calculated RBEs were adjusted assuming an RBE of Cs-137 of 1.07. Error bars are SE.

## Rat brain microtissue response to proton irradiation

### Size

Rat brain microtissues (RBMTs) were exposed to radiation of different qualities and followed by a longitudinal study of the size response. Control radiation was photons produced from the decay of Cs-137. Test radiations were protons with LETs of 3, 10, or 16 keV/ $\mu$ m. LET sampling was achieved using columns 7, 9, and 11 of the initial version of the high-throughput irradiation setup. Whole plates of RBMTs were not used due to the longitudinal nature of late effect studies for multiple conditions and the cost associated with the microtissues. The chosen LET conditions represent a broad range of proton LET as well as convenience of comparison as columns 7 and 11 receive half the dose of the peak dose in column 9 for each irradiation.

The size response of RBMTs exposed to the four irradiation conditions was followed for a period of 76 days (Figure 84-Figure 87). Non-irradiated RBMTs grew by a factor of 1.3 - 1.5 before stabilizing and maintaining their size for the remaining duration of the time course. Irradiated spheroids were found to stratify in a dose and LET dependent manner. Size reduction was found to correspond to exposure with higher doses resulting in larger decreases in size. After 40-50 days, a lower bound of approximately half the original spheroid size was seen in the size response as RBMTs receiving the largest doses did not go below this threshold for any of the tested irradiation conditions.

Comparing the size response of the four exposure conditions at 50 days post-irradiation demonstrated the decreasing size of the spheroids towards the lower bound of the response (Figure 88). The response characteristics were similar for the photon, low (3 keV/ $\mu$ m), and intermediate (10 keV/ $\mu$ m) proton LET conditions. The high LET condition (16

keV/ $\mu\text{m}$ ) approached the lower threshold size for much lower doses than the other conditions.

The size data at day 50 was fit to a four-parameter sigmoid model by non-linear regression with GraphPad Prism 7.0 (Figure 89). 50% response doses (D50s) were calculated from the fits and normalized to the Cs-137 response to determine the RBE of the different proton LETs (Figure 90). The RBE values were found to be 1.2, 1.4, and 5.9 for proton LETs of 3, 10, and 16 keV/ $\mu\text{m}$  respectively.

### Viability

Late term RBMT viability was assayed 55 days following irradiation using the RealTime-Glo MT Cell Viability Assay (Figure 91). Above 2 Gy, the viability signal of the photon, 3 keV/ $\mu\text{m}$ , and 10 keV/ $\mu\text{m}$  protons was found to be similar. The RBMTs exposed to 16 keV/ $\mu\text{m}$  protons had a significantly lower viability signal and reached a lower threshold value for lower doses than the other experimental conditions. Surprisingly, the viability trend was found to reverse between the 3 and 16 keV/ $\mu\text{m}$  conditions for the low doses tested near 1Gy. The raw viability data was fit to the four-parameter sigmoid model by non-linear regression with GraphPad Prism 7.0 to enable RBE determination (Figure 92). The RBEs for the proton conditions to achieve a 50% reduction in viability signal vs the Cs-137 condition were found to be 1.04 for 3 keV/ $\mu\text{m}$ , 1.07 for 10 keV/ $\mu\text{m}$ , and 3.65 for 16 keV/ $\mu\text{m}$  (Figure 93).



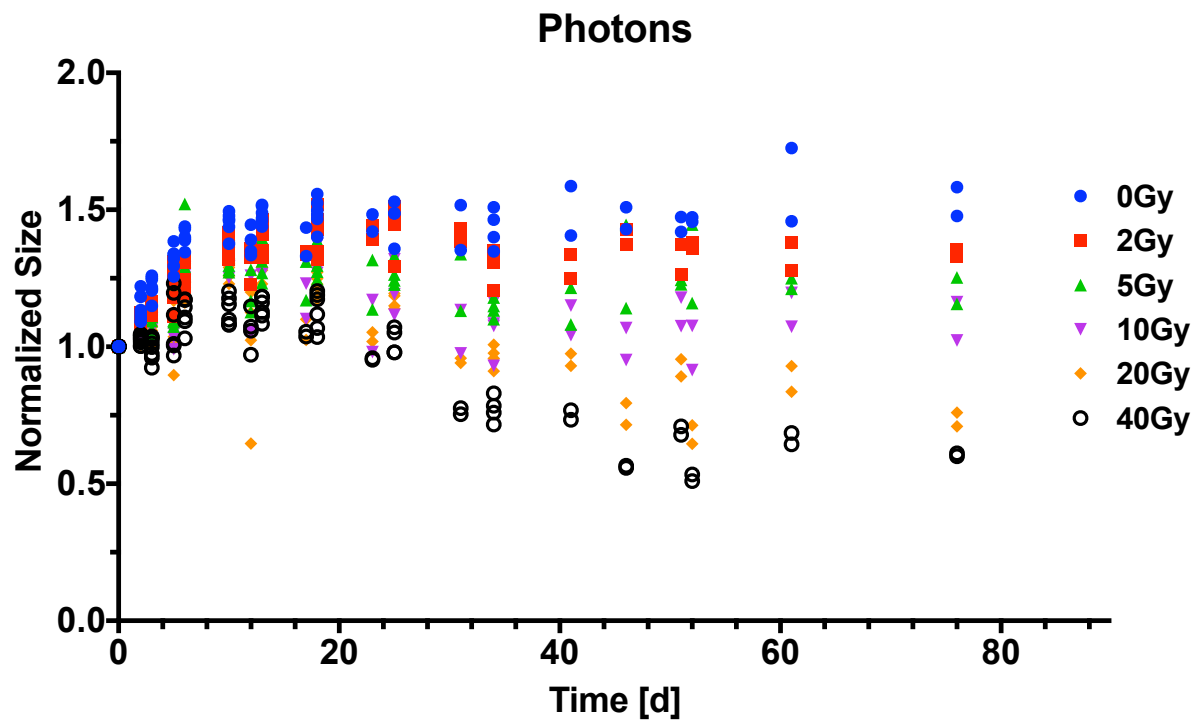


Figure 84. RBMT size response following exposure to photons produced by Cs-137.

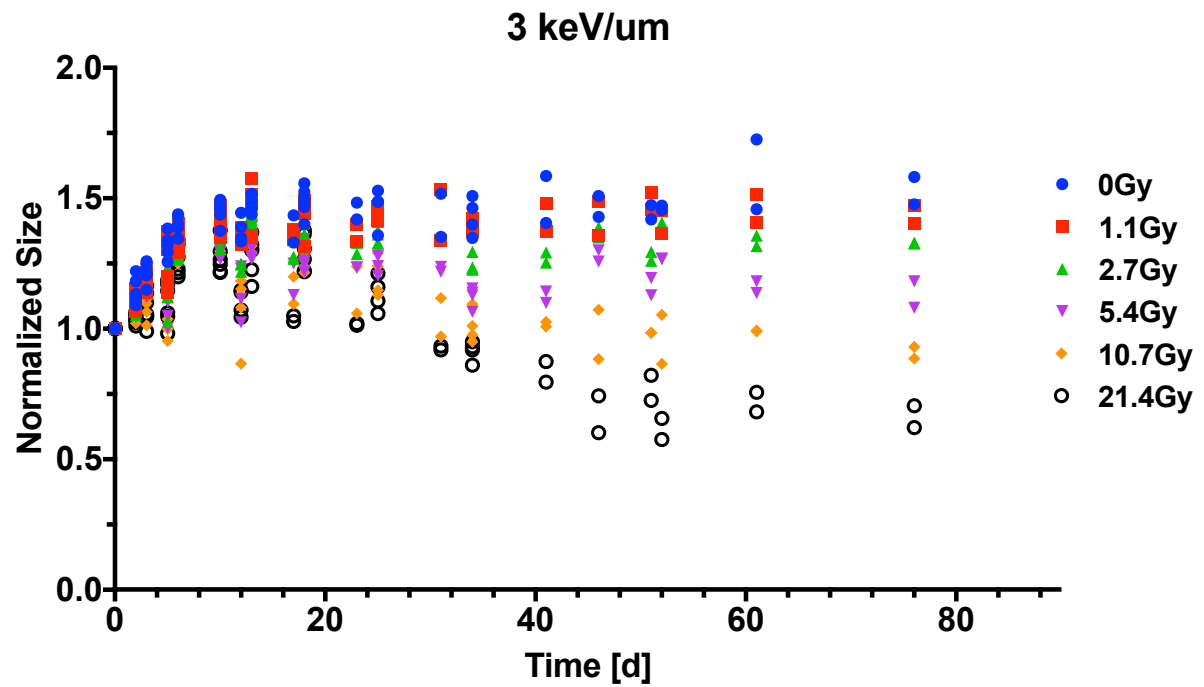


Figure 85. RBMT size response following exposure to 3 keV/ $\mu$ m protons.

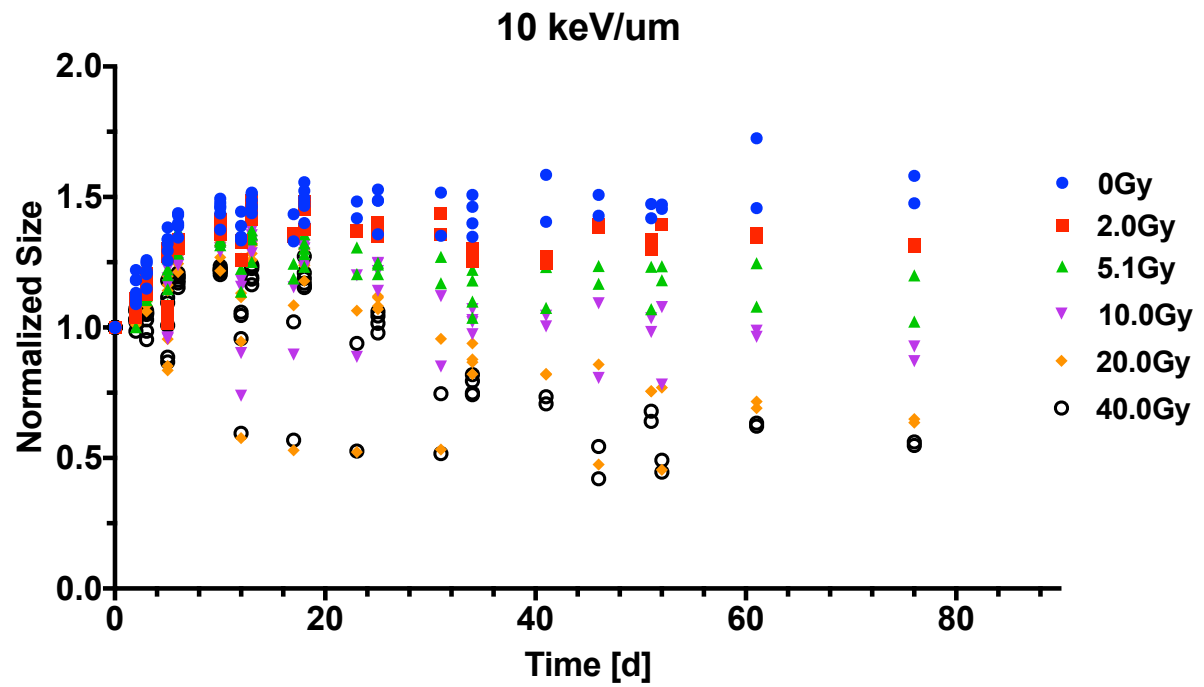


Figure 86. RBMT size response following exposure to 10 keV/ $\mu$ m protons.

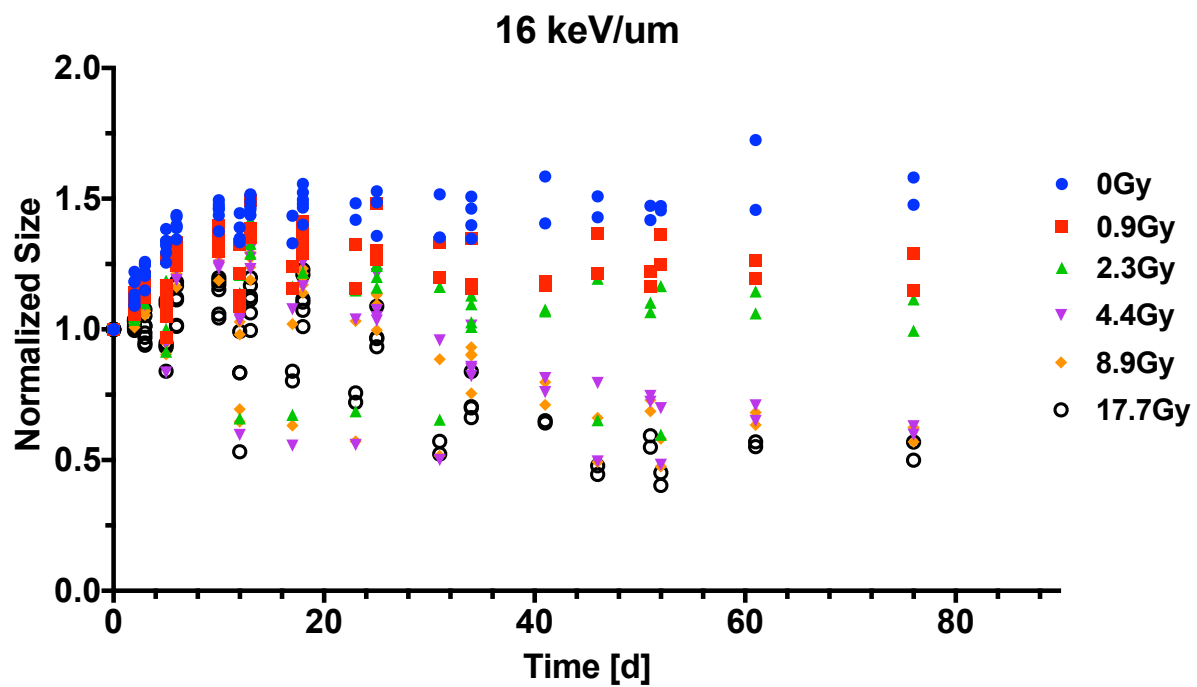


Figure 87. RBMT size response following exposure to 16 keV/ $\mu$ m protons.

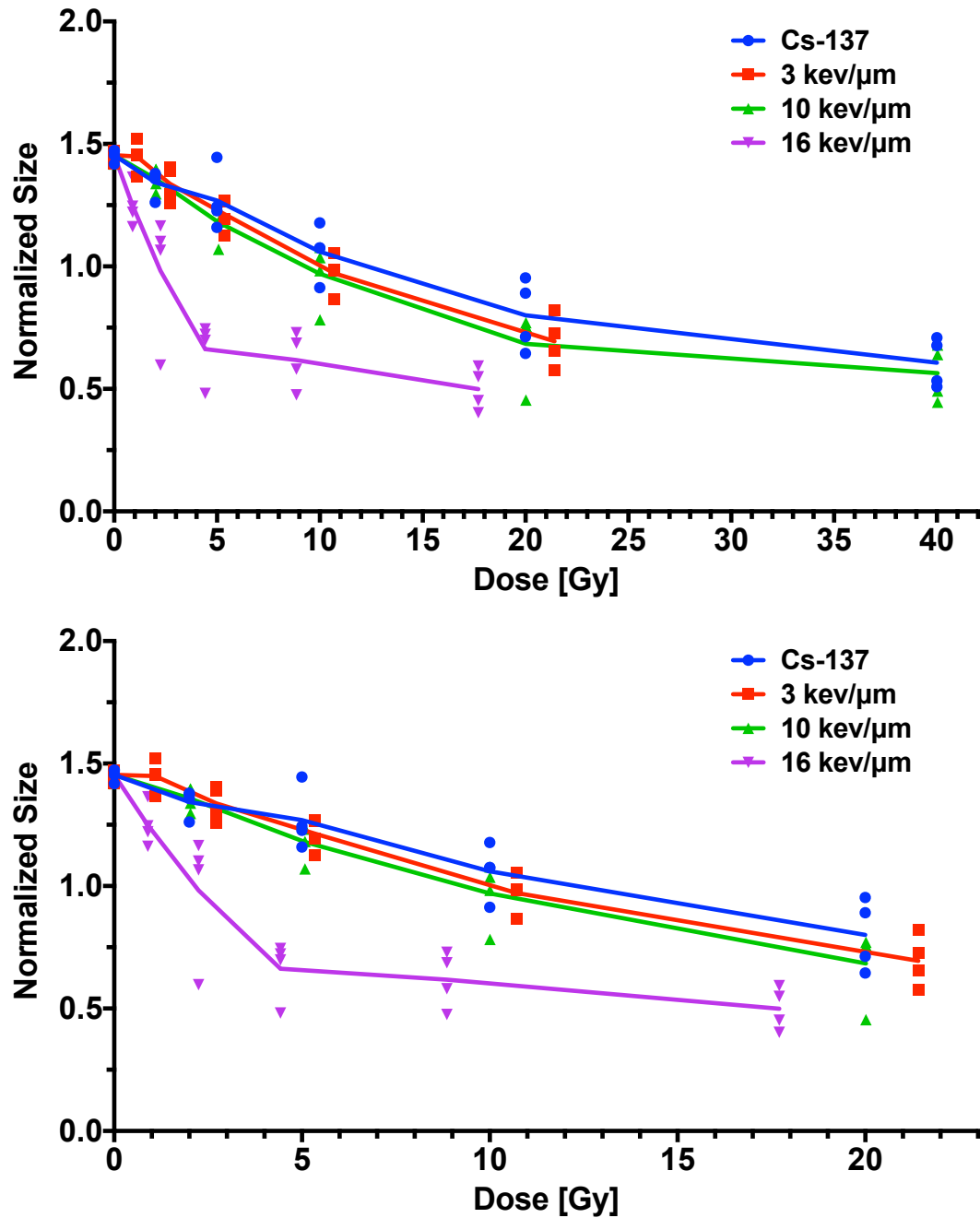


Figure 88. RBMT size comparison at 50 days post-irradiation. Size reduction was found for all RBMTs subjected to any form of radiation. The reduction was dose dependent. The Cs-137, 3 keV/μm, and 10 keV/μm conditions all demonstrated similar size reductions with dose and an overall linear reduction trend from 0 to 20 Gy. The reduction for the Cs-137 and 10 keV/μm from 20 Gy to 40 Gy demonstrated a reduced response rate towards the minimum size achievable. In comparison, the 16 keV/μm exposed RBMTs exhibited a relatively rapid size reduction achieving the minimum size at approximately 5 Gy.

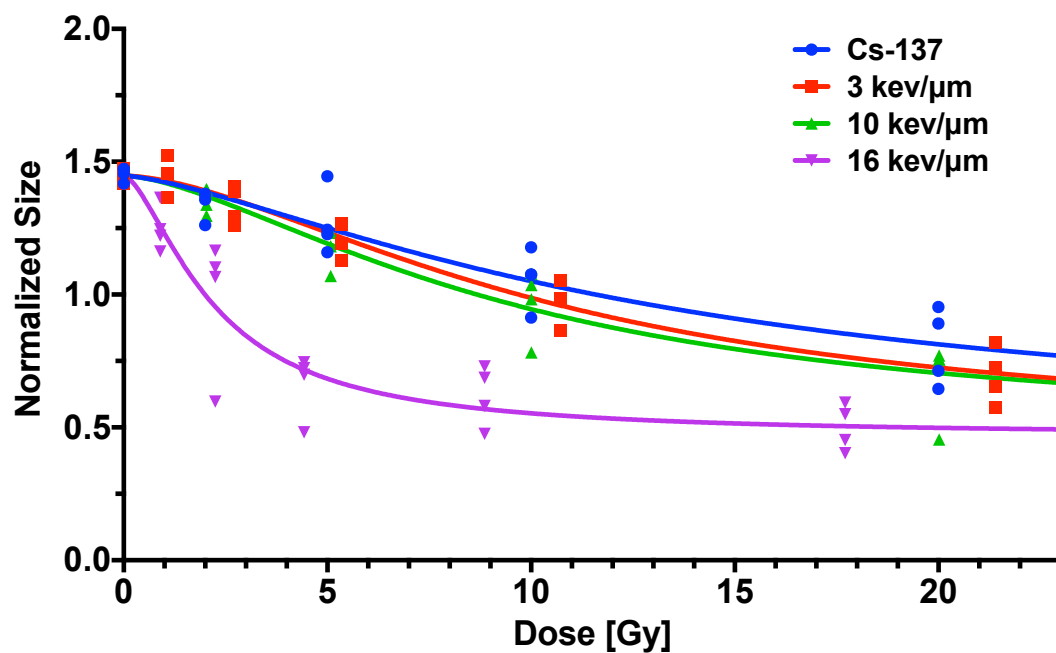


Figure 89. Fit to day 50 RBMT size data. The RBMT size data was fit to a four-parameter sigmoidal response model by non-linear regression to enable the comparison between the radiations by the calculation of the doses to achieve a 50% response (D50).

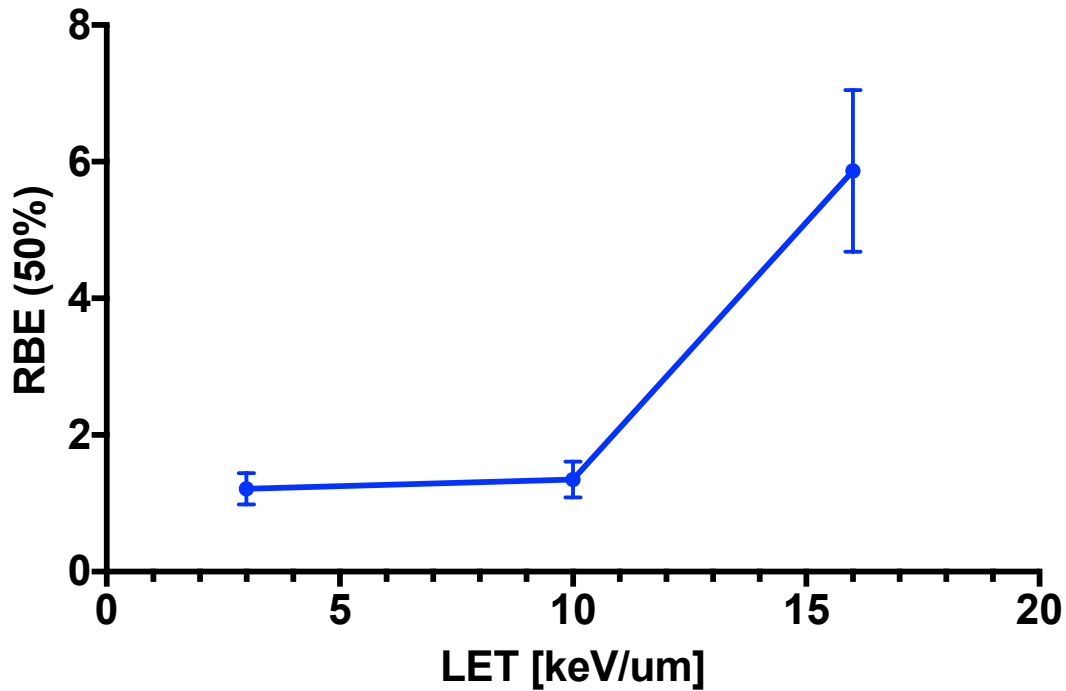


Figure 90. RBE at 50% of RBMT size. D50s were calculated for the terminal RBMT size response following exposure to Cs-137 photons, 3, 10, or 16 keV/ $\mu$ m protons. The calculated D50s were normalized to the value obtained for the Cs-137 condition to determine the RBE at 0.5 response. The observed trend was analogous to the RBE vs LET trends seen for the other model systems where the RBE gradually increased for LETs present in the proximal region of the beam ( $<10$  keV/ $\mu$ m) and then rapidly increased for the distal portion of the beam. The errors present are SE.

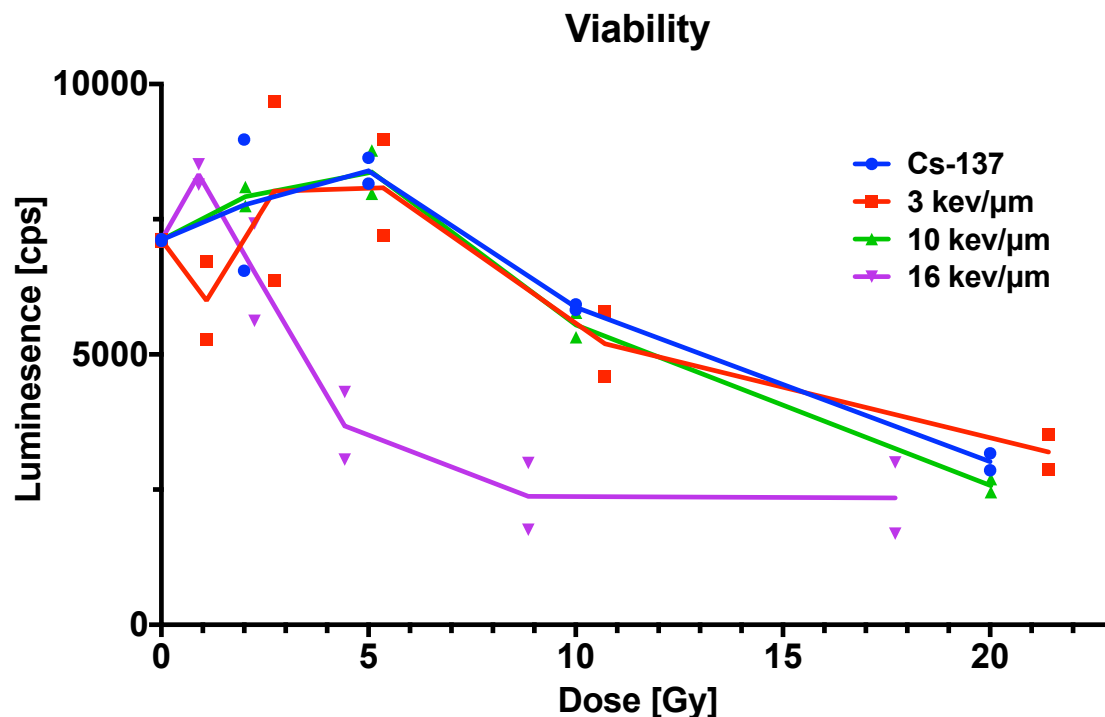


Figure 91. Viability of RBMTs following exposure to photons and protons with LETs of 3, 10, or 16 keV/μm. RBMT viability was assayed using the Realtime-Glo MT cell viability assay. The general viability trends were similar to those found by size measurements. The highest LET sampled, 16 keV/μm, was found to have an initial rise for a dose of 1 Gy followed by a drastic reduction to the minimum viability achieved. The other conditions tested were found to have similar responses with the exception of the 3 keV/μm condition irradiated to 1 Gy. This condition demonstrated a reduced viability signal at 1 Gy. For other doses tested, this condition was found to have similar values as the 10 keV/μm and Cs-137 irradiated RBMTs. The 3 and 10 keV/μm as well as Cs-137 irradiated RBMTs demonstrated an increased viability signal until 5 Gy. At doses higher than 5 Gy, the viability signal was found to decrease to the minimum value at 20 Gy.



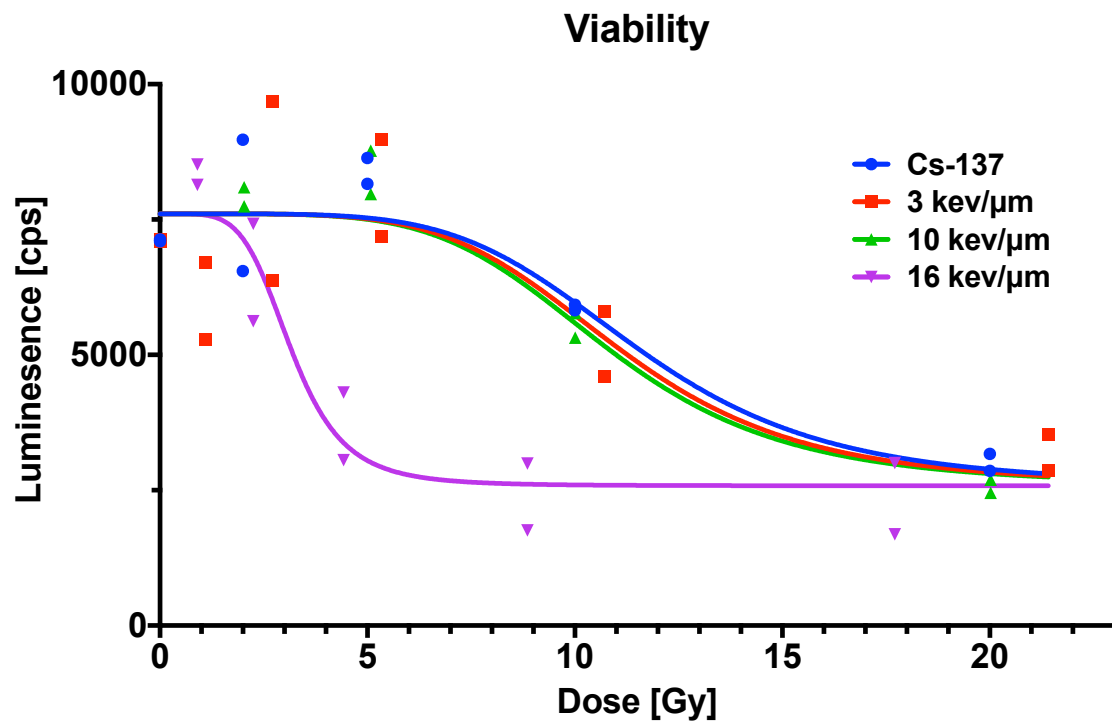
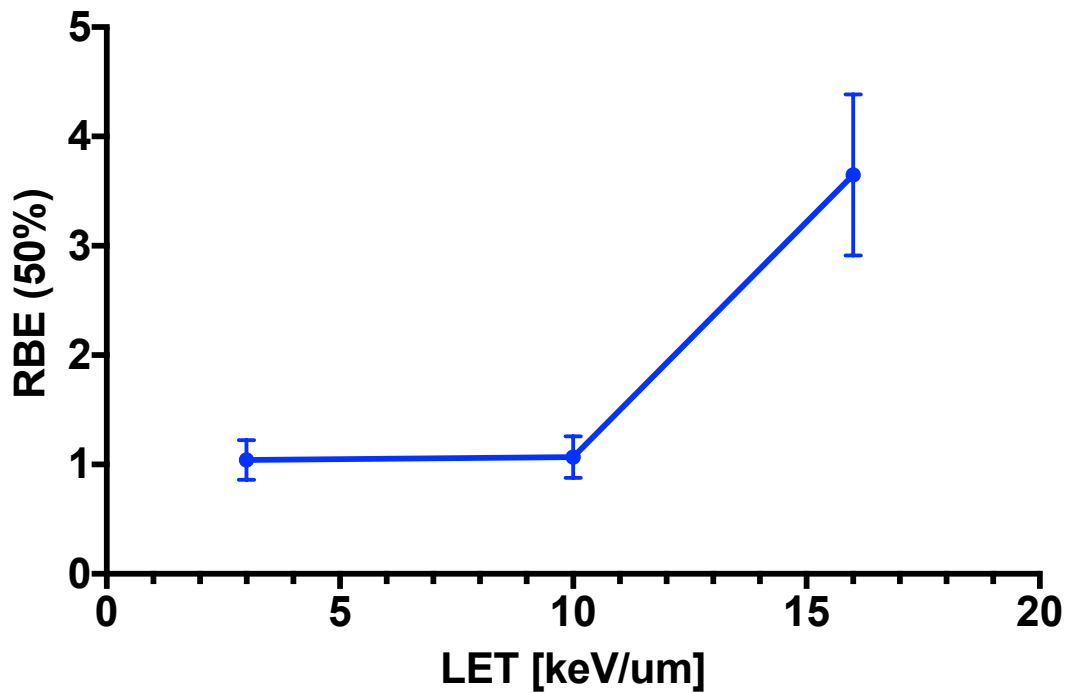


Figure 92. Response fit to RBMT viability data. The RBMT viability data was fit to a four-parameter sigmoidal response model by non-linear regression for calculation of the D50.



*Figure 93. RBE at 50% viability for RBMTs. Using the fits to the viability data, RBEs at 50% response were calculated compared to the response achieved from the Cs-137 group. A large increase in RBE was present for the RBMTs exposed to the 16 keV/ $\mu$ m protons. A modest RBE increase was demonstrated for RBMTs exposed to the 3 and 10 keV/ $\mu$ m protons. Errors are SE.*

## RBMT composition after radiation

### Immunofluorescent staining

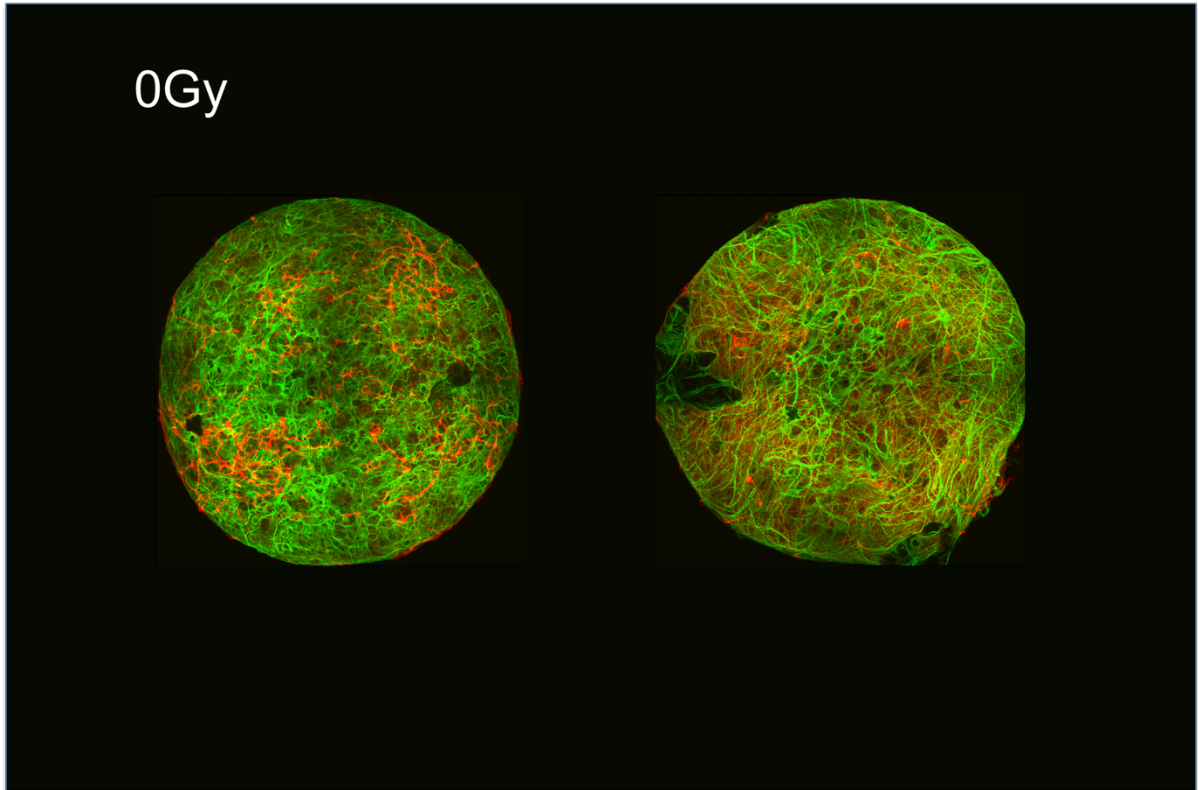
The bulk composition of RBMT spheroids 80 days post-irradiation was visualized with immunofluorescent staining of neurons and glia using the markers of beta-III tubulin and glial GFAP respectively (Figure 94-Figure 100).

The images for the RBMTs exposed to high LET protons demonstrated that for the lowest dose of 0.9 Gy, there was an increased expression of beta-III tubulin compared to the unirradiated control tissues. This effect was also present in one of the replicates for the 2.25 Gy exposure; however, the other replicate demonstrated a significantly lower expression. An increase in the beta-III tubulin expression was also observed for the low and intermediate LET protons at higher doses (2.75 - 5.35Gy) than for the 16 keV/ $\mu$ m protons but not in the Cs-137 irradiated replicates. For doses above 2.25 Gy for the 16 keV/ $\mu$ m protons and 5 Gy for the 3 and 10 keV/ $\mu$ m protons, the beta-III tubulin expression declined. The beta-III tubulin expression was found to continually decrease above 2 Gy for the photon condition. The beta-III tubulin expression appeared to be the same for all conditions as doses approached 20 Gy.

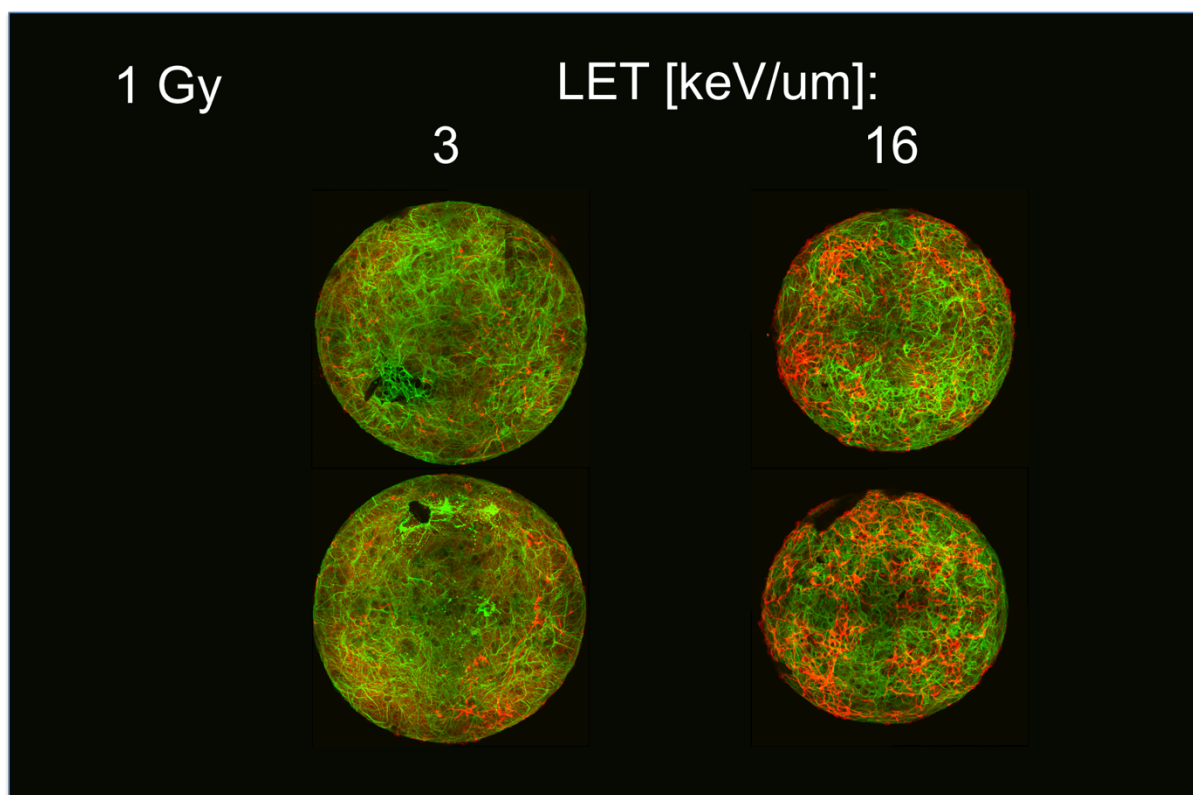
The GFAP expression was observed to generally decrease with increasing doses for all the tested radiation qualities compared to the non-irradiated control tissues. Exposure to increasing 16 keV/ $\mu$ m protons reduced the GFAP expression at a much faster rate than for the other conditions. The other irradiation conditions did not appear to achieve the low GFAP expression values reached by the 16 keV/ $\mu$ m protons.

Image analysis was performed by calculating the integrated pixel intensities of the images by thresholding the images using Fiji. This semi-quantitative analysis confirmed the

results achieved by manual inspection (Figure 101, Figure 102). However, this analysis found that the GFAP expression for the RBMTs exposed to 10 Gy of Cs-137 photons or 10 keV/ $\mu\text{m}$  protons increased from previous dose level of 5 Gy before further reduction.



*Figure 94. Immunofluorescent staining of unirradiated control RBMTs at 80 days.*



*Figure 95. Immunofluorescent staining of RBMTs at 80 days following exposure to 1Gy.*

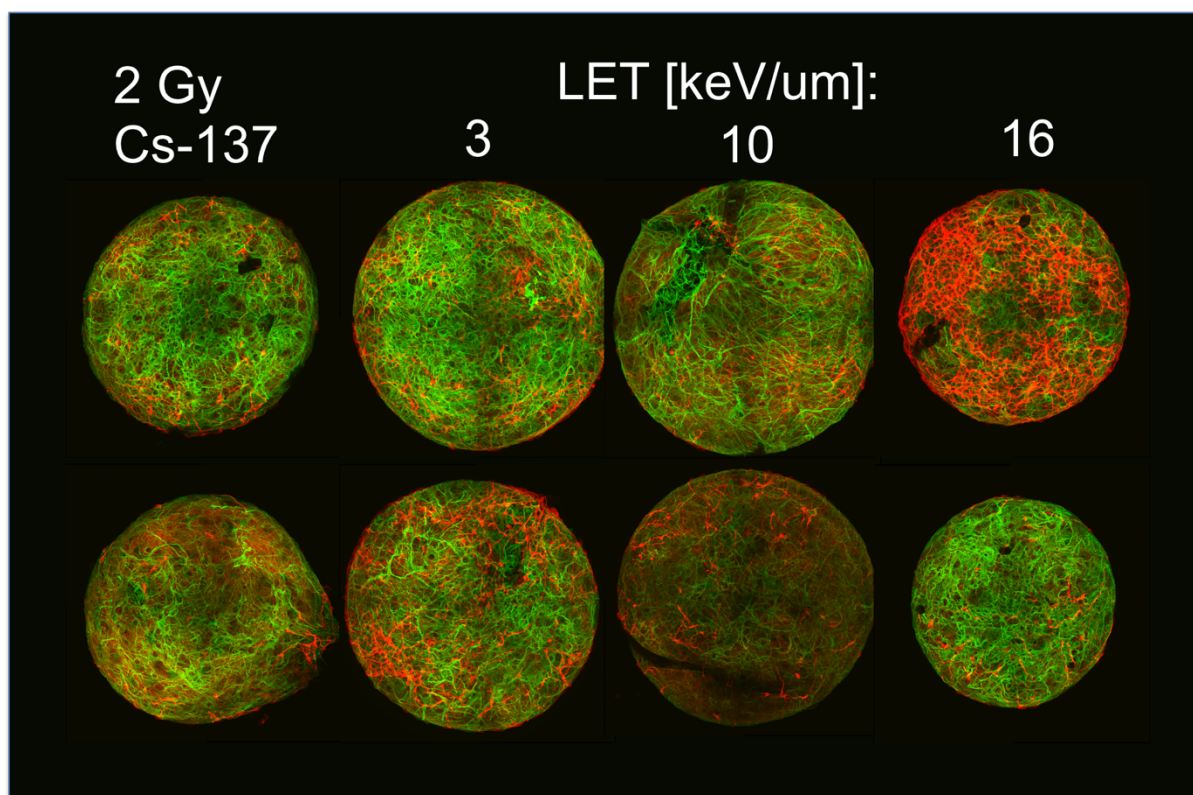


*Figure 96. Immunofluorescent staining of RBMTs at 80 days following exposure to 2Gy.*

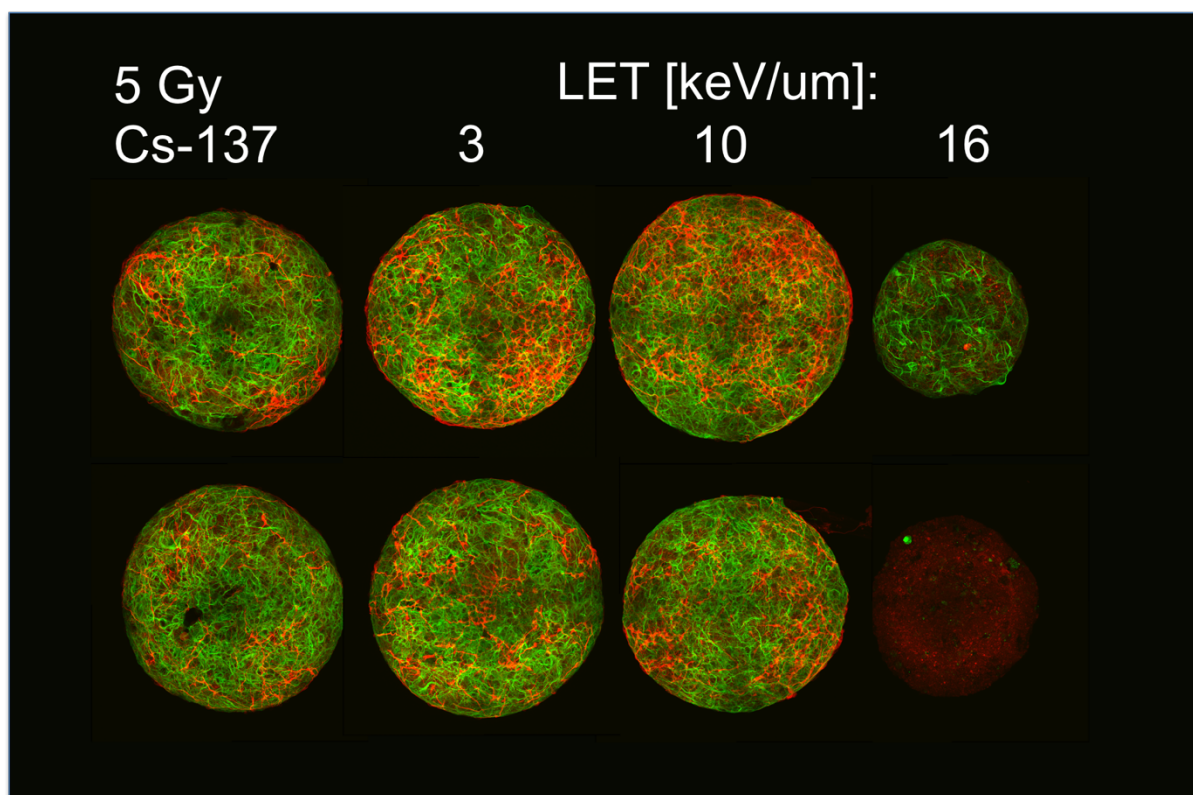
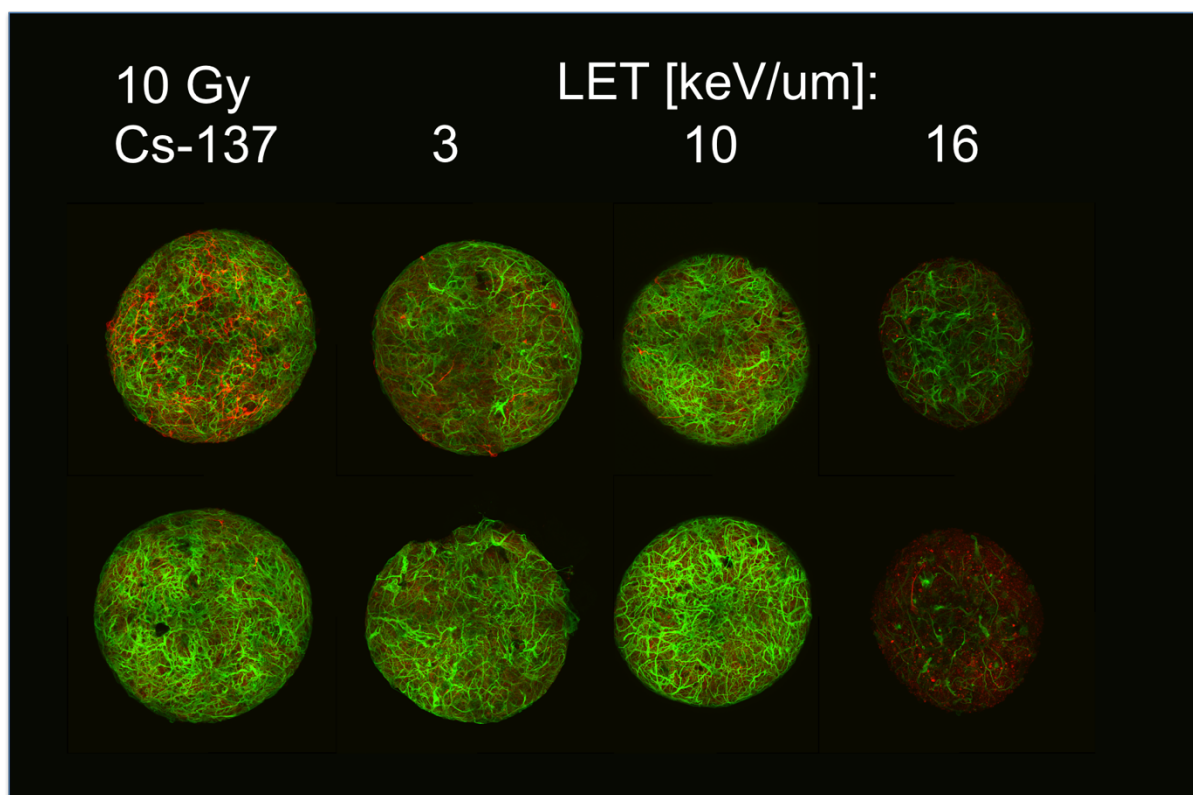
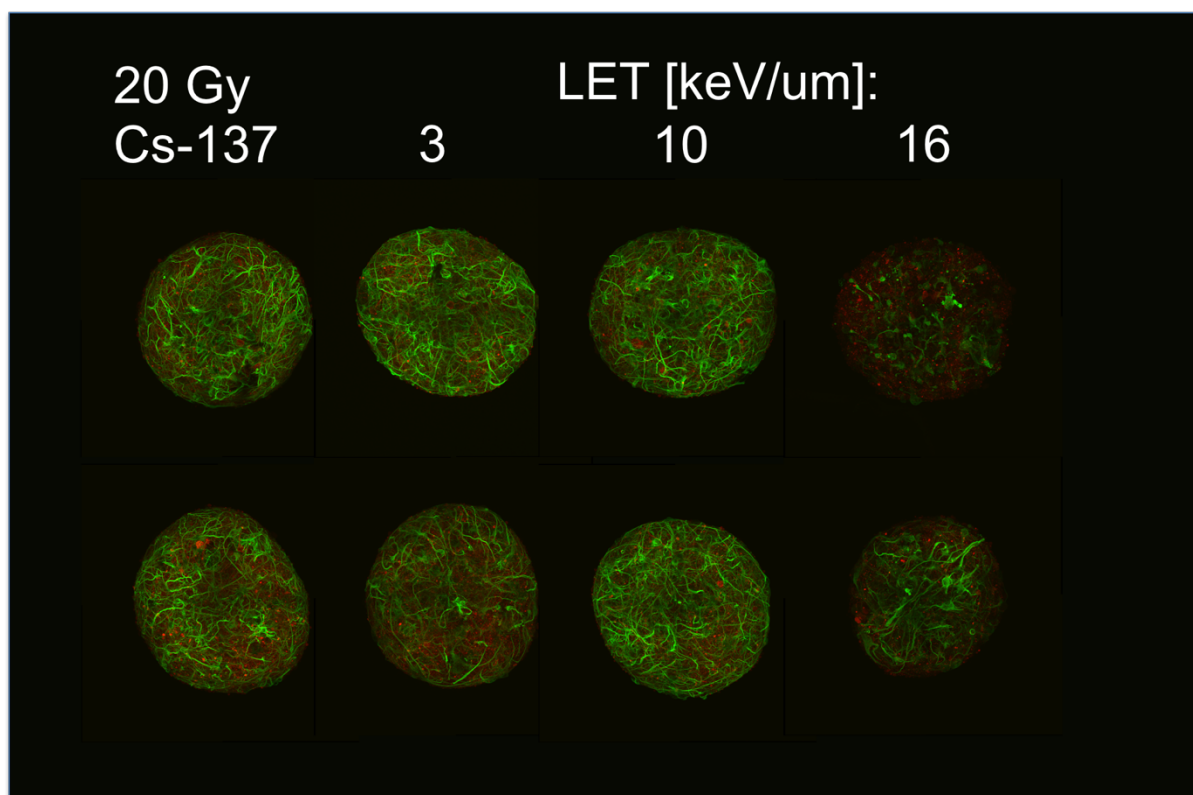


Figure 97. Immunofluorescent staining of RBMTs at 80 days following exposure to 5Gy.





*Figure 98. Immunofluorescent staining of RBMTs at 80 days following exposure to 10Gy.*



*Figure 99. Immunofluorescent staining of RBMTs at 80 days following exposure to 20Gy.*

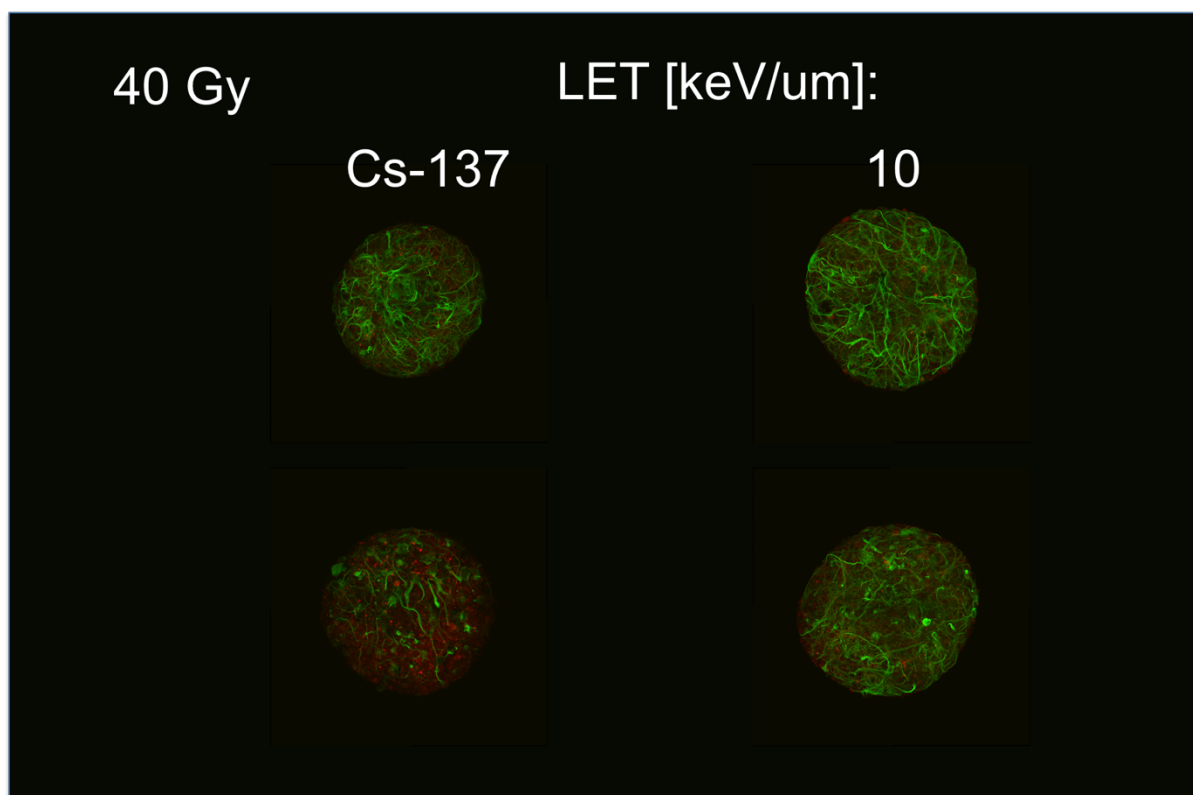


*Figure 100. Immunofluorescent staining of RBMTs at 80 days following exposure to 40Gy.*

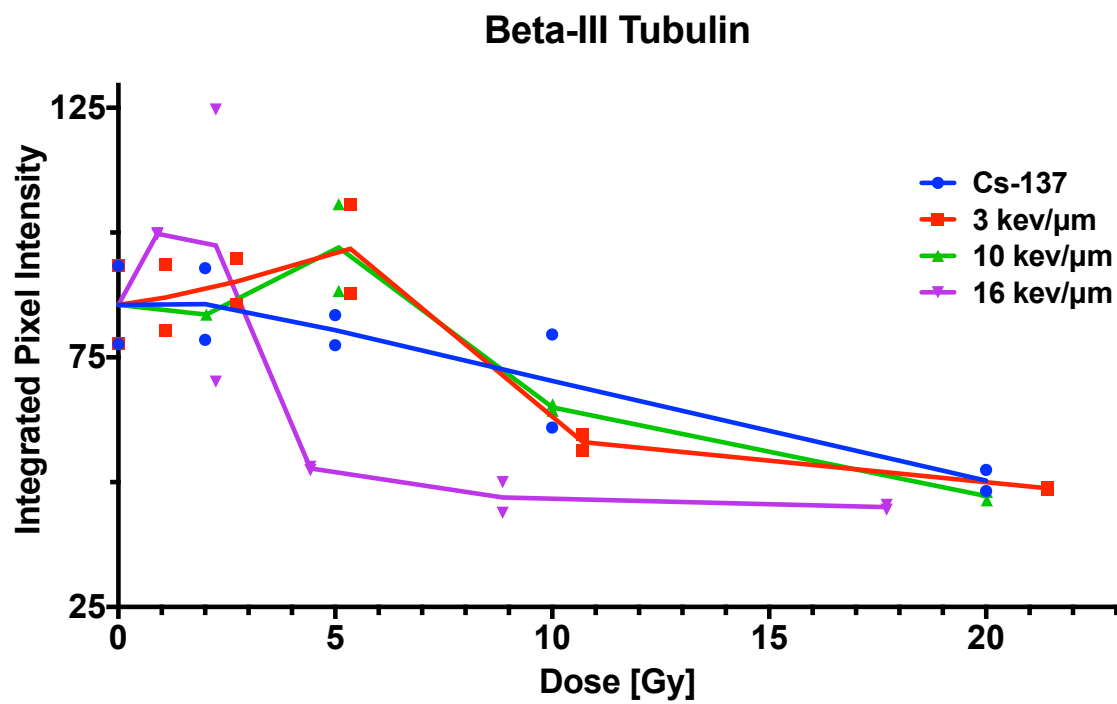
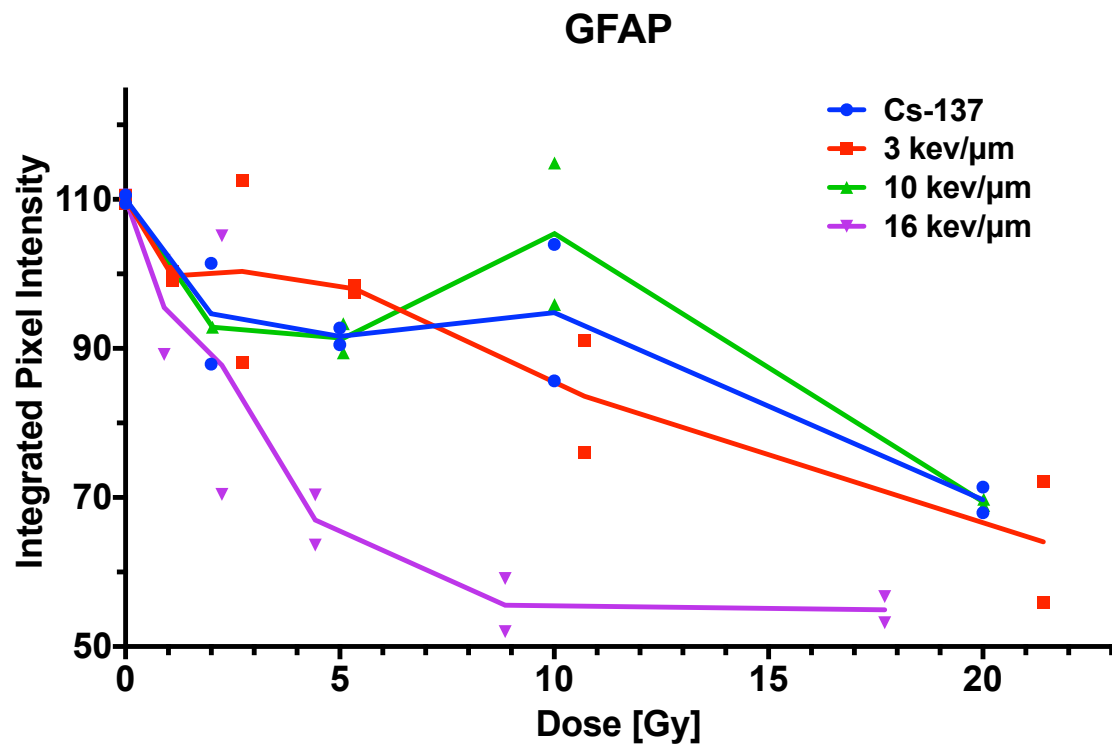


Figure 101. Quantification of beta III tubulin expression. Semi-quantitative analysis of the RBMT  $\beta$ -III tubulin expression indicated that the response is related to the viability results observed.



*Figure 102. Quantification of GFAP expression. Preliminary results indicated a reduction in GFAP expression with increasing dose. Additionally, a reduction in GFAP expression achieved by the 16 keV/μm was found.*

## Discussion

This work establishes the methodology to design and apply generalized screening techniques with the purpose of achieving a dramatic increase in the quantity and quality of data acquired from charged particle beam irradiation experiments. This dissertation presents the results obtained using the developed high-throughput (HT) irradiation apparatus in three biological effect model systems. In each of the model biological systems utilized, all endpoint results demonstrated a non-linear trend in RBE and proton LET. Although recent studies have indicated that RBE and LET scale linearly, our results suggest that the relationship between LET and biologic effect may not be so straightforward and suggests the need to account for such effects proactively in the treatment planning process (9, 101, 102).

The overall goal of this work was to increase the quality and speed of obtaining particle beam radiobiological data. To the author's knowledge, no other studies have demonstrated a comprehensive method of applying high-throughput techniques to map the biological effect of charged particle radiation. However, when developing an iterative improvement on established methods, it is imperative to place the results in the proper comparative context. In this regard, other groups have performed similar rigorous studies using the lower-throughput, traditional methods to assay biological effects along charged particle beams (16, 101-103). Furthermore, these studies have been indexed in comprehensive reviews and databases such as the particle irradiation data ensemble (PIDE) (5).

Before placing our results in the context of the literature, it should be noted that the experimental results obtained for the H460 cell line with exposure to photons of differing energy spectra demonstrate that the selection of control radiation can have a significant

impact on the overall reported results. Additionally, the biological endpoint selected for SF and RBE calculation can affect the results (49). RBEs for particle radiations presented have been calculated at 0.1 SF compared to Cs-137 photon irradiation. The selection of Cs-137 as the control radiation for this work was due to convenience. Experimental irradiations typically took place from late night to early mornings or over the weekends (or both). As such, access to a clinically used linear accelerator was limited compared to the preclinical biological irradiator. RBEs at 0.1 were calculated in correspondence with the most common value observed in the relevant literature.

For the H460 and H1437 adherent cell lines exposed to proton radiation, the measured RBEs in the distal falloff region of the beam are considerably higher than those typically reported in the literature as well as the clinically used value of 1.1. However, as previously mentioned there is a large spread in proton RBE results in the literature. As such, the RBE values obtained with the HT system fall within the range of the spectrum of values that have been reported (8, 9, 104). Similar RBE values to our data were observed by Chaudhary *et al.* in the human cell lines AG01522 and U87, derived from fibroblasts and glioblastoma, respectively (101). Similar to the presented results, the relationship between RBE and LET in this work appears supralinear. This trend was especially evident for the human glioblastoma U87 cell line at RBEs calculated for a 0.5 SF.

The general trend measured between RBE and LET and absolute values for helium and carbon ions are similar to the literature values compiled within the PIDE 2.0 database (5). In both helium and carbon irradiations, the overkill effect, a reduction in biological effectiveness at high LET, was noted to occur for the highest LETs tested for each particle, an effect not observed in any of the proton experiments. For helium ion irradiations

performed at HIT with the HT system, the maximum RBE was measured at 52.6 keV/ $\mu$ m. This result is significantly lower than published literature values. Tracy et al. measured as well as compiled published RBE(0.1 SF) for mammalian cells exposed to He ions (105). Within their work, they measured a maximum RBE at 131 keV/ $\mu$ m in V79-4 cells. Folkard et al. found a maximum RBE at 88.3 keV/ $\mu$ m for V79 cells (106). Furusawa et al. did not achieve overkill with He ions in V79 or HSG cells for maximum LETs tested of 90.8 and 71.0 keV/ $\mu$ m respectively (107).

For carbon ions, the maximum RBE was measured at an LET of 90.4 keV/ $\mu$ m. This value is also lower than measured by previous studies. Weyrather et al. measured a maximum RBE in CHO and V79 cells at 153.5 keV/ $\mu$ m (108). For V79 and HSG cells Furusawa et al. measured the maximum carbon ion at 137 keV/ $\mu$ m. For T1 cells the maximum RBE inflection point was measured at 109 keV/ $\mu$ m (107).

The lack of overkill effect for the highest proton LETs measured in the HT irradiations is not unexpected as the overkill effect for protons is expected to occur for LETs greater than 20 keV/ $\mu$ m. The literature examining the exposure of cells to proton LETs above the 20-23 keV/ $\mu$ m range is limited. Published results with proton LETs higher than this range utilized a Van de Graff generator to produce low energy protons. Belli et al. reported a maximum proton RBE(0.1 SF) for 30.5 keV/ $\mu$ m protons in V79 cells (109). Overkill was observed for the higher LETs tested, 34.6 and 37.8 keV/ $\mu$ m. Folkard et al. exposed V79 cells to proton radiation with LETs of 10.1, 17.8, and 27.6 keV/ $\mu$ m (106). Consistent with the Belli results, the overkill effect was not observed as the corresponding RBEs were measured to be 1.25, 1.40, and 1.91.



Determining the underlying mechanisms behind the observed differences between the presented RBE vs LET results, particularly for the higher LETs present within a given particle type, is a complex task. A possible explanation for the observed differences between the literature and the presented RBE vs LET results could be variations in the experimental setups utilized. Much of the data available for high LET interactions within the literature were measured with either non-clinical Van de Graff generators or cyclotrons which produce beams with very narrow energy spectra. Other data points have been measured with clinical setups utilizing SOBPs which serves to broaden the energy spectra at a given location within a beam. The current work utilizes a system that falls in the middle of these two experimental setups. An additional confounding factor is the simulation parameter setups used to calculate dose and LETs between the numerous groups studying charged particle RBE. It has been shown that even in the simplest geometry of a homogeneous water medium that different MC packages will calculate different dose and LETs (110).

LET effects aside, an additional consideration for RBE comparison is inherent sensitivity to particle radiation. While there are many data points for the various charged particles under study for use in cancer treatments, many studies have used either non-human or non-cancer derived cell lines. While the DDR is highly conserved pathway between species, the mutations carried by cancer cells result in an increased amount of variation in the response space. Using a panel of 17 NSCLC cell lines, Liu et al. recently displayed a large spread of RBEs measured at the mid-SOBP of a clinical proton beam (111). Cancer cell lines derived from human cells, the same type of cancer, and irradiated under the same conditions exhibited strikingly different RBEs.

The high-throughput clonogenic methodology is subject to the inherent as well as unique constraints compared with traditional clonogenic assay techniques. For the general clonogenic assays methods, we attempted to remove and minimize possible artifacts. Semi-automated, pre-plating was used to quickly seed all cells from a single stock solution within 10-15 minutes. The use of a single seeding solution per experiment results in a single multiplicity correction (42, 43). A single stock solution also reduces the number of counting uncertainties present within a given clonogenic experiment to the minimum value of one. Complicating biological processes from cellular manipulation were minimized from the readout of colony formation by pre-plating the cells.

The largest difference to consider when performing the clonogenic assay in a 96-well microplate is the well growth area of a standard 96-well plates is considerably smaller than a 6-well plate, petri dish, or flask. This reduced area effectively limits the number of cells that can be seeded for colony formation in a cell line specific colony morphology-dependent manner. Only cell lines that form distinct colonies can effectively utilize the limited growth area. The maximum number of cells that can be seeded without substantial colony overlap in high-SF plates is limited to approximately 200 (112). The seeding density limitation restricts the range of measureable SFs, making achievable doses cell line-dependent. This obstacle may be possible to circumvent for some cell lines by altering the seeding density within each well based on the expected cell kill as is done in the traditional clonogenic assay (113). Our attempts to increase the seeding density beyond 250 cells per well for the H460 and H1437 lines resulted in a population of quiescent cells that were found to limit and obscure colony growth. Additionally, we desired to avoid any cell seeding density effects on the results and as such utilized a constant seeding density.

Throughout the course of this body of work, it has become evident that immunofluorescent techniques and the HT system are well suited for use together. The relationship between the HT measured RBE at 0.1 SF and the number of persistent DSB induced per Gy are well correlated indicative of the casual nature of the relationship. Many of the issues present for the HT clonogenic are not problematic with the use of immunofluorescent assays. Rather, with immunofluorescence assays, the largest obstacle (aside from the increased material cost) is the increase in the amount of data generated per irradiation. Analysis of considerably large image datasets requires automated analysis software. The initial setup and benchmarking of automated software is time consuming. However, once developed, the analysis recipe can be easily shared, and if robust, applied to additional experiments (114-116). Images with artifacts effecting automated scoring need to be reduced and removed from the overall tallied results. As the number of conditions increases, the time spent manually verifying results becomes unreasonable. Improvements in machine learning algorithms are already reducing the time needed for automatic scoring implementation with a higher accuracy than previous static iterations. Additional applications of immunofluorescent labeling techniques may also be useful in future experiments to determine persistent foci for time points later than 24-30 hours post-irradiation. It has recently been shown that the relative change in the number of DAPI- stained nuclei in such studies correlates well to SF (117). This approach coupled with the high-throughput irradiation method could be used to simultaneously perform mechanistic studies and determine RBE. Furthermore, the combination of these methodologies would eliminate susceptibility to the colony size limitation present with the HT clonogenic assay enabling the use of cell lines previously unsuitable for the HT clonogenic assay.

There is evidence in the literature indicating differential DSB repair pathway utilization following irradiation with protons or carbon ions. However, contradictory findings in relation to the effects of irradiation with increased LET on the DSB repair pathway have been reported (118, 119). In future HT mechanistic studies, markers downstream of the initial damage response may be utilized to differentiate between the DNA repair pathways to validate and further elucidate the LET-dependence for the formation of persist foci. Markers of particular interest would be DNA-PKcs for NHEJ and Rad51 for HR.

The current application of spheroidal cancer cell line cultures utilizes the HT irradiation methodology at the expense of multiple colonies per well. However, this method demonstrates an increase in throughput when compared to previous studies where GSC clonogenicity was measured using single cell per well dilutions. The size distributions measured within each experimental condition showed little variation between replicates.

Our work utilizing rat brain microtissues is unique in that the toxicities in normal tissues following radiation have been understudied because methods to do so are limited. In terms of late effects associated with brain irradiation, cognitive impairment receives the most attention (120). Furthermore, there are very few studies examining normal brain tissue response following exposure to charged particle radiation. Studies demonstrating the response of photon radiation on neuronal cultures are more numerous, and there are a few sources in the literature for particle beams (121, 122). These studies do not account for the presence of additional cell types making up the neuronal microenvironment and the subsequent interactions following radiation insult. In the context of more advanced *ex vivo* studies, organotypic slice cultures have been used to study the normal brain response (123, 124). General results with these models are in agreement with the findings reported in this

work. However, additional studies will need to be performed to determine the induction and progression of radiation therapy toxicities such as necrosis.

For the proton RBE studies involving size based measurements, the RBEs for LETs  $>10 \text{ keV}/\mu\text{m}$  in GSC and RBMTs are higher than those found when using adherent or other biological endpoints. This is an unexpected finding as LET effects are expected to diminish over larger target volumes. The concept of LET is problematic for spheroids because their geometry is not conducive to the calculation of particles crossing two parallel surfaces.

While our work demonstrates high reproducibility between repeated experiments under the same conditions, the effect of the MC simulations on the dose and LET calculations needs to be carefully considered. The simulation ultimately affects the experimental results found by altering the independent axis of the experiments. Within this work, there was a difference noted between the HT proton irradiations performed at MDA and HIT. This feature is the result of the differences in MC implementation between the experiments. When the MC simulations utilize the same setup parameters, the results and trends are found to be a significantly closer match. Thus, the dose and LET calculations derived from the MC simulations are potentially problematic due to limited knowledge of the physical description of particle interactions, especially at low energies and for materials aside from water. As all current iterations of the high-throughput irradiation apparatus have been constructed with Lucite, considerable effort from our group has been placed to determine the physical parameters of Lucite to be used within the Monte Carlo simulations. The effects of density, ionization potential, tracking step size, target volume size, selected physics lists, etc. have been investigated in part due to the need to understand these metrics for this work.

In addition to uncertainty in biologic assays, using LET to quantitatively report the RBE of charged particles is of limited value. When the physical quantity LET was first introduced by physicists, it was intended to serve as a bridge to connect physics and biology. LET, in some conditions, is convenient to explain radiobiologic observations. However, when the LET spectrum is broad, such as at the Bragg peak or beyond, the usage of an averaged quantity such as  $LET_d$  cannot reflect the total effect of cell kill from all protons in the spectrum and may introduce inaccuracy in reporting and quantifying RBE. Previous studies from our group have shown that two very different LET spectra can result in the same  $LET_d$  but cause distinguishable cell survivals (125).

Despite these limitations, LET continues to be applied in particle radiobiology due to its conceptual simplicity and convenience. Although using LET as a qualitative indicator of biological effect can be convenient, one must be cautious when applying LET to quantify RBE because doing so may result in misleading conclusions (3). In the ICRU Report No. 78 the committee stated that LET has utility in understanding the variation of RBE, but that LET does not predict biological response with high accuracy for different cell or tissue systems (10). In addition, the ICRU Report No. 86 warns that the use of macroscopic physical quantities such as dose and  $LET_d$  may obscure the finer details of the interactions between ionizing particles and the biological system such as a cells or DNA (126). To overcome the limitations of using LET, microdosimetry was introduced (127, 128). Our group is working towards using microdosimetry to measure the stochastic analogs of dose and LET, specific energy and lineal energy, to describe the detailed energy deposition spectrum at a small site (micrometer scale) in order to better describe the consequent biologic effects.

All results presented here are derived from *in vitro* or modified *ex vivo* systems. The lack of *in vivo* biological response data is the main shortcoming of this work. While the correlation between the clonogenic assay and tumor control probability is well established, the setup to perform LET-based *in vivo* experiments in small animals is technically challenging requiring high-precision custom holders (9, 50-53). This line of work is being pursued and ongoing at the MD Anderson Proton Therapy Center.

An additional shortcoming of the presented work is the limited number of cell lines and RBMTs used. Having developed the HT particle therapy irradiation methodology and gained experience with its application including establishing the required infrastructure will enable for immediate additional experiments. Future studies will focus on expanding the repertoire of characterized cell lines. This is an especially significant task as there is data suggesting proton RBE is dependent on a cell's mutational profile. In particular, Liu et al. found increased proton radiation sensitivity to be related to mutations in the Fanconi anemia pathway. Their results are indicative of diverging DNA damage induction between photons and clinically used protons (111). The identification of genetic markers correlated to increased radiosensitivity to radiations containing higher LETs than photons could be used to improve therapeutic outcomes by patient treatment stratification. The costs associated with RBMT organoid model were prohibitive in the expansion of the studies which is why only 3 LETs are presented in this work. With additional funding, the entire range of LETs present within a given ion beam will be sampled.

Overall, the HT measurements of proton beams indicate expected increases in RBE with increasing LET. This phenomenon is especially pertinent at and beyond the Bragg peak of the proton beam (Figure 103). Within the current clinical context, these findings indicate a

non-static RBE which increases with depth and reaches a peak at the farthest distal regions of an SOBP (Figure 104). Based on these findings, it will now be possible for the increased biological effectiveness to be accounted for in treatment planning (Figure 105). To achieve a biologically optimized IMPT treatment, the high LET regions of the beam would be preferentially shifted within the tumor volume. One method this effect could be achieved is with a form of proton-arc therapy; however, for the time, such a treatment would be difficult to deliver due to the current size and subsequent rotation speed of gantries. Our results imply that the evaluation of biologic effect must ensure comprehensive characterization and suggest that additional studies using high-precision methods are required to further advance the development of models of biologic effect for biologically optimized treatment planning.



### 148.8 MeV, NSCLC H460 cells

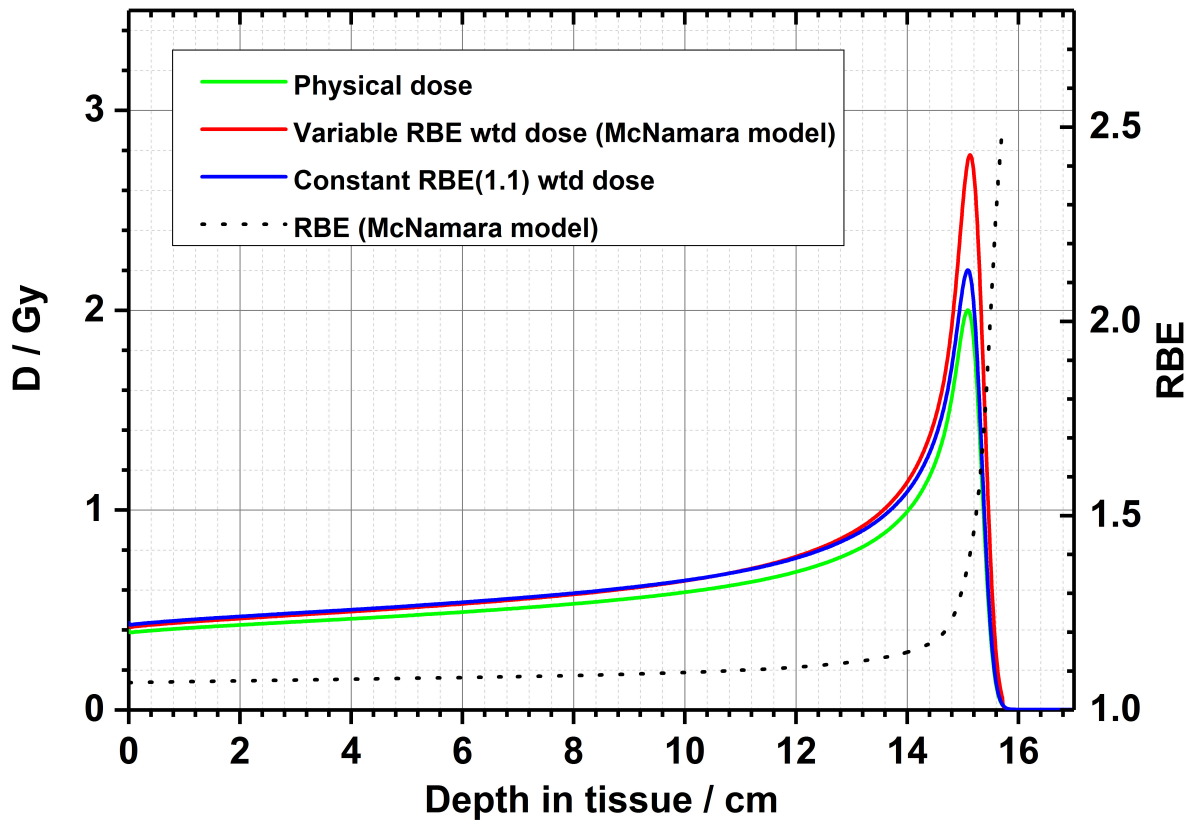


Figure 103. Application of measured RBEs to pristine proton beam. The data measured from the HT clonogenic experiments can be applied to the physical dose (green) deposited to weight the dose by the expected biological effects produced from a scanned proton beam in an LET dependent manner using a biological response model such as the McNamara model (red)(84). The expected RBE increase with LET serves to increase the differential biological effects expected for a proton beam compared to a static RBE vs LET response (blue).

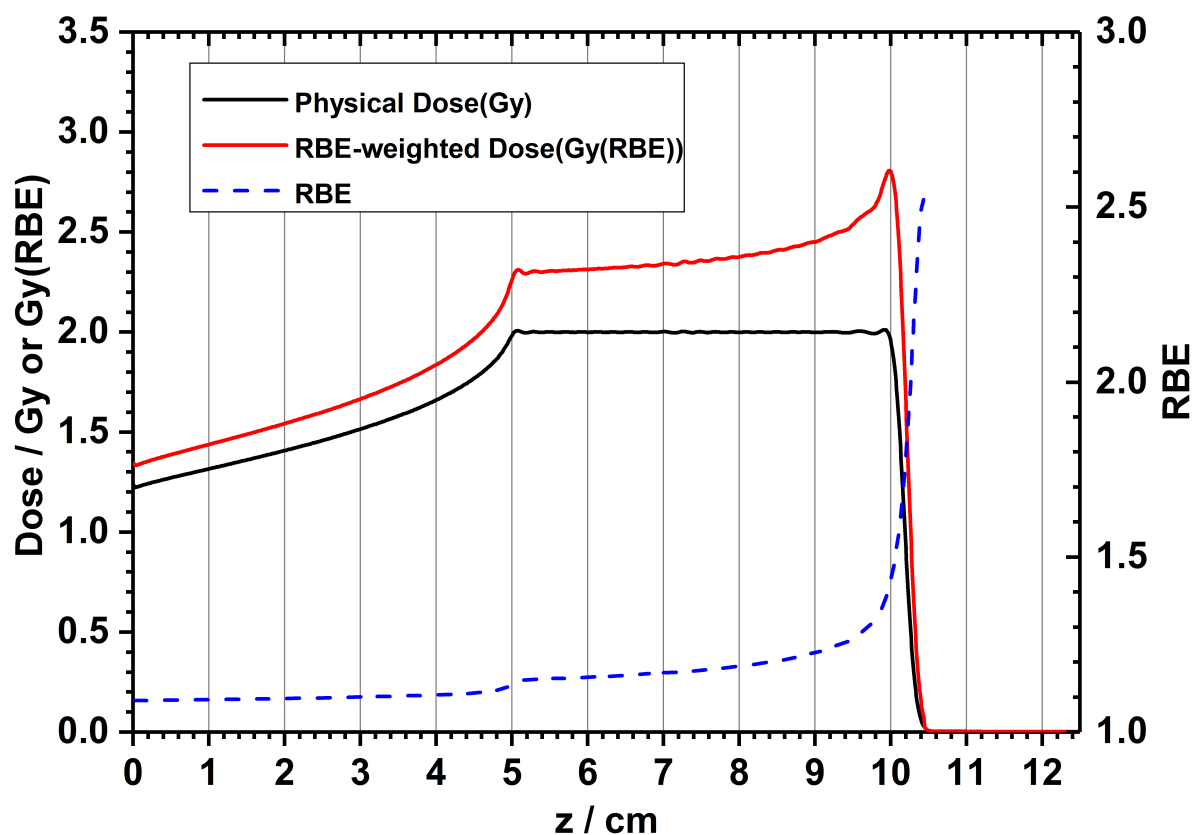


Figure 104. RBEs applied to a traditional SOBP. In the context of the SOBPs currently used in clinical practice, the application of the modeled RBE results yield an expected increase in the biologically-weighted dose with increasing depth (red). This biological effect would be most prominent in at the end and within the distal fall off of the SOBP.

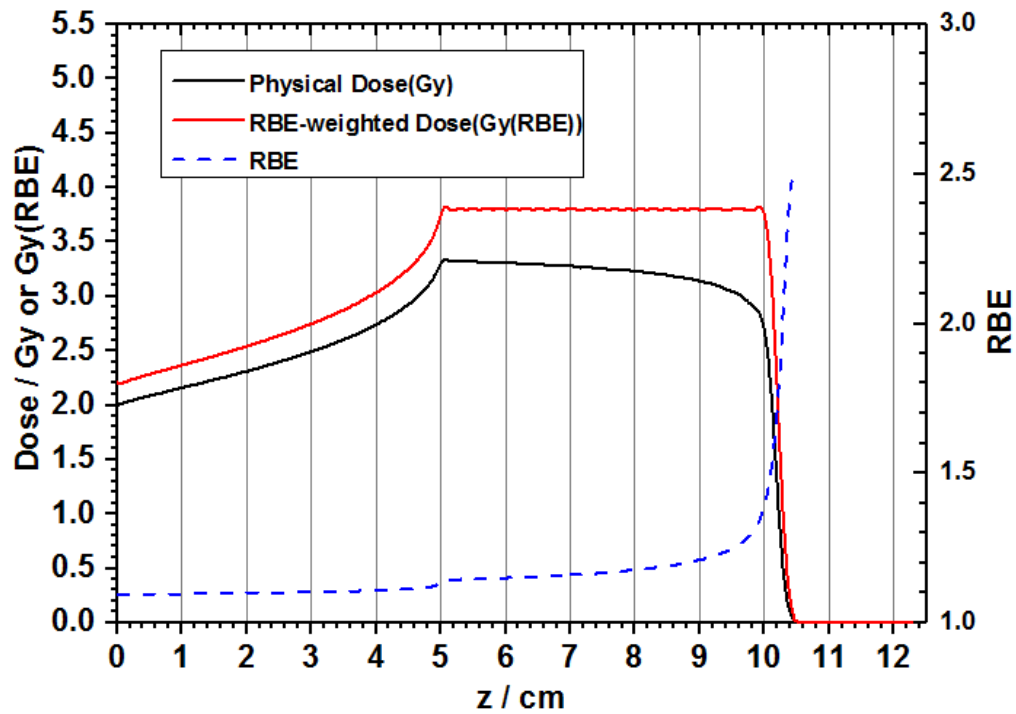


Figure 105. Achieving a uniform SOBP response. Within the present results, to achieve a uniformly effective biological response with protons (red) requires the physical dose (black) be lowered with depth in the SOBP. This dose deposition profile contains features analogous to those in clinically used carbon ion plans.

## Conclusion

We have developed a methodology to perform high-throughput irradiations with therapeutic particle beams. Using this framework, we have found the RBE to rapidly rise for LETs present in the distal portions of protons beams in several *in vitro* biological response models including adherent lung cancer cell lines, glioblastoma stem cell spheroidal cultures, and normal rat brain microtissue organoids. Taken together, our results indicate that the biological damage caused by proton radiation systematically increases with the LET of the proton exposure for both cancerous and normal tissues. This finding suggests a non-static proton RBE should be taken into consideration when performing treatment planning, especially when using scanning beams. These results are applicable to traditional SOBPs in areas that are subject to the lateral and distal portion of a beam where the resulting dose deposition is from a single initial beam energy. In general practice these portions of the beam are placed beyond the tumor volume, within the normal tissue. Overall, the proton results suggest that therapeutic gains may be achieved for proton therapy if the higher LET regions of the beam are selectively placed within the tumor volume by reducing the biologically effective dose received by the normal tissue while increasing the biologically effective dose received by the tumor. The selective placement of higher LETs regions of the beams is possible with the increasing use of IMPT.

While protons certainly offer improved dose distributions compared with current photon-based therapies, with the potential to reduce normal tissue toxicities and late effects, the region of the beam exhibiting significantly increased biologic activity, at and beyond the Bragg peak, is a relatively small region of the total beam when compared to heavier ions. This fact coupled with tissue repair repopulation effects and variations in patient setup over

the course of a protracted fractionated treatment has conceivably played a significant role in why the use of a static proton RBE value of 1.1 has been clinically effective with acceptable rates of radiation induced side effects. However, a recent study by Peeler et al. detected the first clinically derived evidence of dose and LET-dependent variable proton RBE in pediatric ependymoma patients using MRI imaging changes (129). The results presented within this work as well as found in the literature indicate that increased biological effects would be observed in cases where the most biologically active portion of the beam is consistently delivered. Within the current clinical environment of utilizing SOBPs, as patient setup uncertainties are reduced or if special procedures involving hypofractionation are utilized, additional toxicities would be expected in regions distal to the tumor volume. Utilizing biologically-weighted IMPT will enable the delivery of protons to achieve optimal outcomes.

Looking towards the future of particle therapy, ions heavier than protons exhibit increased differential and absolute biological effects over the entire beam range. Of major importance are recent studies demonstrating unique biological consequences following heavy ion therapy, in particular reduced metastatic potential and host-immune activation against the tumor (6, 7, 35-38). Additional study is still required to appropriately cover the range of potential biological outcomes for the numerous subtypes of cancer. Additionally, this data is required to benchmark the results of comprehensive biophysical models needed for treatment planning to the unique conditions present within the therapeutic region of the beam as well as the fragmentation tail of heavier ion beams. It is the author's hope that the results presented or the application of the general methodology developed to produce high-throughput irradiation data will be utilized in part to aid in this pursuit. In conclusion, the current results presented, as well as global ongoing studies coupled with cost reducing technological

developments present a future full of potential for the application of charged particle radiation in the eradication of cancer.

## References

1. Baskar R, Lee KA, Yeo R, Yeoh KW. 2012. Cancer and radiation therapy: current advances and future directions. *Int J Med Sci* 9: 193-9
2. Delaney G, Jacob S, Featherstone C, Barton M. 2005. The role of radiotherapy in cancer treatment: estimating optimal utilization from a review of evidence-based clinical guidelines. *Cancer* 104: 1129-37
3. Hall EJ, Giaccia AJ. 2006. *Radiobiology for the Radiologist*: Lippincott Williams & Wilkins
4. Marx V. 2014. Cancer treatment: Sharp shooters. *Nature* 508: 133-8
5. Friedrich T, Scholz U, Elsasser T, Durante M, Scholz M. 2013. Systematic analysis of RBE and related quantities using a database of cell survival experiments with ion beam irradiation. *J Radiat Res* 54: 494-514
6. Matsunaga A, Ueda Y, Yamada S, Harada Y, Shimada H, Hasegawa M, Tsujii H, Ochiai T, Yonemitsu Y. 2010. Carbon-ion beam treatment induces systemic antitumor immunity against murine squamous cell carcinoma. *Cancer* 116: 3740-8

7. Fernandez-Gonzalo R, Baatout S, Moreels M. 2017. Impact of Particle Irradiation on the Immune System: From the Clinic to Mars. *Front Immunol* 8: 177
8. Paganetti H, Niemierko A, Ancukiewicz M, Gerweck LE, Goitein M, Loeffler JS, Suit HD. 2002. Relative biological effectiveness (RBE) values for proton beam therapy. *International Journal of Radiation Oncology\*Biology\*Physics* 53: 407-21
9. Paganetti H. 2014. Relative biological effectiveness (RBE) values for proton beam therapy. Variations as a function of biological endpoint, dose, and linear energy transfer. *Phys Med Biol* 59: R419-72
10. ICRU. 2007. PRESCRIBING, RECORDING, AND REPORTING PROTON-BEAM THERAPY (ICRU Report 78). *J ICRU* 7: NP
11. Guan F, Bronk L, Titt U, Lin SH, Mirkovic D, Kerr MD, Zhu XR, Dinh J, Sobieski M, Stephan C, Peeler CR, Taleei R, Mohan R, Grosshans DR. 2015. Spatial mapping of the biologic effectiveness of scanned particle beams: towards biologically optimized particle therapy. *Sci Rep* 5: 9850
12. Dinh JQ, Mahajan A, Palmer MB, Grosshans DR. 2012. Particle therapy for central nervous system tumors in pediatric and adult patients. *Translational Cancer Research* 1: 137-49



13. Wroe AJ, Bush DA, Slater JD. 2014. Immobilization considerations for proton radiation therapy. *Technol Cancer Res Treat* 13: 217-26
14. Hanahan D, Weinberg RA. 2000. The hallmarks of cancer. *Cell* 100: 57-70
15. Hanahan D, Weinberg RA. 2011. Hallmarks of cancer: the next generation. *Cell* 144: 646-74
16. Calugaru V, Nauraye C, Noel G, Giocanti N, Favaudon V, Megnin-Chanet F. 2011. Radiobiological characterization of two therapeutic proton beams with different initial energy spectra used at the Institut Curie Proton Therapy Center in Orsay. *Int J Radiat Oncol Biol Phys* 81: 1136-43
17. Grosshans DR, Zhu XR, Melancon A, Allen PK, Poenisch F, Palmer M, McAleer MF, McGovern SL, Gillin M, DeMonte F, Chang EL, Brown PD, Mahajan A. 2014. Spot scanning proton therapy for malignancies of the base of skull: treatment planning, acute toxicities, and preliminary clinical outcomes. *Int J Radiat Oncol Biol Phys*. 90: 540-6. doi: 10.1016/j.ijrobp.2014.07.005. Epub Sep 26.
18. Zhu XR, Poenisch F, Li H, Zhang X, Sahoo N, Wu RY, Li X, Lee AK, Chang EL, Choi S, Pugh T, Frank SJ, Gillin MT, Mahajan A, Grosshans DR. 2014. A single-field integrated boost treatment planning technique for spot scanning proton therapy. *Radiat Oncol*. 9:202.: 10.1186/748-717X-9-202.

19. Dinh J, Stoker J, Georges RH, Sahoo N, Zhu XR, Rath S, Mahajan A, Grosshans DR. 2013. Comparison of proton therapy techniques for treatment of the whole brain as a component of craniospinal radiation. *Radiat Oncol* 8: 289
20. Safai S, Trofimov A, Adams JA, Engelsman M, Bortfeld T. 2013. The rationale for intensity-modulated proton therapy in geometrically challenging cases. *Phys Med Biol* 58: 6337-53
21. Frank SJ, Cox JD, Gillin M, Mohan R, Garden AS, Rosenthal DI, Gunn GB, Weber RS, Kies MS, Lewin JS, Munsell MF, Palmer MB, Sahoo N, Zhang X, Liu W, Zhu XR. 2014. Multifield optimization intensity modulated proton therapy for head and neck tumors: a translation to practice. *Int J Radiat Oncol Biol Phys*. 89: 846-53. doi: 10.1016/j.ijrobp.2014.04.019. Epub May 24.
22. Giantsoudi D, Adams J, MacDonald SM, Paganetti H. 2017. Proton Treatment Techniques for Posterior Fossa Tumors: Consequences for Linear Energy Transfer and Dose-Volume Parameters for the Brainstem and Organs at Risk. *Int J Radiat Oncol Biol Phys* 97: 401-10
23. Munshi A, Hobbs M, Meyn RE. 2005. Clonogenic cell survival assay. *Methods Mol Med* 110: 21-8

24. Franken NA, Rodermond HM, Stap J, Haveman J, van Bree C. 2006. Clonogenic assay of cells in vitro. *Nat Protoc* 1: 2315-9
25. Chamberlain AC, Turner FM. 1952. Errors and Variations in White-Cell Counts. *Biometrics* 8: 55-65
26. Willén E. 1976. A simplified method of phytoplankton counting. *British Phycological Journal* 11: 265-78
27. Voger EA, Bussian RW. 1987. Short-term cell-attachment rates: a surface-sensitive test of cell-substrate compatibility. *J Biomed Mater Res* 21: 1197-211
28. Twentyman PR. 1979. Timing of assays: an important consideration in the determination of clonogenic cell survival both in vitro and in vivo. *Int J Radiat Oncol Biol Phys* 5: 1213-20
29. Wu RC, Schonthal AH. 1997. Activation of p53-p21waf1 pathway in response to disruption of cell-matrix interactions. *J Biol Chem* 272: 29091-8
30. Kapiszewska M, Reddy NM, Lange CS. 1991. Trypsin-induced changes in cell shape and chromatin structure result in radiosensitization of monolayer Chinese hamster V79 cells. *Int J Radiat Biol* 60: 635-46

31. Reddy NM, Kapiszewska M, Lange CS. 1992. Detection of X-ray damage repair by the immediate versus delayed plating technique is dependent on cell shape and cell concentration. *Scanning Microsc* 6: 543-55; discussion 56-9
32. Lewis JM, Truong TN, Schwartz MA. 2002. Integrins regulate the apoptotic response to DNA damage through modulation of p53. *Proc Natl Acad Sci U S A* 99: 3627-32
33. Kang MA, So EY, Ouchi T. 2012. Deregulation of DNA damage response pathway by intercellular contact. *J Biol Chem* 287: 16246-55
34. Huang HL, Hsing HW, Lai TC, Chen YW, Lee TR, Chan HT, Lyu PC, Wu CL, Lu YC, Lin ST, Lin CW, Lai CH, Chang HT, Chou HC, Chan HL. 2010. Trypsin-induced proteome alteration during cell subculture in mammalian cells. *J Biomed Sci* 17: 36
35. Ogata T, Teshima T, Kagawa K, Hishikawa Y, Takahashi Y, Kawaguchi A, Suzumoto Y, Nojima K, Furusawa Y, Matsuura N. 2005. Particle irradiation suppresses metastatic potential of cancer cells. *Cancer Res* 65: 113-20
36. Akino Y, Teshima T, Kihara A, Koder-Suzumoto Y, Inaoka M, Higashiyama S, Furusawa Y, Matsuura N. 2009. Carbon-ion beam irradiation effectively suppresses migration and invasion of human non-small-cell lung cancer cells. *Int J Radiat Oncol Biol Phys* 75: 475-81

37. Suetens A, Moreels M, Quintens R, Soors E, Buset J, Chiriotti S, Tabury K, Gregoire V, Baatout S. 2014. Dose- and time-dependent gene expression alterations in prostate and colon cancer cells after in vitro exposure to carbon ion and X-irradiation. *J Radiat Res*
38. Fujita M, Imadome K, Shoji Y, Isozaki T, Endo S, Yamada S, Imai T. 2015. Carbon-Ion Irradiation Suppresses Migration and Invasiveness of Human Pancreatic Carcinoma Cells MIAPaCa-2 via Rac1 and RhoA Degradation. *Int J Radiat Oncol Biol Phys* 93: 173-80
39. van Bree C, Rodermond HM, ten Cate R, de Vos J, Stalpers LJ, Haveman J, Medema JP, Franken NA. 2008. G0 cell cycle arrest alone is insufficient for enabling the repair of ionizing radiation-induced potentially lethal damage. *Radiat Res* 170: 184-91
40. Barendsen GW, Van Bree C, Franken NA. 2001. Importance of cell proliferative state and potentially lethal damage repair on radiation effectiveness: implications for combined tumor treatments (review). *Int J Oncol* 19: 247-56
41. Little JB. 1973. Factors influencing the repair of potentially lethal radiation damage in growth-inhibited human cells. *Radiat Res* 56: 320-33

42. Gerweck LE, Dullea R, Zaidi ST, Budach W, Hartford A. 1994. Influence of experimental factors on intrinsic radiosensitivity assays at low doses of radiation: cell multiplicity. *Radiat Res* 138: 361-6
43. Elkind MM, Whitmore GF. 1967. The Radiobiology of Cultured Mammalian Cells.
44. Rockwell S. 1985. Effects of clumps and clusters on survival measurements with clonogenic assays. *Cancer Res* 45: 1601-7
45. Pomp J, Wike JL, Ouwerkerk IJ, Hoogstraten C, Davelaar J, Schrier PI, Leer JW, Thames HD, Brock WA. 1996. Cell density dependent plating efficiency affects outcome and interpretation of colony forming assays. *Radiother Oncol* 40: 121-5
46. Sawant SG, Zheng W, Hopkins KM, Randers-Pehrson G, Lieberman HB, Hall EJ. 2002. The radiation-induced bystander effect for clonogenic survival. *Radiat Res* 157: 361-4
47. Puck TT, Marcus PI. 1956. Action of x-rays on mammalian cells. *J Exp Med* 103: 653-66

48. Nias AH, Gilbert CW, Lajtha LG, Lange CS. 1965. Clone-Size Analysis in the Study of Cell Growth Following Single or during Continuous Irradiation. *Int J Radiat Biol Relat Stud Phys Chem Med* 9: 275-90
49. Yohem KH, Bregman MD, Meyskens FL, Jr. 1987. Effect of tumor colony definition on ionizing radiation survival curves of melanoma-colony forming cells. *Int J Radiat Oncol Biol Phys* 13: 1725-33
50. Freedman VH, Shin SI. 1974. Cellular tumorigenicity in nude mice: correlation with cell growth in semi-solid medium. *Cell* 3: 355-9
51. Fiebig HH, Maier A, Burger AM. 2004. Clonogenic assay with established human tumour xenografts: correlation of in vitro to in vivo activity as a basis for anticancer drug discovery. *Eur J Cancer* 40: 802-20
52. Scholz CC, Berger DP, Winterhalter BR, Henss H, Fiebig HH. 1990. Correlation of drug response in patients and in the clonogenic assay with solid human tumour xenografts. *Eur J Cancer* 26: 901-5
53. Fertil B, Malaise EP. 1985. Intrinsic radiosensitivity of human cell lines is correlated with radioresponsiveness of human tumors: analysis of 101 published survival curves. *Int J Radiat Oncol Biol Phys* 11: 1699-707

54. Brenner DJ. 2008. The linear-quadratic model is an appropriate methodology for determining isoeffective doses at large doses per fraction. *Semin Radiat Oncol* 18: 234-9
55. Fu KK, Phillips TL, Heilbron DC, Ross G, Kane LJ. 1979. Relative Biological Effectiveness of Low- and High-LET Radiotherapy Beams for Jejunal Crypt Cell Survival at Low Doses Per Fraction. *Radiology* 132: 205-9
56. Hall EJ. 1961. The relative biological efficiency of x rays generated at 220 kVp and gamma radiation from a cobalt 60 therapy unit. *Br J Radiol* 34: 313-7
57. Spadinger I, Palcic B. 1992. The relative biological effectiveness of <sup>60</sup>Co gamma-rays, 55 kVp X-rays, 250 kVp X-rays, and 11 MeV electrons at low doses. *Int J Radiat Biol* 61: 345-53
58. Schardt D, Elsaesser T, Schulz-Ertner D. 2010. Heavy-ion tumor therapy: Physical and radiobiological benefits. *Reviews of Modern Physics* 82
59. Santivasi WL, Xia F. 2014. Ionizing radiation-induced DNA damage, response, and repair. *Antioxid Redox Signal* 21: 251-9
60. Jackson SP, Bartek J. 2009. The DNA-damage response in human biology and disease. *Nature* 461: 1071-8



61. Panier S, Boulton SJ. 2014. Double-strand break repair: 53BP1 comes into focus. *Nat Rev Mol Cell Biol* 15: 7-18
62. Kakarougkas A, Jeggo PA. 2014. DNA DSB repair pathway choice: an orchestrated handover mechanism. *Br J Radiol* 87: 20130685
63. Ceccaldi R, Rondinelli B, D'Andrea AD. 2016. Repair Pathway Choices and Consequences at the Double-Strand Break. *Trends Cell Biol* 26: 52-64
64. Groesser T, Chang H, Fontenay G, Chen J, Costes SV, Helen Barcellos-Hoff M, Parvin B, Rydberg B. 2011. Persistence of gamma-H2AX and 53BP1 foci in proliferating and non-proliferating human mammary epithelial cells after exposure to gamma-rays or iron ions. *Int J Radiat Biol* 87: 696-710
65. Markova E, Schultz N, Belyaev IY. 2007. Kinetics and dose-response of residual 53BP1/gamma-H2AX foci: co-localization, relationship with DSB repair and clonogenic survival. *Int J Radiat Biol* 83: 319-29
66. Chua ML, Somaiah N, A'Hern R, Davies S, Gothard L, Yarnold J, Rothkamm K. 2011. Residual DNA and chromosomal damage in ex vivo irradiated blood lymphocytes correlated with late normal tissue response to breast radiotherapy. *Radiother Oncol* 99: 362-6

67. Hufnagl A, Herr L, Friedrich T, Durante M, Taucher-Scholz G, Scholz M. 2015. The link between cell-cycle dependent radiosensitivity and repair pathways: a model based on the local, sister-chromatid conformation dependent switch between NHEJ and HR. *DNA Repair (Amst)* 27: 28-39
68. Banath JP, Klovov D, MacPhail SH, Banuelos CA, Olive PL. 2010. Residual gammaH2AX foci as an indication of lethal DNA lesions. *BMC Cancer* 10: 4
69. Menegakis A, Yaromina A, Eicheler W, Dorfler A, Beuthien-Baumann B, Thames HD, Baumann M, Krause M. 2009. Prediction of clonogenic cell survival curves based on the number of residual DNA double strand breaks measured by gammaH2AX staining. *Int J Radiat Biol* 85: 1032-41
70. Desai N, Davis E, O'Neill P, Durante M, Cucinotta FA, Wu H. 2005. Immunofluorescence detection of clustered gamma-H2AX foci induced by HZE-particle radiation. *Radiat Res* 164: 518-22
71. Hada M, Sutherland BM. 2006. Spectrum of complex DNA damages depends on the incident radiation. *Radiat Res* 165: 223-30
72. Schmid TE, Dollinger G, Beisker W, Hable V, Greubel C, Auer S, Mittag A, Tarnok A, Friedl AA, Molls M, Roper B. 2010. Differences in the kinetics of gamma-H2AX fluorescence decay after exposure to low and high LET radiation. *Int J Radiat Biol* 86: 682-91

73. Du G, Drexler GA, Friedland W, Greubel C, Hable V, Krucken R, Kugler A, Tonelli L, Friedl AA, Dollinger G. 2011. Spatial dynamics of DNA damage response protein foci along the ion trajectory of high-LET particles. *Radiat Res* 176: 706-15
74. Griffith LG, Swartz MA. 2006. Capturing complex 3D tissue physiology in vitro. *Nat Rev Mol Cell Biol* 7: 211-24
75. Edmondson R, Broglie JJ, Adcock AF, Yang L. 2014. Three-dimensional cell culture systems and their applications in drug discovery and cell-based biosensors. *Assay Drug Dev Technol* 12: 207-18
76. Howes AL, Richardson RD, Finlay D, Vuori K. 2014. 3-Dimensional culture systems for anti-cancer compound profiling and high-throughput screening reveal increases in EGFR inhibitor-mediated cytotoxicity compared to monolayer culture systems. *PLoS One* 9: e108283
77. Chambers KF, Mosaad EM, Russell PJ, Clements JA, Doran MR. 2014. 3D cultures of prostate cancer cells cultured in a novel high-throughput culture platform are more resistant to chemotherapeutics compared to cells cultured in monolayer. *PLoS One* 9: e111029
78. Li H, Fan X, Houghton J. 2007. Tumor microenvironment: the role of the tumor stroma in cancer. *J Cell Biochem* 101: 805-15

79. Mbeunkui F, Johann DJ, Jr. 2009. Cancer and the tumor microenvironment: a review of an essential relationship. *Cancer Chemother Pharmacol* 63: 571-82
  
80. Chen F, Zhuang X, Lin L, Yu P, Wang Y, Shi Y, Hu G, Sun Y. 2015. New horizons in tumor microenvironment biology: challenges and opportunities. *BMC Med* 13: 45
  
81. Rosenberg SA, Restifo NP, Yang JC, Morgan RA, Dudley ME. 2008. Adoptive cell transfer: a clinical path to effective cancer immunotherapy. *Nat Rev Cancer* 8: 299-308
  
82. Yang Y. 2015. Cancer immunotherapy: harnessing the immune system to battle cancer. *J Clin Invest* 125: 3335-7
  
83. Birgersdotter A, Sandberg R, Ernberg I. 2005. Gene expression perturbation in vitro--a growing case for three-dimensional (3D) culture systems. *Semin Cancer Biol* 15: 405-12
  
84. McNamara AL, Schuemann J, Paganetti H. 2015. A phenomenological relative biological effectiveness (RBE) model for proton therapy based on all published in vitro cell survival data. *Phys Med Biol* 60: 8399-416

85. Wilkens JJ, Oelfke U. 2004. A phenomenological model for the relative biological effectiveness in therapeutic proton beams. *Phys Med Biol* 49: 2811-25
86. Carabe A, Moteabbed M, Depauw N, Schuemann J, Paganetti H. 2012. Range uncertainty in proton therapy due to variable biological effectiveness. *Physics in Medicine and Biology* 57: 1159
87. Wedenberg M, Lind BK, Hårdemark B. 2013. A model for the relative biological effectiveness of protons: the tissue specific parameter  $\alpha/\beta$  of photons is a predictor for the sensitivity to LET changes. *Acta oncologica* 52: 580-8
88. Chen Y, Ahmad S. 2012. Empirical model estimation of relative biological effectiveness for proton beam therapy. *Radiation protection dosimetry* 149: 116-23
89. Grün R, Friedrich T, Krämer M, Scholz M. 2017. Systematics of relative biological effectiveness measurements for proton radiation along the spread out Bragg peak: experimental validation of the local effect model. *Physics in Medicine and Biology* 62: 890

90. Frese MC, Yu VK, Stewart RD, Carlson DJ. 2012. A mechanism-based approach to predict the relative biological effectiveness of protons and carbon ions in radiation therapy. *Int J Radiat Oncol Biol Phys* 83: 442-50
91. Hawkins RB. 1994. A statistical theory of cell killing by radiation of varying linear energy transfer. *Radiat Res* 140: 366-74
92. Kase Y, Kanai T, Matsufuji N, Furusawa Y, Elsässer T, Scholz M. 2007. Biophysical calculation of cell survival probabilities using amorphous track structure models for heavy-ion irradiation. *Physics in Medicine and Biology* 53: 37
93. Butts J, Katz R. 1967. Theory of RBE for heavy ion bombardment of dry enzymes and viruses. *Radiat Res* 30: 855-71
94. Polster L, Schuemann J, Rinaldi I, Burigo L, McNamara AL, Stewart RD, Attili A, Carlson DJ, Sato T, Méndez JR. 2015. Extension of TOPAS for the simulation of proton radiation effects considering molecular and cellular endpoints. *Physics in Medicine and Biology* 60: 5053
95. Allison J, Amako K, Apostolakis J, Araujo H, Dubois PA, Asai M, Barrand G, Capra R, Chauvie S, Chytrcek R. 2006. Geant4 developments and applications. *IEEE TRANSACTIONS ON NUCLEAR SCIENCE* 53: 270-8

96. Agostinelli S, Allison J, Amako K, Apostolakis J, Araujo H, Arce P, Asai M, Axen D, Banerjee S. 2003. Geant4—a simulation toolkit. *Nuclear Instruments and Methods in Physics Research Section A* 506: 250-303
97. Lundholt BK, Scudder KM, Pagliaro L. 2003. A simple technique for reducing edge effect in cell-based assays. *J Biomol Screen* 8: 566-70
98. Levasseur LM, Faessel H, Slocum HK, Greco WR. 1998. Implications for clinical pharmacodynamic studies of the statistical characterization of an in vitro antiproliferation assay. *J Pharmacokinet Biopharm* 26: 717-33
99. Demidenko E. 2010. Three endpoints of in vivo tumour radiobiology and their statistical estimation. *Int J Radiat Biol* 86: 164-73
100. Preibisch S, Saalfeld S, Tomancak P. 2009. Globally optimal stitching of tiled 3D microscopic image acquisitions. *Bioinformatics* 25: 1463-5
101. Chaudhary P, Marshall TI, Perozziello FM, Manti L, Currell FJ, Hanton F, McMahon SJ, Kavanagh JN, Cirrone GAP, Romano F, Prise KM, Schettino G. 2014. Relative Biological Effectiveness Variation Along Monoenergetic and Modulated Bragg Peaks of a 62-MeV Therapeutic Proton Beam: A Preclinical Assessment. *International Journal of Radiation Oncology\*Biophysics* 90: 27-35

102. Britten RA, Nazaryan V, Davis LK, Klein SB, Nichiporov D, Mendonca MS, Wolanski M, Nie X, George J, Keppel C. 2013. Variations in the RBE for cell killing along the depth-dose profile of a modulated proton therapy beam. *Radiat Res* 179: 21-8
103. Belli M, Bettega D, Calzolari P, Cera F, Cherubini R, Dalla Vecchia M, Durante M, Favaretto S, Gialanella G, Grossi G, Marchesini R, Moschini G, Piazzola A, Poli G, Pugliese M, Saporita O, Scamporrì P, Simone G, Sorrentino E, Tabocchini MA, Tallone L, Tiveron P. 2000. Inactivation of human normal and tumour cells irradiated with low energy protons. *Int J Radiat Biol* 76: 831-9
104. Petrovic I, Ristic-Fira A, Todorovic D, Koricanac L, Valastro L, Cirrone P, Cuttone G. 2010. Response of a radioresistant human melanoma cell line along the proton spread-out Bragg peak. *Int J Radiat Biol* 86: 742-51
105. Tracy BL, Stevens DL, Goodhead DT, Hill MA. 2015. Variation in RBE for Survival of V79-4 Cells as a Function of Alpha-Particle (Helium Ion) Energy. *Radiat Res* 184: 33-45
106. Folkard M, Prise KM, Vojnovic B, Newman HC, Roper MJ, Michael BD. 1996. Inactivation of V79 cells by low-energy protons, deuterons and helium-3 ions. *Int J Radiat Biol* 69: 729-38



107. Furusawa Y, Fukutsu K, Aoki M, Itsukaichi H, Eguchi-Kasai K, Ohara H, Yatagai F, Kanai T, Ando K. 2000. Inactivation of aerobic and hypoxic cells from three different cell lines by accelerated (3)He-, (12)C- and (20)Ne-ion beams. *Radiat Res* 154: 485-96
108. Weyrather WK, Ritter S, Scholz M, Kraft G. 1999. RBE for carbon track-segment irradiation in cell lines of differing repair capacity. *Int J Radiat Biol* 75: 1357-64
109. Belli M, Cera F, Cherubini R, Dalla Vecchia M, Haque AM, Ianzini F, Moschini G, Saporita O, Simone G, Tabocchini MA, Tiveron P. 1998. RBE-LET relationships for cell inactivation and mutation induced by low energy protons in V79 cells: further results at the LNL facility. *Int J Radiat Biol* 74: 501-9
110. Taleei R, Guan F, Peeler C, Bronk L, Patel D, Mirkovic D, Grosshans DR, Mohan R, Titt U. 2016. Monte Carlo simulations of (3)He ion physical characteristics in a water phantom and evaluation of radiobiological effectiveness. *Med Phys* 43: 761-76
111. Liu Q, Ghosh P, Magpayo N, Testa M, Tang S, Gheorghiu L, Biggs P, Paganetti H, Efsthathiou JA, Lu HM, Held KD, Willers H. 2015. Lung cancer cell line screen links fanconi anemia/BRCA pathway defects to increased relative biological effectiveness of proton radiation. *Int J Radiat Oncol Biol Phys* 91: 1081-9

112. Lin SH, Zhang J, Giri U, Stephan C, Sobieski M, Zhong L, Mason KA, Molkentine J, Thames HD, Yoo SS, Heymach JV. 2014. A high content clonogenic survival drug screen identifies mek inhibitors as potent radiation sensitizers for KRAS mutant non-small-cell lung cancer. *J Thorac Oncol* 9: 965-73
113. Katz D, Ito E, Lau KS, Mocanu JD, Bastianutto C, Schimmer AD, Liu FF. 2008. Increased efficiency for performing colony formation assays in 96-well plates: novel applications to combination therapies and high-throughput screening. *Biotechniques* 44: ix-xiv
114. Choudhry P. 2016. High-Throughput Method for Automated Colony and Cell Counting by Digital Image Analysis Based on Edge Detection. *PLoS One* 11: e0148469
115. Niyazi M, Niyazi I, Belka C. 2007. Counting colonies of clonogenic assays by using densitometric software. *Radiat Oncol* 2: 4
116. Ivashkevich AN, Martin OA, Smith AJ, Redon CE, Bonner WM, Martin RF, Lobachevsky PN. 2011. gammaH2AX foci as a measure of DNA damage: a computational approach to automatic analysis. *Mutat Res* 711: 49-60
117. Hodzic J, Dingjan I, Maas MJ, van der Meulen-Muileman IH, de Menezes RX, Heukelom S, Verheij M, Gerritsen WR, Geldof AA, van Triest B, van

- Beusechem VW. 2015. A cell-based high-throughput screening assay for radiation susceptibility using automated cell counting. *Radiat Oncol* 10: 55
118. Gerelchuluun A, Manabe E, Ishikawa T, Sun L, Itoh K, Sakae T, Suzuki K, Hirayama R, Asaithamby A, Chen DJ, Tsuboi K. 2015. The major DNA repair pathway after both proton and carbon-ion radiation is NHEJ, but the HR pathway is more relevant in carbon ions. *Radiat Res* 183: 345-56
  119. Fontana AO, Augsburger MA, Grosse N, Guckenberger M, Lomax AJ, Sartori AA, Pruschy MN. 2015. Differential DNA repair pathway choice in cancer cells after proton- and photon-irradiation. *Radiother Oncol* 116: 374-80
  120. Greene-Schloesser D, Robbins ME, Peiffer AM, Shaw EG, Wheeler KT, Chan MD. 2012. Radiation-induced brain injury: A review. *Front Oncol* 2: 73
  121. Al-Jahdari WS, Suzuki Y, Yoshida Y, Hamada N, Shirai K, Noda SE, Funayama T, Sakashita T, Kobayashi Y, Saito S, Goto F, Nakano T. 2009. The radiobiological effectiveness of carbon-ion beams on growing neurons. *Int J Radiat Biol* 85: 700-9
  122. Kaminuma T, Suzuki Y, Shirai K, Mizui T, Noda SE, Yoshida Y, Funayama T, Takahashi T, Kobayashi Y, Shirao T, Nakano T. 2010. Effectiveness of carbon-ion beams for apoptosis induction in rat primary immature hippocampal neurons. *J Radiat Res* 51: 627-31

123. Merz F, Gaunitz F, Dehghani F, Renner C, Meixensberger J, Gutenberg A, Giese A, Schopow K, Hellwig C, Schafer M, Bauer M, Stocker H, Taucher-Scholz G, Durante M, Bechmann I. 2013. Organotypic slice cultures of human glioblastoma reveal different susceptibilities to treatments. *Neuro Oncol* 15: 670-81
124. Yoshida Y, Suzuki Y, Al-Jahdari WS, Hamada N, Funayama T, Shirai K, Katoh H, Sakashita T, Kobayashi Y, Nakano T. 2012. Evaluation of the relative biological effectiveness of carbon ion beams in the cerebellum using the rat organotypic slice culture system. *J Radiat Res* 53: 87-92
125. Guan F, Bronk L, Kerr M, Wang X, Li Y, Peeler C, Sahoo N, Patel D, Mirkovic D, Titt U. 2016. WE-H-BRA-05: Investigation of LET Spectral Dependence of the Biological Effects of Therapeutic Protons. *Medical Physics* 43: 3843-
126. ICRU. 2011. Report 86: Quantification and reporting of low-dose and other heterogeneous exposures. *J ICRU* 11: 1-77
127. Zaider M, Rossi BHH, Zaider M. 1996. *Microdosimetry and its Applications*: Springer
128. ICRU. 1983. Report 36: Microdosimetry, International Commission on Radiation Units and Measurements, Bethesda, MD, 1983. *ICRU*

129. Peeler CR, Mirkovic D, Titt U, Blanchard P, Gunther JR, Mahajan A, Mohan R, Grosshans DR. 2016. Clinical evidence of variable proton biological effectiveness in pediatric patients treated for ependymoma. *Radiother Oncol* 121: 395-401

## **Vita**

Lawrence Fernando Bronk was born in Royal Tunbridge Wells, Tonbridge, Kent UK on February 4, 1986, the son of Minerva and Lawrence Ronald. After completing his work at Cypress Creek High School, Houston, Texas in 2004, he entered The Massachusetts Institute of Technology (MIT) in Cambridge, Massachusetts. He received the degree of Bachelor of Science with a major in physics from MIT in June, 2008. For one year, he worked as a graduate research assistant in the Department of Nuclear Engineering at The University of Texas in Austin. He received the degree of Master of Science in Engineering with a major in nuclear engineering from The University of Texas in Austin in May, 2010. In August of 2009 he entered The University of Texas MD Anderson Cancer Center UTHealth Graduate School of Biomedical Sciences.

Permanent address:

2300 Old Spanish Trail #1135  
Houston, Texas 77054